Vers une source mésoscopique à n-électrons basée sur des pulses de tensions Lorentziens

Julie Dubois

THESE DE DOCTORAT DE
L'UNIVERSITE PIERRE ET MARIE CURIE

Spécialité: Physique quantique

Physique de la Région Parisienne
(Ecole Doctorale)

Présentée par

Mme Julie Dubois

Pour obtenir le grade de

DOCTEUR de L'UNIVERSITÉ PIERRE ET MARIE CURIE

Sujet de la thèse:

Vers une source mésoscopique à n-électrons basée sur des pulses de tensions Lorentziens
Towards a n-electron source based on Lorentzian voltage pulses

Soutenue le 4 octobre 2012

Devant le jury composé de:

M. Jean-Marc BERROIR,	Examinateur
Mme Hélène BOUCHIAT,	Examinatrice
M. Christian GLATTLI,	Directeur de thèse
M. Leonid LEVITOV,	Rapporteur
M. Thierry MARTIN,	Examinateur
M. Tristan MEUNIER,	Rapporteur

Towards a n-electron source based on Lorentzian voltage pulses

Injecting a small controlled number of indistinguishable electrons in a quantum ballistic conductor opens the way to new kind of quantum experiments, involving interference with several electrons. This requires the implementation of a yet never done reliable source that can emit a coherent wave-packet of an arbitrary number of electrons above the Fermi sea. Here we consider an electron source based on short time voltage pulses, which is expected to deliver q quanta of charge per pulse when the flux $q = \int eV(t)dt/h$ is integer [84]. For most of the voltage pulses V(t), this charge is accompagnied by a statistical number N_+ of quasi-particles (holes and electrons), the total charge of which being neutral. However, for Lorentzian-shaped voltage pulses, these extra neutral excitations remarkably vanish, as shown by Ivanov et al [59]. This leads to a minimal excitation n-electron source, with a reliable number of emitted quasi-particles.

In this thesis we present a first attempt to experimentally implement this n-electron source. Sub-nanosecond pulses are applied on a quantum point contact (QPC) realized in a clean two-dimensionnal electron gas of GaAs/AlGaAs heterostructure. When the single channel of the QPC is not perfectly transmitted, shot-noise occurs and reveals the excess number N_+ of quasi-particles emitted by the pulses. Thus the property of the minimal excitation number of the integer Lorentzian pulses can be tested. Moreover, shot-noise gives access to the spectroscopy of the photo-absorption and photon-emission processes that give rise to the excited quasi-particles. In our experiments, the sine, square and Lorentzian shape pulses are compared. The distinct character of the quasi-particles excitations of Lorentzian voltage pulses is demonstrated and results are in quantitative agreement with the theoretical predictions at finite temperature.

keywords: n-quasiparticle source, ballistic quantum wire, shotnoise

Vers une source mésoscopique à n-électrons basée sur des pulses de tension Lorentziens

Injecter quelques quasi-particules indiscernables de manière contrôlée dans un conducteur mésoscopique ouvrirait un champ d'investigation en optique électronique, en permettant notamment des expériences d'interférences à quelques électrons. Ceci nécessite de disposer d'une source inédite de quasi-particule capable d'émettre de manière systématique un nombre n arbitraire de quasi-particules formant un paquet d'onde cohérent.

Considérons une source de courant résultant de l'application de pulses de tensions V(t) sur un canal unidimensionnel balistique. Celle-ci émet exactement q quanta de charge, où le nombre de flux $q = \int eV(t)dt/h$ est entier [84] . Généralement, cette charge est accompagnée d'une quantité statistique N_+ d'électrons et de trous, de charge totale nulle. Cependant, ces excitations supplémentaires disparaissent pour des pulses Lorentziens, comme l'ont démontré Ivanov et al [59]. Alors le nombre de quasi-particules émises est certain, et on peut ainsi réaliser une source fiable à n-électrons indiscernable.

Dans ce travail de thèse, nous proposons de mettre en uvre cette source à n-électrons en appliquant des pulses de tension sub-nanosecondes sur un contact ponctuel quantique (QPC) réalisé sur le gaz bidimensionnel d'électron d'une hétérostructure d'GaAs/AlGaAs. Lorsque le QPC n'est pas utilisé à transmission parfaite, le bruit de partition des quasi-particules sur cette lame séparatrice permet de détecter le nombre de quasi-particules produites en excès N_+. Cette mesure permet de tester la disparition de N_+ pour des pulses Lorentziens injectant des charges entières, mais apporte également bien d'autres informations sur la nature des quasi-particules excitées par des pulses de tensions, notamment une spectroscopie des processus d'absorption et d'émission de photon qui leur donnent naissance. Nos expériences comparent des pulses Lorentziens, sinusodaux et carrés et met en évidence les particularités de l'excitation générée par les pulses Lorentziens. Les résultats expérimentaux, qui incluent également les effets de température, sont en bon accord quantitatif avec les prédictions théoriques.

mots clefs: source à n quasiparticules, conducteur unidimensionnel balistique, bruit de grenaille

Cette thèse a été préparée au sein du groupe de nanoélectronique,
Service de Physique de l'Etat Condensé (SPEC),
CEA Saclay, Orme des Merisiers,
91191 Gif-sur-Yvette Cedex FRANCE

Résumé de la thèse

0.1 Introduction

Les conducteurs mésoscopiques sont des composants dont les dimensions sont inférieures à la longueur de cohérence de phase l_ϕ des électrons et pour lesquels le caractère ondulatoire des électrons et la statistique de Fermi se manifestent dans le transport électronique. A basse température, les interactions électron-phonons se rarifient et l_ϕ est essentiellement limitée par les collisions inélastiques entre électrons, caractérisée par la longueur l_{e-e}. Celle-ci peut atteindre quelques centaines de micromètres dans le gaz bidimensionnel de l'hétérostructure d'$Al_xGa_{1-x}As/GaAs$, et dans ce gaz de Fermi, les excitations collectives de faible énergie se comportent comme des quasi-particules libres de durée de vie l_ϕ.

A l'échelle mésoscopique, les fluctuations du courant mettent en lumière la nature stochastique des processus quantiques. Par exemple, lorsque des quasi-particules traversent un canal unidimensionnel qui ne transmet pas parfaitement, elles produisent un bruit de grenaille qui traduit le processus aléatoire du passage tunnel. La distribution de probabilité $P(N)$ du transfert de N charges durant un temps t_0 au travers d'un conducteur mesoscopique permet d'accéder à toutes les informations du système [86]. Cependant l'optention des cumulants de $P(N)$ est expérimentalement difficile et se limite actuellement à quelques cumulants [53, 54, 77, 117, 146].

Une autre approche consiste à injecter quelques électrons dans le conducteur mésoscopique puis à détecter le nombre exact de charge qui en est sorti, et à répéter cette expérience jusqu'à obtenir la distribution $P(N)$. Ceci nécessite de disposer d'une source inédite capable d'injecter quelques électrons indiscernables au dessus de la mer de Fermi. Ainsi le paquet d'onde associé doit-il avoir une extension bien plus petite que l_ϕ [55]. Par rapport aux sources à électrons existantes (section 0.2), cette source apporterait une avancée supplémentaire en ouvrant le champ à de nouvelles expériences d'interférences à plusieurs électrons.

Nous appuyant sur les travaux des groupes de Levitov et Lesovik [59, 69, 84] (section 0.3), nous proposons de mettre en œuvre une telle source en appliquant des pulses de tension Lorentziens sub-nanoseconde sur un contact ponctuel quantique réalisé sur le gaz bidi-

mensionnel d'électron d'une hétérostructure d'$Al_xGa_{1-x}As/GaAs$ (section 0.4). Un montage expérimental dédié permet d'injecter des pulses de tension jusqu'à 24GHz (section0.6) et de détecter le bruit de partition proportionnel aux nombre de quasi-particules émises par pulses (section 0.5). Ainsi, l'émission de quasi-particules par des pulses de tension de différentes formes peut être étudiée pour mettre en évidence les particularités des pulses lorentziens et valider le modèle théorique proposé par Levitov et Lesovik [84, 86]. (section 0.7)

0.2 Des sources à quelques électrons pour l'électronique mésoscopique

Au cours de deux dernières décennies, plusieurs dispositifs ont été mis au point en tant que source à un électron unique. Cependant il faut distinguer, dans ces sources dites à un ou quelques électrons, les sources de quanta de charge des sources à quasi-particules

0.2.1 Les sources de quanta de charge:

La quantité qu'on cherche à contrôler est en fait la charge transferrée.

Les plus anciennes sont les pompes [112] et les tourniquets [45] à électrons, basées sur le blocage de Coulomb dans des ilots métalliques séparés par des jonctions tunnel. Pour assurer le transfert de la charge unique à travers jonctions tunnel, ces systèmes sont limités à des fréquences de cycle de l'ordre du MHz.

En 1996, Shilton et al. [127], puis Talyanskii et al. [135] mettent au point une autre source de courant, basée sur des ondes acoustiques de surface. Elle permet d'atteindre des fréquences de transfert de l'ordre du quelques GHz. Le dispositif se présente comme une longue barrière tunnel entièrement déplétée, réalisée dans un gaz bidimensionnel de l'hétérostructure de $Al_xGa_{1-x}As/GaAs$. Une onde acoustique générée par effet piezo-électrique de l'Arsenic de Gallium piège des charges dans les boites quantiques mouvantes au niveau de cette barrière. Lorsque la puissance de l'onde acoustique est suffisante, ces boites quantiques traversent la barrière et transferent des charges quantifiées d'un réservoir à l'autre.

Dans les deux technologies de source, la quantification de la charge se traduit par une quantification du courant à la valeur ef, où f est la fréquence du cycle, et la précision de ces sources peuvent atteindre des qualités métrologiques. Cependant l'excitation sous-jacente à la charge n'est pas contrôlée: le nombre et l'énergie d'électrons et de trous qui sont émis dans le circuit et qui correspondent à cette charge sont aléatoires.

De plus pour les acousto-pompes, des calculs théoriques indique des excitations de haute énergies dans des boites quantiques mouvantes, ce qui laissent à penser que les quasi-particules émises auront un temps de cohérence réduit.

En ce qui concerne les pompes à électrons, les électrons transférés sont nécessairement discernables les uns des autres au vu de la fréquence de cycle de quelques MHz.

En conséquence, l'emploi de ces pompes pour des expériences d'interférence électroniques reste limité.

0.2.2 Les sources de quasi-particules:

Ces sources cherchent à contrôler l'excitation émise dans le circuit. Elles doivent permettre de générer de manière fiable des quasi-particules indiscernables et cohérentes sur un temps appréciable afin de pouvoir les utiliser dans des expériences d'interférence à quelques électrons, ou dans des expériences déterminant la statistique de comptage complète des électrons traversant un circuit mésoscopique.

Fève et al. [36] et Mahe et al. [94] ont démontré qu'une boite quantique couplée à un réservoir par une barrière tunnel pouvait injecter de manière fiable un électron puis un trou au cours d'un cycle opératoire consistant à déplacer le dernier niveau de la boite quantique au dessus et au dessous du niveau de Fermi du réservoir. Seul un bruit haute fréquence, traduisant l'incertitude sur le temps d'échappement de la quasi-particule, persistait. C'est actuellement la source privilégiée pour aboutir à des expériences d'interférences électroniques [15, 51, 55].

Une autre technologie de pompe à électrons, remplaçant les ilôts métalliques par des boites quantiques, semblent transférer un quantum de charge sous forme d'une quasi-particule unique d'un réservoir à l'autre, même si les niveaux d'énergies atteints par ces quasi-particules ne sont pas encore bien maitrisés [66].

0.2.3 La source en pulse en tension, une nouvelle source de quasi-particules:

De part le principe de Pauli, une tension continue aux bornes d'un conducteur unidimensionnel balistique à un canal transfère un électron tous les eV/h, et ceci sans aucune fluctuation. Si un pulse de tension V(t) est appliqué durant un temps très court, tel que $e\int V(t)dt/h = q$, avec q entier, alors la charge q est transférée au travers du conducteur. Cependant, la charge q ne correspond pas généralement à $|q|$ électrons (ou $|q|$ trous) excités, car un excès de quasi-particules N_+, dont la charge totale est nulle, est en plus produite de manière statistique par le pulse de tension.

Cependant, Ivanov et al. [59] ont montré que pour des tensions V(t) correspondant à des sommes de pulses lorenztiens de charge entière de même signe, $N_+ = 0$. Ces pulses injectent uniquement q électrons ou q trous dans le circuit, et ce de manière certaine. La taille du paquet de quasi-particules est donnée par la durée du pulse, si celle-ci est petite devant le temps de cohérence, les particules sont alors indiscernables et peuvent être utilisées dans des expériences d'interférences à plusieurs électrons.

En conséquence, cette source en pulse de tension Lorentzien apparait comme une alternative séduisante pour une nouvelle source de quasi-particules.

0.3 Quel courant génère un potentiel variable sur un fil quantique?

0.3.1 Moyenne et fluctuations du courant induit par un potentiel variable

Un pulse de tension est un potentiel $V_p(t)$ dont l'intégrale temporelle $\int_{-\infty}^{\infty} V_p(t)dt$ est finie. La proposition de Levitov et Lesovik s'inscrit dans une problèmatique plus vaste du courant généré par l'application d'une tension variable $V(t)$ aux bornes d'un fil quantique. Dans notre cas, $V(t)$ sera constituée d'une répétition périodique de pulses $V_p(t)$. Considérons un conducteur balistique unidimensionnel sans interactions (figure (1)). La tension appliquée étant de quelques dizaines de microvolts, la mer de Fermi est considérée infinie et la relation de dispersion est linéarisée autour du niveau de Fermi qui est pris pour référence: $\varepsilon_{R/L} = \pm v_F p$, où v_F designe la vitesse de Fermi. De plus on considère que la chute de potentiel se produit sur une région négligeable autour de $x = 0$, c'est à dire que $V(t)$ peut être considéré comme quasi-statique durant le temps de vol des électrons au travers de cette région.

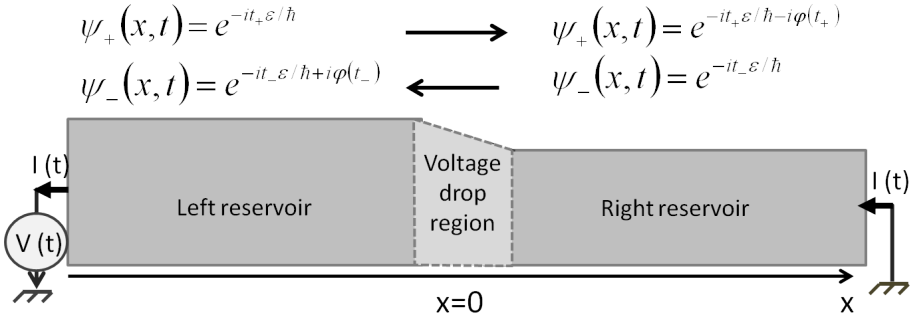

Figure 1: En traversant la chute de potentiel entre les deux réservoirs, les électrons venant de la gauche acquièrent une phase $\varphi(t_+)$, tandis que ceux venant de la droite acquièrent une phase $-\varphi(t_-)$, avec $t_+ = t - x/v_F$ et $t_- = t + x/v_F$.

Alors les états propres du système sont:

$$\psi_+ = \exp\left(-i\varepsilon\left(t - x/v_F\right) - i\frac{e}{\hbar}A\left(t - \frac{x}{v_F}\right)\Theta\left(x\right)\right) \tag{1}$$

$$\psi_- = \exp\left(-i\varepsilon\left(t + x/v_F\right) + i\frac{e}{\hbar}A\left(t + \frac{x}{v_F}\right)\Theta\left(-x\right)\right) \tag{2}$$

Ce qui s'interprète par le fait que les électrons qui traversent la chute de potentiel acquièrent une phase $\varphi(t - x/v_F)$ (resp. $-\varphi(t + x/v_F)$) lorsqu'ils se déplacent vers la droite (resp. vers la gauche). $\exp\left(i\varphi(t)\right)$ possède le spectre de Fourier suivant:

$$e^{i\varphi(t)} = \int_{-\infty}^{\infty} P^* \left(\frac{\eta}{\hbar}\right) e^{i\eta t} \frac{d\eta}{2\pi\hbar} \tag{3}$$

Lorsque V(t) est périodique, elle se décompose en une moyenne continue et une partie alternative $V(t) = V_{AC}(t) + V_{DC}$. Alors la transformée de Fourier P^* est discrète et égale au spectre P^*_{AC} de $exp(i\varphi_{AC}(t))$ translatée de $eV_{DC}/h\nu$:

$$P^*(\varepsilon) = \sum_{n=-\infty}^{\infty} P^*_{AC}(n) h\delta(\frac{\varepsilon - nh\nu - eV_{DC}}{\hbar})$$

En conséquence, un électron provenant de la gauche (resp. de la droite) et occupant l'état d'énergie ε en $x < 0$ peut absorber la quantité d'énergie η si $\eta > 0$ ou émettre η si $\eta < 0$ avec une probabilité $|P(\eta/\hbar)|^2$. Il se retrouve alors dans une superposition d'états $\varepsilon' = \varepsilon + \eta$ en $x > 0$, dont les amplitudes de probabilités sont données par la transformée de Fourier P^* de $exp(i\varphi(t))$:

$$\psi_+(x,t) = e^{(-i\varepsilon t_+ - i\varphi(t_+))} = \int_{-\infty}^{\infty} P \left(\frac{\varepsilon' - \varepsilon}{\hbar}\right) e^{-i\varepsilon' t_+} \frac{d\varepsilon}{2\pi\hbar} \tag{4}$$

$$\psi_-(x,t) = e^{(-i\varepsilon t_- + i\varphi(t_-))} = \int_{-\infty}^{\infty} P^* \left(\frac{\varepsilon' - \varepsilon}{\hbar}\right) e^{-i\varepsilon' t_-} \frac{d\varepsilon}{2\pi\hbar} \tag{5}$$

Les effets de $V(t)$ peuvent donc être analysés dans le formalisme de matrice de dispersion [22,122], en introduisant la matrice **P** qui relie les états se propageant dans la même direction:

$$P_{\varepsilon\varepsilon'} = P(\frac{\varepsilon' - \varepsilon}{\hbar}) \tag{6}$$

Si de plus l'interface entre les deux réservoirs n'est pas parfaitement transparente, la matrice **P** se combine à la matrice de transmission **S** de l'interface pour donner une matrice totale **U** qui relient les états entrant $a_\alpha(\varepsilon)$ aux états sortant $b_\alpha(\varepsilon)$:

$$\begin{pmatrix} b_L(\varepsilon) \\ b_R(\varepsilon) \end{pmatrix} \mathbf{U} \begin{pmatrix} a_L(\varepsilon) \\ a_R(\varepsilon) \end{pmatrix} = \begin{pmatrix} b_L(\varepsilon) \\ b_R(\varepsilon) \end{pmatrix} \begin{pmatrix} \mathbf{P}^\dagger & 0 \\ 0 & \mathbf{1} \end{pmatrix} \times \mathbf{S} \times \begin{pmatrix} \mathbf{P} & 0 \\ 0 & \mathbf{1} \end{pmatrix} \begin{pmatrix} a_L(\varepsilon) \\ a_R(\varepsilon) \end{pmatrix} \tag{7}$$

La matrice de dispersion **U** permet de retrouver toutes les caractéristiques du transport. Ainsi, la moyenne statistique du courant $\langle I(t) \rangle$ répond à une version dynamique de la formule de Landauer-Büttiker [23]:

$$\langle I(t,x) \rangle = \frac{e^2 D}{h} V(t - x/v_F) \tag{8}$$

où D est la transmission. Lorsque $D = 1$, la charge Q en moyenne transferrée par un pulse $V_p(t)$ est égale à $q = \varphi(\infty)/2\pi$. q est aussi égale à la charge transférée par période $eV_{DC}/h\nu$, où V_{DC} est la composante continue de la tension.

Un fil quantique polarisé par des pulses de tension pourra être utilisé comme une source à quelques électrons si la charge Q transférée par pulse est fiable, i.e. si $\sqrt{\langle \Delta Q^2 \rangle} \ll \langle Q \rangle$. Les fluctuations de la charge Q se calculent à partir du corrélateur de courant $\langle I(t)I(t') \rangle$ qu'on intègre sur le temps.

Dans le cas d'un pulse unique de flux $q = \phi(\infty)/(2\pi)$, la quantification de la charge se manifeste par le fait que les fluctuations de la charge tranferrée divergent dès que $\langle Q \rangle = q$ n'est pas entier. Plus précisemment, Lee et Levitov [82] ont montré que la variance de la charge transférée entre $[-t, t]$ par un pulse de tension d'extension $2w$ était égal à:

$$\left\langle \Delta Q^2_{[-t,t]} \right\rangle = e^2 D(1-D) \left(\frac{2}{\pi^2} \sin^2(q\pi) \ln\left(\frac{t}{w}\right) + q + o(q) \right) \tag{9}$$

Dans le cas d'une répétition périodique du pulse $V_p(t)$, les fluctuations de la charge Q sont régularisées même pour des valeurs non entières. $2\langle \Delta Q^2 \rangle \nu = S_I(0)$ est en fait égale à la densité spectrale du bruit en courant à fréquence nulle:

$$S_I(0) = 4\frac{e^2 D^2}{h} k_B T + 2\frac{e^2}{h} D(1-D) \sum_{n \in \mathbb{Z}} |P_{AC}(n)|^2 (h(q+n)\nu) \coth\left(\frac{h(q+n)\nu}{2kT} \right) \tag{10}$$

Le premier terme se compose des fluctuations thermiques dans les deux réservoirs, tandis que le deuxième terme est un bruit de partition des quasi-particules excitées par V(t) et émises dans le réservoir de droite. A température nulle:

$$S_{part}(0) = 2\frac{e^2}{h} D\,(1-D)\, h\nu\, (\langle N_e \rangle + \langle N_h \rangle) \tag{11}$$

avec les définitions des électrons et trous excités suivantes:

$$\langle N_e \rangle\, h\nu = \int_{-\infty}^{\infty} d\varepsilon \sum_{n \in \mathbb{Z}} |P_{AC}(n)|^2 (1 - f_R(\varepsilon)) f_L(\varepsilon + (q+n)h\nu) \tag{12}$$

$$\langle N_h \rangle\, h\nu = \int_{-\infty}^{\infty} d\varepsilon \sum_{n \in \mathbb{Z}} |P_{AC}(n)|^2 f_R(\varepsilon)(1 - f_L(\varepsilon + (q+n)h\nu)) \tag{13}$$

Lorsque $D < 1$ et T=0, le terme de partition dans $S_I(0)$ nous donne accès au nombre total de particules excitées $\langle N_e \rangle + \langle N_h \rangle = |q| + N_+$ qui est en général supérieur au nombre absolu de charge transferrée, d'un nombre d'excitations globalement neutre N_+. A température

finie, N_+ ne comptabilise plus strictement le nombre de quasi-particules en excès, mais nous garderons cette notation pour quantifier le bruit de partition en excès par rapport au bruit de partition de la charge transmise:

$$S_I(0) = 4\frac{e^2D^2}{h}k_BT + 2\frac{e^2}{h}D(1-D)h\nu(q\coth(\frac{qh\nu}{2k_BT}) + N_+) \tag{14}$$

0.3.2 Une source de quasi-particules parfaite

Lorsque le fil quantique transmet parfaitement (D=1) et que la température est nulle, $\langle\Delta Q^2\rangle = 0$ quelque soit $\langle\Delta Q\rangle = q$ dans le cas périodique. La charge émise par pulse (qui est aussi égale à celle émise par période) est alors certaine et le canal unidimensionnel agit comme une source idéale de quanta de charge. En revanche, il n'est pas nécessairement une bonne source de quasi-particules, car les fluctuations du nombre d'électrons et de trous excités demeurent.

De fait, les fluctuations du nombre d'électrons excités N_e sont mesurées par sa variance:

$$\left\langle\Delta N_e^2\right\rangle = \int_{-\infty}^{\infty}\int_{-\infty}^{\infty} d\varepsilon d\varepsilon' f(\varepsilon)(1-f(\varepsilon'))\left\|\int_0^{\infty} dp P^*_{p\varepsilon}P_{p\varepsilon'}\right\|^2 \tag{15}$$

A température nulle, celle-ci ne s'annulent que si P est nul sur $\mathbb{R}^+$ ou $\mathbb{R}^-$, ce qui signifie que soit $\langle N_e\rangle = 0$, soit $\langle N_h\rangle = 0$. En conséquence, les nombres d'électrons et de trous émis ne fluctuent pas si la charge transférée par pulse correspond à une excitation minimale, i.e. qu'il n'y a pas de quasi-particules produite en excès.

Ivanov et al. [59] ont montré que les seules fonctions qui vérifient cette propriété étaient les sommes de pulses Lorentziens de flux entier et de même signe. Pour ces tensions, P est nul sur $\mathbb{R}^+$ ou $\mathbb{R}^-$, si bien les électrons ne font qu'absorber ou qu'émettre de l'énergie.

La figure (2) montre l'évolution de N_+ en fonction de q pour différents trains périodiques de pulses: carrés, sinusoidaux ou Lorentzien de largeur $w = 0.1\mathcal{T}$ at zero temperature [142]. On note que N_+ passe par des minima pour q entier pour toutes ces formes de pulses, et que ces minima s'annulent uniquement pour les pulses lorentzien [59]. L'augmentation de N_+ pour des valeurs non entière de q est une riminiscence dans le cas périodique de la divergence logarithmique des fluctuations de la charge analysée par Lee et Levitov [82] dans l'équation (9). D'ailleurs l'analyse des variations de N_+ pour des lorentziens de largeurs variables w (figure (3)) montre clairement la suppression exponentielle de N_+ quelque soit q lorsque $w >> \mathcal{T}$, i.e. lorsque les pulses sont de plus en plus rapprochés les une des autres, et au contraire la divergence de N_+ lorsque les pulses sont de plus en plus éloignés.

Les oscillations de N_+ sont rapidement affectés par la température. Comme le montrent les figures (4) pour des pulses lorentzien et (5) pour des sinus, les minima locaux sont déplacés

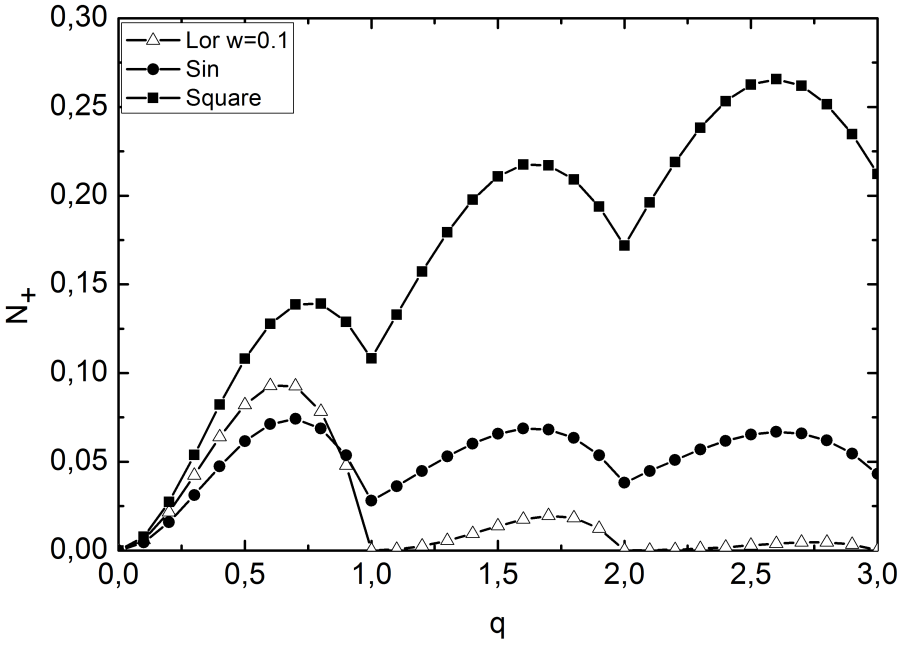

Figure 2: Nombre moyen de particules en excès N_+ en fonction du nombre de charge par pulse q pour des pulses carré, sinusoidaux et lorentziens de largeur $w = 0.1\mathcal{T}$

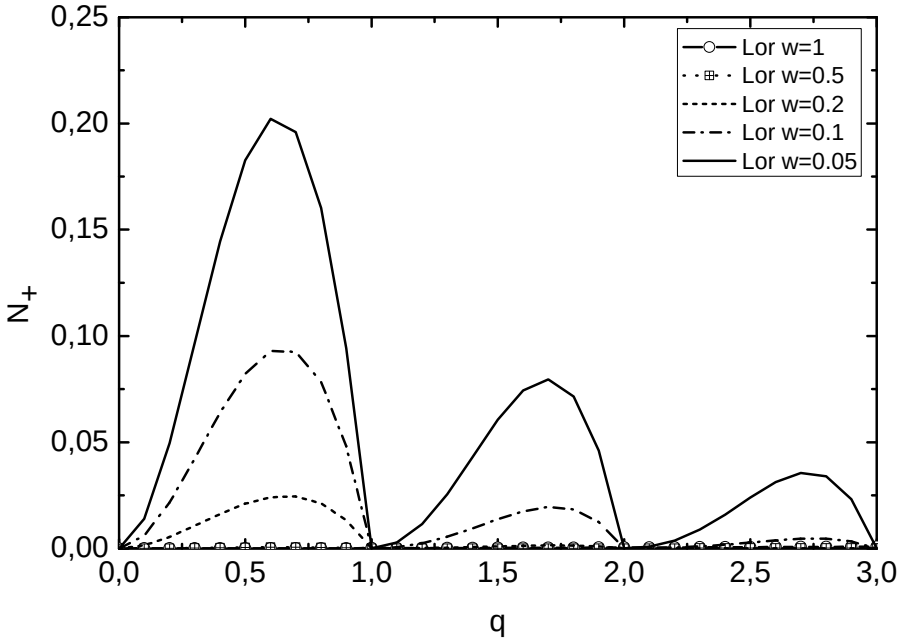

Figure 3: Nombre moyen de particules en excès N_+ en fonction du nombre de charge par pulse q pour des pulses lorentziens de largeur w

et atténués. Ils disparaissent dès que $kT > 0.2h\nu$.

Pour mesurer le nombre de quasi-particules en excès N_+ et en distinguer les minima locaux, il est donc nécessaire de travailler à des températures telles $kT/h\nu \ll 0.2$, au minimum 0.1. Dans un cryostat à dilution où les températures peuvent descendre à 15mK, ceci impose de travailler avec des pulses de tension dont la fréquence est supérieur à 3GHz. Pour des pulses lorentziens, N_+ est également affecté par la largeur des pulses, et il est préférable de travailler avec $w/\mathcal{T} < 0.2$ pour détecter un bruit en excès fini lorsque q n'est pas entier. Enfin, la sensibilité de la mesure doit dépasser les $10^{-29}A^2/Hz$, car le nombre de particules en excès N_+ reste modeste quelque soit la forme des pulses de tension.

0.4 Quel dispositif quantique pour implémenter la source de Levitov?

Le gaz bidimensionnel (2DEG) dans l'hétérostructure crystalline d'GaAs/$Al_xGa_{1-x}As$ possède à basse température des longueurs de cohérence l_ϕ dépassant la centaine de micromètres et des longueurs de collisions élastique l_e de l'ordre de 10μm: il constitue le matériau de choix de l'électronique mésoscopique. A partir du 2DEG nous proposons deux dispositifs capables de réaliser une source de Levitov, i.e. une source à n-électrons commandée par pulse de tension.

0.4.1 Le contact ponctuel quantique en champ nul

Lorsqu'on place une grille à la surface de l'hétérostructure de GaAs/$Al_xGa_{1-x}As$ et qu'on la polarise négativement, le gaz bidimensionnel se déplète localement sous la grille : on peut donc modeler capacitivement le gaz 2DEG dans son plan. Le contact ponctuel quantique (QPC) est une constriction du gaz bidimensionnel obtenu par la déplétion du gaz sous une grille constituée de deux pointes séparées de quelques centaine de nanomètre. Les fonctions d'onde électroniques se retrouvent localement quantifiées au niveau du QPC qui fonctionne comme un conducteur unidimensionnel balistique de quelques centaines de nanomètres de longueur. La conductance du QPC est donc quantifiée et présente des plateaux [141, 144]. En champ magnétique nul, lorsqu'un canal est transmis, la résistance du QPC est égal à $R_0 = 12900\Omega$, et donc très supérieure à la résistance du reste du 2DEG (une centaine d'Ohms). En conséquence, si une tension est appliquée aux contacts d'un échantillon constitué d'un QPC au centre d'un mesa de 2DEG (figure (6)), la chute de potentiel a essentiellement lieu au niveau même de la constriction. Le temps typique de traversée des électrons dans le QPC, de l'ordre de la picoseconde, est bien négligeable devant le échelles de temps de variations des pulses de tension que nous allons employer (au minimum de 40ps). La condition de quasi-stationnarité du potentiel de la théorie de Levitov et Lesovik est remplie et ce dispositif est un bon candidat pour réaliser une source à n-electrons en pulse de tension.

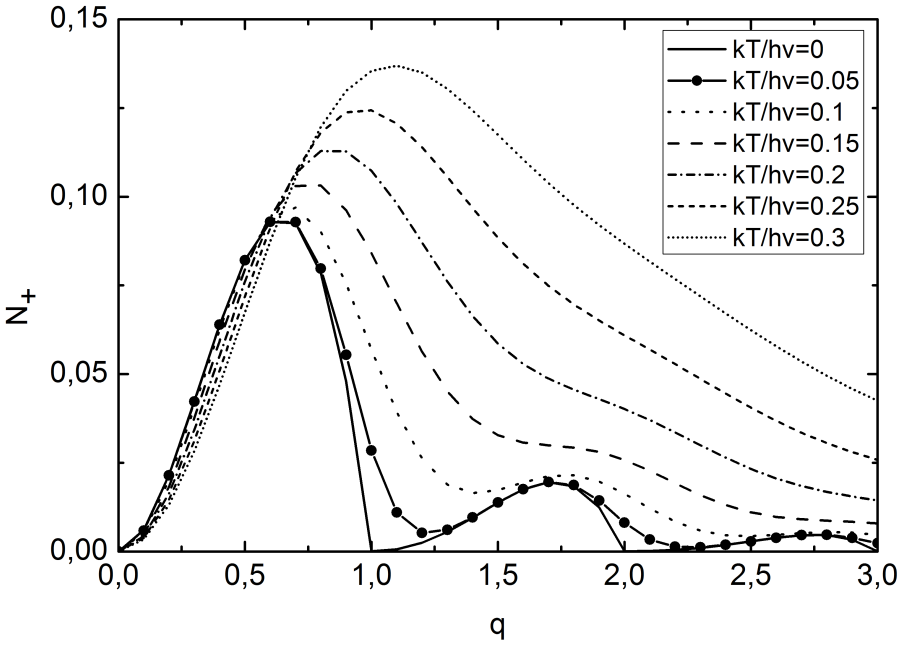

Figure 4: Nombre moyen de particules en excès N_+ en fonction du nombre de charge par pulse q pour des pulses lorentziens de largeur $w = 0.1\mathcal{T}$, à différentes températures

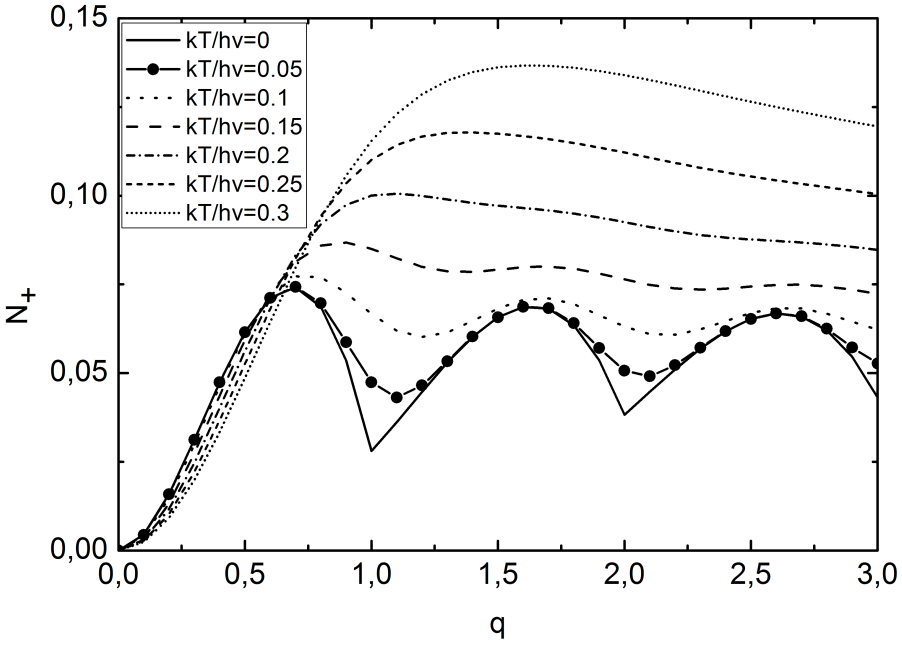

Figure 5: Nombre moyen de particules en excès N_+ en fonction du nombre de charge par pulse q pour un sinus à différentes températures

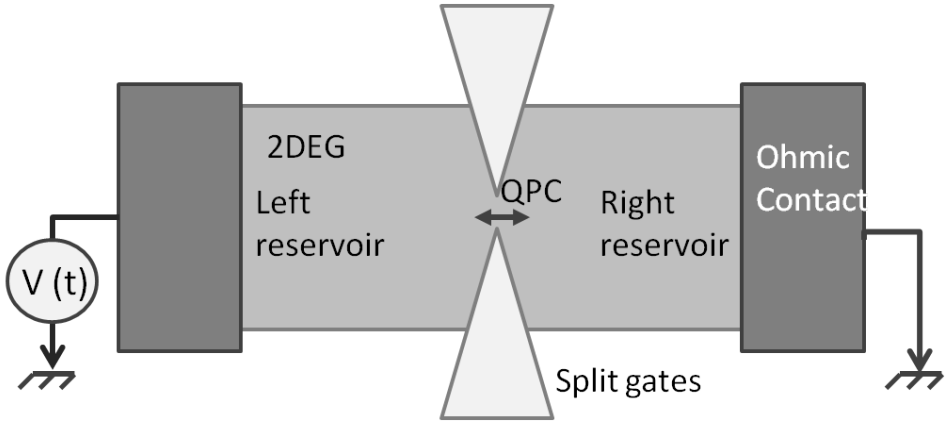

Figure 6: le contact ponctuel quantique joue le rôle de la source de Levitov

0.4.2 Les états de bords en régime Hall quantique

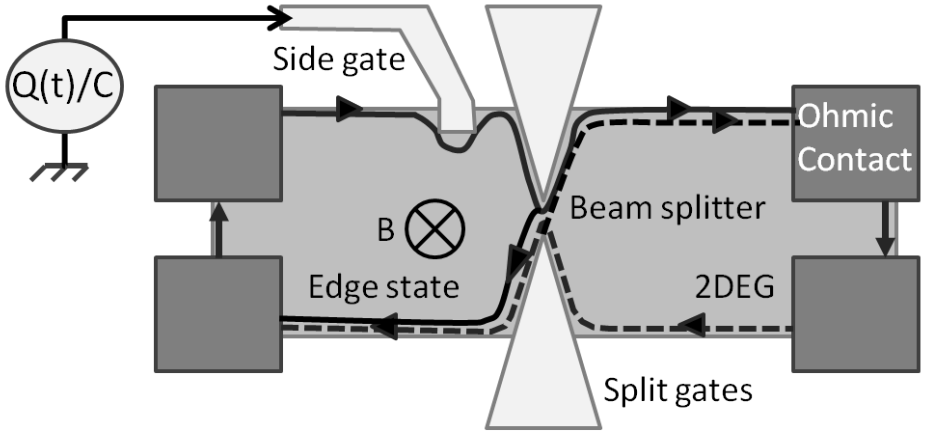

Figure 7: Une grille capacitive modulant la trajectoire des états de bords peut réaliser une source de Levitov

Lorsqu'on applique un fort champ magnétique perpendiculairement au gaz bidimensionnel, les électrons de conductions se retrouvent confinés le long des bords du mesa, de part la quantification des états de Landau en énergie. Ces états de bords sont unidimensionnels et chiraux, les électrons circulant selon le sens des orbites cyclotrons imposé par le champ magnétique (figure 7). Dans la proposition initiale de Levitov et Lesovik, le source à un électron n'est pas réalisée par une chute de tension $V(t)$ au niveau d'une petite région du fil quantique, mais par l'application d'un flux magnetique variable au niveau de cette région, qui a le même effet que $V(t)$ pour un potentiel vecteur $A(t) = \int V(t)$. Dans le regime d'effet Hall quantique, cette variation de flux peut être préférentiellement réalisée par la

modulation de la surface des orbites cyclotron. On déforme les trajectoires des états de bords en polarisant une grille couplée capacitivement avec les états, où la capacité C est donnée par la capacité mésoscopique et la capacité géomètrique: $C^{-1} = C_Q^{-1} + C_{Geo}^{-1}$ [3, 42]. Ainsi, de manière équivalente à l'application de V(t) aux bornes d'un QPC, l'application d'un potentiel $C^{-1}\varphi(t)/2\pi$ génère un courant $I(t) = G_0 V(t)$ dans un canal de bord et émet la charge $q = \varphi(t)/2\pi$.

Un contact ponctuel quantique peut être ajouté à la suite de cette grille capacitive afin de détecter les quasi-particules émises par la source via le bruit de partition. Il est alors nécessaire que la distance séparant la grille du QPC soit inférieure à la longueur de décohérence des électrons, qui limite le temps de vie des quasi-particules. Une solution est d'utiliser l'une des grilles du QPC comme grille source en ajoutant à la la tension nécessaire pour positionner le QPC à la transmission D voulue la modulation $C^{-1}\varphi(t)/2\pi$. Les états de bords courant le long du QPC sur quelques micromètres, la capacité de couplage peut atteindre quelques femtoFarad. L'amplitude de la modulation ne devrait donc pas excéder quelques centaines de microvolts, ce qui devrait laisser la transmission inchangée.

0.4.3 Caractéristique des échantillons réalisés

Dans ce travail expérimental, nous avons réalisé le premier dispositif constitué d'un QPC. Ce dispositif présente l'avantage de pouvoir injecter un courant de même signe indéfiniment, tandis que le dispositif capacitif en effet Hall est limité par le fait que la tension sur la grille augmente avec la charge émise. Les échantillons ont été réalisés sur des gaz haute mobilité ($\mu \approx 2.10^6 cm^2/Vs$) fournis par le Professeur Weggscheider de l'ETHZ, et lithographiés au SPEC. Les photographies optique et électronique (8) montrent le coeur de l'échantillon et le QPC. La caractéristique I(V) (fig. (9)) montre au moins cinq plateaux de conductance et une structure 0.7, typique des QPC dont la longueur est égale ou supérieure à leut largueur. Afin de limiter le bruit télégraphique et les courants de fuite entre la grille et le 2DEG, on polarise la grille du QPC avec une tension positive au moment de la mise à froid pour rapprocher la transition du premier plateau au pinch-off de $V_g = 0$.

0.5 Détection de l'émission de quasi-particules par cross-corrélation

0.5.1 Principe et sensibilité du montage expérimental

Nous inspirant des travaux de Kumar et al. [77], Roche et al. [121] et Reydellet et al. [118], nous proposons de détecter la puissance spectrale de bruit de partition S_I à fréquence nulle (c'est-à-dire entre 100 et 300kHz) par une technique de corrélation croisée. Le montage expérimental est schématisé sur la figure (10). Les signaux RF peuvent être injectés via deux lignes coaxiales testées jusqu'à 24GHz jusqu'aux contacts de l'échantillon. Le générateur

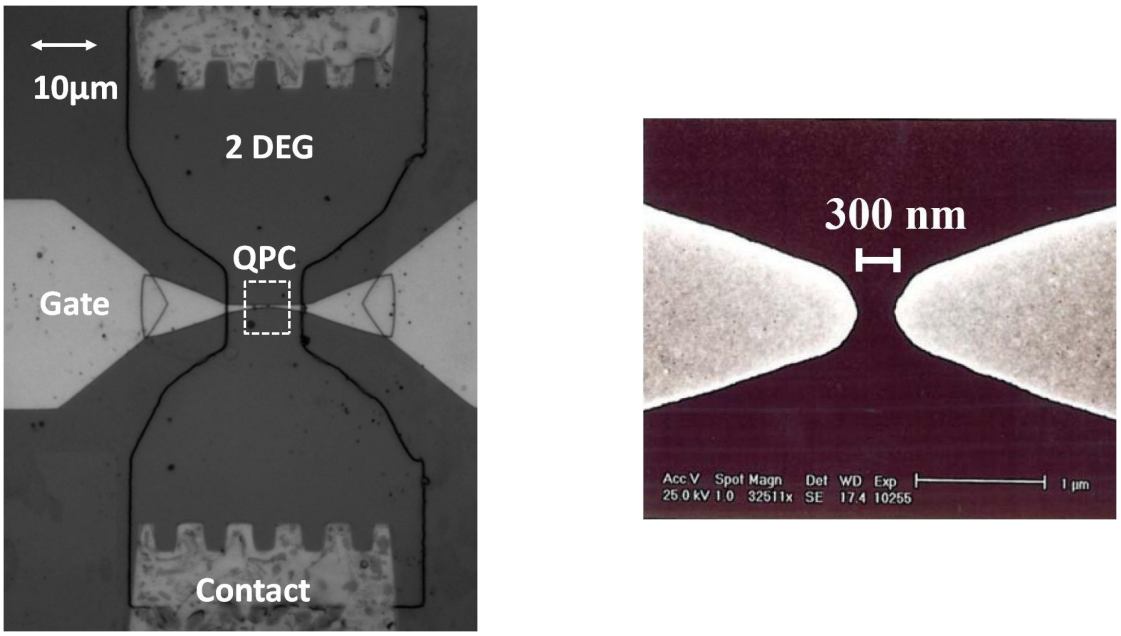

Figure 8: photographie optique du mesa (gauche) et photographie électronique de la région du QPC (droit)

de signaux arbitraires est un AWG de Tektronix avec un taux d'échantillage allant jusqu'à 24GS/s. Des tensions continues et basses fréquences sont recombinées avec les signaux RF au niveau de deux bias Tee Anritsu K250 dont la fréquence de coupure est environ 100MHz. Ainsi la détection s'effectue par les lignes basses fréquences et haute impédance, le bruit en courant émis par l'échantillon étant mesuré par la tension aux bornes de deux résistances de 2500Ω. Du fait de la capacité des cables coaxiaux (environ 130pF), la bande passante du circuit de mesure est de 300kHz.

Les deux tensions sont ensuite amplifiées, filtrées et recueillies par une carte d'acquisition rapide Acquiris dont le pas d'échantillonage est choisi à 1μs pour ajuster la détection à la bande passante du circuit. Le signal est enregistré durant une durée typique de 65ms puis traité par le logiciel Labview pour obtenir le spectre en fréquence du bruit.

$$\langle Re(V_A V_B^*)\rangle = \left|\left|\frac{Z}{2Z+R}\right|\right|^2 Re(Z^*(Z+R))\left(\langle i_A^2\rangle + \langle i_B^2\rangle\right) - \left|\left|\frac{ZR}{2Z+R}\right|\right|^2 \langle i_C^2\rangle \qquad (16)$$

Les tensions V_A et V_B aux bornes des impédences Z sont produites par l'ensemble des bruits en courant du circuit, représentés dans le schéma (11) par i_A, i_B et i_C, le bruit en courant de l'échantillon. En pratique, i_A et i_B proviennent essentiellement du bruit en courant des amplificateurs (environ $130fA/\sqrt{Hz}$). A ces tensions s'ajoutent le bruit en tension des amplificateurs U_A et U_B, qui sont plusieurs ordre de grandeur au dessus de V_A et V_B. Comme

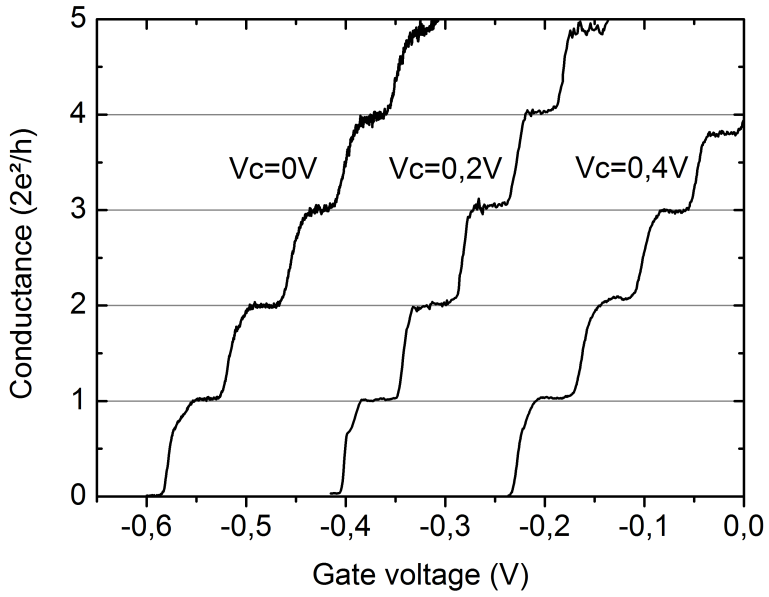

Figure 9: Conductance de l'échantillon en fonction de la tension de grille V_g pour différentes tensions de refroidissement V_c

$\langle Re(U_A U_B^*)\rangle = 0$, le bruit en tension des amplificateurs n'apparait pas dans le terme de corrélation croisée (eq.16). Cependant, la précision de la mesure est limitée par les fluctuations statistiques de $U_A U_B^*$, dont l'écart type $\left\langle U_{amp}^2 \right\rangle \sim 25 \cdot 10^{-20} V^2/Hz$. En conséquence la mesure est répétée un grand nombre de fois N, et le nombre totale de moyennage nécessaire $N\tau\Delta f$ ($\tau = 65ms$) est donné par la formule:

$$N\tau >> \frac{2\pi C \left\langle U_{amp}^2 \right\rangle^2}{\left\langle i_C^2 \right\rangle^2 R_m^3} \tag{17}$$

dans laquelle C est la capacité des cables coaxiaux et $R_m = 2500\Omega$ les résistances de mesure. Pour avoir une sensibilité d'un électron par nanoseconde sur un QPC de transmission 0.5, i.e. $\langle i_C^2 \rangle = 10^{-29} A^2/Hz$, il faut que $N\tau >> 36s$.

0.5.2 Installation du montage dans un cryostat sans bain d'Helium

Le montage expérimental a été installé dans un cryostat Helium free de dernière génération, qui fonctionne avec un tube pulsé. Le cahier des charges est le suivant:

- Le flux thermique conduit le long des cables du montage ne doit pas dépasser la puissance supportée par chaque étage de temperature du cryostat : $300\mu W$ à 4K, $100\mu W$ à 100mK et quelques μW pour 13mK.

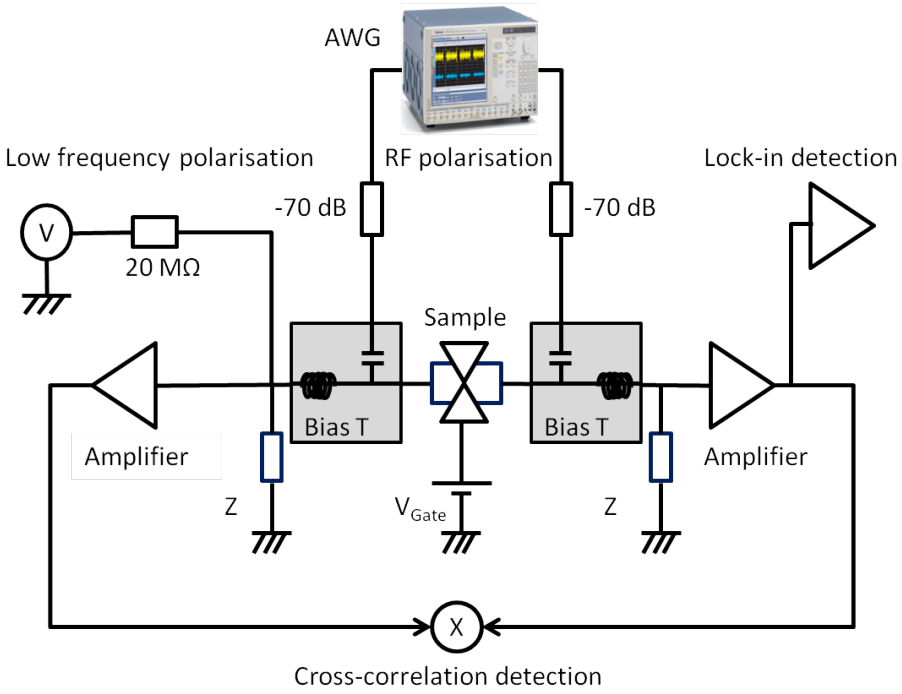

Figure 10: Montage expérimental

- Le montage doit être très bien ancré thermiquement à chaque étage, afin de permettre la thermalisation des masses et des âmes des coaxes pour atteindre la température minimale au niveau de l'échantillon.

- Il faut protèger l'échantillon des bruits environnementaux, notamment du flux radiatif en provenance des hautes temperatures qui est conduit par les coaxes.

- Il faut permettre une bonne conduction des signaux RF, et limiter la coupure capacitive des cables de mesure.

Il faut donc trouver un compromis entre les trois premiers points qui tendent à privilégier l'utilisation de cables longs et résistifs, ainsi que d'un fort filtrage capacitif, et le dernier point qui au contraire requière la minimisation de la longueur des cables et de leur résistance.

Ainsi nous avons privilègié l'utilisation de cable en cupronickel pour les lignes RF ainsi qu'une forte atténuation du signal par des atténuateurs cryogéniques pour limiter la conduction thermique et le flux radiatif, et pour les mêmes raisons l'emploi de cables très résistifs mais de capacité linéaire 100pF/m dans les lignes de mesures. La température de l'échantillon est mesurée à 22mK. En revanche, le bruit de partition du à l'application d'une tension continue aux bornes du QPC (figure 12) nous indique une température électronique nominale de 110mK, estimée selon la formule [77]:

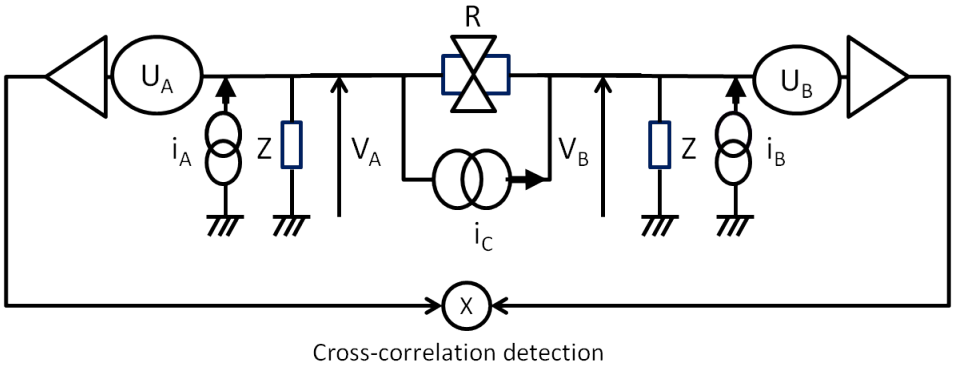

Figure 11: Différents bruits en courant et en tension dans le circuit

$$S_I = 2\frac{2e^2}{h}D(1-D)eV\coth\frac{eV}{2k_BT} \tag{18}$$

Cette température électronique ne s'explique pas par le résidu de flux radiatif, le bruit en courant généré par des résistances à haute température ou la thermalisation des coaxes internes. A notre connaissance, peu de mesure de bruit de grenaille ont été réalisées dans des cryostat à tube pulsé, dont la vanne tournante occasionne de nouvelles perturbations électromagnétiques, notamment dans la gamme 0-100kHz. Poussant notre investigation, nous avons synchronisé la carte d'Acquiris avec le cycle de la vanne tournante du tube pulsé, afin d'effectuer la prise de mesure uniquement dans des périodes où la vanne génère un minimum de bruit électromagnetique. La température électronique est alors descendu sous les 70mK. Cependant, cette technique multiplie le temps de mesure par six, ce qui n'est pas valable pour des mesures longues.

0.6 Implémentation du circuit haute fréquence

0.6.1 Un contact pontuel quantique dans un environnement RF

Afin de travailler à des énergies supérieures à l'énergie thermique k_BT, nous devons utiliser des pulses de tension dans la gamme du gigahertz. Ces pulses, notamment des lorentziens, ne sont pas monochromatiques et doivent être amenés jusqu'aux contacts de l'échantillon avec le moins de déformation possible. Il faut donc disposer d'un circuit RF avec une réponse la plus plate possible sur une large bande de fréquence (0-24Ghz). L'adaptation électrique de l'échantillon au circuit coaxial standard doit donc être particulièrement soignée, d'autant qu'il faut prolonger la configuration en guide d'onde jusqu'au coeur de l'échantillon.

Les photographies (13) montrent un échantillon dans son ensemble (à gauche) et son porte-échantillon (à droite) au centre duquel il est placé. On distingue quatre lignes coplanaires

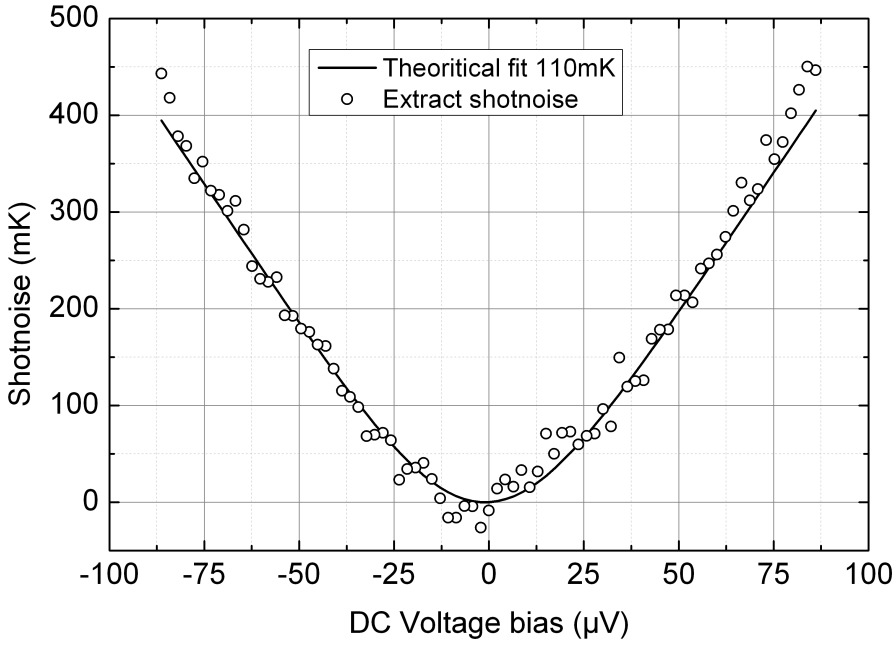

Figure 12: Température du bruit de grenaille généré par l'application d'une tension continue aux bornes du QPC (ronds). Fit théorique indiquant une température électronique nominale de 110MK (ligne)

permettant d'acheminer le signal RF jusqu'aux contacts (pistes horizontales), ou jusqu'aux grilles du QPC (pistes verticales). Les courbes particulières des pistes ont été mises aux point pour permettre la réduction en taille des guides coplanaires avec le moins de réflexion possible sur la gamme 0-30Ghz (pour les cotes exactes voir annexe C). Le maintien de la configuration coplanaire, en particulier la présence des masses au plus près de la région active limite le cross-talk entre les lignes et l'atténuation des hautes fréquences.

Le porte échantillon est gravé sur les faces cuivrées d'un substrat de TMM10, dont la constante diélectrique est proche de celle de l'Arsenic de Gallium ($\varepsilon_R \approx 11 - 12.5$). Des adaptateurs mini-SMP coudés dont l'empreinte de soudure à été spécialement dessinée permettent de se connecter au circuit coaxial sans réflexion majeure jusqu'à 30Ghz (pour les cotes voir annexe C).

0.6.2 Calibration in-situ de la transmission RF

La haute impédance de l'échantillon, typiquement plusieurs dizaine de kOhms, ne permet pas une calibration par des méthodes standard du signal haute fréquence qui est effectivement appliqué à ces bornes. Cependant, nous pouvons proposer une caractérisation in-situ de l'amplitude de la tension appliquée grâce à une mesure de photocourant.

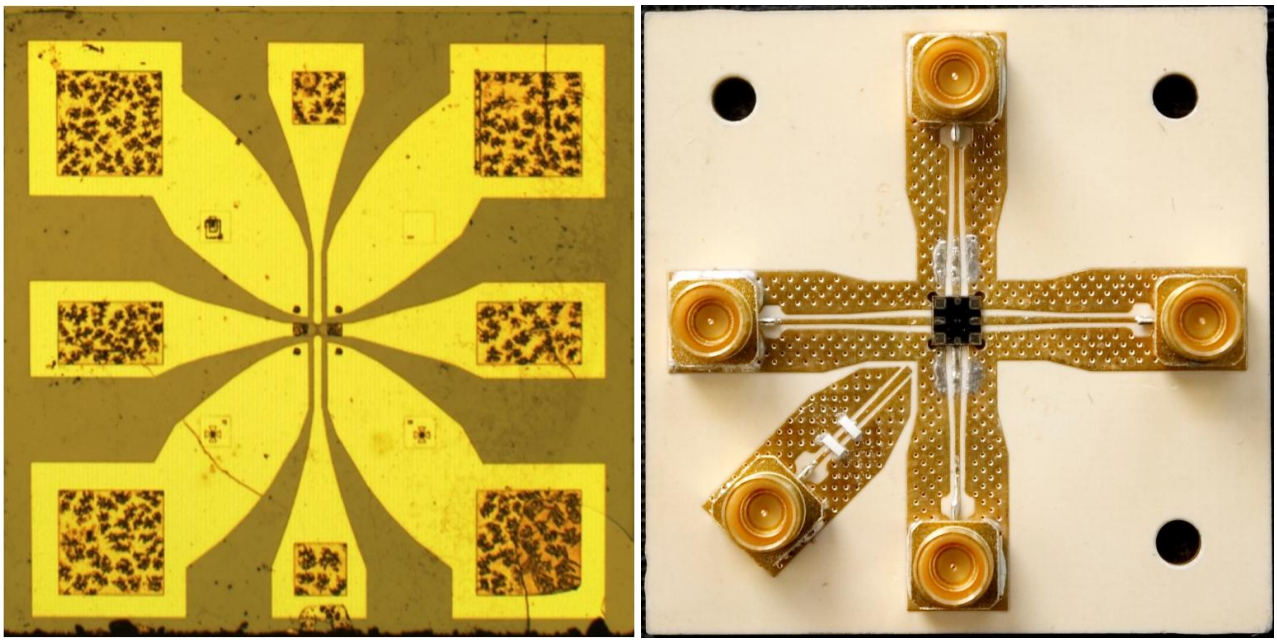

Figure 13: photographie de l'échantillon (gauche) et du porte-échantillon RF (droite).

Le photocourant est une résultante continue due à la dépendence de la transmission du QPC avec l'énergie. Lorqu'une tension alternative est appliquée, les électrons et les trous excités ne sont pas transmis identiquement, impliquant l'apparition d'un courant continu, le photocourant, dont on peut montrer qu'il est proportionnel à la puissance du signal:

$$\begin{aligned}\langle I\rangle &= e\int_{-\infty}^{\infty}\left(\left(D\left(0\right)+\frac{\partial D}{\partial\varepsilon}\varepsilon\right)\left\|\mathbf{P}_{\varepsilon\varepsilon'}\right\|^2-\left(D\left(0\right)+\frac{\partial D}{\partial\varepsilon}\varepsilon'\right)\left\|\mathbf{P}_{\varepsilon'\varepsilon}\right\|^2\right)f\left(\varepsilon\right)\left(1-f\left(\varepsilon'\right)\right)\frac{d\varepsilon d\varepsilon'}{\left(2\pi\hbar\right)^2}\\ &= -\frac{2e^2}{\hbar}e\frac{\partial D}{\partial\varepsilon}\frac{\langle V^2\rangle}{2}\end{aligned} \tag{19}$$

Par ailleurs, la dérivée de la transmission en énergie peut être mesurée indépendamment par deux méthodes (figure 14). La première consiste à mesurer à tension de grille fixée la variation de la conductance différentielle en fonction d'une tension drain-source continue V_{DS}, et à en extraire la dérivée à tension V_{DS} nulle. La seconde consiste à polariser l'échantillon avec une tension basse fréquence $V(t) = V_0\cos(\omega t)$,à mesurer la réponse en courant à la fréquence double, qui est issue de la redressement du courant:

$$I(t) = I\left(V\left(t\right)\right) = GV_0\cos(\omega t) + \frac{\partial G}{\partial V}\frac{V_0^2(1-\cos(2\omega t))}{4} \tag{20}$$

En comparant la réponse en photocourant à des signaux harmoniques à ces deux mesures

de $\partial G/\partial V_{DS}$ (figure 14), on peut en déduire la puissance du signal reçu par l'échantillon et donc le spectre en fréquence de l'atténuation dans les lignes RF du circuit (figure (15))

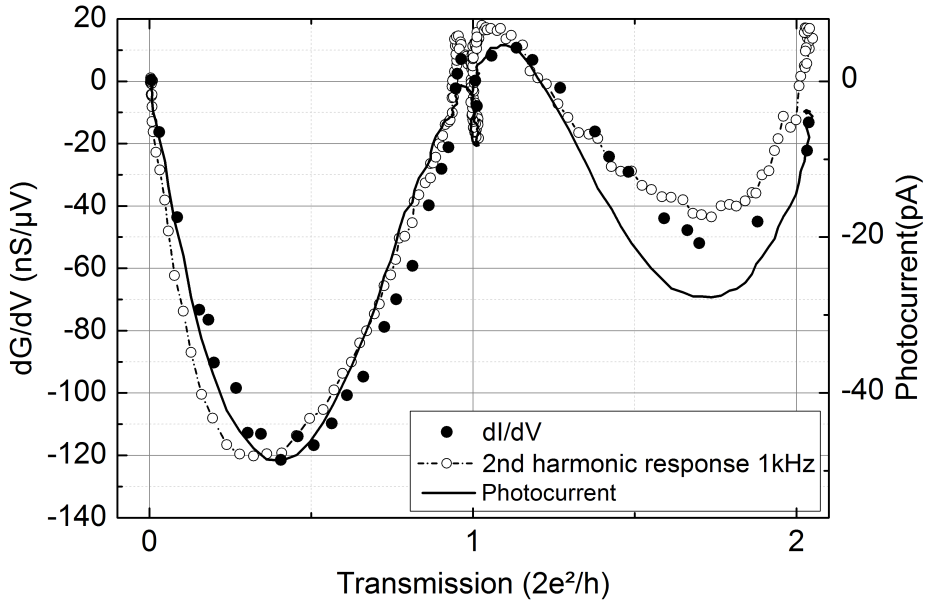

Figure 14: $\partial G/\partial V_{DS}$ en fonction de la transmission à excitation nulle, (ronds pleins) obtenue par la variation de la conductance differentielle en fonction d'une tension drain source continue, (ronds blancs et line pointillée) obtenue par la deuxième harmonique de la réponse en courant I2f à une excitation basse fréquence (1kHz). Le photocourant est proportionnel à cette dérivée (ligne pleine).

L'atténuation des lignes est d'environ -72 dB à 2.5GHz, ce qui en accord avec l'atténuation totale des atténuateurs cryogéniques (-70dB) ajoutées à l'atténuation attendue pour des cables coaxiaux de 2m de long à cette fréquence. La ligne A présente une réponse particulièrement plate jusqu'à 20GHz, tandis que la ligne B perd plus de signal aux hautes fréquences, mais cette perte reste acceptable.

0.7 Ce que révèle le bruit de grenaille sur les pulses de tension

0.7.1 La signature spectroscopique dans le bruit en excès

Considérons une tension périodique V(t) constituée de la répétition de pulses à fréquence ν. Cette tension se décompose en $V_{DC}+V_{AC}(t)$. La composante continue fixe le nombre de charge

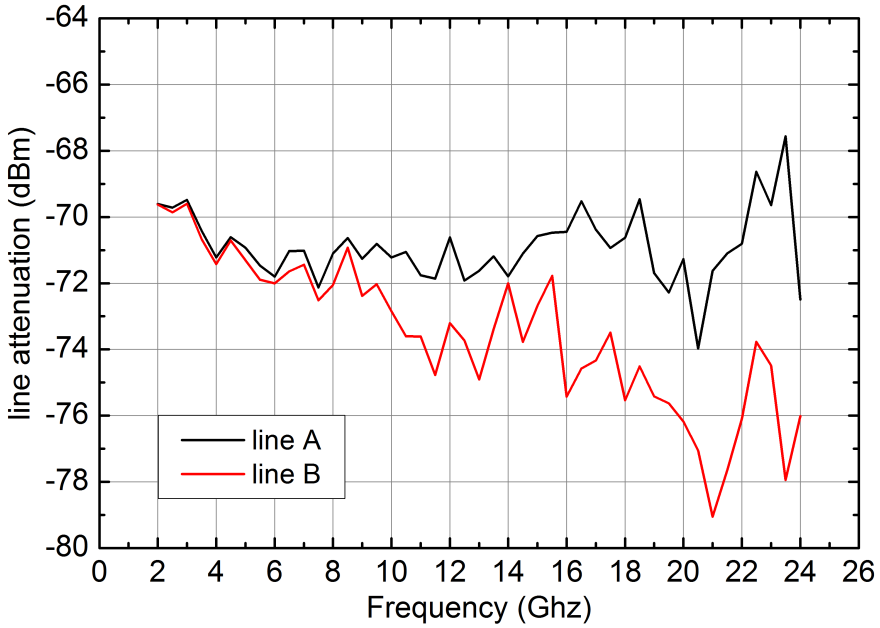

Figure 15: Spectre en fréquence de l'atténuation des lignes haute-fréquence du montage total (circuit+porte échantillon+échantillon), extrait de la mesure de photocourant

transféré par pulse $q = eV_{DC}/h\nu$, tandis que le nombre d'électrons et de trous excités N_e et N_h sont reliés à la transformée de Fourier P^* de $exp(i\varphi(t))$, qui est égale à P^*_{AC} translatée de $eV_{DC}/\hbar$, où P^*_{AC} est la transformée de Fourier de $exp(i\varphi_{AC}(t))$ associé à $V_{AC}(t)$.

A température nulle, $P(\varepsilon)$, $\varepsilon > 0$, (resp. $P(\varepsilon)$, $\varepsilon < 0$) est responsable de l'excitation d'électrons au dessus de E_F (resp. de trous au dessous de E_F). De fait, si on fixe $V_{AC}(t)$ et qu'on balaye V_{DC}, on déplace P^*_{AC} le long de l'axe des énergies (fig. 16), modifiant ainsi le nombre d'électrons et de trous émis, de sorte que le nombre de quasi-particules en excès $N_+ = \langle N_e \rangle + \langle N_h \rangle - |q|$ donne un accès indirect à l'amplitude de P_{AC}:

$$\frac{\partial^2 N_+}{\partial (eV_{DC})^2}(eV_{DC}) = 2 \sum_{n \in \mathbb{Z}} |P_{AC}(-n)|^2 \, \delta(eV_{DC} - nh\nu) - \delta(eV_{DC}) \tag{21}$$

D'un point de vue physique, l'ajout d'une tension continue (fig. 16) provoque l'anti-bunching des excitations qui se trouvent entre E_F et $E_F + eV_{DC}$, ce qui supprime leur contribution au bruit.

Cette spectroscopie des états excités a été effectuée pour des pulses sinusoïdaux à 16GHz (17), Lorentziens à 4.8Ghz (18) et carré à 5Ghz(19). Pour chacune des courbes, l'amplitude de la partie alternative des pulses à été fixée par le générateur RF, tandis que la tension continue a été balayée séparément. L'amplitude de V_{AC} est échelonnée selon le paramètre $\alpha = V_{AC}/V^1_{AC}$, où V^1_{AC} désigne la partie alternative associée au pulse total injectant un électron:

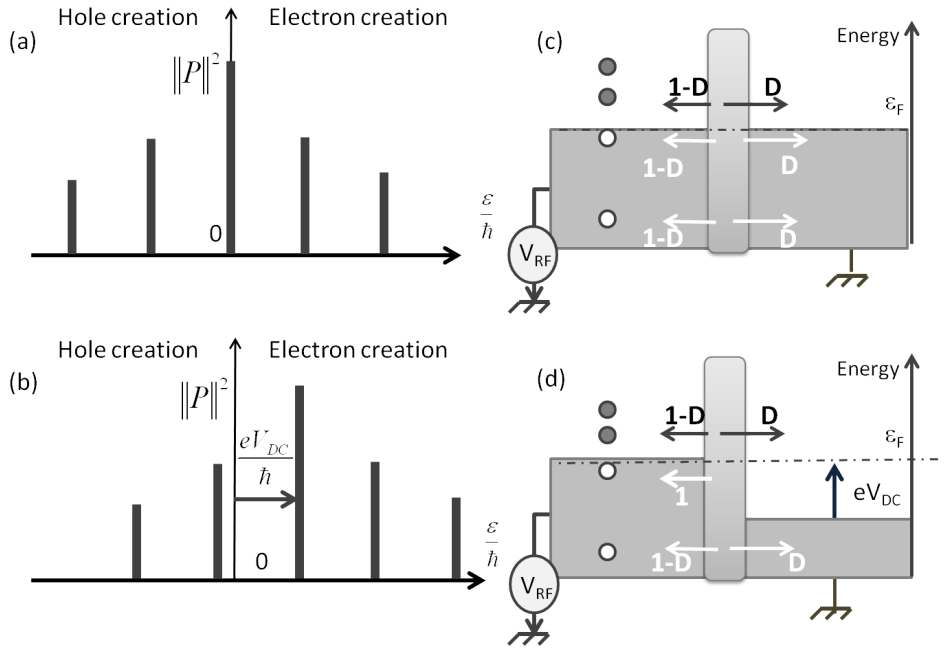

Figure 16: Principe de la spectroscopie des excitations par la mesure du nombre de particules en excès

- sinus:

$$V_{AC}(t) = \alpha \frac{h\nu}{e} \sin(2\pi\nu t)$$

- carré:

$$V_{AC}(t) = \alpha \frac{h\nu}{e} \quad si \quad 0 < t < \mathcal{T}/2, \quad V(t) = -\alpha \frac{h\nu}{e} \quad si \quad \mathcal{T}/2 < t < \mathcal{T}$$

- lorentzien:

$$V_{AC}(t) = \frac{\alpha h\nu}{e} \frac{\cos(2\pi\nu t) - e^{-2\pi w\nu}}{\cosh(2\pi w\nu) - \cos(2\pi\nu t)}$$

Les données expérimentales sont en bon accord avec les courbes théoriques dont les seuls paramètres ajustables sont la température électronique de base et l'atténuation de la ligne RF, dont l'estimation a été obtenue par ailleurs via la mesure du bruit de partition du courant continu (12), et la calibration via le photo-courant (15). L'augmentation de la température électronique de l'échantillon du à l'effet Joule est pris en compte dans les courbes théoriques grâce à la formule donnée par Kumar et al. [77]:

$$T^2 = T_0^2 + \frac{6e^2}{\pi^2 k_B^2} \frac{R_{Contacts} D G_0}{4} \left(1 + \frac{R_{Contacts} D G_0}{2}\right) \langle V_{DS}^2 \rangle \tag{22}$$

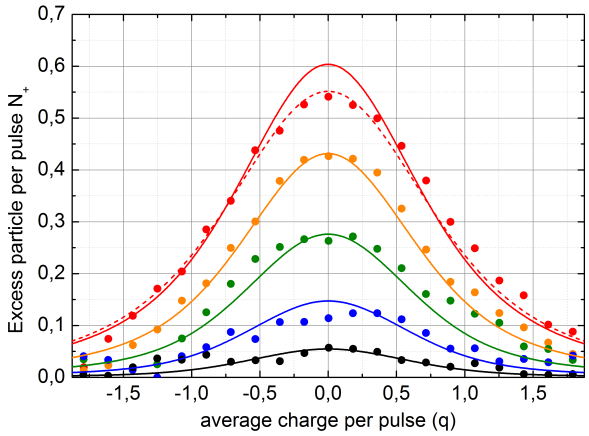

Figure 17: spectroscopie par bruit en excès pour un sinus de $\nu = 16$GHz. Les données expérimentales (points) correspondent aux valeurs théoriques (lignes) avec α=[0.38,0.63,0.88,1.13,1.38] et T_0=120mK, sauf pour α=1.38 pour laquelle T_0=150mK est en meilleur accord.

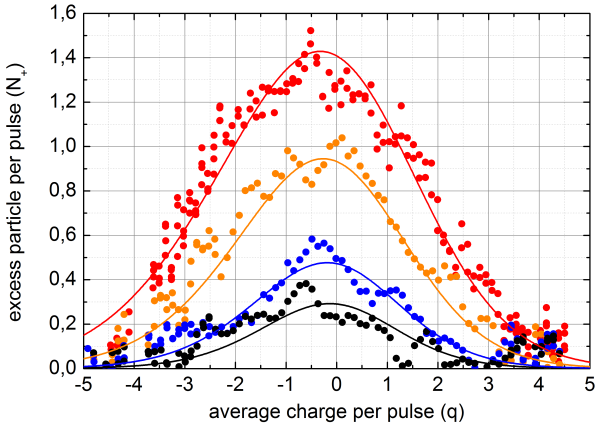

Figure 18: spectroscopie par bruit en excès pour des pulses lorentzien de largeur w=50ps répétés à $\nu = 4.8$GHz. Les données expérimentales (points) correspondent aux valeurs théoriques (lignes) avec α=[2.4,3.2,4.8,6.4] et T_0=120mK.

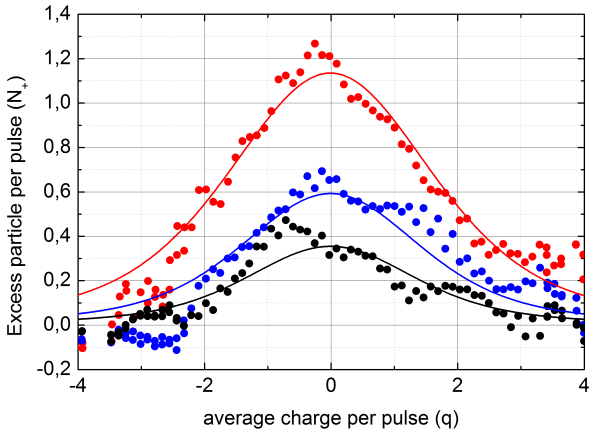

Figure 19: spectroscopie par bruit en excès pour des pulses carré répétés à $\nu = 5$GHz. Les données expérimentales (points) correspondent aux valeurs théoriques (lignes) avec α=[1.3,1.8,2.62] et T_0=120mK.

dans laquelle $R_{Contacts}$ désigne la résistance des contacts en série, D la transmission du QPC et T_0 la température électronique de base. Le meilleur accord est obtenu pour $T_0 = 120mK$ (à comparer aux 110mK trouvé pour la mesure de bruit de grenaille), sauf pour la courbe rouge dans la spectroscopie du sinus, qui s'ajuste mieux avec 150mK, indiquant ainsi la présence de chauffage supplémentaire dans le circuit pour cette grande amplitude.

Tout comme le spectre P^*_{AC}, le bruit en excès N_+ est symétrique pour le sinus et asymétrique pour les pulses lorentziens. On constate un légère asymétrie dans N_+ pour le carré alors que le bruit devrait être symétrique, qui peut s'expliquer par la déformation du signal carré. en effet, il est difficile de générer et transmettre un signal carré dont les harmoniques restent non négligeables jusqu'à des ordres importants.

0.7.2 Bruit de la source de quasi-particule

Reprenons le problème de la source de quasi-particule. Il s'agit de regarder dans les spectres ci-dessous les valeurs $q = \alpha$. La figure (20) reporte ces points particuliers. Les données pour les pulses lorentzien et carré, qui ont été réalisés avec des fréquences de répétition similaires, peuvent être comparées. Les valeurs indiquent qu'en général les pulses lorentziens excitent moins de quasi-particules en excès que les pulses carrés, même pour des valeurs non entière. Les données obtenues pour le sinus ont été obtenues à une fréquence de répétition trois fois plus grande, si bien que les effets de température sont moindre: on voit apparaitre clairement un saturation du bruit en excès.

A 16GHz et 120mK de température électronique, $k_BT = 0.15h\nu$ et les minima locaux de N_+ lorsque q est entier devrait pouvoir se détecter. La figure (21) reporte cette mesure pour des pulses sinusoïdaux. Les oscillations de N_+ ne sont pas visibles à cause de l'augmentation de la température par effet Joule, cependant les données expérimentales sont en très bon accord avec la courbe théorique qui notamment indique une élévation de la température électronique au delà de 200mK lorsque $q > 1$. Les données expérimentales ne peuvent s'expliquer par une approximation quasi-statique dans laquelle le bruit serait égal à la moyenne du bruit de partition DC produit à chaque instant à V(t). Le bruit en excès mesuré ne s'explique que par l'excitation photo-assistée de quasi-particules propre à la forme du potentiel variable V(t).

0.7.3 Quel est l'effet de la superposition de pulses?

La mesure du bruit en excès apportent de nombreuses informations sur l'injection de quasi-particules. Une autre question intéressante à aborder est l'effet de la superposition des pulses et de son effet sur les paquets d'excitation générés. On a vu précédemment que la répétition périodique de pulses de flux non-entier supprimait la divergence logarithmique des fluctuations de la charge transférée, et qu'alors N_+ dépendait du rapport entre la largeur des pulses et la période de répétition, comme $|\ln(w/\mathcal{T})|$. Ceci signifie que les pulses ont une influence à longue portée temporelle sur la production de quasi-particules des uns et des autres.

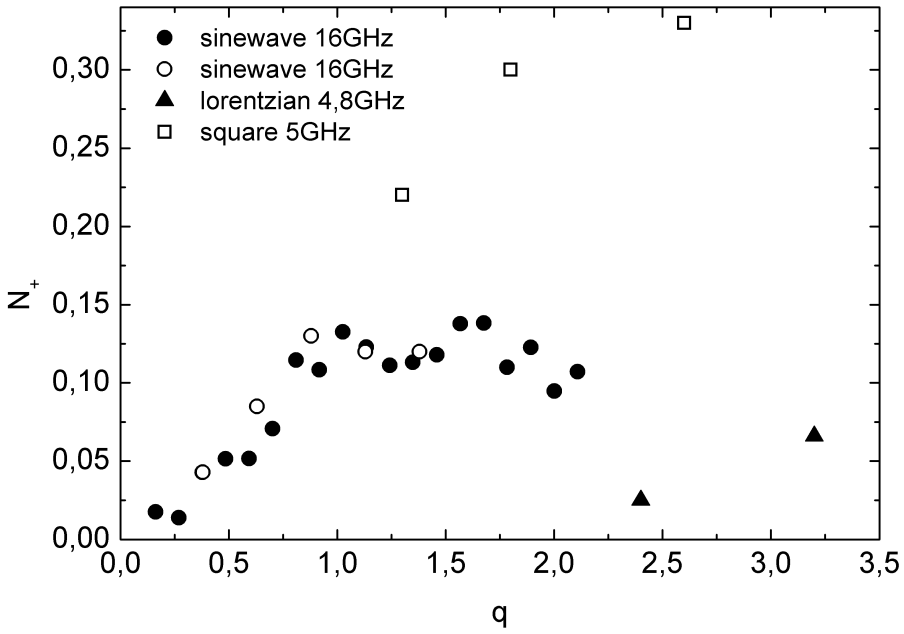

Figure 20: Bruit en excès N_+ produit par les pulses lorentziens (triangles pleins), carrés (carrés ouverts) et sinusoïdaux (ronds ouverts) lorsque $q = \alpha$ dans les data des figures 17, 18 et 19, et bruit en excès produit par des pulses sinusoïdaux à 16GHz $q\frac{h\nu}{e}(\sin(2\pi\nu t)+1)$ (ronds pleins)

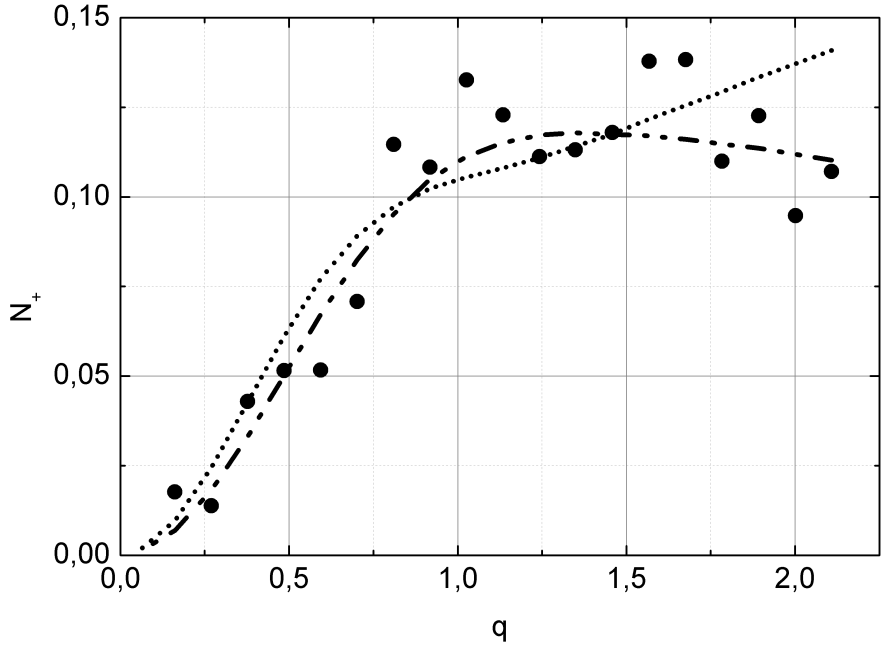

Figure 21: Mesure du bruit en excès N_+ produit par des pulses sinusoïdaux: $q\frac{h\nu}{e}(\sin(2\pi\nu t)+1)$ (points), et son estimation théorique (ligne).

Une autre manière d'aborder le sujet est d'effectuer une expérience de type Hong Ou Mandel [58], avec des excitations électroniques. Cependant, on peut montrer théoriquement par le principe d'invariance de jauge qu' injecter deux tensions déphasées $V(t)$ et $V(t+\theta)$ de part et d'autre du QPC revient exactement à injecter la différence $V(t)-V(t+\theta)$ sur un seul côté, et l'expérience de collision de quasi-particules avec un QPC revient à analyser l'émission de quasi-particule due à une alternance de pulses positifs et négatifs déphasés de θ.

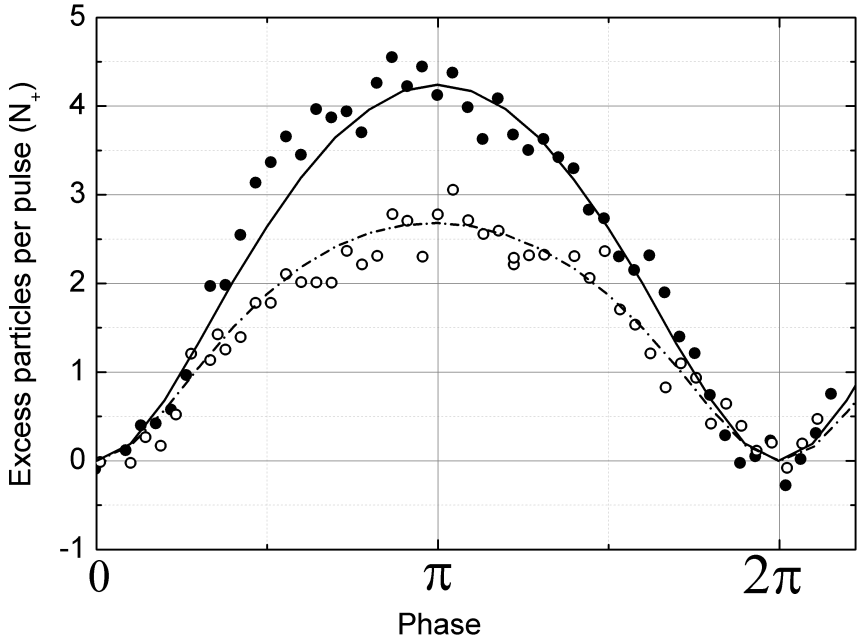

Figure 22: Mesure du nombre de quasi-particules généré par $V(t)-V(t+\theta)$, pour des pulses sinusoidaux (points noirs) et lorentzien (points blancs) de fréquence de répétition 2.6Ghz et de flux $q = 4.5$. Les estimations théoriques sont représentées par les lignes continues et pointillées.

Nous avons effectué cette expérience pour de pulses sinusoidaux et lorentzien de fréquence de répétition 2.6Ghz et injectant 4.5 charges par pulse (fig. 22). La largeur des pulses lorentziens est de $w = 0.16\mathcal{T}$. Le bruit en excès est représenté en fonction du déphasage entre les deux lignes d'injection. Les données expérimentales sont en bon accord avec les courbes théoriques qui ont été obtenu en tenant compte des effets de chauffage à partir d'une température électronique de base de 120mK. La région de suppression du bruit autour de $\theta = 0$ donne accès à l'extension des pulses et montre l'influence de la température qui élargit cette zone en fonction de l'énergie typique des excitations.

0.8 Conclusion et Perspectives

Afin de mettre en oeuvre une source à n-électrons indiscernables commandée en pulses de tension Lorentziens subnanoseconde, nous avons mis en place l'un des tous premiers montages de mesure de bruit de partition dans un cryostat à tube pulsé. Ce montage permet l'injection de pulses RF de forme arbitraire sur une large gamme de fréquence (0-24Ghz), et donc l'étude de la généralisation du bruit photo-assité [118, 125] à d'autres signaux que les tensions harmoniques.

Nous appuyant sur la mesure du bruit en excès générés par différentes tensions appliquées sur un contact pontuel quantique, nous avons pu montré la validité du modèle théorique de Levitov et Lesovik [84] décrivant l'effet Aharonov-Bohm non-stationnaire. Les particularités des pulses lorentziens ont été mises en évidence notamment par la spectroscopie des états excités.

La mesure du bruit en excès est une mine d'information: elle renseigne sur les processus d'absorption et d'émission de photons qui excitent les électrons de la mer de Fermi, permet d'étudier les effets de recouvrements des paquets d'ondes lorsqu'on rapproche ou écarte des pulses opposés ou des pulses de flux non-entier. Enfin il doit fournir un test sur la fiabilité de la source en pulses de tension Lorentzien.

En perspective, la diminution de la température de bruit du montage permettrait de mettre en évidence l'oscillation du nombre de quasi-particules avec la charge transférée et les minima locaux existants lorsque la charge est entière.

Plus généralement, la représentation en terme de photo-absorption et émission de l'excitation provoqué par des pulses de tensions sur la mer de Fermi permet de dégager l'élément clef de la source à n-électrons: Les pulses Lorentzien de flux entiers provoquent uniquement de l'absorption ou uniquement de l'émission de photon, avec pour conséquence l'emission d'uniquement des électrons ou uniquement des trous. Ceci nous permet d'entrevoir une possible généralisation de la source Lorentzienne à d'autres systèmes, notamment à des systèmes à gap qui pourraient nous affranchir des problèmes de température finie.

Contents

List of Figures

List of Tables

Chapter 1

Introduction

Mesoscopic transport addresses the physics of electronic devices which sizes are smaller than the coherence length l_ϕ of the carriers. Thus, even composed of a large number of particles, they show some quantum manifestations of the wave-particle duality and the Fermionic statistics of electrons. The **coherence length** of an electron l_ϕ is defined by distance travelled by an electron before completely losing its phase (typically the phase is changed by 2π). l_ϕ is smaller or comparable to the inelastic collision length over which an excited electron loses its energy by inelastic collisions with phonons and electrons, which irreversibly breaks its coherence.

At room temperature, electron-phonons interactions are dominant and limit l_ϕ to the characteristic length l_{e-ph}. At low temperature, phonons freeze and electron-phonon interactions vanish. The electron coherence is then comparable to the electron-electron collision length l_{e-e}. At very low temperatures, l_{e-e} reaches tens of micrometers in the two-dimensionnal gas trapped at the interface of extremely pure and crystalline epitaxied $Al_xGa_{1-x}As/GaAs$ heterostructure where interesting mesoscopic devices can be realized by lithography. In this Fermi liquid, collective excitations of small energy can be described as free quasi-particles [78, 79], of which life time is limited by the inelastic electron-electron collision rate.

As charge transport is carried by discrete particles, fluctuations of the current, called **shot-noise**, occur. In a mesoscopic conductor, these fluctuations are closely related to the Fermionic statistics of the particles and reveal the stochastic nature of the quantum mechanics.

For example, when a DC voltage bias is applied on a contact of a one-dimensionnal channel, no current noise is observed for any perfectly transmitted mode, because of Pauli exclusion. On the contrary, a quantum shot noise occurs when the mode is not perfectly transmitted: it comes from the uncertainty introduced by the tunneling process of electrons through the barrier.

The **full counting statistics** (FCS) of the transport is the probability distribution $P(N)$ to transfer N charges across the mesoscopic device during a time t_0. This distribution $P(N)$,

or equivalently its cumulant generating function, gives a complete picture of the transport, containing information about the statistics of particles (fermions/bosons), correlations and interactions.

The binomial distribution of the FCS in a quantum-wire was theoretically demonstrated by Levitov and Lesovik [86] in 1993. However, measuring higher cumulants of the current is a very difficult task. Quantum shotnoise was measured in the years 1996 [77]. Only in 2005, Reulet et al. and Yu et al. succeeded in measuring the third cumulant of the noise in a tunnel junction, proving that the charge statistics is non-Gaussian [117, 146]. In 2007, Gustasson et al. achieve to measure up to the fourth and fifth moments of the full counting statistics in a semiconductor quantum dot [53, 54].

While these experiments try to reconstitute the FCS by measuring the higher moment of a continuous flow of electrons, the long term aim of the present project is the reconstitution of $P(N)$ by the statistical measure on series of shots. This new approach consists in injecting small controlled number of electrons in a conductor followed by the detection of the exact number of electrons arrived in the contacts.

This requires an **electron injector**, that generates a coherent wave-packet of arbitrary n electrons, in the sense that these electrons form undistinguishable quasi-particles excited just above the Fermi sea. This implies that the time emission of these quasi-particles must be far below the coherence life time τ_ϕ [55].
Following the works of Levitov and Lesovik's groups [59, 84], we propose to emit these n-electrons packets in a mesoscopic circuit by applying subnanosecond Lorentzian voltage pulses on a single mode ballistic quantum wire.

The emitted charge transferred by a voltage pulse is equal to its number of action $q = e/h \int V(t)dt$. When q is an integer and for other pulse shape than Lorentzian, the q emitted electrons are accompagnied by spurious quasi-particles. Their total charge is neutral and their number N_+ is statistical. For Lorentzian shape pulse of integer flux q, N_+ is remarkably suppressed and an n-electron source that exactly emits q electrons in the circuit is realized. This approach should allow not only a full characterization of the electron statistics but also will open the way to new quantum interference experiments involving few electrons.

The outline of this thesis is as follows: in chapter 2, an overview of the existing single-electron sources underlines the difference between charge sources and quasi-particle sources and enlights the particularities of the Lorentzian voltage pulse source. Levitov and Lesovik's theorical description of the source is detailed in chapter 3, where average and fluctuations of the transferred charge are computed especially for periodic train of pulses. In chapter 4, we discuss about the hypothesis under Levitov and Lesovik's theory and why a quantum point contact in a 2DEG of GaAs/AlGaAs can implement an the n-electron source. The implementation of a new set-up for cross-correlation detection in a Helium free cryostat is detailed in chapter 5. Chapter 6 describes the high-frequency lines design and calibrations. Finally, the experimental results on noise produced by high frequency pulses are shown and

discussed in chapters 7 and 8.

Chapter 2

Mesoscopic electrons sources for quantum electronics

Transport experiments have been able to probe the quantum properties of mesoscopic electronic devices. The quantification of the conductance predicted by Landauer, Imry and Büttiker [23, 81] can be observed in many quasi-one-dimensionnal quantum conductors [144]. This is a remarkable quantization related to the Pauli exclusion property. Also due to the Pauli prinicipe, the shotnoise in a quantum wire shows the noiseless nature of the electron flow [12] [11]. Quantum coherence can be tested in interference experiments, such as in Max-Zehnder interferometers [61]. However most of those phenomena were observed in the DC regime with a high number of electrons flowing through the devices. Following the same path than in optics, the natural evolution of the transport experiments turns now towards the manipulation of single or few charges injected in a quantum ballistic conductors. This enables the investigation of the full quantum statistics of mesoscopic circuits. This can also lead to the realization of entangled quasi-particles and the implementation of charge flying qubits in conductors. But how can we fabricate a reliable quasi-particle source, in a quantum world that is intrisically statistic?

Single-charge sources have already been achieved in the past decades, such as electrons pumps (section 2.1), and the surface acoustic wave pumps detailed in section 2.2. However, one must distinguishes the quantized number of charges transferred from the actual number of excitations of the Fermi sea involved in this transfer. Most of the time these single-charge pumps do not control the kind of quasi-particles excitations they emit. To investigate the full counting statistics of a mesoscopic conductor and to extend coherence experiments to few particles, a reliable electron source, i.e. a source that can inject an arbitrary number of electrons without extra excitations, is required. Furthermore, for inteference experiments with several electrons, the quasi-particles must be indistinguishable, and coherent over a sufficient length.

More recently, a step in this direction was demonstrated through a coherent single-quasiparticle source based on a quantum-dot reservoir (section 2.4). This current source operates alternatively, giving sequentially one electron and then one hole to the circuit. An other approach was investigated by the groups of Lesovik and Levitov. They demonstrated that Lorentzian pulses applied on a 1D ballistic channel transfer an integer number of charge composed only by electrons or only holes (section 2.6). Consequently this device would realize an n-electron source that could inject coherent wavepackets of an arbitrary and controlled number of indistinguishable electrons.

2.1 Electrons sources based on tunnel junctions and Coulomb blockade

In the early 90s were built the first single charge sources, based on tunnel transport and Coulomb blockade phenomena [34,45,112]. Those electron pumps consisted in series of tunnel junction defining several metallic islands, the potential of which are monitored by side gates. Tunnel junctions are made of a very thin isolating layer between to metallic leads, so thin that electrons can tunnel through the barrier. In metals or semi-conductors, as current is a collective phenomenon of delocalized electrons, the charge flow is a continuous process. On the contrary, tunnel transport in a junction is a discrete process. Thus the amount of electrons in the metallic islands defined by the junction can only change by quantized number of electrons [40]. The current through a series of tunnel junction consists in electrons hopping from one island to another.
Coulomb blockade is the second ingredient of the electron pump, because it provides a control of the amount of charge transferred through the serie of metallic islands. Indeed, at low temperature, the charging energy $e^2/2C$ of a metallic island that is a few dozen of nanometers large becomes bigger than k_BT. Then it limits the number of excess charge on the island. Thus the charging energy of the islands limits the transfer to a single charge from one island to the other. This single charge corresponds to several electrons that tunnel sequentially through the barriers. Taking in account the capacitive energy of the dot and potential energy applied, the tunneling rate of the electrons through the junctions however limits the operating frequency cycle to the MHz range [34].

2.1.1 The electron pump

This device consists in at least two islands, each one controlled by a side gate (Fig. (2.1)). The first device was demonstrated in 1990 by Pothier et al. [112]. Alternative gate voltages are applied to the side gates, each one phase-shifted compared to the previous one so that the minimum of potential moves along the islands. This minimum potential trap the conduction electrons and transfer them from one lead to the other. Consequently this source is reversible:

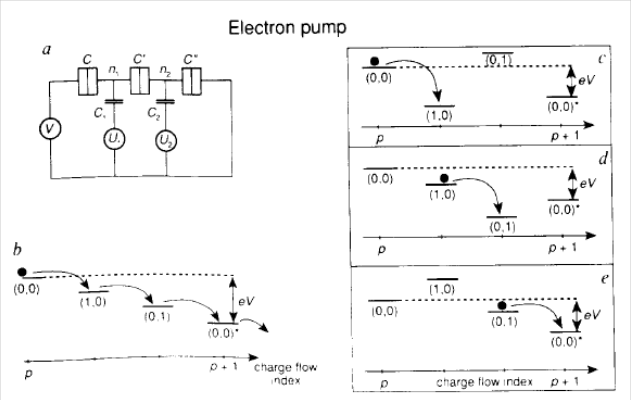

Figure 2.1: A three-junction single-electron pump operating principle (from Devoret review [34]). the alternating capacitive voltage applied on the two islands push the electron from one contact to the other by moving the minimum potential

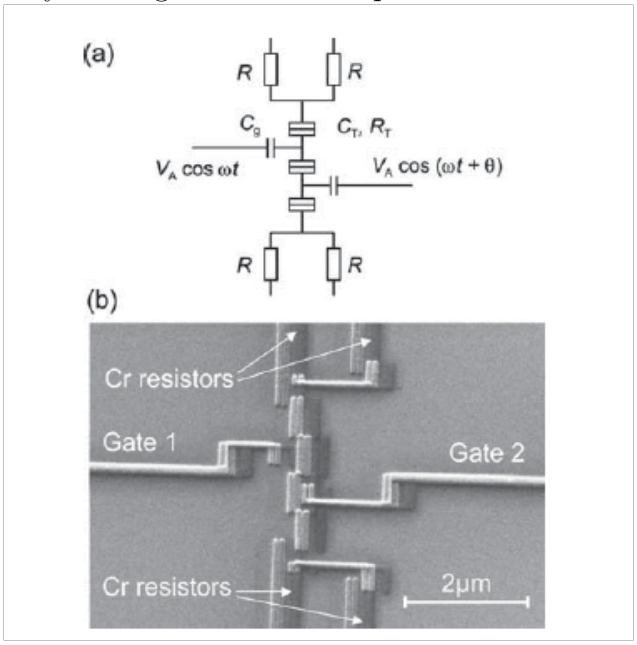

Figure 2.2: Equivalent circuit (a) and SEM image (b) of a three-junction single-electron pump developped by Lotkhov et al. [93].

the charge flow can establish without a drain-source voltage, or even be in the wrong way, from low potential to high potential. That why this device is called an electron pump.

2.1.2 The turnstile electron source

At the same time of Pothier et al. work, Geerligs et al. developped the turnstile electron source, which differs from the electron pump by its irreversible design [45]. It consists in at least three metallic islands, and there is only one gate that controls the central island (Figure (2.3)). Above a threshold of positive (negative) voltage gate, the central island traps (releases) one electron. Those thresholds are fixed by the charging energy of the outer islands. When a drain-source voltage is applied, the center island always traps an electron from the source and gives it to the drain: consequently an alternating potential of frequency f applied to the side gate generates a current response $I = ef$, that is one electron transferred per period.

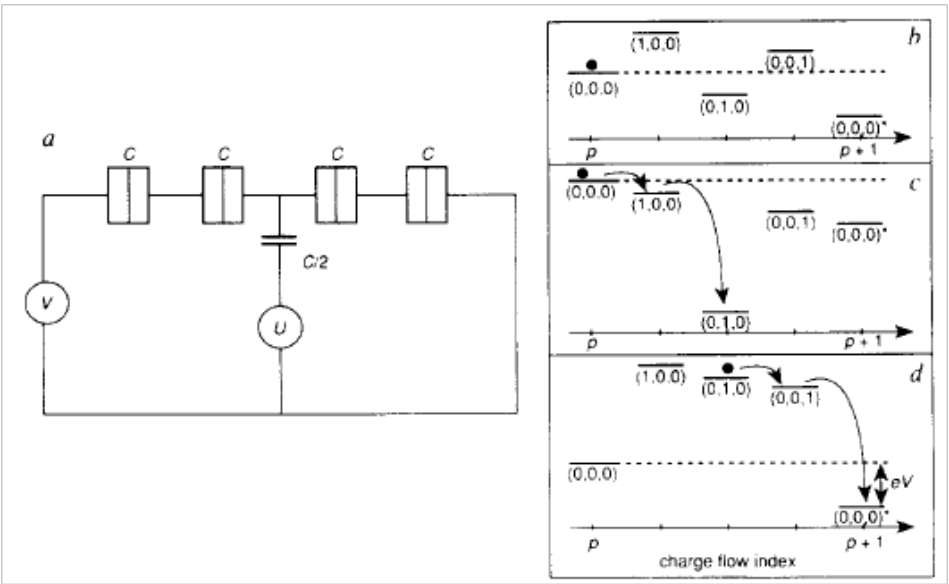

Figure 2.3: Schematics of the turnstile electron source (a) Evolution of the energy levels of the islands during the operating cycle (b,c,d). From Devoret et al. review [34] on single-electron transfer in metallic nanostructures

2.2 Electrons sources based on surface acoustic waves

2.2.1 Traping electrons in moving potential wells

In 1996, another single electron source was demonstrated using surface acoustic wave (SAW) to carry electrons one by one through a one-dimensional channel [127]. The 1D channel is

obtained in a bidimensional electron gaz of $GaAs/Al_{1-x}Ga_xAs$ heterostructure by split gates. The SAW is launched parallel to the channel by an interdigitated transducer. The piezoelectric property of GaAs causes a wave of electrical potential in response to a periodic voltage applied on the transducer when the frequency matches the SAW wavelength [41]. When the quantum point contact is longer than the SAW wavelength and used at very small transmission (pinch-off), the potential minima create travelling dots in the channel that can trap electrons and carry them through the barrier. The size of these dots is comparable to the wavelength of the SAW, so when the SAW frequency is about 3 GHz and the wavelength below $1\mu m$, Coulomb interactions quantify the number of electrons confined in a dot. So the effective current is $I = nef$, where f is the wave frequency. Experimentally, the current increases with the power of the SAW by quantized steps, because the dots, deeper in energy, can accomodate more electrons. It increases in the same manner with the barrier transmission, because the size of the dots increases and can transfer several electrons [135].

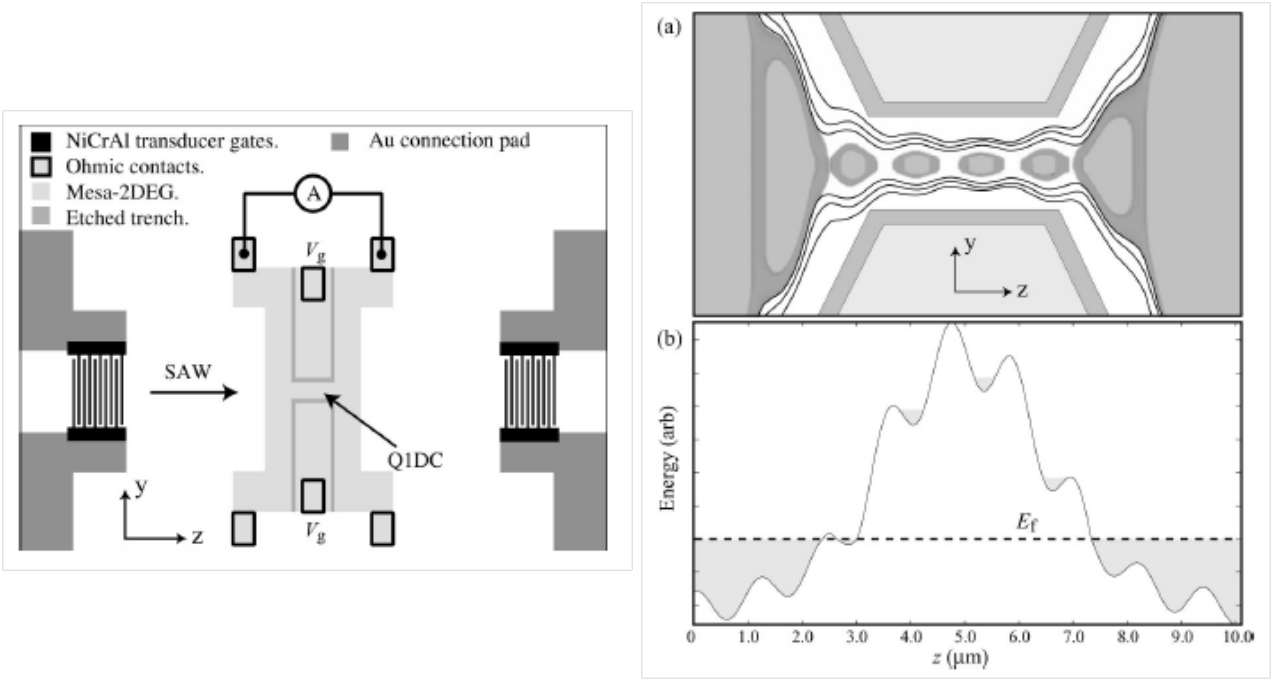

Figure 2.4: (left)Schematics of an SAW single-charge source from Barnes et al. [8]. (right) Schematics of the moving quantum dots in the QPC channel created by the surface acoustic wave.

The operation of the acousto-pump is roughly understood, but the dynamics of the electrons trapping in the travelling dots are not exactly known. From this mechanism arise the quantum errors of the number of electrons per dots.

In Shilton et al. scheme [127], when the electrical potential minima enter the constriction, the number of electrons in the subsequently formed dots steadily decreases with the size of

the dots towards the value fixed by Coulomb potential. The deviation from this value is due to the unwanted escape of trapped electrons towards the leads. Maksym [96] suggest that tunnel effect comes from the coupling of Landau-Zener levels in the dots and the leads continuum. Flensberg [37] and Aizin [6] have proposed out-of equilibrium transport models that show charge fluctuations. Following Robinson [120], the electrons escape produces high energy states that dissipate in the dots. Their temperature rises and limits the SAW accuracy performance to a effective temperature of 1K.

2.2.2 SAW pump for transferring for spin-qubit

Because of the high energy excitations generated by the SAW pumping, injected electrons are likely to loose their momentum coherence in the transfer process [66]. However, spin-coherence is more robust and exchange of electrons between spin-qubits could be promoted by SAW pump. Recently Hermelin et al. and McNeil et al. [57,99] carry a single electron from a first quantum dot along a 1D channel of several micrometers long towards a second quantum dot with an efficiency of 96% (see figure 2.5). Moreover, each quantum-dot is capacitively coupled to a quantum point contact that detects the charge in the dot: the emitted electron is trapped by the second quantum dot with an efficiency of 92%. The transfer of the electron can be triggered on a timescale shorter than the coherence time T_2^* of GaAs spin qubits. Thus this device opens the way to interesting developments about the exchange of entangled spins between qubits.

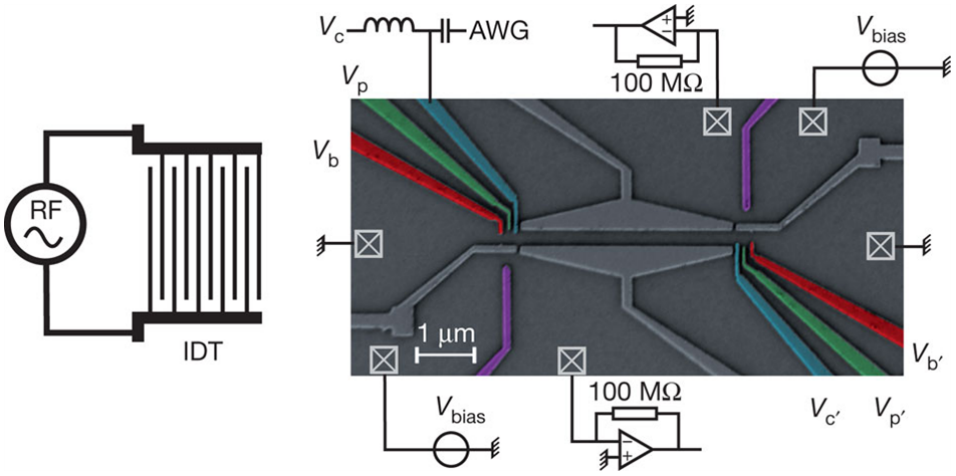

Figure 2.5: Scanning electron microscope image of the single-electron transfer device, and diagram of the experimental setup of Hermelin et al. [57]. Two quantum dots, which can be brought into the single-electron regime, are separated by a 1D channel . Each quantum dot is capacitively coupled to a quantum point contact close by that is used as an electrometer.

2.3 Single-charge source versus quasi-particles sources

2.3.1 Accuracy for metrological application

Application as a quantum standard of electrical current requires a source having a combination of accuracy, simplicity of operation and ability to generate a reasonably high current (at least 100pA). Many pump technologies have been investigated to achieve this goal, and electrons pumps are still the most up-to-date single-charge source for metrological applications. Among several designs we can mention chains of sub-micron normal-metal tunnel junctions [93, 98] and hybrid normal-metalsuperconductor turnstile [107]. Although 0.015 ppm accuracy has been demonstrated for 1 pA by Keller et al. seven junctions electron pump [71], the low operating frequency of these devices (restricted to MHz) prevent them to get to higher current.

Quantized acousto-electric current sources are also a possible way to produce a standard of electrical current. Until the recent development of high-frequency electron pumps (see subsection 2.5.2), acousto-pumps had the advantage of operating at gigahertz frequencies, meanwhile multi-tunnel junctions devices were restricted to megahertz frequencies. Consequently the effective current produced by the SAW electron pump is about a thousand larger than the electron pump one. However the present accuracy of a SAW sources does not match the metrological requirement yet. For metrological applications, the current produced by a device should be measured with an accuracy better than 100 parts per billion [26–28]. The accuracy of the SAW source is measured in the flatness of its plateaus. The best SAW sources to date have shown steps that were flat to within 100 parts per million for a current of 500 pA [60]. As explained before, the limitation of the SAW pump accuracy arises from the dynamics of electron trapping phase, which is still under debate [6, 37, 120]. Consequently the theoretical maximum accuracy of the source is still not known, but high energy excitations [120] are suspected to limit the SAW accuracy performance.

2.3.2 But unsuitable sources for quantum optics

Both the electron pumps and acousto-electrical sources are able to inject a controlled number of charge in a circuit, but the control of the number of emitted electrons and holes corresponding to this charge has not been demonstrated yet. Furthermore, the wave-functions of these particles is unsuitable for coherent processing.

On one hand, electron pumps lack of quantum coherence between the emitted electrons. Indeed, their very principle is to wait enough time for the transferred charge to relax in the islands. So the charge is sequentially sent to the circuit and electrons emitted by these devices are fondamently distiguishable.

As for the SAW electron pump, the high energy processes and the dissipation predicted by theoretical models [120] suggest that the quasi-particles momentum coherence is rapidely lost during the transfer, so that this source cannot be used for interference experiments.

2.4 The mesoscopic capacitor electron source

2.4.1 An on demand coherent single electron source

Charge sources are devices able to transfer a few quanta of charge with high precision. Among them, quasi-particle sources control more specifically the excitations that are emitted in the mesoscopic circuit. Interference experiments with few electrons require the injection of quasi-particles that are well defined in number, energy and wavefunction, otherwise the interference pattern would be disturbed by the fluctuations of the source, as optics interference experiment can suffer from the lack of coherence of the photons source. That's why reliable quasi-particle sources are those that emit electrons or emit holes with certainty.

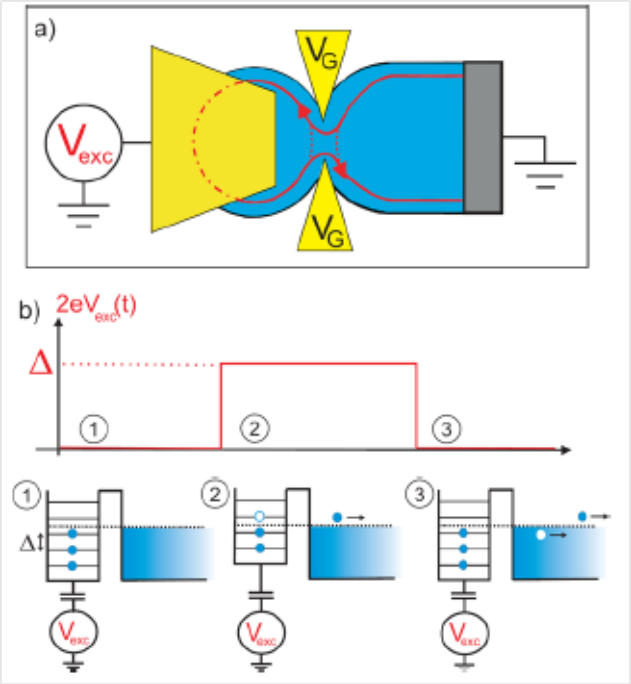

Figure 2.6: a)schematics of the mesoscopic capacitor single electron source from Mahe et al. [94]. c) potential energy variation of the levels in the quantum dot as a periodic voltage gate is applied b). The upper energy level is driven periodically above and below the Fermi energy of the circuit, consequently emitting or absorbing an electron.

If we consider again a single-electron transistor (SET) and reduce the size of the metallic island to obtain a quantum dot, the difference between energy level becomes sufficiently important for the charge transfer to only address the last energy level of the dot. When this level is pushed above (resp. below) the Fermi level of the drain by a side gate, it emits one electron (resp. one hole) to the circuit. The full coherence of such an resistance-capacitance

mesoscopic circuit (gate driven dot and quantum point contact barrier) was experimentally demonstrated by Gabelli et al. [42] in the quantum Hall regime. Indeed they show that the device impedance is no longer that of a resistance and a capacitor in series, in agreement with the works of Prêtre, Thomas and Bütikker [104, 113].

The emitted electrons and holes are well defined in energy and in wavefunction. The time extension of the wavepacket is given by the escape rate of the electron in the reservoir and is well below the phase coherence time in the 2DEG, so the emitted excitation can be used for single-electron interferometry experiments [55]. In 2005 Feve et al. [36] operate this device as an on-demand single electron source by applying an AC voltage on the capacitor. Further experiments achieved by Mahe et al. [94] [95] show through high frequency correlation measurement that the source actually emits one single particle at a time during half the period $\mathcal{T}$ of the operating cycle.

2.4.2 Quality of the single-electron source

The successful realization of the electronic on-demand source [36] was followed by a number of theoretical works investigating the accuracy of the on-demand source [70, 102]. The quality of this single electron source depends on the transmission D of the tunnel barrier between the dot and the circuit. Indeed the probability to achieve the emission of an electron or a hole depends on the comparison between the tunneling time through the barrier and $\mathcal{T}/2$. When the dot is open, $\langle N_e \rangle$, the electron number exchanged between the dot and the reservoir is not quantized and the fluctuations of this number is large [51, 70]. For $D << 1$, the mean escape time of the particle through the tunnel barrier is longer than $\mathcal{T}/2$, the electron (resp. hole) is not emitted with certainty. $\langle N_e \rangle$ decays and the relative fluctuations increases towards $\left[\langle N_e^2 \rangle - \langle N_e \rangle^2\right] / \langle N_e \rangle \to 1/2$, in agreement with the models of Albert et al., of Mahe et al., and of Jonckheere et al. [3, 51, 64, 94].

However, for a broad range of intermediate transmission, the quantization of the emitted number of electron excitations per period is observed. In this regime, Mahe et al. [94] experimentally observe that the only remaining statistical process was the quantum-jitter, i.e. the randomness of the time emission during the $\mathcal{T}/2$.

2.4.3 First implementations of the mesoscopic capacitor source in a collider

Bocquillon et al. [15] have coupled this source to a quantum point contact that plays the role of a beam-splitter. Then the partitioning noise reveals the average number of particles produced per cycle [106]. By choosing the shape the driving voltage on the quantum dot reservoir, using either sines or square waves, they are able to tune the energy distribution of the emitted particles and then check that there is a possible regime where these quasi-particles

can be injected without interaction with the thermal excitation of the Fermi sea [51].

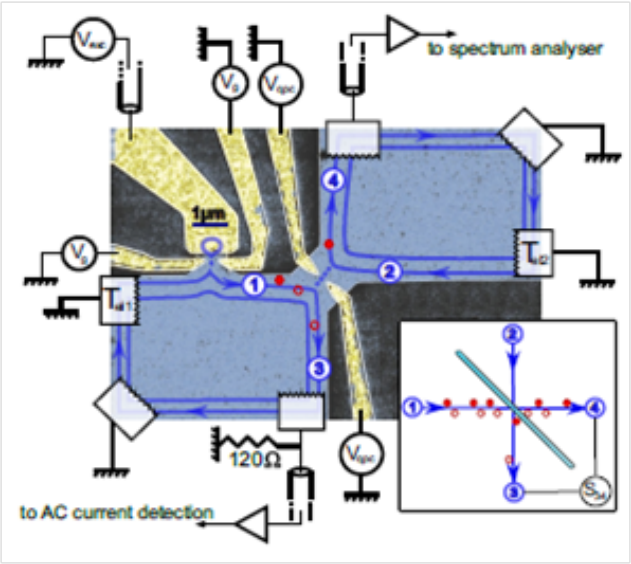

Figure 2.7: Bocquillon et al. collider sample [15]. The single-electron source is placed in the top left path of the split-gate (center). Current cross-correlation is measured on each side of the quantum point contact.

The Bocquillon et al. device is the first step towards a collider set-up that would open the experimental path to quantum optics analogs, like Hanbury-Brown-Twiss [56] or Hong-Ou-Mandel [58], provided that another mesoscopic source is added to the circuit. Meanwhile, this device can perform a tomography of the emitted quasi-particle states, as suggested by Grenier et al. [51], by applying a monochromatic voltage on another arm of this beam splitter and measuring the resulting Hanbury Brown Twiss current correlations.

The success of the mesoscopic RC current source have triggered great interest from the theoretical community. Haack et al. [55] propose to inject the emitted particles in a Machs Zehnder interferometer in order to measure the coherence length of electrons. Splettoesser et al. propose to couple two mesoscopic capacitor sources to perform a two-particle emitter or a single-particle fast detection [130]. Another work of the same group propose to combine two uncorrelated single-particle sources and two distant Mach-Zehnder interferometers in order to produce orbitally entangled electrons and verify the violation of Bell inequality [129].

2.5 Quantum-dot turnstile and electron pump

2.5.1 Adiabatic sources

The mesoscopic capacitor source produces a single stream with alternating electrons and holes; the current has no dc component, only ac component. For quantum information tasks, it would be desirable to have a quantum source that injects only electrons or only holes.

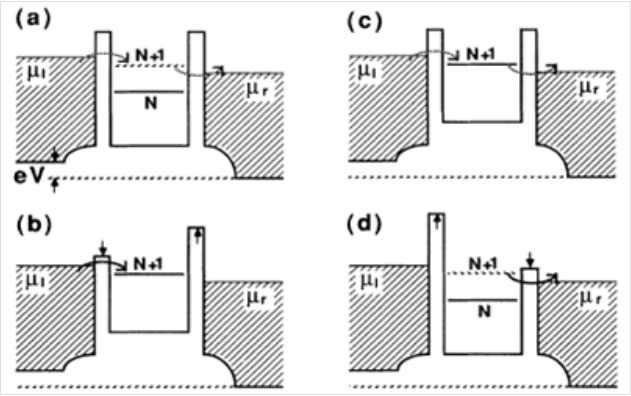

Figure 2.8: Potential landscape during the operating cycle of the quantum dot turnstile electron pump operating. μ_1 and μ_2 are the chemical potential of the left and right reservoirs, and $eV_{DC} = \mu_1 - \mu_2$. N and N+1 indicates the energy level of the quantum dot when N or N+1 electrons are confined in the dot. The electron tunneling probability is represented by a dash line when it is small, and a solid line, when it high. [73]

A way to combine directionnality and energy resolution is to replace the metalic islands of a electron turnstile by a quantum dot. Such devices were first realized in the 1991 by Kouwenhoven et al. [74]. The device consists in a double barrier formed by two quantum point contacts modulated periodically in time. A bias voltage is applied between the two sides of the turnstile, to have one resonant level of the double barrier in the bias window. Contrary to tunnel junctions electron sources operation, the capacitive gate that sets the level energy in the dot is fixed. Here, the transfer of the electron is achieved by the modulation of the barriers transparency. These quantum-dot versions of the electron pumps are also implemented and tested in an adiabatic regime by Switkes et al. [134].

In a recent work, Battista and Samuelson [9, 101] study in detail the transport statistics of the quantum-dot source turnstile in the quantum hall regime (Fig. 2.9 b, c).

As the quantum point contacts alternatively open and close with an operating frequency in the GHz range, a single electron would be trapped in the double barrier, while the corresponding hole would follow the edge channel in terminal 3. Thus during the cycle exactly one hole and one electron are emitted into different terminals. The authors studied the average and noise of the current produced by the device (Fig. 2.9 a) with respect to the operating

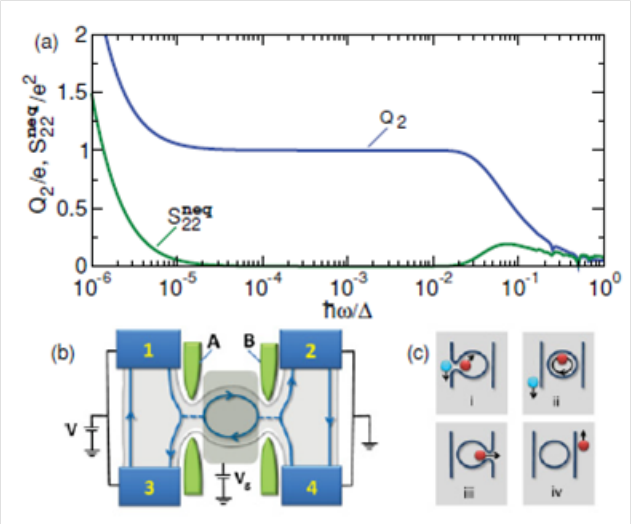

Figure 2.9: Battista and Samuelson's non-local turnstile electron pump [9]. b) describes the double barrier sample. c) schemes the electron trapping and releasing during the operation cycle. a) reports the computation of the current and noise produced by the device with respect to the ratio $\hbar\omega/\Delta$

frequency $\omega/2\pi$. They found a regime (when the energy spacing of the quantum box Δ is between 100 and 10000 times bigger than $\hbar\omega$) for which the transferred charge per cycle is quantified and the noise suppressed. Today, the energy spacing Δ of a experimental quantum dot in GaAs/AlGaAs 2DEG is of the order of 10-100 eμV. This reduces the operating frequency to a dozen of Mhz, and this adiabatic device would emit a current too small for noise measurements or metrological applications. However, other materials, such as nanotubes, where quantum dots can have higher spacing energy Δ could be considered to implement this concept [14, 136].

2.5.2 Double barrier non-adiabatic pumps

Recent experimental developments on the sample type of double barrier electron pumps achieve very high performance for metrological interest. They may be also of great interest for quantum optics. Their operating regime completly differ from the adiabatic cycle of Switkes et al. [134]. Here the operating frequency is increased up to non-adiabatic regimes to the gigaherzt range (so comparable to Δ). The barrier that separates the dot and the drain is kept at a low transmission. The loading gate first put in contact the dot with the source reservoir. Then it pushes the trapped electron to high energy in order to transfer it to the drain reservoir. In consequence the dot undergoes strong potential deformations that is completely different from the adiabatic model of Battista and Samuelson.

These devices are developped on silicon nanowire metal-oxide-semiconductor field-effect transistors [39], or in GaAs/$Al_xGa_{1-x}As$ heterostructures [13]. The high current level is achieved by placing a the device in a high magnetic field (up to 14 T), so that Gigahertz frequencies can be used to drive the device. A recent work by Giblin et al. [46] report a semiconductor quantum dot pump which a current accuracy better than 1.2 parts per million (ppm), with theoretical evidence of a true accuracy approaching 0.01 ppm.

Would these electron-pumps could deliver coherent quasi-particles? The physics of this devices are not fully understood yet [46]. Non-adiatic processes [39, 67] are suspected to be involved during the operating cycle, and in high frequency limit Kataoka et al. show that the trapped electron has non-neglectable probabilities to occupy upper energy level of the dot.

2.6 Electrons sources based on voltage pulses

2.6.1 Lesovik and Levitov 's proposal

When a bias voltage V_{DC} is applied across a one-dimensionnal ballistic channel of perfect transmission, the current is remarkably noiseless. In the wavepacket approach of Laudauer and Martin [97], the electrons flow one by one in the channel due to Pauli principle, and the time separation of the wavepackets is such as there is no fluctuation in the current. The time τ that separated one electron from the other is simply given by h/eV_{ds}, leading the quantized current [81]:

$$I = \frac{e^2}{h} V_{ds} \tag{2.1}$$

Thus, one would expect that applying voltages pulses of amplitude V_{ds} during a time $q\tau$ would transfer q electrons through the quantum wire. That would be the simplest coherent n-electron source. In fact, for a voltage bias $V(t)$ that have a quantized action, i.e. $\int_{-\infty}^{\infty} eV(t)\,dt = qh$, exactly q charges flow through the quantum wire. However, this charge is in general accompagnied by spurious excited $N_+/2$ holes and $N_+/2$ electrons. Contrary to the charge q that is certain, the number $N_+ + |q|$ of quasi-particles (i.e. the holes and electrons excitations) is statistical, so that the quantum wire will be a good current source, but an unreliable quasi-particle source.

Remarkably Ivanov et al. [59] have shown that for voltage pulses with Lorentzian shape, exactly $|q|$ electrons or (resp. q holes) occupying states right above the Fermi sea (resp. right below) are created with no extra spurious excitations. In this exceptionnal case, the quantum wire become a reliable and interesting q electrons coherent source. The remarkable results of Levitov and Lesovik's groups has triggered several relevant theoretical contributions in which the property and potential use of the Lorentzian voltage pulses are discussed. Klich et al. [69] has derived an analytic expression of the Fermi sea excited by several Lorentzian pulses of

flux one: the collective response of the Fermi sea can be seen as the creation of unentangled quasi-particles right above an unperturbed Fermi sea. Degiovanni group [33, 51] discuss how the Lorentzian pulses could be used to probe the interactions between channels in a quantum Hall regime. The case of a non-integer flux q is also discussed by Lee and Levitov for a single pulse, and by Vanevic for periodic pulses [82, 142]. This case presents an analogy with Anderson's orthogonal catastrophy problem [4]. We will come back more into details about all this theoretical discussion in the next chapter.

2.6.2 The advantages of the voltage-pulse source

Most of the available single-electron sources are essentially single-charge injectors. They control the transferred charge sometimes up to metrological standards [46, 71], but have not demonstrated yet the capability to control the kind of quasi-particles excitations they emit. The mesoscopic capacitor source [36, 94] is the only single-quasiparticle available today that emits a coherent electron followed by a hole. It opens the field to interference experiments with a single particle [15, 51, 55].

However, to investigate the full counting statistics of a mesoscopic conductor and to extend coherence experiments to few particles, an n-electron source that could inject coherent wavepackets of an arbitrary and controlled number of indistinguishable electrons is required. The Lorentzian voltage pulse source offers the possibility to send repeatedly coherent packets of an arbitrary number of electrons, so that a finite DC current is emitted in contrast with the mesoscopic capacitor. Furthermore, while the Feve et al. source can tune the energy of the electron above the Fermi sea by the amplitude and shape of the capacitor voltage, the voltage-pulse source emits electrons immediately above the Fermi level, the energy extension of the extension beeing given by h/w. The latter case presents the advantage of longer coherence time [145].

As the following chapter details, this source is totally noiseless even at finite frequency and the physical parameters of the excitations are controlled by the shape of the Voltage pulses. One can wonder why Lorentzian voltage pulses are so peculiar to be the only kind of pulses that produce minimal excitations of the Fermi sea. To understand how this n-electron source works, we need to go into details of the dynamical transport through the quantum wire when a variable voltage V(t) is applied.

Chapter 3

What is the effect of a time-variable voltage on a quantum wire?

Levitov and Lesovik's proposal relates to a more general problem about the current flow induced by a time dependent voltage V(t) applied across a quantum wire. This physics can be addressed by the Landauer-Büttiker scattering formalism [22], and particularly the Floquet scattering formalism [102] (section 3.1). The fondamental statistical quantities of the current flow, i.e. the average $\langle I(t)\rangle$ and the current-current correlator $\langle I(t)\, I(t')\rangle$, are derived from the scattering matrix. In our case of interest, V(t) refers to a single voltage pulse $V_p(t)$, or a periodic repetition of it. By voltage pulse we mean that it has a limited time extension, and more precisely that $\int_{-\infty}^{\infty} V_p(t)dt$ is finite.

In the frame of absorption and emission processes of the photons associated to the voltage excitation (section 3.4), the average and the variance of the transferred charge can be respectively identified with the difference and sum of the average number of the excited electrons $\langle N_e\rangle$ and holes $\langle N_h\rangle$ produced in the reservoir. This convenient interpretation let us understand why only Lorentzian pulses lead to an ideal quasi-particle source (section 3.6). In section 3.7, numerical computations of $\langle N_e\rangle$ and $\langle N_h\rangle$ for several periodic pulses help to better understand the influence of parameters such as the waveform shape, the repetition frequency or the average number of charge transferred per pulse. This enable us to put some orders of magnitude for the excess noise to be measured and to study the impact of temperature, which is the main limitation in our experiments (section 3.7).

3.1 The scattering formalism in an infinite Fermi sea

Levitov and Lesovik's proposal considers a one-dimensional ballistic channel connected to metallic contacts (Figure (3.1)). The right contact is connected to the ground, whereas the voltage pulses $V_p(t)$ are applied on the left reservoir. Note that the convention sign of

voltage and current (Figure (3.1)) is choosen so that a positive voltage V corresponds to a an energy drop eV for electrons between the left and the right reservoirs, so to an injection of electron in the right reservoir. The approach can be easily generalized to multiterminal and multichannel mesoscopic conductors [20, 22, 122]. An essential working hypothesis is that the voltage drop can be applied over a region around $x = 0$, which is small compared with the characteristic electron wavepacket extension. Then the voltage can be considered as quasi-static during the time an electron flows through this region. The quantum wire is long enough to be considered as infinite and to neglect the boundaries conditions. Through the gauge invariance transformation described by equation (3.1), applying a voltage $V(t)\Theta(-x)$ is equivalent to apply a magnetic flux $A(t)\delta(x)$, where $V(t)$ is the time derivative of $A(t)$:

$$\begin{aligned} A &\to A + \nabla\chi \\ V &\to V - \frac{\partial\chi}{\partial t} \end{aligned} \tag{3.1}$$

So the Schrödinger equation of the problem can be written as followed:

$$i\hbar\frac{\partial\phi}{\partial t} = \frac{(p + eA(t))^2}{2m}\phi \tag{3.2}$$

As the energies involved by the voltage excitations are small compared with the Fermi energy, we can proceed in calculation to a linear approximation of the dispersion relations close to the Fermi points $\varepsilon_{R/L} = \pm v_F p$, where v_F denotes the Fermi velocity. Then the Fermi sea can be considered as infinitely deep. Consequently the linear spectrum approximation disconnects the dispersion relation of the right (R) and left (L) moving electrons. The Fermi level is set at the reference energy ($E_F = 0$). States can be decomposed as $\phi = \psi_F\psi$, where ψ_F is the state at the Fermi level. So the time-dependent Schrödinger equation can be developped as followed:

$$\begin{aligned} H\phi &= \frac{(p + eA)^2}{2m}\phi \\ &= \left(\frac{p^2}{2m} + \frac{e}{2m}\left(2A\cdot p + \frac{\hbar}{i}\frac{\partial A}{\partial x}\right) + A^2\right)\psi_F\psi \\ &= \left(E_F\psi \pm \frac{\hbar^2 k_F}{im}\frac{\partial\psi}{\partial x} + \frac{e}{m}A\hbar k_F\psi + o(k_F)\right)\psi_F \end{aligned} \tag{3.3}$$

In the following we note $t_+ = t - x/v_F$ and $t_- = t + x/v_F$. Then the following right-moving states (eq.(3.5)) and left-moving states (eq.(3.6)) are solutions of the linearized Schrödinger equation Eq. (3.4):

$$i\hbar\left(\frac{\partial\psi}{\partial t} + v_F\frac{\partial\psi}{\partial x}\right) = ev_F A\psi \tag{3.4}$$

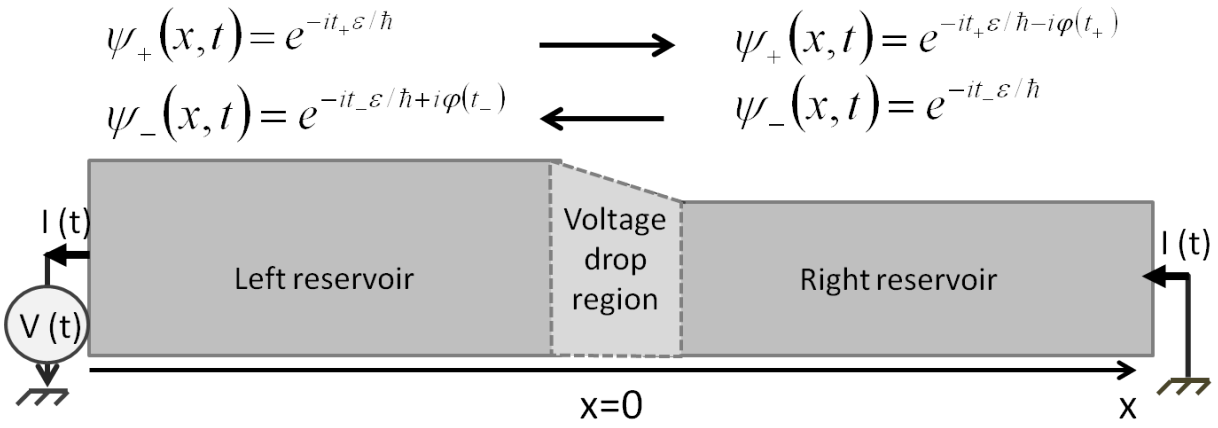

Figure 3.1: Due to the voltage drop V(t) between the left and the right reservoirs, the right moving electrons coming from the left reservoir acquire a phase $\varphi(t_+)$ when they pass the voltage drop region, whereas the left moving electrons coming from the right reservoir acquire a phase $-\varphi(t_-)$ when they pass from the right reservoir to the left one. Here we note $t_+ = t - x/v_F$ and $t_- = t + x/v_F$.

$$\psi_+ = \exp\left(-i\frac{\varepsilon t_+}{\hbar} - i\frac{e}{\hbar}A\left(t_+\right)\Theta\left(x\right)\right) \tag{3.5}$$

$$\psi_- = \exp\left(-i\frac{\varepsilon t_-}{\hbar} + i\frac{e}{\hbar}A\left(t_-\right)\Theta\left(-x\right)\right) \tag{3.6}$$

This means that an electron coming from the left reservoir acquires a phase $\varphi(t_+)$ (eq.(3.7)) when passing through the voltage drop region to the right reservoir (respectively an electron coming from the right reservoir acquires a phase $-\varphi(t_-)$) (figure (3.1)). For a voltage pulse $V_p(t)$, $\varphi(\infty)$ is equal to $2\pi q$, where q is the number of flux associated to $V_p(t)$. The section (3.2) shows that q is also equal to the number of charge transferred per pulse.

$$\varphi(t) = \frac{e}{\hbar}\int_{-\infty}^{t} V(t)dt = \frac{e}{\hbar}A\left(t\right) \tag{3.7}$$

The Fourier transform of $\exp\left(i\varphi(t)\right)$ P^* plays a central role:

$$e^{i\varphi(t)} = \int_{-\infty}^{\infty} P^*\left(\frac{\eta}{\hbar}\right)e^{i\eta t}\frac{d\eta}{2\pi\hbar} \tag{3.8}$$

Indeed, P (resp. P^*) defines the amplitude of probability of a left coming electron (resp. a right coming electron) to absorb the energy η if $\eta > 0$ or emit η if $\eta < 0$ when it passes

the voltage drop region. Consequently, a left (resp. right) coming electron in an eigenstate of energy ε in $x < 0$ (resp. $x > 0$) is in a superposition of states of energies $\varepsilon' = \varepsilon + \eta$ at $x > 0$ (resp $x < 0$), of which amplitude coefficients are given by the Fourier transform P of $exp(-i\varphi(t))$ (resp. P^* of $exp(i\varphi(t))$):

$$\psi_+(x,t) = e^{(-i\varepsilon t_+ - i\varphi(t_+))} = \int_{-\infty}^{\infty} P\left(\frac{\varepsilon' - \varepsilon}{\hbar}\right) e^{-i\varepsilon' t_+} \frac{d\varepsilon}{2\pi\hbar}$$
$$\psi_-(x,t) = e^{(-i\varepsilon t_- + i\varphi(t_-))} = \int_{-\infty}^{\infty} P^*\left(\frac{\varepsilon' - \varepsilon}{\hbar}\right) e^{-i\varepsilon' t_-} \frac{d\varepsilon}{2\pi\hbar} \tag{3.9}$$

Thus the effects of the voltage drop can be treated in a scattering formalism [20, 122], provided we introduce the scattering matrix $\mathbf{P}$ which connects the states propagating in the same direction but of different energy. The elements of the matrix $\mathbf{P}$ are equal to:

$$P_{\varepsilon\varepsilon'} = P(\frac{\varepsilon' - \varepsilon}{\hbar}) \tag{3.10}$$

To complete a more realistic description of the one-ballistic channel we consider an imperfect transmission of states between the reservoirs, that can be modelled by a elastic scatterer at x=0. Without voltage drop, incoming states are transmitted with probability D to the other reservoir. In this chapter the transmission coefficient is considered as energy independent (fig. (3.2)). The scattering matrix $\mathbf{S}$ gives the reflexion and transmission coefficients between incoming and outgoing states. The effect of $\mathbf{P}$ multiplies the effect of $\mathbf{S}$, so that the total scattering matrix $\mathbf{U}$ that links the incoming states $a_\alpha(\varepsilon)$ and outgoing states $b_\alpha(\varepsilon)$ is equal to:

$$\begin{pmatrix} b_L(\varepsilon) \\ b_R(\varepsilon) \end{pmatrix} \mathbf{U} \begin{pmatrix} a_L(\varepsilon) \\ a_R(\varepsilon) \end{pmatrix} = \begin{pmatrix} b_L(\varepsilon) \\ b_R(\varepsilon) \end{pmatrix} \begin{pmatrix} \mathbf{P}^\dagger & 0 \\ 0 & \mathbf{1} \end{pmatrix} \times \mathbf{S} \times \begin{pmatrix} \mathbf{P} & 0 \\ 0 & \mathbf{1} \end{pmatrix} \begin{pmatrix} a_L(\varepsilon) \\ a_R(\varepsilon) \end{pmatrix} \tag{3.11}$$

Thus we introduce the annihilition operators $\mathbf{a}_\alpha(\varepsilon)$ (resp. $\mathbf{b}_\alpha(\varepsilon)$) of incoming (resp. outgoing) states $|a_\alpha(\varepsilon)\rangle$ (resp. $|b_\alpha(\varepsilon)\rangle$) of energy ε in the reservoir α.

3.2 Statistical average of the transferred charge per pulse $\langle Q \rangle$

A voltage-pulse driven quantum wire may be used as a few-quanta charge source if the transferred charge per pulse Q is reliable. This means that the fluctuations of Q are zero or small compared to its mean value: $\sqrt{\langle \Delta Q^2 \rangle} \ll \langle Q \rangle$. In the classical regime, i.e at high number of

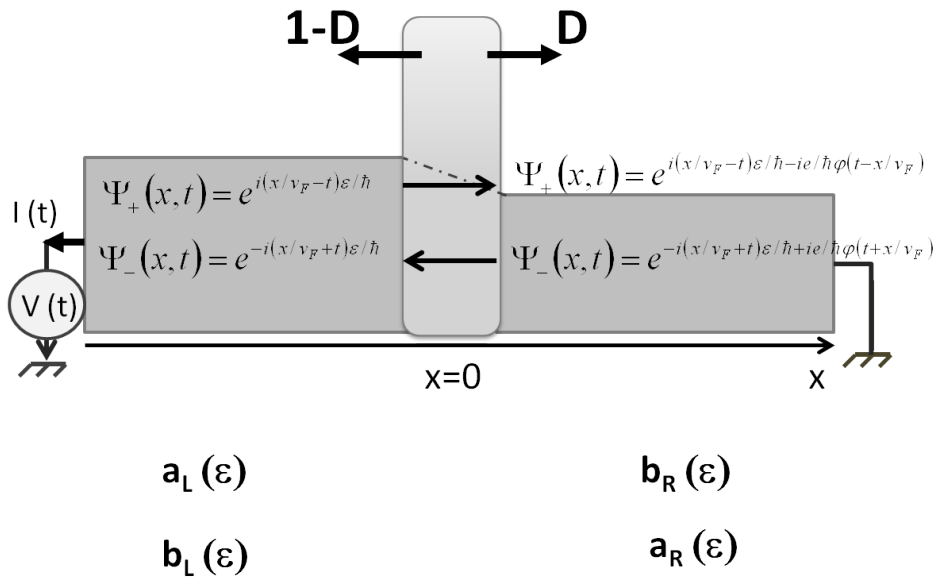

Figure 3.2: Incoming electrons $a_{L,R}$ are elastically scattered at the interface region between the two reservoirs. The scattering mattrix **S** gives the transmission and reflexion coefficients between $a_{L,R}$ and the outgoing states $b_{L,R}$. when a voltage drop is applied between the reservoir, the scattering effects of the mattrix **P** combine with **S** into a total scattering mattrix **U** (eq. (3.11)).

charge transferred per pulse, this condition is fulfilled. On the contrary, the smaller $\langle Q \rangle$, the more the statistical nature of Q can be put in evidence. So when $\langle Q \rangle$ is equal to few quanta, we expect that the fluctuations of Q are not small.

To define the transferred charge Q per pulse, we will consider two cases. For a single pulse V_p of finite flux q, we can consider the limit:

$$lim_{t\to\infty} Q_{[-t,t]} = lim_{t\to\infty} \int_{-t}^{t} I(u)du$$

When the pulse V_p is repeated periodically with at the frequency $\nu = 1/\mathcal{T}$, the transferred charge Q per pulse is in fact equal to the transferred charge per period:

$$Q = lim_{t\to\infty} \frac{\mathcal{T}}{2t} Q_{[-t,t]} = \int_{0}^{\mathcal{T}} I(u)du$$

.

The single pulse case is of historical consideration [69, 82]. Remarkably it enables the analytical computation of the excitations eigenstates above the Fermi sea in the case of a Lorentzian pulse of integer flux (section 3.6). Considering periodic pulses is definitely closer to the experimental implementation of the source, because we need to repeat pulses at high frequency in order to produce current and noise that can be detected to a significant level. Consequently the further developpements focus on the periodic case. The general formalism for non-periodic voltage $V(t)$ is developped in the appendix A.

When $V(t)$ is a periodic repetition of pulses $V_p(t)$, $\varphi(t) = \varphi_{AC}(t) + eV_{DC}t/\hbar$, where $\varphi_{AC}(t)$ is the periodic phase associated to the alternative part V_{AC}, and V_{DC} is the mean value of V(t). The Fourier transform P^*_{AC} of $exp(i\varphi_{AC}(t))$ is discrete because $\varphi_{AC}(t)$ is periodic.

On the other hand, adding a DC part to a voltage $V_{AC}(t)$ only shifts the P^*_{AC} by a translation of $eV_{DC}/\hbar$, which is a remarkable property we will discuss in chapter 7. Consequently the spectrum of $exp(i\varphi(t))$ is discrete and can be written as:

$$P^*(\varepsilon) = \sum_{n=-\infty}^{\infty} P^*_{AC}(n) h\delta(\frac{\varepsilon - nh\nu - eV_{DC}}{\hbar})$$

Furthermore, the number of flux q associated to one voltage pulse is also equal to $eV_{DC}/h\nu$:

$$q = \frac{e}{h}\int_{-\infty}^{\infty} V_p(t)dt = \frac{e}{h}\int_0^{\mathcal{T}}\sum_{n\in\mathbb{Z}} V_p(t+n\mathcal{T})dt = \frac{e}{h}\int_0^{\mathcal{T}} V(t)dt = \frac{eV_{DC}}{h\nu} \tag{3.12}$$

In this section, the time dependent version of the Landauer formula that links $\langle I(t)\rangle$ to $V(t)$ is recovered from the scattering mattrix $\mathbf{U}$. So whatever the shape of $V(t)$, the average transferred charge per pulse Q is equal to the number of flux q.

The probability amplitude of incoming states $a_R(\varepsilon')$ and outgoing states $b_R(\varepsilon')$ are:

$$\begin{aligned} a_R(\varepsilon') &= e^{i\varepsilon'/\hbar t_-} \\ b_R(\varepsilon') &= e^{i\varepsilon'/\hbar t_+} \end{aligned}$$

In the case of free electrons with linear dispersion, the density of state ρ is simply equal to $(v_F h)^{-1}$. In this chapter, the computations are done for one spin channel. The particle density operator at $x > 0$ can be written as:

$$\begin{aligned} \Psi_R(t,x) &= \int_{-\infty}^{\infty} \sqrt{\rho\left(\varepsilon'\right)} d\varepsilon' \left(e^{i\varepsilon'/\hbar t_+} \mathbf{b_R}\left(\varepsilon'\right) + e^{i\varepsilon'/\hbar t_-} \mathbf{a_R}\left(\varepsilon'\right)\right) \\ &= \sum_\beta \int_{-\infty}^{\infty} \frac{d\varepsilon'}{\sqrt{v_F h}} \int_{-\infty}^{\infty} d\varepsilon e^{i\varepsilon'/\hbar t_+} \mathbf{U}_{R,\varepsilon',\beta,\varepsilon} + e^{i\varepsilon'/\hbar t_-} \delta\left(\varepsilon' - \varepsilon\right) \delta_{R\beta} \mathbf{a}_\beta\left(\varepsilon\right) \end{aligned} \tag{3.13}$$

It is essential to note that the above integration does not commute: we would find a zero current if we switched the integrations on ε and ε'. On the contrary, computed in this order the integration gives a finite current. This mathematical problem is due to the infinite linear Fermi sea approximation. We actually compute for each energy the resulting current due to the difference of occupation of the left moving and the right moving states. Then we integrate this difference over all the energy will give us the finite current. On the contrary, we are not allowed to compute separately the total left and right current and then make the difference, first because they are infinite, and second because they are strictly equal in the linear approximation.

From equation (3.13) the statistic average of the current operator can be derived:

$$\langle I(t,x) \rangle = \frac{-ie\hbar}{2m} \left\langle \Psi^\dagger(t,x) \frac{\partial \Psi(t,x)}{\partial x} - \frac{\partial \Psi^\dagger(t,x)}{\partial x} \Psi(t,x) \right\rangle$$

$$\langle I(t,x) \rangle = \frac{eD}{h} \int_{-\infty}^{\infty} d\eta \sum_{n,m \in \mathbb{Z}} \left(P^*_{AC}(n) P_{AC}(m) e^{2i\pi\nu(n-m)t_+} f_L(\eta + (q+n)h\nu) \right) - f_R(\eta) \quad (3.14)$$

Lets suppose that the fermi distribution of the two reservoirs are the same and correspond to a temperature T. Then we note that

$$\sum_{n,m \in \mathbb{Z}} P^*_{AC}(n) P_{AC}(m) e^{2i\pi\nu(n-m)t_+} f(\eta) = e^{-i\varphi_{AC}(t) + i\varphi_{AC}(t)} f(\eta) = f(\eta) \quad (3.15)$$

In consequence:

$$\langle I(t,x) \rangle = \frac{eD}{h} \int_{-\infty}^{\infty} d\eta \sum_{n,m \in \mathbb{Z}} P^*_{AC}(n) P_{AC}(m) e^{2i\pi\nu(n-m)t_+} (f(\eta + (q+n)h\nu) - f(\eta)) \quad (3.16)$$

It is now possible to exchange the sums over n and m and the integral over η. This leads to:

$$\langle I(t,x) \rangle = \frac{eD}{h} \sum_{n,m \in \mathbb{Z}} P^*_{AC}(n) P_{AC}(m) e^{2i\pi\nu(n-m)t_+} (q+n)h\nu \quad (3.17)$$

The above formula simplifies into the Fourier transform expression of the product of $V(t_+)e^{i\varphi(t_+)}$ and $e^{-i\varphi(t_+)}$:

$$\sum_{n=-\infty}^{\infty} (q+n)h\nu P^*_{AC}(n) e^{2i\pi\nu(q+n)t_+} = eV(t_+)e^{i\varphi(t_+)}$$

$$\sum_{m=-\infty}^{\infty} P_{AC}(m) e^{-2i\pi\nu(m+q)/\hbar t_+} = e^{-i\varphi(t_+)}$$

We finally recover the temporal Landauer formula:

$$\langle I(t,x)\rangle = \frac{e^2 D}{h} V(t - x/v_F) \tag{3.18}$$

The transferred charge per pulse $\langle Q\rangle$ is given by the integral of $V(t)$ over the period:

$$\langle Q\rangle = \int_0^{\mathcal{T}} dt\, \langle I(t,x)\rangle = \frac{e^2 D}{h} \int_0^{\mathcal{T}} V(t) dt = eqD \tag{3.19}$$

3.3 The fluctuations of the charge per pulse

3.3.1 Computation of ΔQ^2 for periodic pulses

The charge fluctuation ΔQ^2 is given by the integration over time of the current-current correlators $\langle I(t,x) I(t',x)\rangle$.

$$\langle I(t,x) I(t',x)\rangle = \left(\frac{-ie\hbar}{2m}\right)^2 \left\langle \left(\Psi^*(t)\frac{\partial\Psi(t)}{\partial x} - \frac{\partial\Psi(t)}{\partial x}\Psi(t)\right)\left(\Psi^*(t')\frac{\partial\Psi(t')}{\partial x} - \frac{\partial\Psi(t')}{\partial x}\Psi(t')\right)\right\rangle$$

The current correlator implies the integration over the four operators statistical average $\left\langle \mathbf{a}_\alpha^\dagger(\varepsilon)\, \mathbf{a}_\beta(\varepsilon')\, \mathbf{a}_\gamma^\dagger(\eta)\, \mathbf{a}_\delta(\eta')\right\rangle$ that can be divide in two parts.

The direct term:

$$\left\langle \mathbf{a}_\alpha^\dagger(\varepsilon)\, \mathbf{a}_\alpha(\varepsilon)\, \mathbf{a}_\gamma^\dagger(\eta)\, \mathbf{a}_\gamma(\eta)\right\rangle = f_\alpha(\varepsilon)\, f_\gamma(\eta)\, \delta_{\alpha\beta}\delta_{\gamma\delta}\delta(\varepsilon - \varepsilon')\delta(\eta - \eta')$$

It is straitforward to see that this term contributes to the product of average $\langle I(t)\rangle \langle I(t')\rangle$

The exchange term:

$$\left\langle \mathbf{a}_\alpha^\dagger(\varepsilon)\, \mathbf{a}_\gamma(\varepsilon')\, \mathbf{a}_\gamma^\dagger(\varepsilon')\, \mathbf{a}_\alpha(\varepsilon)\right\rangle = f_\alpha(\varepsilon)\,(1 - f_\gamma(\varepsilon'))\, \delta_{\alpha\gamma}\delta_{\beta\delta}\delta(\varepsilon - \eta')\delta(\varepsilon' - \eta)$$

This term gives three distinct contributions.

the thermal fluctuation of the left reservoir :
The exchange between two particles coming from the left reservoir leads to the term $L_{Th}(t,t',x)$:

$$\begin{aligned} L_{Th}(t,t',x) &= \frac{e^2D^2}{h^2}\int_{-\infty}^{\infty} d\varepsilon d\varepsilon' \sum_{n,m,k,l\in\mathbb{Z}} f_L(\varepsilon+(q+n)h\nu)(1-f_L(\varepsilon'+(q+k)h\nu)) \\ &\quad P^*_{AC}(n)P_{AC}(m)P^*_{AC}(k)P_{AC}(l)e^{i/\hbar(\varepsilon'-\varepsilon)(t-t')+2i\pi\nu((k-m)t_++(n-l)t'_+)} \end{aligned} \tag{3.20}$$

This term concerns only the left reservoir: it would be the same for any of voltage applied because it must be invariant by gauge transformation. In consequence it is equal to the fluctuation of the left reservoir when no voltage is applied and corresponds only to the thermal fluctuations. This can be recovered by introducing the definition the Fourier transform P^*_{AC} in the above expression:

$$e^{i\varphi_{AC}(t)} = \sum_{-\infty}^{\infty} P^*_{AC}(n)e^{2i\pi\nu nt}$$

$$L_{Th}(t,t',x) = \frac{e^2D^2}{h^2}\int_{-\infty}^{\infty} d\varepsilon d\varepsilon' f_L(\varepsilon)(1-f_L(\varepsilon'))e^{i/\hbar(\varepsilon-\varepsilon')(t-t')} \tag{3.21}$$

the thermal fluctuation of the right reservoir :
The exchange between two particles of the right reservoir leads to the term $R_{Th}(t,t',x)$:

$$\begin{aligned} R_{Th}(t,t',x) &= \frac{e^2}{h^2}\int_{-\infty}^{\infty} d\varepsilon d\varepsilon' f_R(\varepsilon)(1-f_R(\varepsilon'))e^{i/\hbar(\varepsilon'-\varepsilon)(t'-t)} \\ &\quad \times\big((1-D)^2+1-2(1-D)\cos(2(\varepsilon'-\varepsilon)/\hbar x/v_F)\big) \end{aligned} \tag{3.22}$$

The x dependent term is due to propagation. As we look in the ballistic region around $x=0$. In practive, this region is small, i.e. $(\varepsilon'-\varepsilon)/\hbar x/v_F \ll 1$. So $R_{Th}(t,t',x) = L_{Th}(t,t',x)$:

$$R_{Th}(t,t',x) = \frac{e^2D^2}{h^2}\int_{-\infty}^{\infty} d\varepsilon d\varepsilon' f_L(\varepsilon)(1-f_L(\varepsilon'))e^{i/\hbar(\varepsilon-\varepsilon')(t-t')} \tag{3.23}$$

the partition correlator :
The term $B_{ex}(t,t',x)$ (eq. (3.24)) comes from the exchange of two particles issued from different reservoir. This leads to the partition noise on the barrier of transmission D:

$$\begin{aligned} B_{ex}(t,t',x) &= \frac{e^2}{h^3}D(1-D)\sum_{n,m\in\mathbb{Z}} P^*_{AC}(n)P_{AC}(m)\int_{-\infty}^{\infty} d\varepsilon d\varepsilon' \\ &\times[f_R(\varepsilon')(1-f_L(\varepsilon+(q+n)h\nu))e^{2i\pi(n-m)\nu t_+ +(\varepsilon-\varepsilon')(t'_+-t_+))} \\ &+(1-f_R(\varepsilon'))f_L(\varepsilon+(q+n)h\nu)e^{2i\pi(n-m)\nu t'_+ +(\varepsilon-\varepsilon')(t_+-t'_+))}] \end{aligned} \tag{3.24}$$

As the charge transferred per pulse Q is in fact equal to the charge transferred per period, the variance $\langle \Delta Q^2 \rangle$ of the transferred charge per pulse is equal to the integration of $L_{Th}(t,t',x) + R_{Th}(t,t',x) + B_{ex}(t,t',x)$ over t and t' in $[0,\mathcal{T}]^2$. On the other side, the current noise is characterized by its spectral power density, $S_I(\omega)$, which is twice the Fourier transform at frequency ω of the average of current-current correlator [30, 122]:

$$S_I(\omega) = 2\int_{-\infty}^{\infty} d\tau e^{i\omega\tau} \lim_{u\to\infty}\frac{1}{2u}\int_{-u}^{u}\langle I(t+\tau)I(t)\rangle\, dt = 2\frac{1}{\mathcal{T}}\int_0^{\mathcal{T}} d\tau e^{i\omega\tau}\int_0^{\mathcal{T}}\langle I(t+\tau)I(t)\rangle\, dt \tag{3.25}$$

Consequently $2\langle \Delta Q^2\rangle \nu = S_I(0)$. $S_I(0) = S_{Th}(0) + S_{part}(0)$, where S_{Th} (eq.(3.26)) is the thermal fluctuations of the two reservoirs issued from the integration of $L_{Th}(t,t',x)$ and $R_{Th}(t,t',x)$, and $S_{part}(0)$ (eq.(3.27)) is the shot-noise of the particles that flow through the tunnel barrier:

$$S_{Th}(0) = 2\frac{e^2D^2}{h}\int_{-\infty}^{\infty} d\varepsilon f_L(\varepsilon)(1-f_L(\varepsilon)) + f_R(\varepsilon)(1-f_R(\varepsilon)) \tag{3.26}$$

$$\begin{aligned} S_{part}(0) &= 2\frac{e^2}{h}D(1-D)\sum_{n\in\mathbb{Z}}|P_{AC}(n)|^2\int_{-\infty}^{\infty} d\varepsilon \\ &[f_R(\varepsilon)(1-f_L(\varepsilon+(q+n)h\nu)) + (1-f_R(\varepsilon))f_L(\varepsilon+(q+n)h\nu)] \end{aligned} \tag{3.27}$$

When both reservoirs have the same Fermi distribution characterized by the temperature kT, these expressions simplify into:

$$S_I(0) = 4\frac{e^2D^2}{h}k_BT + 2\frac{e^2}{h}D(1-D)\sum_{n\in\mathbb{Z}}|P_{AC}(n)|^2 h(q+n)\nu\coth\left(\frac{h(q+n)\nu}{2k_BT}\right) \tag{3.28}$$

If the voltage waveform is a DC voltage, we recover the shotnoise equation [77], and in the case of sine waveforms we find the Photon-assisted shotnoise formula [86].

3.3.2 Discussion about the historical case of the single pulse

In their works, Lee and Levitov [82] or Keeling et al. [69] considered the case of a single pulse $V_p(t)$ with a total flux $q = \phi(\infty)/(2\pi)$. It is a very interesting theoretical situation: it indeed enlights the key features that can be found in the more realistic case of a periodic train of pulses, especially the fluctuations of the transferred charge Q. For a single pulse $V_p(t)$ of total flux $q = \phi(\infty)/(2\pi)$, the fluctuations of Q present a dramatic difference between integer and non-integer values of q. Actually, Lee and Levitov [82] have shown that the variance of the charge transferred between $[-t, t]$ contains a logarithmically divergent term periodic with q:

$$\left\langle \Delta Q^2_{[-t,t]} \right\rangle = e^2 D(1-D) \left(\frac{2}{\pi^2} \sin^2(q\pi) \ln\left(\frac{t}{w}\right) + q + o(q) \right) \tag{3.29}$$

Their expression was obtained at zero temperature, when only the shotnoise correlator $B_{ex}(t, t', x)$ contributes to the fluctuations. They considered a voltage pulse $V_p(t)$ of very small time extension $2w$ that gives a phase φ that rises steadily from 0 to $2\pi q$. In their result (3.29), one can distinguish the logarithmically time divergence that is suppressed only for integer values of q. The periodic function that multiply the logarithmic divergence may not be strictly the same for all waveforms $V_p(t)$, nevertheless it should have zeros at integer number q.

When $\langle Q \rangle = q$ is an integer, $\langle \Delta Q^2 \rangle$ is finite and equal to the second and third terms of the Lee and Levitov formula (eq. (3.29)). It can be identified to the shotnoise of emitted quasiparticles, which number is $q+o(q)$, i.e. the charge plus an extra number of quasi-particle, that depends on the voltage shape (see appendix A for the exact formula derived from the integration of $B_{ex}(t, t', x)$ in the single pulse case).

When the pulses $V_p(t)$ are repeated periodically, the transferred charge per pulse is identified to the charge transferred per period and the low divergence are regularized. Consequently $\langle \Delta Q^2 \rangle$ is available for any value of q.

3.4 Photo-absorption interpretation of the results

The expression of the noise we directly derived in section can be easily understood in terms of photo-absorption [69]. When an electron from the source reservoir acquires a phase $\varphi(t)$, its wavefunction changes from an eigenstate of energy ε to a superposition of states of energy ε' which probabilities are given by $|P_{\varepsilon\varepsilon'}|^2$. This means that the electron has absorbed (or more properly emitted when $\varepsilon' - \varepsilon$ is negative) a photon of energy $\varepsilon' - \varepsilon$ with a probability $|P_{\varepsilon\varepsilon'}|^2$.

In the excited Fermi sea, the operator $\mathbf{c}_\varepsilon$ are associated with the excited states $\psi_+ = exp(-i(t_+\varepsilon/\hbar + i\varphi(t_+)))$ of equation(3.9), so $\mathbf{c}_\varepsilon = \int d\varepsilon' P_{\varepsilon'\varepsilon} \mathbf{a}_{\varepsilon'}$ [69]. Then the operators N_e and N_h count the electrons created above the Fermi sea and the holes created below the Fermi level:

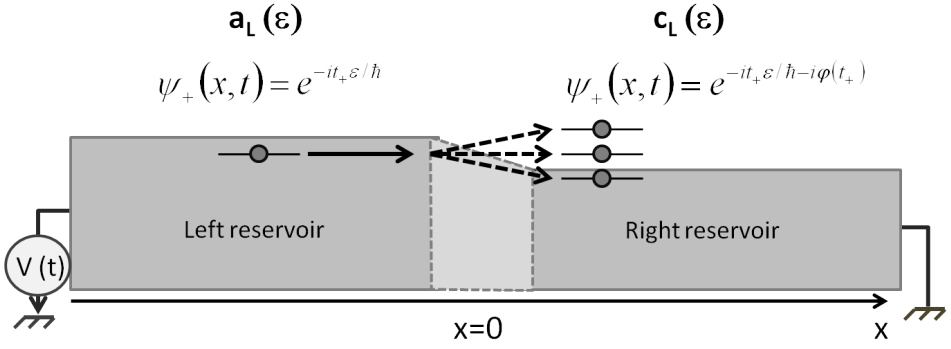

Figure 3.3: The operator $\mathbf{c}_\varepsilon$ associated with $|\varepsilon\rangle = exp(-i(t_+\varepsilon/\hbar + i\varphi(t_+)))$ is equal to $\mathbf{c}_\varepsilon = \int d\varepsilon' P_{\varepsilon'\varepsilon}\mathbf{a}_{\varepsilon'}$

$$N_e = \int_{-\infty}^{\infty} d\varepsilon (1 - f(\varepsilon)) \mathbf{c}^\dagger{}_\varepsilon \mathbf{c}_\varepsilon$$
$$N_h = \int_{-\infty}^{\infty} d\varepsilon f(\varepsilon) \mathbf{c}_\varepsilon \mathbf{c}^\dagger{}_\varepsilon \tag{3.30}$$

Here we mean by hole (resp. electrons) a lack (resp. an excess) of occupation of the eigenstates compared to the unperturbed Fermi sea distribution at temperature T. This definition extends the proper notion at zero temperature to the case of finite temperature.

Computing the average number $\langle N_e\rangle = \langle \Phi_F|N_e|\Phi_F\rangle$ and $\langle \Phi_F|N_h|\Phi_F\rangle$, we recover the fact that we only have to consider the probabilities of photo-absorption for each level:

$$\langle N_e\rangle = \int_{-\infty}^{\infty} \frac{d\varepsilon}{h\nu} \sum_{n\in\mathbb{Z}} |P_{AC}(n)|^2 (1 - f_R(\varepsilon)) f_L(\varepsilon + (q+n)h\nu) \tag{3.31}$$

$$\langle N_h\rangle = \int_{-\infty}^{\infty} \frac{d\varepsilon}{h\nu} \sum_{n\in\mathbb{Z}} |P_{AC}(n)|^2 f_R(\varepsilon) (1 - f_L(\varepsilon + (q+n)h\nu)) \tag{3.32}$$

Identifying these terms in the partition noise of equation (3.27), we recover the fact that the partition noise of the transferred charge is indeed produced by the statistical process of scattering of all excited quasi-particles:

$$S_{part}(0) = 2\frac{e^2}{h} D\,(1-D)\,h\nu\,(\langle N_e\rangle + \langle N_h\rangle) \tag{3.33}$$

Thus, applying voltage pulses of arbitrary shape can be understand in a generalized frame of the photon-assited shotnoise already studied in the case of a monochromatic voltage excitation (sinewave) [118, 122, 125].

When both reservoirs are at zero temperature, these equations simplify into:

$$\langle N_e \rangle = \sum_{n>-q}^{\infty} |n+q||P_{AC}(n)|^2 = \sum_{m>0,\, m-q\in\mathbb{Z}} m|P(\frac{mh\nu}{\hbar})|^2 \tag{3.34}$$

$$\langle N_h \rangle = \sum_{-\infty}^{n<-q} |n+q||P_{AC}(n)|^2 = \sum_{m<0,\, m-q\in\mathbb{Z}} |m||P(\frac{mh\nu}{\hbar})|^2 \tag{3.35}$$

There is a clear contribution of the both parts of the spectrum of $\exp(i\varphi(t))$ to excited particles production. $P(\varepsilon)$, $\varepsilon > 0$, which corresponds to photon absorption, promotes electrons above the Fermi sea, whereas $P(\varepsilon)$, $\varepsilon < 0$, which corresponds to photon emission, promotes holes below the Fermi level. Generally, the excited quasiparticles do not correspond to one single absorption or emission process, but are the result of a collective excitation of the infinite Fermi sea. In consequence holes are created below the Fermi level because the electrons loose energy by emission.

In conclusion, the variance of the transmitted charge per pulse ΔQ^2 is given by the thermal fluctuations of the reservoirs and the shotnoise of excited holes and electrons due to the voltage $V(t)$. The average number of the emitted quasi-particles depend on the shape of the voltage $V(t)$ through the distribution $|P|^2$, that define the probability of absorption or emission of photons.

3.5 Is a noiseless charge source a good quasi-particle source?

3.5.1 A perfect charge source at D=1

When D=1, the fano factor is equal to zero and the fluctuations of the charge due to partition noise vanish. Only the thermal fluctuations of the reservoirs contributes to ΔQ^2. When T=0, this fluctuations vanish and the total transferred charge is certain. Consequently, the quantum wire can be used as a perfect charge source whatever the voltage pulses.

Yet, this does not mean at all that the number of emitted electrons and holes is certain and that the quantum wire behaves as a perfect quasi-particle source. Actually ΔQ^2 does not show the average number of emitted quasiparticles when D=1.

That $\Delta Q^2 = 0$ whatever the average value $\langle Q \rangle$ seems strange, especially when $\langle Q \rangle$ is a non-integer number: because of the granularity of the charge, we would expect that the number of charge transferred per pulse should be statistical even at D=1. In the case of pulses

of flux 2/3 for example, the effective charge transferred during each pulse should fluctuate: sometimes e, sometimes 2e, sometimes -e and so on and so forth, so that on average the charge transferred is -2/3.

As $S_I(0)$ is somehow a long time measurement, one could expect that it lacks some piece of information about the time emission of the charge. Indeed periodic pulse of flux 2/3 can be conceptually gathered in packets of three that has a total flux of two, and ΔQ^2 is the same in both case even at transmission $D < 1$. The same problem occurs for the mesoscopic capacitor source: measuring $S_I(0)$ gives no information, whereas measuring the noise near the cycle frequency $S_I(\omega)$ reveals the quantum-jitter, which is due to the statistics of the time emission of the charge [94]. Does the high-frequency noise bring some new information in the case of the 1-dimensionnal channel source?

At $T = 0$, the emission spectral power density of the noise at finite frequency ω (eq.3.25) is equal to:

$$\begin{aligned} S_I(\omega) &= 2\frac{e^2}{h}D(1-D)\sum_{n\in\mathbb{Z}}\int_{-\infty}^{\infty} d\varepsilon |P_{AC}(n)|^2 \\ &\quad \times \left(f(\varepsilon)\left(1-f(\varepsilon+(n+q)h\nu-\hbar\omega)\right)+f(\varepsilon+(n+q)h\nu+\hbar\omega)\left(1-f(\varepsilon)\right)\right) \\ &= 2\frac{e^2}{h}D(1-D)\sum_{n\in\mathbb{Z},\,|2\pi(n+q)\nu|>\omega} |P_{AC}(n)|^2|n+q|h\nu \end{aligned} \tag{3.36}$$

The term measure the partition noise of the electrons excited above $E_F + \hbar\omega$ and the holes excited below $E_F - \hbar\omega$. When the voltage $V(t) = V_{DC}$ one recovers the high frequency noise formula measured by Schoelkopf et al. [124] in a diffusive wire and Bajjani et al. [7] in a quantum point contact.

The partition term of $S_I(\omega)$ also vanishes at perfect transmission D=1. The quantum wire source is a perfectly noiseless charge source at D=1, and shows no quantum jitter. This remarks can be related to the conclusion of Martin and Landauer [97], who show in a wave-packets approach that electrons flows noiselessly through the quantum wire. When $D < 1$, the channel acts as a beam splitter that makes the position of the quasi-particles on the left or on the right of the voltage drop region an observable. On the contrary, when $D = 1$ the electrons can stay in a superposition of states in the right and in the left reservoir. As the reservoir absorbs by definition any coming electron whatever its energy, no fluctuation is therefore observable.

3.5.2 The difference between the mesoscopic capacitor source and the 1-D channel source

Why does the mesoscopic-capacitor source show a time-emission statistics and not the voltage driven quantum wire? This difference is related to the question of the size of the reservoir. The electron trajectory is finite in the mesoscopic capacitor. The trajectory loop in the capacitor defines a time-scale τ_0 to the system (see the model of Mahe et al. [94]). This is responsible for the apparition of a quantum-jitter. The spectral power of the noise $S_I(\omega)$ produced by the mesoscopic noise is given by the following formula (Albert et al. [3], Jonckheere et al. [64]):

$$S_I(\omega) = \frac{2}{\mathcal{T}} \tanh\left(\frac{\mathcal{T}}{4\tau}\right) \frac{\omega^2\tau^2}{1+\omega^2\tau^2} \tag{3.37}$$

$\mathcal{T}$ is the driving frequency of $V_g(t)$ that pushes the quantum dot higher level above or below the Fermi level of the circuit. D is the probability of the electron to be emitted or absorbed in the capacitor and $\tau = \tau_0/|\ln(1-D)|$ is the correlation time that determines the time scale over which the system looses memory about the initial conditions, i.e. the time when the electron enters the dot. In the quantum-jitter regime, $\tau \ll \mathcal{T}$, and the noise tends to:

$$S_I(\omega) = \frac{2}{\mathcal{T}} \frac{\omega^2\tau^2}{1+\omega^2\tau^2} \tag{3.38}$$

As demonstrated by Mahe et al. [94], this quantity corresponds to the current phase noise due to the uncertainty on time emission, and we remark that it is entirely determined by this time scale τ. On the other hand, when the mesoscopic capacitor is extended in size, τ_0 and τ tends to infinity. Even for D is close to 1, we are in the other limit of equation (3.37) and the noise $S_I(\omega)$ disappears :

$$S_I(\omega) = \frac{1}{2\tau} \tag{3.39}$$

In the limit of large size, the capacitor is comparable to the infinite left reservoir of the quantum-wire problem, except that no DC voltage can be applied. In the case of the voltage driven quantum wire, the electrons trajectories pass only one time on the voltage drop and then are absorbed. In consequence there is no time-scale in the system clocking the device, and so no jitter.

3.5.3 Quasi-particle statistics

Lets us emphasize again on the fact that even if at $D = 1$ the transferred charge $Q = eq$ per pulse is certain, this does not imply that the number of quasi-particles produced per pulse is certain. The emitted electrons and holes that constitute this charge depend on the voltage shape according to equations (3.31) and (3.32).

To study quantum optics experiments on a mesoscopic circuit, we are actually more interested in the statistics of the emitted quasi-particles than in this the charge transfer. In order to decide whether a voltage pulse can be applied on a quantum wire to emit quasi-particles with certainty, the true criterion is whether the number of electrons and holes excited are certain, i.e. $\langle \Delta N_e^2 \rangle = 0$ and $\langle \Delta N_h^2 \rangle = 0$.

This is a different problem from the minimal excitation question discussed by Ivanov et al. [59]. Indeed, Ivanov et al. have looked for the type of voltage pulses that emit only electrons or holes, and consequently minimize the number of quasiparticles emitted for a given number of transferred charge q [59,69]. They have shown that only lorentzian pulses of integer number q emit only electrons and only holes. In this case, $\langle \Delta N_e^2 \rangle = 0$ and $\langle \Delta N_h^2 \rangle = 0$ is also fulfilled.

But we may ask if there is no other voltage pulse that fulfills the reliability criterion, i.e. $\langle \Delta N_e^2 \rangle = 0$ and $\langle \Delta N_h^2 \rangle = 0$, even if it does not minimize the emitted quasi-particles number (i.e. $N_e + N_h = |q| + N_+$ and $N_+ > 0$). For example, some voltage that would produce an electron and an hole per pulse with certainty would fulfill the condition to make a good quasi-particle source, and even be an interesting case in an experimental point of vue.

Lets see which kind of constraints this implied on the voltage pulse shape. The variance of the operator N_e defined in section (3.4) is equal to:

$$\begin{aligned} \left\langle \Delta N_e^2 \right\rangle &= \int_0^\infty \int_0^\infty dp dq \int_{-\infty}^{\infty} d\varepsilon d\varepsilon' P^*_{p\varepsilon} P_{q\varepsilon} P^*_{p\varepsilon'} P_{q\varepsilon'} f(\varepsilon)(1-f(\varepsilon')) \\ 0 &= \int_{-\infty}^\infty \int_{-\infty}^\infty d\varepsilon d\varepsilon' f(\varepsilon)(1-f(\varepsilon')) \left\| \int_0^\infty dp P^*_{p\varepsilon} P_{p\varepsilon'} \right\|^2 \end{aligned} \tag{3.40}$$

At zero temperature,this implies:

$$\forall (p,\varepsilon,\varepsilon') \in \mathbb{R}^+ \times \mathbb{R}^- \times \mathbb{R}^+, \int_0^\infty dp P^*_{p\varepsilon} P_{p\varepsilon'} = 0 \tag{3.41}$$

We can differentiate this late expression with respect of ε or ε', then adding these two expressions we find that:

$$\forall (p,\varepsilon,\varepsilon') \in \mathbb{R}^+ \times \mathbb{R}^- \times \mathbb{R}^+, \int_0^\infty dp \frac{\partial (P^*_{p\varepsilon} P_{p\varepsilon'})}{\partial p} = 0 \tag{3.42}$$

$$\forall (\varepsilon,\varepsilon') \in \mathbb{R}^- \times \mathbb{R}^+, \; P(-\varepsilon)^* P(-\varepsilon') = 0 \tag{3.43}$$

This implies that P is null either over $\mathbb{R}^+$ or $\mathbb{R}^-$, and if we report it in equations (3.31) and (3.32), that only $V(t)$ that injects either only electrons or only holes can be a reliable quasi-particles source. As soon as electrons and holes can be produced by the voltage shape, then the number of quasi particle become statistic, because there is always a none zero probability that the electron and the hole creation compensate each other. As Ivanov et al. [59], only Lorentzian pulses with integer flux q inject only electrons or only holes in the circuit. Consequently the only reliable quasi-particle sources are these that produce minimal excitation states, i.e. the Lorentzian voltage-pulse source.

There is however some approaching cases that enable to inject simultaneously electrons and holes with almost certainty. For example, applying a voltage pulse that is the sum of a positive and a negative lorentzian pulses with very different widths produce an hole and an electron with a great probability, because the typical energies of the two particles are very different.

Consider two lorentzian pulses of flux of 1 and -1 and widths w_1 and w_2 respectively, that are applied simultaneously on a quantum wire. They can inject either one electron and one hole, or no particle at all. The probability to inject succesfully the electron-hole pair can be estimated by the average number $\langle N_e \rangle + \langle N_h \rangle = (\frac{w_1 - w_2}{w_1 + w_2})^2$ (see equations (A.11) and (A.12) in appendix A). When $w_1 \ll w_2$, $P = 1 - 4w_1/w_2$. The ultimate case is to choose one of the Lorentzian equal to a DC voltage ($w = \infty$) or to a dirac voltage ($w = 0$), which leads to P=1. In the repeating case, the repetition period $\mathcal{T}$ introduces another timescale that reduces the probability when a lorentzian and an opposite DC voltage is applied: $1 - P \sim w_1/\mathcal{T}$ (see numerical computation fig.(3.5) in section 3.7).

3.6 The ideal case of lorentzian pulses

3.6.1 The unique spectrum of integer Lorentzian pulses

As we mention in the previous section, excited electrons and excited holes are respectively related to $P(\varepsilon)$, $\varepsilon > 0$ and $P(\varepsilon)$, $\varepsilon < 0$. Thus the necessary and sufficient condition to emit only electron (resp. only holes) in the circuit is that P is null on $\mathbb{R}^-$ (resp. $\mathbb{R}^+$). Ivanov et al. [59] demonstrate that this conditions is fulfilled by only superposition of lorentzian shape pulses of integer flux q. Furthermore, when D=1, $\Delta \langle N_e^2 \rangle = \Delta \langle N_h^2 \rangle = 0$. This means that we can obtain a perfect n-quasi-particle source by applying lorentzian pulses on a quantum wire. This is actually the only voltage shape that can be used as a reliable quasi-particle source, as we demonstrated in the previous section.

In fact the spectrum P for a single lorentzian pulse $V_q = \frac{\hbar}{e} \frac{2wq}{t^2 + w^2}$ that creates integer number q electrons has the following simple expression:

$$P(\frac{\varepsilon}{\hbar}) = \sum_{k=1}^{q} 2\pi C_q^k (\frac{\varepsilon}{\hbar})^{k-1} \frac{(-2w)^k}{(n-1)!} e^{-w\frac{\varepsilon}{\hbar}} \Theta(\varepsilon) + 2\pi\delta(\varepsilon) \tag{3.44}$$

When the lorentzian pulse of flux q is repeated at frequency ν, the voltage expression $V(t)$ becomes:

$$V_q(t) = \frac{qh\nu}{e} \frac{1 - e^{-4\pi w\nu}}{1 + e^{-4\pi w\nu} - 2e^{-2\pi w\nu}\cos(2\pi\nu t)} \tag{3.45}$$

For $q > 0$, the spectrum P^*_{AC} of $exp(i\varphi_{AC}(t))$ has the following analytic form:
For $l \geq 0$

$$P_{AC}(l) = qe^{iq\pi - 2l\pi w\nu} \sum_{k=0}^{\infty} (-1)^k \frac{(q+l+k-1)!}{k!(q-k)!(l+k)!} e^{-4k\pi w\nu} \tag{3.46}$$

For $l \leq 0$

$$P_{AC}(l) = (-1)^l qe^{iq\pi + 2l\pi w\nu} \sum_{k=0}^{\infty} (-1)^k \frac{(q+k-1)!}{k!(q-k+l)!(k-l)!} e^{-4k\pi w\nu} \tag{3.47}$$

The expressions of P^*_{AC} when $q < 0$ are the symmetric of $-q$. When q is not an integer number, the spectrum P_{AC} shows components for all number l and excess holes and electrons add to the number q. On the contrary, $1/n! = 0$ when n is a negative integer number. So for integer values of q, P_{AC} is null below $-q$ when q is positive (resp. above $-q$ when q is negative). As $P(\varepsilon/\hbar)$ is equal to P_{AC} shifted by q, there is no hole produced.

3.6.2 Expression of excited Fermi sea for Lorentzian pulses

Remarkably, the excitation of the Fermi sea due to single lorentzian pulse of flux $q = 1$ centered around $t = 0$ and of width w can be expressed [69]:

$$\mathbf{U}|\Phi_F\rangle = \mathbf{A}^\dagger|\Phi_F\rangle = \sqrt{2w} \int_0^\infty e^{-w\varepsilon/h} \mathbf{a}^\dagger_\varepsilon |\Phi_F\rangle \tag{3.48}$$

When several lorentzian pulses of $q = 1$, that have different widths w_k and centering times t_k are superposed, they also produce non-entangled excited electrons above the Fermi sea [69]:

$$\mathbf{U}|\Phi_F\rangle = \prod_{k=1}^{q} \prod_{k'=k+1}^{q} \frac{\xi_{k'} + \xi_k}{\xi_{k'} - \xi_k} \prod_{k=1}^{q} \mathbf{A}^\dagger_\mathbf{k} |\Phi_F\rangle \tag{3.49}$$

where $\xi_k = w_k - it_k$ and $\mathbf{A}^\dagger_\mathbf{k} = \sqrt{2w_k} \int_0^\infty e^{-\xi_k\varepsilon/h} \mathbf{a}^\dagger_\varepsilon$

To obtain the excitation of the Fermi sea produced by a lorentzian pulse that injects q electrons, we add recursively one electron to the excitation obtained for a lorentzian injecting $q-1$ electrons in the above expression and take the limit when $\xi_k = w_k - it_k$ tend to the same value:

$$\mathbf{U}|\Phi_F\rangle = (2w)^{\frac{n(n-1)}{2}} \prod_{k=1}^{q} \mathbf{L}_{\mathbf{k}}^{\dagger}|\Phi_F\rangle \tag{3.50}$$

where $\mathbf{L}_{\mathbf{k}}^{\dagger} = \sqrt{2w} \int_0^{\infty} e^{-\xi\varepsilon/h} \frac{\varepsilon^k}{h^k k!} \mathbf{a}_{\varepsilon}^{\dagger} d\varepsilon$

The excited electrons are produced just above the Fermi level, with a dispersion in energy that decreases exponentially on the scale h/w for the first electron. When several electrons are send simultaneously by the pulse, they piled up in energy, the nth electron beeing around the energy nh/w. Consequently the life time of these quasi-particles are given by the formula [24, 48, 145]:

$$\tau^{-1} \approx \frac{E_F}{2h} \left(\frac{nh}{wE_F}\right)^2 \ln\left(\frac{wE_F}{nh}\right) \tag{3.51}$$

For a pulse width of w=0.1ns, the life time of the nth electron is about n^{-2} times 6ns, which is largely enough for interference experiments: the coherence of a few electrons wavepacket will not be limited by the phase coherence time.

3.7 Numerical study for periodic pulses

3.7.1 Excess particles production

At zero temperature, the average number of charge is the difference between the average number of electrons and holes transferred and $S_{part}(0)$ is the sum of the average number of electrons and holes. Then we can rewrite $S_{part}(0)$ in equation (3.33) as the sum of $|q|$ and the average excess number of particles produced per pulse N_+ :

$$S_{part}(0) = 2eD(1-D)(|q| + N_+) \tag{3.52}$$

The first term is equal to the DC shot-noise of the same transferred charge, whereas the additional noise due to extra quasi-particle emission is a signature of the AC voltage. Thus at transmission $D < 1$, the excess shotnoise $S_{part}(0)$ counts the total number of excited quasi-particles, and so reveals the excess number of particles that do not appear in the current measurement because their total charge is neutral.

In this section we study the dependence of N_+ on q for different kind of experimentally realizable voltage pulses with repetition frequency ν, that are defined as followed:

- the sinewave:

$$V(t) = q\frac{h\nu}{e}\left(\sin(2\pi\nu t) + 1\right)$$

- the squarewave:

$$V(t) = 2q\frac{h\nu}{e} \quad if \quad 0 < t < \mathcal{T}/2, \quad V(t) = 0 \quad if \quad \mathcal{T}/2 < t < \mathcal{T}$$

- the rectangularwave:

$$V(t) = q\frac{\mathcal{T}h\nu}{we} \quad if \quad 0 < t < w, \quad V(t) = 0 \quad if \quad w < t < \mathcal{T}$$

- the lorentzian pulses:

$$V = \frac{qh\nu}{e}\frac{1 - e^{-4\pi w\nu}}{1 + e^{-4\pi w\nu} - 2e^{-2\pi w\nu}\cos(2\pi\nu t)}$$

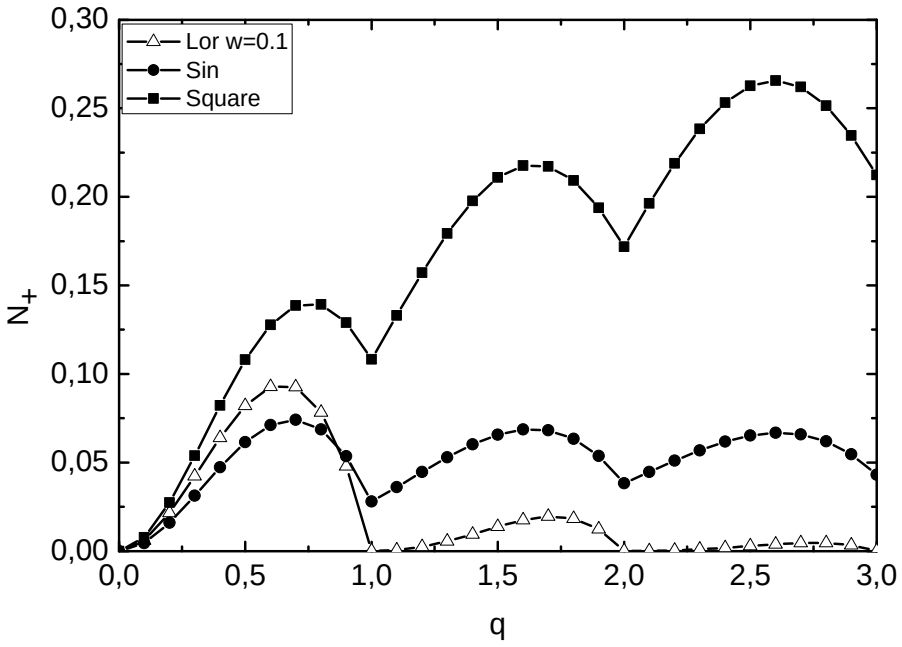

Figure 3.4: Average number of excess excited quasiparticles N_+ with respect to the average charge q transferred per pulses for three voltage pulses: sine, square and Lorentzian of width $w = 0.1T$

Figure (3.4) shows the evolution of N_+ versus q from 0 to 3 for a squarewave, a sinewave and a Lorentzian wave of width $w = 0.1\nu^{-1}$ at zero temperature. The results are in complete

agreement with thoses of Vanevic [142]. Remarkably N_+ presents local minima at integer number of transferred charge of all the waveforms. In agreement with Ivanov et al. [59], these minima are equal to zero for Lorentzian pulses, whereas some extra excitations remain for the other waveforms. Furthermore, the hierarchy of N_+ for these integer values between for the three waveforms is not fortuitous. Indeed N_+ is a kind of measure of the difference in shape of a waveform with respect to the ideal case of the Lorentzian pulse, and in that respect, a square wave differs much more from a lorentzian train that a sine wave.

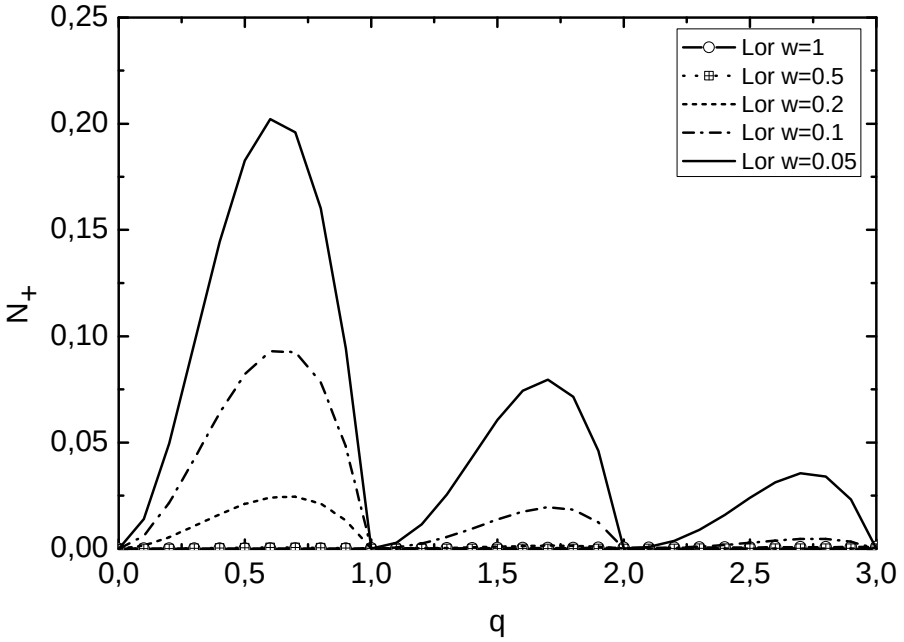

Figure 3.5: Average number of excess excited quasiparticle N_+ with respect to the average charge q transferred per pulses for Lorentzian of different width w

As mentionned in section (3.2), the periodic repetition of pulses of non-integer flux q enables the regularization of the fluctuations of the transferred charge that diverge in the single pulse case (eq.(3.29)). However the residual of the divergence is observed through the increase of the number of excess quasi-particles in the case of a non-integer q compared to the integer case, which explains local minima of N_+ at integer number of q for all voltage shape. Figures (3.5) and (3.6) illustrate very well this effect related to the orthogonal-catastrophy problem [82]. Figure (3.5) reports the dependence of N_+ with respect to the ratio of the lorentzian width to the repetition period $w/\mathcal{T}$. Figure (3.6) reports the same dependence for rectangular voltage pulses with various widths w. When $w/\mathcal{T}$ increases, pulses are actually brought closer to each other until they overlap to a DC voltage limit. In consequence N_+ exponentially disappears because the problem of splitting electrons in several distinguishable pulses (in time) is less critical. On the other hand, when w/T tends towards zero, the pulses

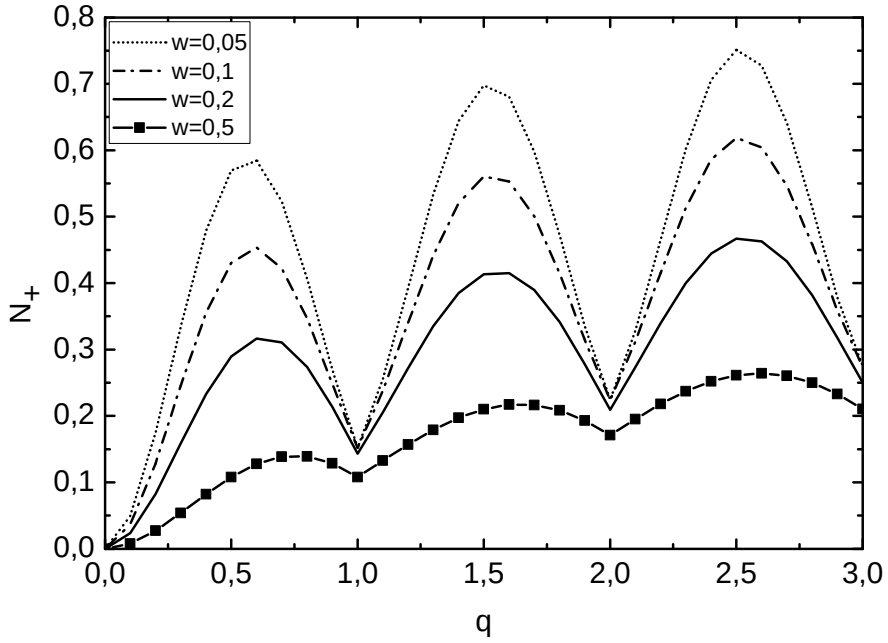

Figure 3.6: Average number of excess excited quasiparticle N_+ with respect to the average charge q transferred per pulses for rectangular pulse of different widths w expressed in ratio $w/\mathcal{T}$

are more and more separated and we tend to the single pulse situation. Thus N_+ diverge logarithmically as predicted by the orthogonal catastrophe problem of Lee and Levitov [82]. Rectangular pulses of $w/T < 0.5$ produce far more noise that Lorentzian pulses or even squarewave, because their spectrum P is far more extended to high values.

This oscillations of N_+ with q clearly show that the transport of a few charges per pulse is a quantum process. On the other hand it is interesting to consider the classical limit of transport, i.e. when q increases to high number and to estimate what is the limit between quantum and classical transport in terms of q. As N_+ somehow quantifies the fluctuations in the number of emitted quasi-particles, we can define the classical limit when $N_+ \ll q$.

The behaviour of N_+ is analytically computable in the case of square, sine and lorentzian. In the case of square, $N_+ \sim 2/\pi^2 \ln(q)$, whereas $N_+ = O(1)$ for sinewave and converges to zero in the case of Lorentzian pulses. Interestingly the classical regime appears well before the standard gaussian limit would predict, as $N_+/q \ll 1/\sqrt{q}$. Furthermore the classical limit is somehow voltage dependent: for lorentzian or sinewave, N_+ is very small compared with q even below 1, and can be safely negleted when q is above few quanta, whereas in the case of square or rectangular wave, it is clear that the classical approximation is valid for q above at least a dozen of quanta.

3.7.2 Temperature effects

It is crucial to study how the temperature affects the excess noise. Note that as mentioned previously N_+ is now no longer a direct measure of the number of excess electron and hole quasiparticles but just a measure of the excess noise in reduced units (equation (3.53)):

$$S_I(0) = 4\frac{e^2D^2}{h}k_BT + 2\frac{e^2}{h}D(1-D)h\nu(q\coth(\frac{qh\nu}{2k_BT}) + N_+) \tag{3.53}$$

For simplicity we will keep the same notation but call it now the effective excess particle number. For sine and square waves there is only one energy scale to compare with the temperature, i.e. $h\nu$. For the Lorentzian case there are two energy scales $h\nu$ and h/w. Figure (3.7) shows the sine wave case. The oscillations of N_+ are quickly damped by the temperature and become almost unoservable at $kT \geq 0.2h\nu$. Note that the minima occur to higher q values. This last effect is even more pronounced for the case of Lorentzian voltage pulses (fig. (3.8)), which is related to the exponential energy spectrum of the quasiparticles produced by Lorentzian pulses that strongly overlaps the thermal excited region around E_F.

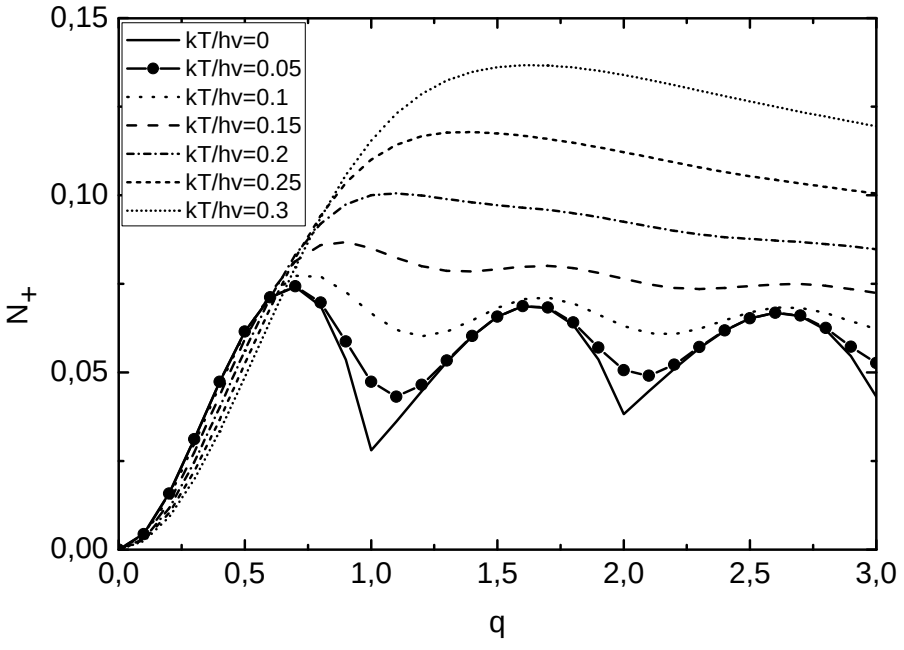

Figure 3.7: Average number of excess excited quasiparticle N_+ with respect to the average charge q transferred per pulses for a sine waveform for different temperature

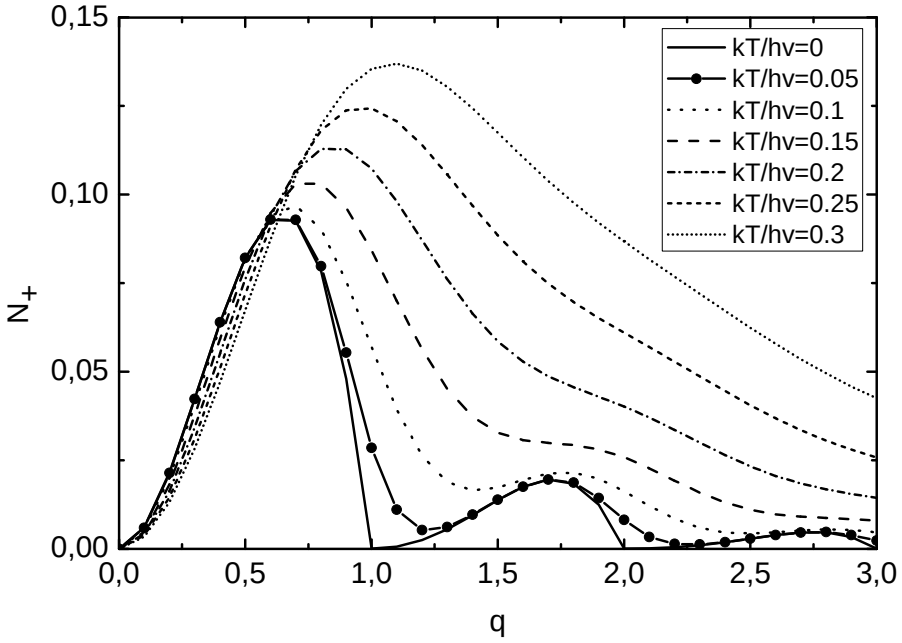

Figure 3.8: Average number of excess excited quasiparticle N_+ with respect to the average charge q transferred per pulses for a Lorentzian width $w = 0.1T$ for different temperature

3.8 Conclusion: experimental constraints

To summarize, a voltage pulse $V(t)$ applied across a quantum wire induce a current flow that is given by the Landauer Formula:

$$\langle I(t,x)\rangle = \frac{e^2 D}{h} V(t - x/v_F)$$

Thus the charge transferred per pulse is equal to eDq where q is the flux associated to $V_p(t)$, equal to $\varphi(\infty)/2\pi$. The fluctuations of the transferred charge ΔQ^2 is equal to the spectral power of the current noise at zero frequency $S_I(0)\mathcal{T}/2$. At $T = 0$, $S_I(0)$ the shotnoise produced by the excited electrons and holes due to $V(t)$:

$$S_I(0) = 2\frac{e^2}{h} D(1-D)\left(\langle N_e\rangle + \langle N_h\rangle\right)$$

So the measure of $S_I(0)$ at $D < 1$ gives access to the total number of the excited particles $\langle N_e\rangle + \langle N_h\rangle = |q| + N_+$, that generally excess the number of transferred charge. Only the lorentzian pulses of the integer flux do not produce excess particle, i.e. $N_+ = 0$. For any periodic voltage, N_+ oscillates with q with local minima at integer number of q.

At finite temperature, thermal fluctuations of the reservoirs adds to the partition noise

that is now equal to the shotnoise of the charge plus an excess noise produced by an effective number N_+:

$$S_I(0) = 4\frac{e^2D^2}{h}k_BT + 2\frac{e^2}{h}D(1-D)h\nu\left(q\coth(\frac{qh\nu}{2k_BT}) + \langle N_+\rangle\right)$$

To distinguish the oscillations of N_+, the numerical computation indicate that the energy ratio $kT/h\nu$ must be largely smaller than 0.2. $kT/h\nu < 0.1$ would be even more confortable. As the lowest temperature obtained in a dilution cryostat is about 15mK, the working repetition frequency ν must be of the order of 3 Ghz. As far as the Lorentzian pulses are concerned, the width of the pulse must be small compared to $\mathcal{T}$ to be able to detect the excess noise for non-integer flux pulses. $w/\mathcal{T} < 0.2$ is necessary, which implies that the definition of the voltage shape must be at least 60ps. N_+ remain below one electron per pulse, and even below 0.1 electron per pulse in the case of sine and lorentzian pulses. In consequence, the sensitivity of the set-up necessary to be able to measure N_+ is of the order of $10^{-29}A^2/Hz$.

Chapter 4

The quantum point contact as the one dimensionnal channel

Applying RF voltage on a quantum wire to realize a quasi-particle source is such an attractive idea that we may wonder why it had not been implemented earlier. As we explain in the previous chapter, finite temperature effects requires to work with voltage pulses repeated with the frequency $\nu \gg k_B T/h$. At 20mK, this means $\nu > 3Ghz$, so we need an arbitrary wave generator (AWG) that sends the pulses with sampling rates above 10Ghz. Arbitrary wave generators working above 10 GHz were not available until recently. The new Tekronix AWG with a sampling rate of 24Gs/s allows us to implement this voltage pulse source. But first we have to discuss what device could play the role of the one ballistic channel. Our choice of ballistic one-dimensionnal wire turns towards the convenient quantum point contact defined in the two electronic gas at the interface of a GaAs and $Al_xGa_{1-x}As$ heterostructure. We discuss in section 4.1 how the physical properties of this device meet the physical requirements discussed in chapter 3 in the two following cases, i.e. the zero magnetic field regime and the quantum Hall regime. Then we detailed the lithography process we used to fabricate our samples in section 4.2. The resistance characterization of the sample is shown in section 4.3.

4.1 Implementing experimentally the voltage pulse electron source

In the past decade bottom-up chemistry have created single objets that show 1-dimensionnal ballistic transport properties, such as carbon-nanotubes [25]. In a top-down approach, narrow constrictions between two wide electrically conducting regions can realize a ballistic quantum wire, provided their width is comparable to the electronic wavelength and their length is shorter than the electron mean free path l_e and the electron coherence length l_ϕ. The more

relevant object for our purpose remains the quantum point contact (QPC) in the bidimensionnal gas (2DEG) ofGaAs/$Ga_xAl_{1-x}As$ heterostructures. The QPC belongs to a larger class of point contacts, such as the one obtained by positioning the tip of a scanning tunneling microscope close to the surface of a conductor, or these obtained more recently by pulling apart a piece of conductor to make a break-junction [75, 126].

4.1.1 Interesting physical properties of the 2DEG in $GaAs/Ga_xAl_{1-x}As$

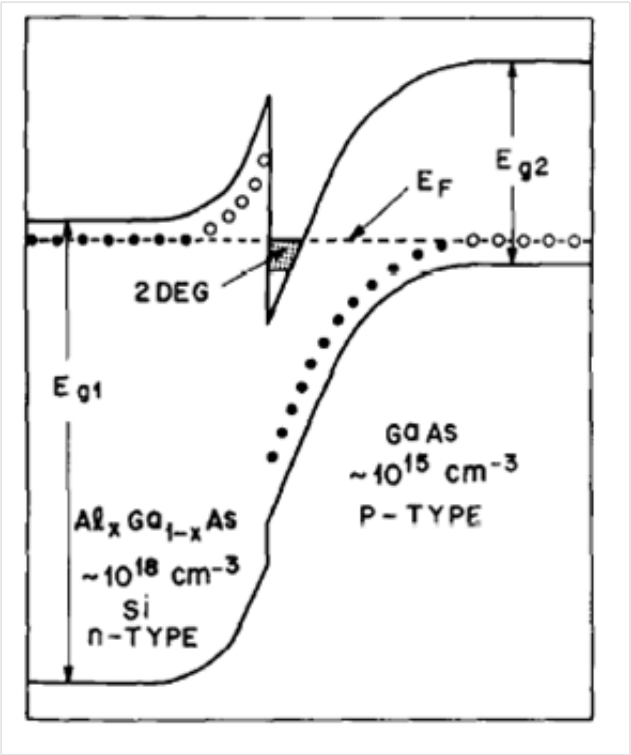

Figure 4.1: Band structure of a modulation-doped $GaAs/Ga_xAl_{1-x}As$ heterojunction. E_F, is the Fermi energy, E_s, are the bandgap energies. GaAs can be either slightly p-type as shown leading to an inversion-type 2DEG or slightly n-type leading to an accumulation-type 2DEG. The Aluminium mole fraction x is typically 30%. From Störmer et al. [131].

First let us describe how a bidimensionnal electron gas can be created in condensed matter. It can be localized at the interface between two layers that have a very different energy gap, for example between a metal and a semi-conductor (MOS) or between GaAs ($E_g = 1,424eV$) and $Al_xGa_{1-x}As$ ($Eg = 1,424 + 1,247xeV$) semiconductor crystals [85]. n-dopants are inserted in the wider gap material; they create an electrical field that confine the gas at the interface.

At the interface, the boundary conditions must respect the continuity of the Fermi level, while there is an abrupt step in the band edges of the two layers (figure 4.1). Then the

impurities (i.e. the n-dopants) ionize and transfer their electrons to the band edge of the narrow gap material [131]. Störmer et al. [132] have shown that it was possible to trap electrons at a single differentially doped GaAs/$Ga_xAl_{1-x}As$ interface, by the combination of the energy discontinuity in the conduction band on one side and the electrostatic potential due to the ionized dopants on the other side (Fig.(4.1)). The width of the electrostatic well is of the order of a dozen of nanometers, so the electronic momentum in this direction is quantized. The energy levels are separated by a few meV, so only the fundamental level is populated at low temperature, and a proper 2DEG is formed. GaAs and $Ga_xAl_{1-x}As$ have a close lattice parameter, so that the crystalline interface present few defects. Furthermore the modulation-doped heterostructure spatially separates the electron gas from the donnor impurities and dramatically enhanced the mobilities which can exceed $10^7 cm^2/Vs$ [108] (Fig.(4.2)).

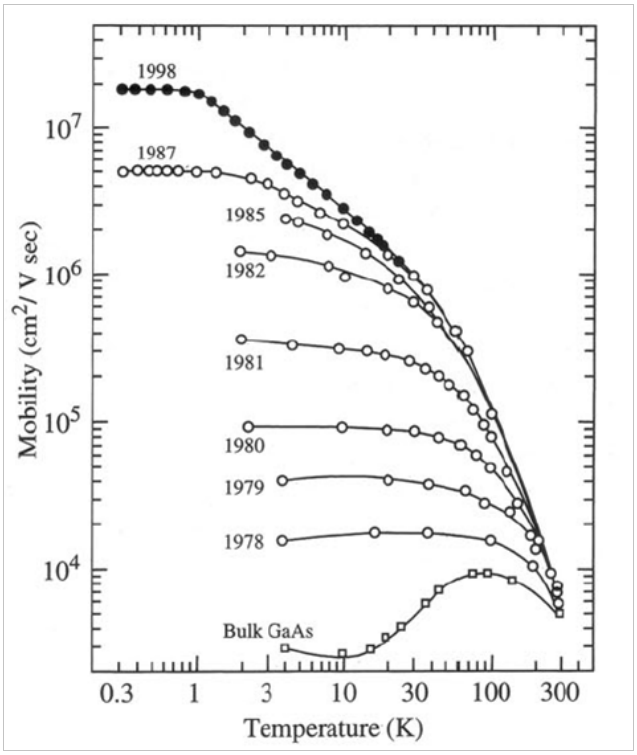

Figure 4.2: Progress made in the mobility μ of the 2DEG in modulation-doped GaAs/$Ga_xAl_{1-x}As$ heterojunctions. At high temperature μ is limited by the phonon scattering. At low temperature it is limited by impurities and defects in the material. From the Nobel lecture of Horst Störmer in 1998 [133].

Can this 2DEG show large enough coherence length and time? Despite the small electron density, the low effective mass $m* = 0.067m_e$ makes the Fermi energy large enough. For a gas density $n \approx 2 \times 10^{11} cm^{-2}$:

$$E_F = \frac{\pi\hbar^2}{m^*} n \approx 6.5meV \approx 75K \tag{4.1}$$

Consequently, the number of electronic excitations k_BT/E_F is small at temperatures below 100mK. This makes the electron-electron collision rate small. At low temperature, the electron-phonon interaction vanish and the electron phase coherence is only limited by this electron-electron interaction which is given by [24, 48, 145]:

$$\tau_{e-e}^{-1} = \frac{E_F}{2h} \left(\frac{k_BT}{E_F}\right)^2 \ln\left(\frac{E_F}{k_BT}\right) \tag{4.2}$$

At 100mK, the excitated quasi-particle life given by the above formula is $\tau_{e-e} \approx 32ns$. As the Fermi velocity v_F is about 200km/s, the coherence phase length is about $l_{e-e} = v_F\tau_{e-e} \approx 6.4mm$! In fact, thermal excitations limit the quasi-particles life to $\hbar/k_BT = 0.8ns$, which corresponds to a length of 100μm.

Levitov and Lesovik's theory assumes that the potential drop (or equivalently the magnetic flux potential A) develops over a small region of length l, so that the dwelling time of the electrons in this region could be neglected compared to the typical time of pulses variations (cf chapter 3). The shorter time scale of the voltage pulses produced by the AWG Tektronux is about 40ps. Consequently, the region where electrons acquire the phase $\varphi(t)$ must be far smaller than $v_F \times 40ps = 8\mu m$.

In a 2DEG in GaAs/$Ga_xAl_{1-x}As$ at low temperature, quasi-particles life time is long enough to enables the coherence of a emitted wavepacket over several dozen of micrometers. The constraint over the voltage drop region size is largely compatible with the lithography techniques. From this substrate, the following two devices can be proposed to implement a voltage pulse source.

4.1.2 Without magnetic field: The QPC as the one ballistic channel

When a top gate is patterned above the GaAs/$Ga_xAl_{1-x}As$ heterostructure and polarized with a negative voltage, the 2DEG can be locally depleted under the gate (Fig.(4.3)). By this method, split gates can be used to convert a 2DEG region into a quantum point contact of adjustable width. The first attempts to create a one dimensionnal channel by this depletion method were lead in silicon [32], then in Gallium Arsenide [10, 139, 147]. Soon after the conductance quantization in quantum point contacts was independently reported in 1988 by Van Wees et al. [141] and Wharam et al. [144].

Consider a quantum point contact between two regions of the 2DEG, without magnetic field (fig. 4.4). This constriction defines a one dimensionnal channel of typically 300nm long. The 2DEG parts and ohmic contacts on each sides define the reservoirs of the system. Moreover, for a 2DEG of mobility $\mu \approx 2 \times 10^6 cm^2/Vs$, the elastic collision length of the electron, that is given by equation (4.3) is about $l_e \approx 15\mu m$, so the quantum point contact is also a ballistic quantum wire.

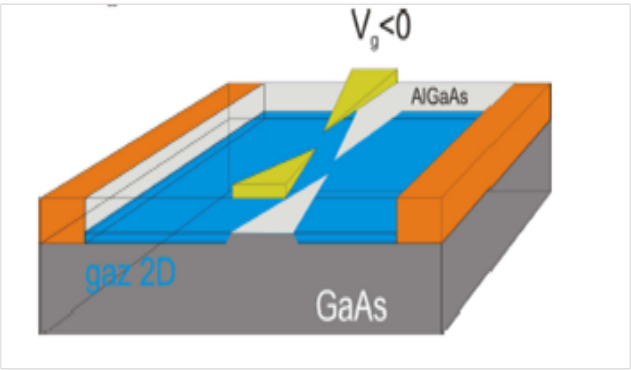

Figure 4.3: Principle of the QPC realization: A bidimensionnal electron gas is confined at the interface of GaAs and $Ga_{1-x}Al_xAs$. Negative voltage is applied on patterned top gates and induces a electrostatic depletion in the 2DEG that reproduces the gates shape. Then a one dimensionnal channel can be created below the space between two split gates separated by a few hundreds of nanometers

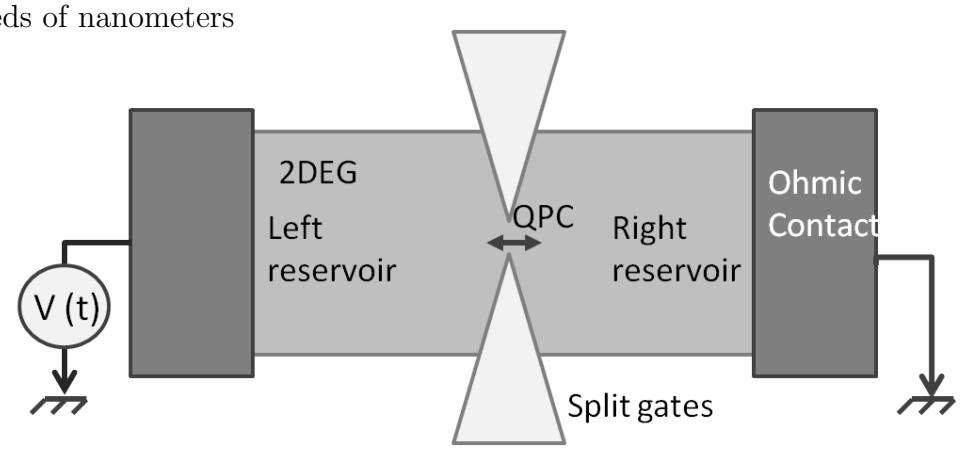

Figure 4.4: A quantum point contact is created by split gates, separating two regions of the 2DEG that define the reservoirs. 2DEG regions are connected by Ohmic contacts, and voltage pulses are applied on one side of the sample. The voltage drop occurs essentially at the QPC, which is crossed by electrons in a time scale much smaller than the typical time variation of the voltage pulses.

$$l_e = \frac{mv_F}{e}\mu \tag{4.3}$$

At low temperature the resistance per square of the mesa drops well below a hundred of Ohms ($R_{sq} = 16\Omega$) and can be neglected compared to the QPC resistance which is typically equal to the quantum of resistance 12900Ω. When a voltage pulse is applied between the two contacts of the device, the electrostatic potential actually drops over the length of the constriction, which is far smaller than $v_F \times 40ps = 8\mu m$. Thus Levitov and Lesovik's hypothesis is fulfilled and this device can implement an n-electron source.

4.1.3 In Quantum Hall regime: Tuning the flux by a side gate

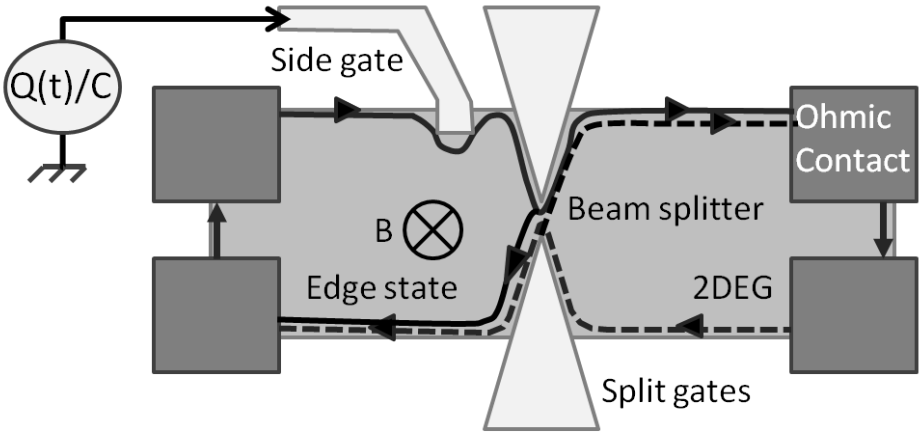

Figure 4.5: A side gate displaces the edge states path on the left arm that induces the emission of quasiparticle in the edge state. A quantum point contact is placed after the source to split the edge states so that quasi-particle can be detected by shotnoise.

An other way to realize a one dimensionnal channel starting from a 2DEG is to apply a high magnetic field perpendicular to the 2DEG plane. Then electrons move in cyclotron orbits of which energies are quantized in discrete values, called the Landau levels [79]. The confining potential that determine the spacial boundaries of the 2DEG bends these Landau levels on the edge of the sample, so that conducting edge channels appear at the crossing between these Landau levels and the Fermi energy level. Due to the cyclotron relation between the momentum components, these edge states are fondamentally one dimensional and chiral.

In the initial proposal [86], Levitov and Lesovik consider a small inducting loop that is able to apply a variable magnetic flux over a very small region of a one dimensionnal channel. In chapter 3, we explained how this protocol is equivalent to apply a voltage drop accross this small region, provided that the voltage $V(t)$ is the time derivative of the potential vector

$A(t) = \int V(t)$. On the other hand, the magnetic flux felt by electrons can be modified by the modulation of their path (that correspond to a modulation of the surface enclosed in the trajectories), while the magnetic field stays fixed. In the quantum Hall regime, this modulation can be realized over a small region by means of a capacitive side gate (figure (4.5)). The voltage applied on the side gate corresponds to the variation of the potential vector $A(t)$. Thus emitting n electrons in the circuit without holes requires a side gate voltage variation of $C^{-1}Ne^2/h\text{atan}(t)$, where C is the capacitance between the gate and the 2DEG. By neutrality, the charge on the side gate is equal to the emitted charge.

A quantum point contact can be added after the modulating side gate and used as a beam splitter. Thus the study of the quasi-particle source can be done through the detection of the shotnoise. However, emitted quasi-particles must not be destroyed by decoherence between their emission at the side gate, and their detection at the QPC. So the distance between the gate and the QPC must be smaller than l_{e-e}. A way to circumvent this problem is to use one of the tips of the split gate as the side gate itself. Edge states run along the split gate of the QPC over a few microns, which set a capacitance between the tip and the edge state to a few femtofarrad. Then the voltage modulation to emit one electron is of the order of 100μV, which is neglectable compared to the voltage scale of the QPC transmission dependence (see fig. (4.8)). As the edge states are chiral, only one channel is affected by the voltage modulation on one tip, so the detection of emitted particle will occur as if the emission has been produced by a separated side gate.

4.2 Sample fabrication

In this thesis, we have realized the first device proposed in subsection (4.1.2) consisting in a QPC. The wafer of GaAs/$Ga_xAl_{1-x}As$ heterostructure is supplied by Pr. Werner Wegscheider from ETHZ Zürich. The nanolithography is performed in our group. We briefly describe in this section the concepts of fabrication. More details of the process are given in Appendix B.

4.2.1 Mesa etching

To minimize possible tunneling between the top gates and the 2DEG, it is convenient to restrict the 2DEG over the essential operating region. An image of the sample is reproduced in figure (4.6). Apart from the sandglass form that indicates the 2DEG region (mesa), the surface of the sample has been etched to remove the 2DEG. The shape of the mesa is chosen to limit the total resistance of the mesa and to offer the minimum surface under the split gates to avoid leakage current (see details in appendix (B)). For the sample geometry (see figure (4.7)), the resistance of the mesa is about 150 Ohms:

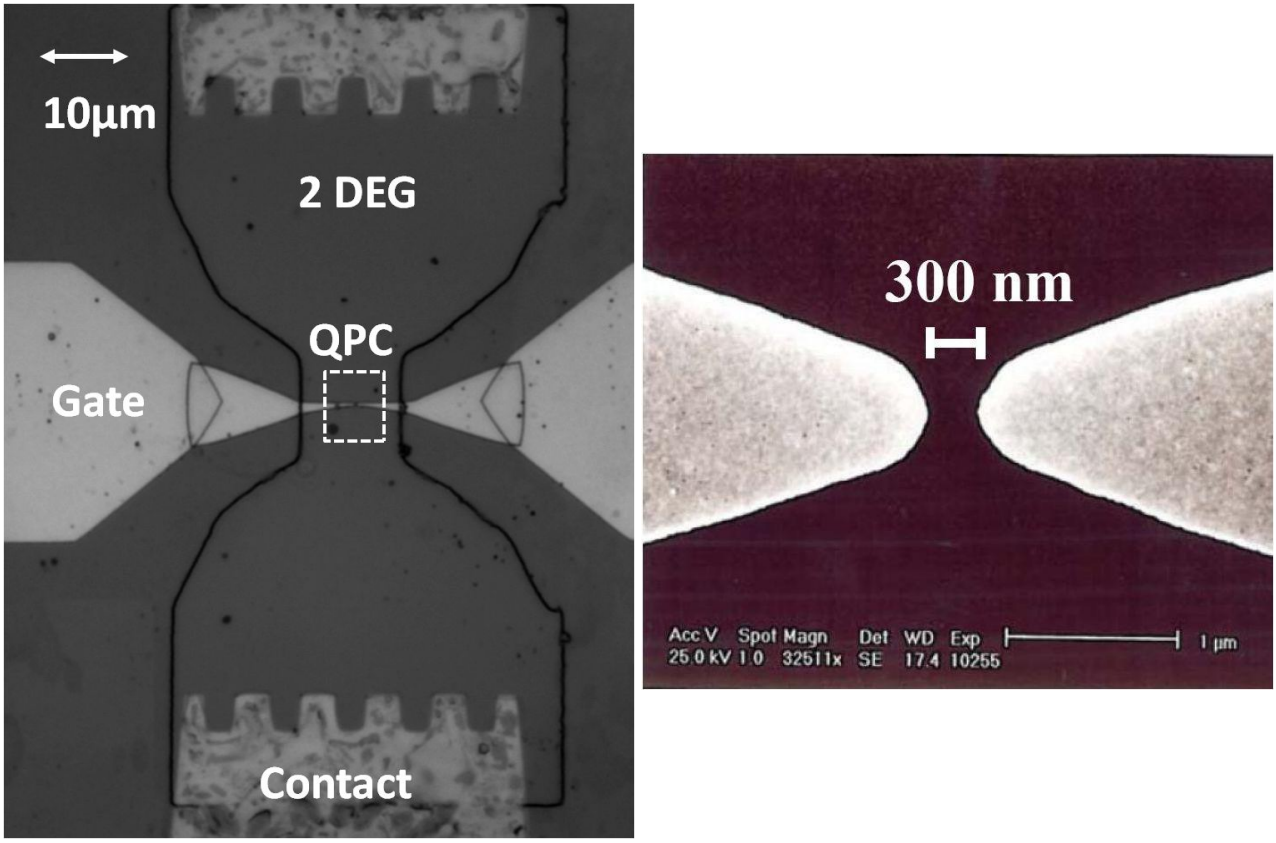

Figure 4.6: optical photography of a whole sample (left) and Electronic photography of the quantum point contact region (right)

$$R = \frac{1}{en\mu}\left(2\ln\left(\frac{L}{l}\right) + \frac{2D}{L} + \frac{2d}{l}\right) \approx \frac{5}{en\mu} \approx 150\Omega$$

4.2.2 Contact deposition

To contact the 2DEG that is typically burried 100nm below the surface of the semi-conducting heterostructure, one has to transform the Schottky barrier formed at the metal-semiconductor interface into a low resistive ohmic contact. The Schottky barrier can be lowered by the diffusion of the metal into the semiconductor that creates a sufficient doping of the interface. The metallic alloy AuGeNi is commonly used to contact the 2DEG.

The AuGeNi alloy is annealed so that it diffuses in the Gallium Arsenide: Gold atom replaces Arsenium, Germanium replaces Gallium [16, 52]. Nickel improves the metal weeting and control the diffusion rate. The annealing process plays a crucial role in the contact formation and should be operated around 465°C [52].

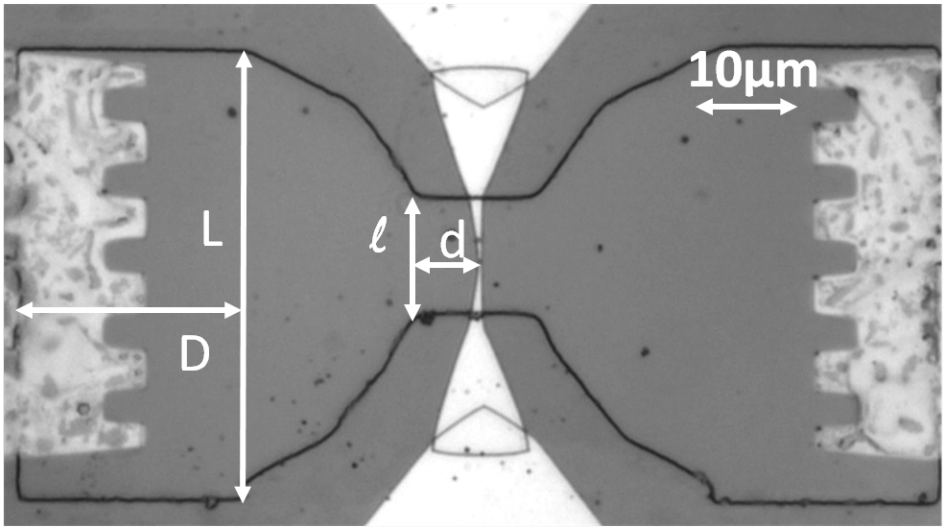

Figure 4.7: Geometry of the mesa

To enable the formation of highly stable and low resistive contact, it is also important to remove the native oxide from the GaAs surface before the metal evaporation. Wet-etching can be used but the better results are obtained by in-situ ion etching [65].

Finally, according to [50], the contact resistance depends on its orientation regarding the crystallographic axis of the GaAs: the resistance is lower (resp. higher) when the limit between the metal and the 2DEG is perpendicular to the axis 011 (resp. 01-1). To avoid this geometric aspect, the contact boundaries on the mesa are often patterned in a crennel shape (fig. 4.6 (left))

4.2.3 Gates depositions

Patterning the split gates requires a resolution of a few hundred of nanometers (see fig.(4.6)), which can only be reached by E-beam lithography. For this level of details, a well controlled set of parameters in the photo-resist deposition, in the exposition dose, and in the developpement time are necessary (see Appendix B). Indeed the shape of the split gates define the main characteristics of the QPC conductance as it is detailed in the next section. The surface of the split gates that overlap the mesa must be reduced to limit leakage current. Furthermore we remark that thin split gate enable us to have better resolution on the gap width contrary to broad gates because it reduces the proximity effect during e-beam exposure. As a result we were able to obtain working QPC with better success using this design than with broad split gates. Finally the very extremities of the the tips are angle shaped at 30°, which is known to be an optimum to produce good QPC.

4.3 Conductance caracterisation of the sample

The quantum point contact is a waveguide for electrons wavefunctions with an adjustable width W. In the constriction, the transverse momentum component $k_\perp$ is locally quantized and define channels. The kinetic energy associated to $k_\perp$ increases as W decreases, until it exceeds the Fermi level and the channel becomes evanescent. There are several models dealing with the QPC physics [80]. Among them, Büttiker [19] describes the QPC as a saddle point voltage which can be expressed with the effective electrostatic potential V_0 set by the split gates, and the spatial frequencies associated to curvature $\omega_\parallel$ and $\omega_\perp$:

$$V(x,y) = V_0 - \frac{1}{2}m\omega_\parallel^2 x^2 + \frac{1}{2}m\omega_\perp^2 y^2 \tag{4.4}$$

Büttiker derives the transmission of the differents channels n:

$$T_n = \frac{1}{1 + e^{-2\pi(E - V_g - \hbar\omega_\perp(n+1/2))/\hbar\omega_\parallel}} \tag{4.5}$$

This leads to a regular step-like suppression of the conducting channels as the gate voltage gets more negative, as shown by the conductance of the QPC reported in figure (4.8). Each plateau corresponds to nG_0, where n is the number of channels that are fully transmitted, and $G_0 = 2e^2/h$ the quantum of conductance. The last partially transmitted channel has an exponentially vanishing transmission while the next channel to be suppressed still keeps a unit transmission.

The shape of the split gates extremities sets both $\omega_\parallel$ and $\omega_\perp$, and so the conductance caracteristics of the QPC. When the constriction is long, the plateaus are well defined and the transitions from one plateau to the others are sharp, because of the exponential decay of the tunneling probability with the barrier length. This was actually the case for Wharam et al. samples [144], which were 500nm wide and 400nm long. On the contrary, a short QPC shows a smooth transition and less defined plateaus, such as the sample used by Bajjani et al. [7], which was only 80nm long.
We tried to achieve a rather long QPC, because in a further experiment we wish to use the QPC as a quantum switch by modulating rapidely its transmission between 0 and 1 [72]. The price to pay is a larger energy dependence of the transmission $\frac{\partial T}{\partial \varepsilon}$, and consequently more non-linearities in the current response. The split gates are separated by 200 to 300nm and their width is about 300nm, like the split gates that are displayed in figure (4.6). The differential conductance of the sample at 20mK is reported in figure (4.8). More than five plateaus are visible, and even a 0.7 structure. This 0.7 structure appears mostly for long constrictions and is not explained by the saddle-point potential model. It is an effect of interactions between electrons in the quantum wire. Its physics remains under debate. It was reported by Thomas et al. [137, 138] as linked to some spontaneous spin polarization. Conforting this hypothesis, the Fano factor of the noise is strongly affected by the 0.7 structure [35, 121]. The Fano factor reduction indicates spontaneous spin degeneracy lifting of the first orbital conduction

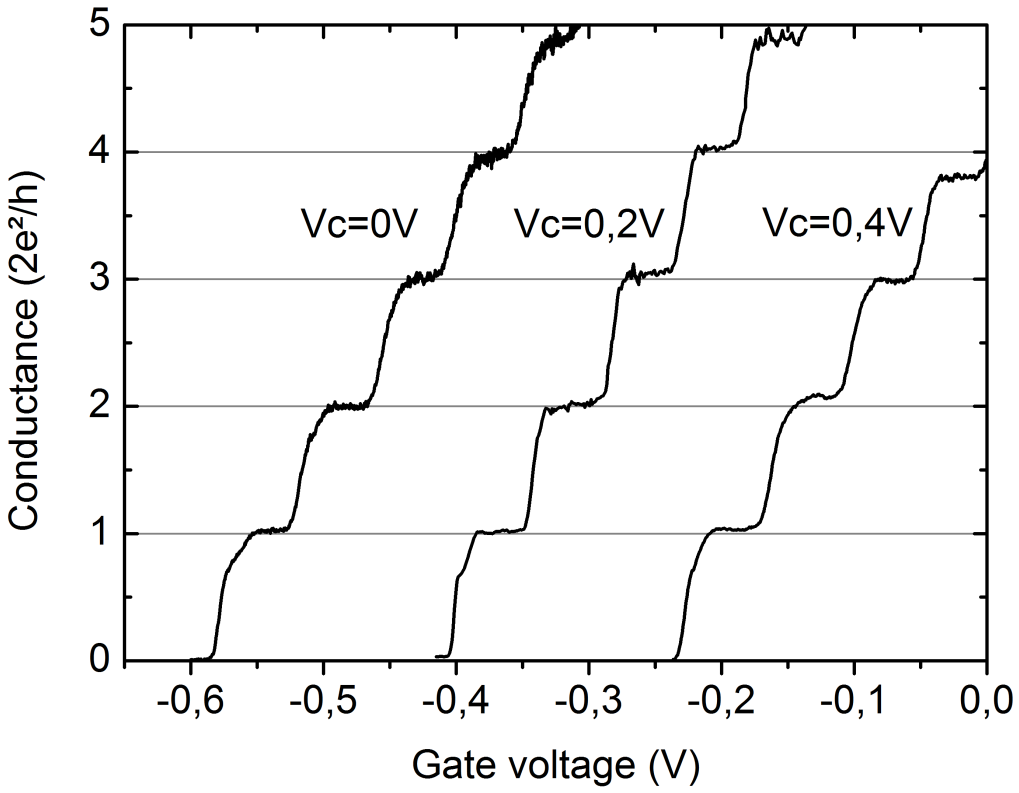

Figure 4.8: Sample conductance with respect to the gate voltage V_g for different bias voltage V_c applied during the cooling

channel [116].

In the following experiments a positive voltage gate of about 0.42V was applied during the cooling to displace the pinch-off of the gate to smaller negative values. This bias-cooling method is known to reduce the telegraph noise [109] and the low frequency noise [88] in the $GaAs/Ga_xAl_{1-x}As$ heterostructures. In fact, cooling with a positive bias on the gates reduces the density of ionized donors. This builds in an effective negative gate voltage so that a smaller negative bias is needed to reach the desired operating point (fig.(4.8)). Meanwhile, the telegraphic noise originates from electrons that tunnel from the gates into the conduction band of the 2DEGand are trapped near the QPC. As the density of ionized donors is reduced, electron tunneling is reduced and so is the conductance noise. Indeed we observe on our sample that telegraphic like jumps of the conductance occur more often for the same working point if the gate voltage was more negative. If we applied the cooling method with a positive

bias 0.42V, the telegraphic noise totally disappear and the conductance stays stable during weeks.

4.4 Conclusion

At low temperature, the coherence length in 2DEG in clean heterostructure of $GaAs/Ga_xAl_{1-x}As$ is larger than 100μm, and the elastic collision length is about 10μm.

Then two implementations of the n-electron source can be proposed. The first one use a quantum point contact as the small unidimensional ballistic region where the voltage drops. When its transmission $D < 1$ it also acts as a beam splitter that reveals the quasi-particle through shotnoise.

The second implementation is based on the unidimensionnal chiral edge states in quantum Hall regime. Quasi-particles are emitted through the capacitive coupling of a side gate that modifies the magnetic flux enclosed in the edge states.

In this thesis, we implement the n-electron source by applying sub-nanosecond pulses on a quantum point contact (QPC). The subnanosecond voltage pulses define quasi-particle wave-packets with an extension far below the phase coherence length in the 2DEG; so they ensure the coherence of this n-electron source that enables interference experiments.

Chapter 5

Experimental cross-correlation set-up

The excess particles produced by the voltage pulses can not be observed in the current measurement because their total charge is neutral. As derived in chapter 3, the partition noise counts the number of excited particles when the QPC transmission is below one. Detecting shotnoise has been a challenge in the 90's [77,119], but current correlation technique have been steadily improved (section 5.1). Following the examples of Kumar et al. [77], Roche et al. [121] and Reydellet et al. [118], we propose to detect the spectral power of the partition noise S_I at low frequency (between 100 and 300 kHz) through the well-established cross-correlation technique.

A dedicaced set-up has been built from scratch in one of the most recent generation of Helium-free cryostat. The cryogenic specifications imposes the following requirements on the set-up:

- The cryostat can accept limited power for each stage: $300mW$ for the 4Kstage , $100\mu W$ for the 50mK stage and few μW for the 13mK stage. In consequence, the wiring must bring as less heat as possible, which imposes minimum conductance to the coaxial lines.

- The set-up must be stronly anchored to the cryostat stages to ensure good thermalization of the outer and inner part of the coaxial cables, so that the sample will be at base temperature.

- Environnemental noise that change the effective electronic temperature must be reduced. Notably the microwave photon radiation coming from the higher temperature stages, including room temperature, are transmitted through the coaxial lines to the sample. They must to be filtered and reduced. Long and resistive coaxial lines help to attenuate the radiation at high frequencies.

- However, wiring length can not be too much extended for two reasons. First, RF coaxial cables add a frequency-dependent attenuation that is proportionnal to their length, so too much attenuation can modify the voltage pulses shape. Second, the capacitance of

the DC lines shunt the measurement impedances, reducing the measurement frequency range and consequently increasing the acquisition time. So there is a tread-off to find in the wiring lenght.

We detail in sections 5.2 and 5.3 the technical choices to ensure these requirements. The validation of the set-up in terms of cryogenic are given by the lower temperature stage. But more relevant for the physics is the electronic temperature of the sample. It can be extracted from a DC shotnoise measurement (section 5.4). To our knowledge, cross-correlation measurement implemented in a dry cryostat is a very new technique, and the pulse-tube technology brings new noise perturbations to be reduced (section 5.4.3).

5.1 the cross-correlation at low frequency

5.1.1 Current correlation technique to detect shot-noise

Measuring frequency range

The first attempt to measure the shot-noise for a QPC was by Li et al. followed later by Washburn and Liekfrink in ballistic and diffusive conductors [87, 89, 90, 143]. However the measurements were performed at below 100kHz, and for the experimental temperature (between 1K and 4K) the $1/f$ noise fluctuations of the conductance were dominant, so that noise power did not show the expected linear dependence with respect to the current in those experiments.

To get rid of 1/f noise and instabilities, a way is to measure the spectral power of the noise at Ghz frequencies. Reznikov et al. [119] observed the fano factor variation by measuring around 10 Ghz. In the intermediate frequency range, Liu et al [91,92] used a resonant tapping circuit peaked around 15.6 MHz.

Another approach is based on the remark that the 1/f noise is proportionnal to k_BT and to the square of the current flowing through the device. So by reducing the temperature below a few hundreds of mK and by using a good filtering that protect the sample from photon radiation, small current can be used and the 1/f noise is dramatically suppressed. That way, Kumar et al. [49,77] successfully detected the shot-noise by averaging the voltage fluctuation spectral density over a 500 Hz bandwidth around 6 kHz.

RF or low frequency noise measurements are relatively equivalent in term of detection time performance. As it is detailed in subsection (5.1.3), the necessary time over which the spectral-power $S_I(\omega)$ has to be averaged depends on the frequency bandwith and the impedance load of the circuit. An RF amplifier bandwidth is several hundreds of MHz. But the impedance of the circuit is necessarily 50Ω and the noise and signal are reduced. On the contrary, in low frequency detection the bandwith is reduced to a hundred of kHz but

high resistance loads can be used and compensate the loss of bandwith (for example, the load resistance in Kumar et al. [77] is the sample resistance itself).

The modulation technique

The auto-correlation technique used in the first experiments of shotnoise was straight-forward: The voltage fluctuations across the sample was sent into an ultralow-noise amplifier, sampled and Fourier transformed with a spectrum analyzer [87, 89, 90, 143]. However these techniques require accurate calibrations [89] of the experimental noises external to the physics of shot-noise, first of all the voltage and current noises of the pre-amplifiers.

It is better to get rid of these external noises during the measurement to avoid slow drift between the calibration and the detection. One can use a ON-OFF technique. Reznikov, et al. [119] introduced a low frequency modulation of their DC excitation and measured the modulated noise at the same frequency by lock-in detection. They were followed by Liu et al. [91]. The same technique was performed by Schoelkopf et al. [125] for photo-assisted shotnoise spectroscopy, which in fact leads to the measurement of the derivative of the noise with respect to the DC voltage. The same group used the modulation technique to measure measure the spectral density of shot-noise at high-frequency in a diffusive quantum-wire [124], as well as Gabelli and Reullet [43] in a tunnel junction.

The cross-correlation detection

On the other hand, Glattli et al. [49] proposed the cross-correlation measurement technique which is analogous to the four-point method used to measure a resistance. By detecting independently the voltage fluctuations through two amplifiers lines and computing the cross-correlation the two signals, the contribution of the voltage noise of the amplifiers and most of the thermal noise of the leads and contacts are suppressed. The determination of the sample noise requires only the knowledge of the current noise of the amplifiers. This cross-correlation technique had been developed and is now currently used in noise experiments among our group and others, for spectral density of noise at zero frequency [**?**, 118, 121], or high-frequency noise [7, 95]. The ON-OFF modulation technique can be combined to the cross-correlation technique to remove the back-ground noise components of the signal (for example thermal noise or current noise of the amplifiers), as it is performed in Zakka-Bajjani et al. [7].

5.1.2 Set-up description and correlations formulas

The cross-correlation measurement set-up used here is described in figure (5.1). Both contacts of the QPC can be fed with RF excitations through coaxial lines in extended SMA standard (up to 26GHz). The bias tee is a diplexer device that splits the signal $V(t)$ into a low frequency

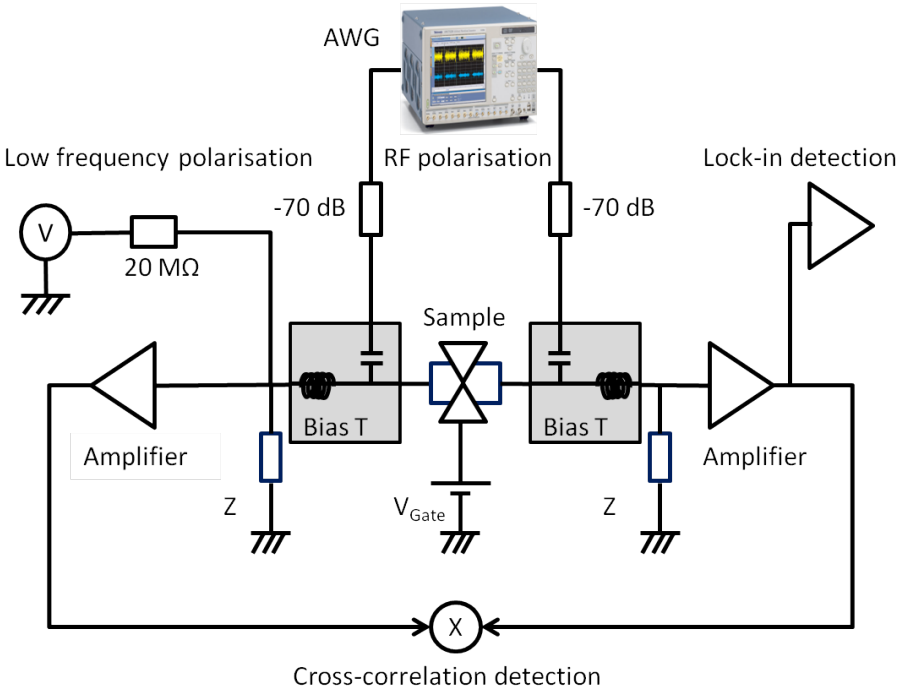

Figure 5.1: cross-correlation set-up

component, that passes through the DC port, and the high frequency component, that passes through the RF port. Each component is blocked on the opposite port. The bias tee used in the set-up are Anritsu K250, of which specifications do not change much from room and low temperatures. Their DC and RF ports work respectively from 0 to 100MHz and 100MHz to 40Ghz.

The bias tee connects the high impedance and low frequency measurement lines to the sample without disturbing the RF injection. It also prevents the load impedance from being shunted by the 50Ω impedance of the RF lines. The total voltage pulses applied on the sample is composed of a AC and a DC parts: $V(t) = V_{DC} + V_{AC}(t)$. The alternating part of the pulses V_{AC} is send through the RF line by the AWG with an attenuation of 70dB. The DC part of V(t) can not be sent with the AC part through the RF line, because the bias-T block the low frequencies on this port. Consequently, V_{DC} has to be applied through the low frequency lines. It is set by a high stability DC generator Yokogawa through a high impedance of $20M\Omega$ at room temperature. Furthermore, small AC polarization of about 1kHz is added to this DC voltage to measure the conductance of the sample by lock-in detection.

The current noise i_C produced by the sample is converted into voltages V_A and V_B across the load impedances Z of the measurement lines. Note that the contributions of i_C to V_A and V_B are of opposite signs (eq. 5.1 and 5.2). In practice, the load resistances R_m are shunted

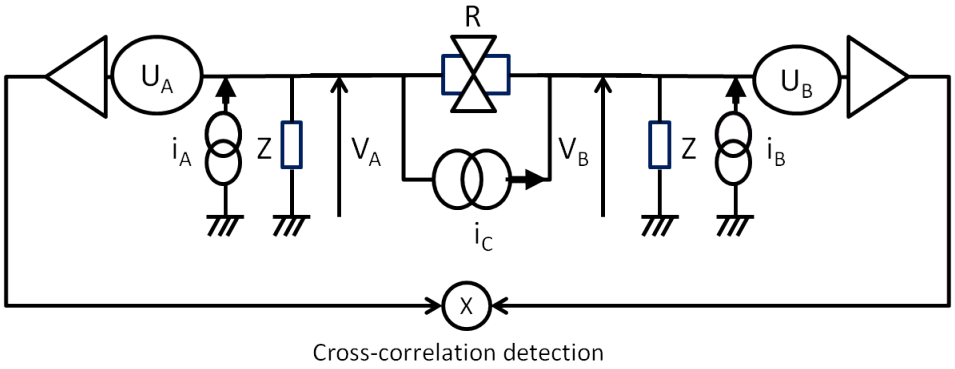

Figure 5.2: Measurement part of the set-up with the different noises

by the capacitance C of the coaxial cables of the DC lines, so that $Z(\omega)^{-1} = R_m^{-1} + C\omega j$. Other current-noises i_A and i_B add to i_C contribution in V_A and V_B. They come from the thermal noise of the circuit resistances and the input impedance of the low-noise amplifiers NF SA-421F5 placed at room temperature. Consequently V_A and V_B are given by equations (5.1)and (5.2):

$$V_A = \frac{Z\,(Z+R)}{2Z+R} i_A + \frac{Z^2}{2Z+R} i_B + \frac{ZR}{2Z+R} i_C \tag{5.1}$$

$$V_B = \frac{Z\,(Z+R)}{2Z+R} i_B + \frac{Z^2}{2Z+R} i_A - \frac{ZR}{2Z+R} i_C \tag{5.2}$$

These equations lead to the following expressions of auto-correlation and cross-correlation :

$$\langle V_A^2 \rangle = \left|\left| \frac{Z\,(Z+R)}{2Z+R} \right|\right|^2 \langle i_A^2 \rangle + \left|\left| \frac{Z^2}{2Z+R} \right|\right|^2 \langle i_B^2 \rangle + \left|\left| \frac{ZR}{2Z+R} \right|\right|^2 \langle i_C^2 \rangle \tag{5.3}$$

$$\langle V_B^2 \rangle = \left|\left| \frac{Z\,(Z+R)}{2Z+R} \right|\right|^2 \langle i_B^2 \rangle + \left|\left| \frac{Z^2}{2Z+R} \right|\right|^2 \langle i_A^2 \rangle + \left|\left| \frac{ZR}{2Z+R} \right|\right|^2 \langle i_C^2 \rangle \tag{5.4}$$

$$\langle Re(V_A V_B^*) \rangle = \left|\left| \frac{Z}{2Z+R} \right|\right|^2 Re(Z^*\,(Z+R)) \left(\langle i_A^2 \rangle + \langle i_B^2 \rangle \right) - \left|\left| \frac{ZR}{2Z+R} \right|\right|^2 \langle i_C^2 \rangle \tag{5.5}$$

V_A and V_B are amplified by low-noise amplifiers SA-421F5 from NF corporation. These amplifiers add their own voltage noise U_A and U_B to V_A and V_B. Then the signals are amplified by post-amplifiers and finally are fed into a fast acquisition card Acquiris. The gain of the amplifiers are respectively 60dB, so that the voltage noise of the post-amplifiers can be negleted. In consequence, the autocorrelation detected by the acquiris card is equal to

$\langle V_A^2 \rangle + \langle U_A^2 \rangle$. On the contrary, $\langle Re(U_A U_B^*) \rangle = 0$ so the voltage noise of the amplifiers does not appear in the cross-correlation.

Current noise from independent source add quadratically, so that $i_A^2 = i_{amp}^2 + 4k_B T_{R_m}/R_m + 4k_B T_{R_{pol}}/R_{pol}$ and $i_B^2 = i_{amp}^2 + 4k_B T_{R_m}/R_m$. Typically i_{amp} is of the order of the thermal noise of the $1M\Omega$ input impedance (about $130fA/\sqrt{Hz}$), and defines the floor of the circuit noise. It is still two order of magnitude above the typical signal we want to measure (about $10^{-29}A^2/Hz$). Consequently the other contributions i_A and i_B must be limited by choosing R_m and R_{pol} so that their noise are negligeable to i_{amp}. This is the reason why R_{pol}, which is at room temperature, must be larger than $1M\Omega$ and R_m which is of a few $k\Omega$ is placed at 50mK.

5.1.3 Amplification lines and detection

Accuracy and acquisiton time

The average $\langle Re(U_A U_B^*) \rangle$ is zero and so the voltage noise of the amplifiers do not appear in the average of the cross-correlation term. However in a measurement, fluctuations of $U_A U_B^*$ around zero are given by the autocorrelation noise $\langle U_A^2 \rangle = \langle U_B^2 \rangle \sim 25 \cdot 10^{-20} V^2/Hz$. This is still few orders of magnitude above the typical partition noise we expect to measure. In consequence, repeating the measure N times and averaging over N is necessary. Considering the time τ of a measurement and the frequency band Δf over which the noise in integrated, the spectral power of the cross-correlation is averaged over $N\tau\Delta f$. To obtain a good sensitivity, N must fulfill:

$$\frac{\langle U_{amp}^2 \rangle}{\sqrt{N\Delta f \tau}} \ll \frac{1}{\Delta f} \int_0^{\Delta f} df \left|\left| \frac{ZR}{2Z+R} \right|\right|^2 \langle i_C^2 \rangle \tag{5.6}$$

In the case of a RC circuit composed by the resistance R_m and the capacitance of the coaxial cable C, the typical frequency bandwith is of the order of the cut-off frequency:

$$Deltaf = \frac{2R_m + R}{2\pi C R R_m}$$

It is more convenient to choose the load resistance $R_m < R$ so that the Δf becomes independent of the resistance variation of the QPC. So typically the total time $N\tau$ of the measurement must fulfill:

$$N\tau >> \frac{2\pi C \langle U_{amp}^2 \rangle^2}{\langle i_C^2 \rangle^2 R_m^3} \tag{5.7}$$

Thus there is a tread-off to find about the value of R_m: if $R_m \ll R$, the contributions of the external noise i_A and i_B in the cross-correlation are reduced, on the other side, choosing a large

R_m limit $N\tau$. Moreover, the coaxial capacitance C must be reduced, which is equivalent to reduce the wiring length as much as possible. A shot-noise produced by a current of one electron per nanosecond for a QPC transmission of 0.5 is of the order of $\langle i_C^2 \rangle = 10^{-29} A^2/Hz$. For experimental values $R_m = 2.5k\Omega$ and $C = 150pF$, it will be resolved as soon as $N\tau >> 36s$.

Amplification and filtering

The signal fed to the Acquiris fast acquisition card is integrated over all the frequency bandwith ΔF_{acq} set by the sampling rate. Because of Shannon folding, the Fourier transform will be reliable only if the signal frequency extension is less than $\Delta F_{acq}/2$. The circuit noise is actually cut-off at $(2\pi R_m C)^{-1} = 400kHz$, but the voltage noise of the amplifiers is white over the whole range of the amplification (10MHz). In consequence, the output of the post-amplifiers are filtered through a pi-filter of capacitance 7nF, followed by a butterworth pass-band filter of 10kHz to 500kHz. Then ΔF_{acq} can be set to 1MHz.

The Acquiris card records the signals from lines A and B during typically 65ms, store them in a buffer and send them to the computer while it registers another set of data. Then the auto-correlations and cross-correlation of the two lines are computed, fourier transformed and averaged through Labview programs.

5.2 Thermalisation of the coaxial lines of the set-up

5.2.1 Limiting the heat conduction through the coaxial lines

Depending on its temperature, each stage of the cryostat is designed to accept a maximum heating power. The lower the temperature is, the smaller is the acceptable power that mainly comes from the thermal short-cut introduced by the electrical wiring. If the set-up brings to much power, then the base temperature of the cryostat establishes at much higher temperature than the nominal base temperature (about 13mK). Consequently, the heat flow carried by the coaxial wiring must be estimated in order to ensure a base temperature as low as possible.

Heat can be carried by electrons or phonons. In metals, the thermal conductivity κ is mostly linear with T at low temperature (below 10K) because phonon excitation are frozen. Then κ can be estimated with good approximation from the electrical conductivity using the Wiedmann-Franz law [5]. At higher temperature, phonon conductivity, proportionnal to T^3, starts to dominates the heat conduction. In insulators where only phonons carry heat flow, κ drops dramatically with temperature, following a law in T^3 for crystals or T^2 for amorphous material such as Teflon. We refer to the values given in reference book for cryogenic such as the Pobell [110], which we report in table (D.3) in appendix (D).

Consequently the heat flow stationnary equations in a coaxial cable are the following (fig. (5.3)):

- in the shield:

$$-\kappa_s T_s \frac{\partial T_s}{\partial x} = \Phi_s(x) \tag{5.8}$$

$$\kappa_s = \kappa_s^1 \pi (r_{ex}^2 - r_{in}^2) \tag{5.9}$$

- in the inner conductor:

$$-\kappa_c T_c \frac{\partial T_c}{\partial x} = \Phi(x) \tag{5.10}$$

$$\kappa_c = \kappa_c^1 \pi r_c^2 \tag{5.11}$$

- in the dielectric:

$$\frac{\partial \Phi_s}{\partial x} = -\frac{\partial \Phi_c}{\partial x} = \kappa_d \left(T_c^3 - T_s^3\right) \tag{5.12}$$

$$\kappa_d = \kappa_d^1 \frac{2\pi}{3} \ln\left(\frac{r_{in}}{r_c}\right)^{-1} \tag{5.13}$$

κ^1 is the thermal conductivity of the material at 1K, r_c the radious of the inner conductor and r_{in} and r_{ex} the inner and outer radius of the metallic shield.

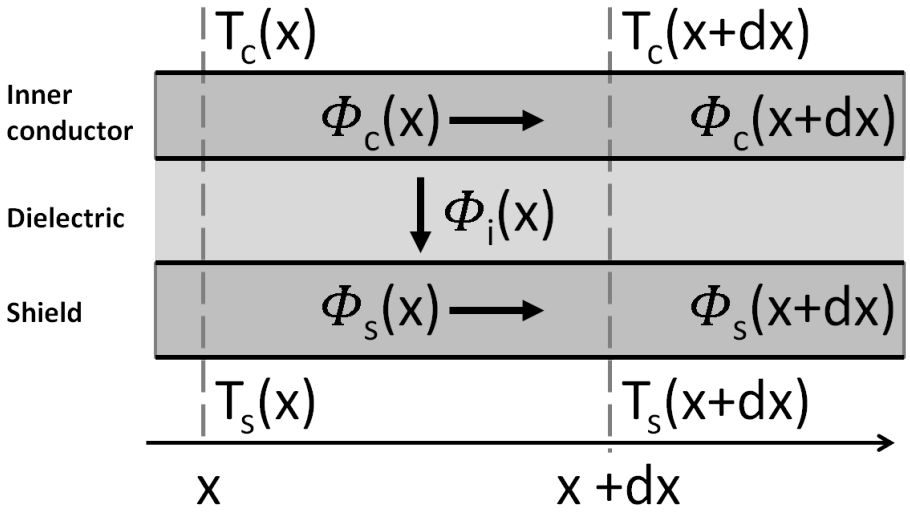

Figure 5.3: schematics of the heat flow in a coaxial line

Even at high temperature the thermal conductivity of dielectric such as teflon is several order of magnitude below those of metals (see table D.3). Furthermore, the inner conductor

of the coaxial cable is much more resistive than the shield because of the surface ratio (see typical specifications in table (D.1) in the appendix (D)). This limitates dramatically the heat flow brought by the inner conductor, and consequently $\Phi_c \ll \Phi_s$. Thus if we consider equations (5.8) and (5.12), we can solve the system by first looking at the flow Φ_s in the shield. In a second step, we deal with the flow in the center Φ_c as a perturbation.

5.2.2 Heat coming from the shield

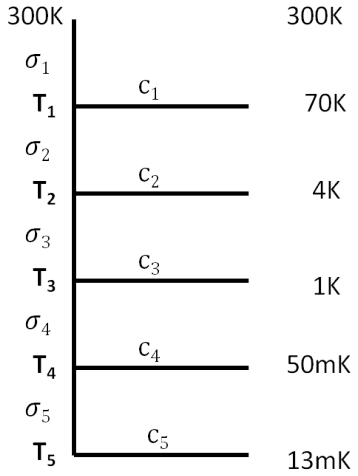

Figure 5.4: Schematics of the shield heat flow

First, we compute the heat flow in the shied connector Φ_s, neglecting the heat flow coming from the inner part of the connector Φ_c. Using a linear dependence of the thermal conductivity with respect to the temperature, on obtains a linear system in T^2 that is sketched in figure (5.4). $\sigma_i = \kappa_s/l_i$ is the thermal conductance of the shield of the coaxial cable i of length l_i at 1K.

$$\begin{cases} s_1\left(T_1^2 - T_2^2\right) + c_1\left(T_1^2 - 70^2\right) &= s_2\left(T_2^2 - T_1^2\right) \\ s_2\left(T_2^2 - T_1^2\right) + c_2\left(T_2^2 - 4^2\right) &= s_3\left(T_3^2 - T_2^2\right) \\ s_3\left(T_3^2 - T_2^2\right) + c_3\left(T_3^2 - 1^2\right) &= s_4\left(T_4^2 - T_3^2\right) \\ s_1\left(T_4^2 - T_3^2\right) + c_4\left(T_4^2 - 0.05^2\right) &= s_5\left(T_5^2 - T_4^2\right) \\ s_1\left(T_5^2 - T_4^2\right) &= s_2\left(0.013^2 - T_5^2\right) \end{cases} \tag{5.14}$$

The critical parameters of the system are the thermal conductances of the thermal anchors c_i at each temperature stages. They need to be better than $0.1mW/K$, which require good contact and care. Thanks to numerical computation, we were able to conclude that KMCO stainless steel coaxial cables were unfortunaly not suitable for stages below 4K because they conduct to much heat, which was the counter part of their high electrical conductance for

RF. We had to prefer Yotem cupro-nickel cables which are more resistive and induce more attenuation for high frequencies. Acceptable lengths for the coaxial cables between each cryogenic stages are reported in table (5.1). A RUO2 thermometer placed near the sample gives an effective temperature of 22mK, in good agreement with the expected values, which means that real thermal conductances c_i are actually around $c_i = 0.1mW/K$.

Stage to Stage	DC cable	length (cm)	T_f (K)	Φ_f (mW)
$300K \rightarrow 70K$	KMCO stainless steel	35	101	0.6×10^3
$70K \rightarrow 4K$	YOTEM Cu-Ni	20	8.5	7
$4K \rightarrow 1K$	YOTEM Cu-Ni	10	1.6	0.2
$1K \rightarrow 50mK$	Homemade Cr-Ni	15	0.07	0.25×10^{-3}
$50mK \rightarrow 13mK$	Homemade Cr-Ni	15	0.018	2×10^{-5}
Stage to Stage	RF cable	length (cm)	T_f	Φ_f
$300K \rightarrow 70K$	KMCO stainless steel	35	101	0.6×10^3
$70K \rightarrow 4K$	YOTEM Cu-Ni	25	8	6
$4K \rightarrow 1K$	YOTEM Cu-Ni	10	1.6	0.2
$1K \rightarrow 50mK$	YOTEM Cu-Ni	15	0.14	2×10^{-3}
$50mK \rightarrow 13mK$	YOTEM Cu-Ni	15	0.021	0.02×10^{-3}

Table 5.1: Temperature and heat flow in the coaxial cable shield for RF and DC lines when the thermal conductance $c_i = 0.1mW/K$

In order to obtain good contacts to anchor the set-up, we used feedthrough connectors on each plates for every cables and we add some copper anchors on the attenuators and the components, so that the contact surface would be the largest at possible (see photos 5.5 and 5.6).

5.2.3 Thermalization of the inner conductor of the coaxial lines

From the non linear equation (5.12) one can extract a typical length of thermalization of the inner conductor L:

$$L = \sqrt{\frac{\kappa_c}{\kappa_d \left(T_c - T_s\right)}} \tag{5.15}$$

Lets consider a coaxial cable of length l which extreme temperatures are T_{in} and T_{out}. To estimate whether the inner conductor is thermalized to the stage temperature or not, we can roughly compute for which temperature T_{eq} in the cable the thermalization length $L(T_{eq})$ is equal to the position $x(T_{eq})$ from the coldest extremity, i.e. the solution of equation 5.16:

$$l\frac{\left(T_{eq}^2 - T_{out}^2\right)}{\left(T_{in}^2 - T_{out}^2\right)} = \sqrt{\frac{\kappa_c}{\kappa_d \left(T_{eq} - T_{out}\right)}} \tag{5.16}$$

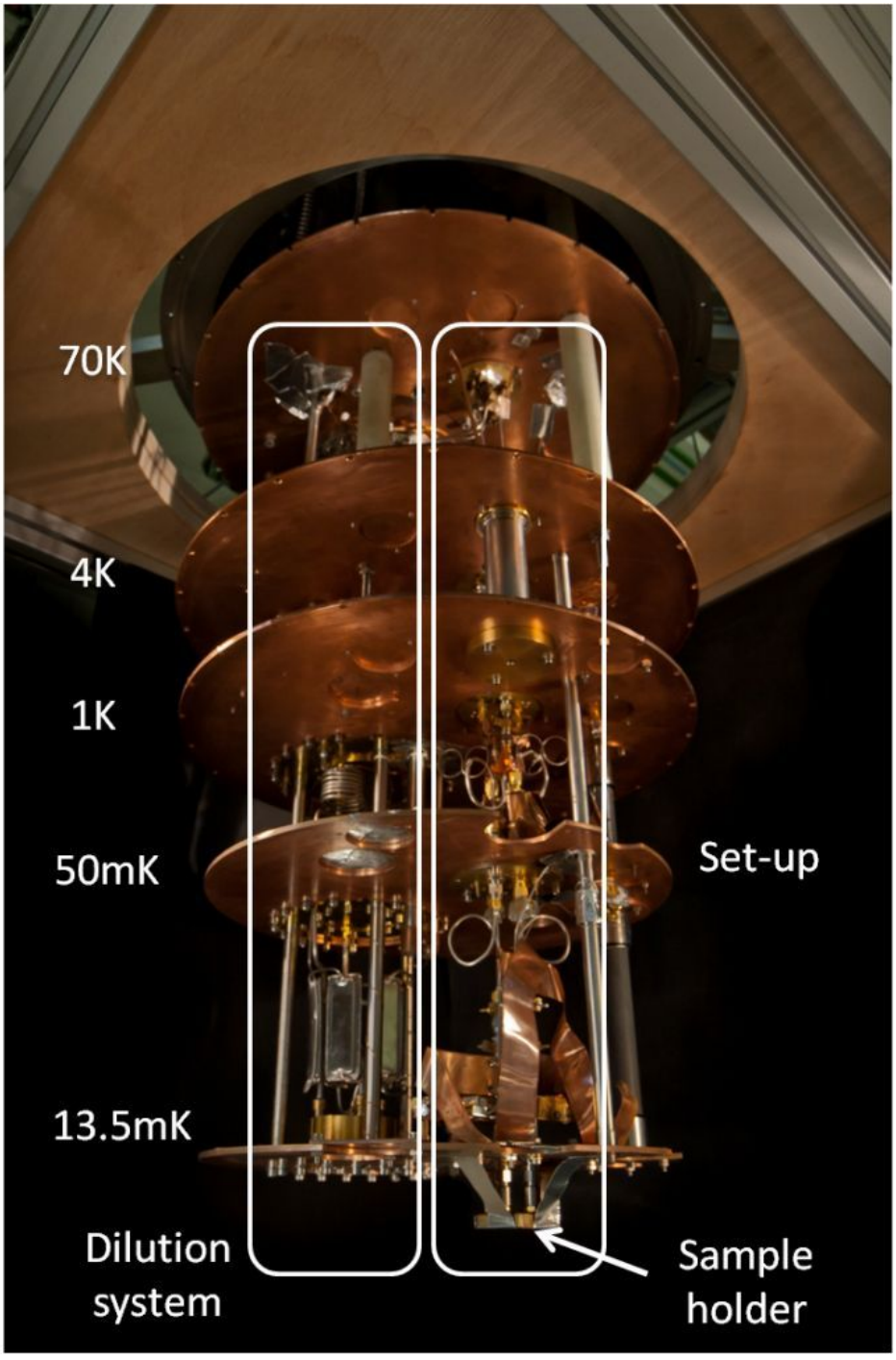

Figure 5.5: Implementation of the set-up in the Helium Free cryostat

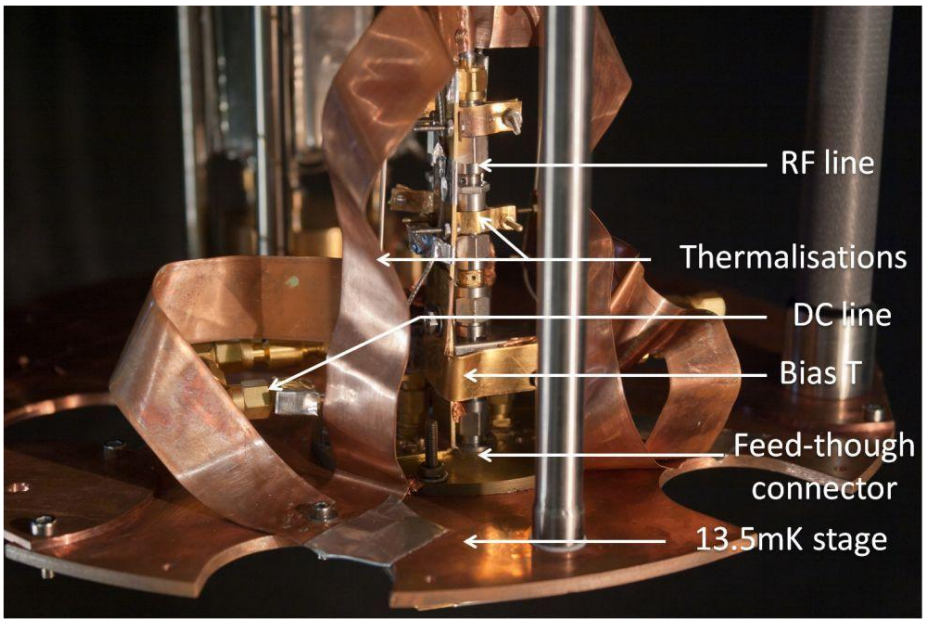

Figure 5.6: The base temperature stage set-up

The values of T_{eq} for the different cables used in the set-up are reported in table (5.2). These estimations show that the thermalization of the inner conductor is efficiently done through the dielectric insluator for temperature above 1K, whereas important deviations between T_c and T_s are to be expected at low temperatures. However the model only consider the free part of the coaxial cable (i.e. the part that does not touch any stage), so by putting large contacting region of thermalization (bigger than the L_{eq}), we will be able to better anchor the inner temperature of the coaxial cable to the temperatures of the stage.

Cable	length D (cm)	T_{eq}(K)	L (mm)
$300K \rightarrow 70K$	35	74.6	1.1
$70K \rightarrow 4K$	25	6	0.8
$4K \rightarrow 1K$	10	1.2	2
$1K \rightarrow 50mK$ (RF)	15	0.16	3.6
$1K \rightarrow 50mK$ (DC)	15	0.11	1.6
$50mK \rightarrow 13mK$(RF)	15	0.02	14
$50mK \rightarrow 13mK$(DC)	15	0.015	6

Table 5.2: Comparison between the lengths of the cables and the typical thermal lengths of the system

The temperature of the sample is linked to the inner conductor temperature of the coaxial lines that arrive on the contacts. The inner conductors of the coaxial cables between the

stage at 50mK and the stage at 13mK need several centimeters to be thermalized (table (5.2)). Fortunately, they are not directely connected to the sample. Several components (attenuator, Bias T, adaptors) separate the coaxial cables from the chip carrier. As shown on figure (5.6), these components are all connected to the base temperature stage to maintain the components shield at 13mK and create a sufficient length (about 10cm) to thermalize the inner conductors of the circuit.

5.2.4 Dissipation in the components

The power that can accept the dilution stage is very small when it is at base temperature. So that we have to consider the dissipation of RF excitations in the attenuators. The dissipated power in an attenuator of 10dB or more can be roughly estimated by the total Joule power of the input voltage $V_{in}^2/50$. The generator output power is about $\frac{V_{in}}{50} = 5mW$. The acceptable powers for the different stages of the cryostat are $100\mu W$ for the 50mK stage and a few μW for the 13mK stage. So an attenuator of at least $20dB$ must be placed on each intermediate stages of 4K, 1K and 50mK.

5.3 Environmental noise

5.3.1 Broadband voltage fluctuations due to Johnson-Nyquist noise

Photons associated to Johnson-Nyquist noise coming from the hot parts of the external circuit affect directly the electronic temperature of the sample, because they induce broadband voltage fluctuations. They also excite the two levels electronic systems that are responsible for the 1/f noise [49, 83]. Nyquist has derived the power spectrum of photons associated to resistor at a temperature T [62, 105]. It is given by the energy of photon $h\nu$ multiplied by the photon occupation number at frequency ν:

$$S_V(\nu) = \frac{2Rh\nu}{e^{\beta h\nu} - 1} \tag{5.17}$$

At frequency far below the cut-off k_BT/h, the formula gives the well known Johnson-Nyquist white noise. In the case of room temperature, broadband filtering up to Terahertz is necessary. For the low frequency lines, we filter high frequencies by mean of commercial discrete filters or resistive coaxial cables. Following the set-up realized by Glattli et al. [49,77], we choose to implement homemade resistive microcoaxes, the specifications of which are described in table (D.1).

The cut-off frequency achieved by these lossy coaxes can be estimated by the dispersion law of the propagating solutions $e^{i(\omega t - k_x x)}$ in the coaxial cable, where r is the linear resistivity and $Z = \sqrt{L/C}$ the characteristic impedance [29]:

$$k_x = \frac{\omega}{c} - \sqrt{\frac{r\omega}{Zc}}\,(i-1) \tag{5.18}$$

In a cable of length l, the effective cut-off frequency for a white power is given by:

$$f_0 = \int_0^\infty e^{-2\sqrt{\frac{2\pi fr}{Zc}}} df = \frac{Zc}{4r\pi l} \tag{5.19}$$

Concerning the low frequency lines, the resistive homemade cables of length 30cm give $f_0 = 50MHz$ (see Appendix (D)). The room temperature thermal noise coming through the low frequency lines induce the voltage noise on the sample $\sqrt{4k_BTR} = 2\mu V$, which corresponds to a noise temperature of 20mK.

5.3.2 Thermal noise coming through the RF coaxial lines

The radiation problem has to be considered even more carefully for the RF lines. Not only does the 50Ω impedance from the RF generator radiates towards the sample, but the resistances components of the attenuators must also be taken into account. Strong cut-off is forbidden by the very fact they must transport high-frequencies. The attenuation formula (5.19) gives a cut-off frequency $f_0 = 30Ghz$ for the RF lines described in the table (5.1), which is in agreement with the losses specifications given by the coaxes constructors.

It is more efficient to put the maximum of attenuation on the down stages, in order to cool the photons associated to Johnson-Nyquist noise coming from all the 50 Ohms impedances of the upper stages. To compute the effective noise received by the sample we have to sum all the power emitted by resistive components in the RF line (including attenuators) integrated over the frequency range:

$$V_{th}^2 = \sum_{emittorsp} \int_0^{24Ghz} \frac{4R_p h\nu}{e^{(k_BT_p)^{-1}h\nu} - 1} d\nu A_p \tag{5.20}$$

For temperatures below 1.2K, we can consider that the noise is equal to $4R\frac{\pi^2}{6}\frac{k_B^2T^2}{h}$, whereas for the upper temperatures, we can consider that the noise is white over the frequency range $4Rk_BT\Delta\nu$. 20dB Attenuators are placed on the 4K, the 1K and the 50mK stages, and a 10dB attenuator is placed on the 13mK stage.

$$\begin{aligned} V_{th}^2 &= 4\times 50[\frac{\pi^2 k_B^2}{6h}\left(0.01^2 + 10^{-1}\times 0.05^2 + 10^{-3}\times 1^2\right) \\ &\quad +24\times 10^9 k_B\left(10^{-5}\times 4 + 10^{-7}\times 300\right)] \end{aligned} \tag{5.21}$$

which gives voltage noise of about $0.4\mu V$, which is equivalent to a noise temperature of 4mK.

5.3.3 Parasitic Noises from electronics

To prevent parasitic noises coming from instruments, working pumps and the 50Hz electrical network, the cryostat ground is totally isolated, except from the AWG generator (appendix (D) for details). Detection instruments grounds are also floating, and a GPIB insulator is inserted between the computer port and the GPIB connections to the instruments. Amplifiers are supplied with separate batteries. Their power supply are filtered with RC capacitors, because the regulators use kHz chopping frequency. The QPC gates are also fed with batteries. Efficient pi-filters are placed on the low frequency lines that enter the cryostat: the QPC gates line, the thermometry lines, the amplifiers output, the battery for amplifiers and the low frequency excitation.

To protect the set-up from external electromagnetic fields, amplifiers are put in a Faraday box and mu-metal shields cover the cryostat and the outer parts of the circuit.

5.4 Effective electronic temperature extracted from DC shotnoise

5.4.1 Calibration

The shotnoise contribution can be extracted from the cross-correlation spectral power by substracting the cross-correlation value when no voltage excitation is applied to the noise measured when the excitation is applied. However doing the substraction between two measurements that last several minutes suffer from long drifts of the sample, of the electronics and of the external background noise. Also a modulation method is more robust [119]. In this spirit, we divide the total averaging measurement in small packets of measurements that last a few second and alternate ON and OFF measurements that we substract in order to eliminate long drifts.

On the other side, the voltage bias applied on the contact of the QPC also changes its conductance. The QPC differential conductance variation with respect to a DC bias is shown on figure (5.7). Each curve corresponds to a fixed value of the voltage gate V_g. We will discuss further the physics of this phenomenon in the section 6.2.4. The transmission can vary up to 25% when $100\mu V$ is applied across the sample.

In consequence, the circuit voltage noises that enter in the cross-correlation term and that depend on the conductance of the QPC are not totally elimitate by the ON-OFF substraction (eq.(5.5)). To prevent the variation of the QPC transmission with the bias voltage, a feedback loop adjusts the voltage gate V_g in order to keep the transmission constant. The error value is

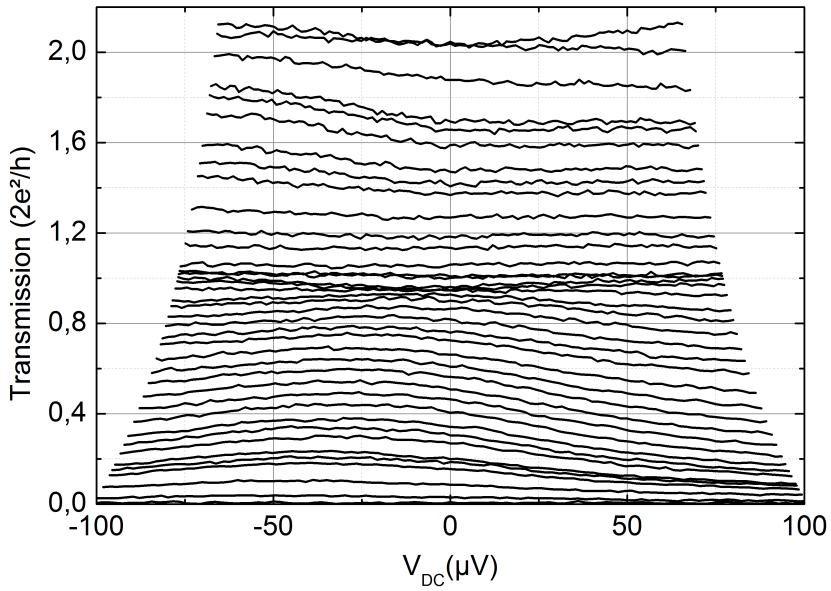

Figure 5.7: Variation of the QPC transmission for a fixed voltage gate when a DC voltage bias is applied to the sample.

given by a dI/dV measure that compares the real QPC conductance to a preset value. Then it is added to the preset V_g to rectify the conductance. With the gate feedback technique, the transmission never vary more than 5%.

Nevertheless, it is important to calibrate the external circuit noises to evaluate correctly their contribution in the signal. The calibration of the amplifier lines can be done by measuring the thermal noise of a 50Ω load and a short load at the input of the amplifiers. When short is used, only the voltage noise of the amplifiers remain. It can be compared to the thermal noise of the 50Ω load at room temperature $4k_BTR = 0.84(nV)^2/Hz$. So we find $U_A^2 = U_B^2 = 0.287(nV)^2/Hz$ (fig. (5.8)).

An efficient way to calibrate the current noise i_A and i_B is to compare the auto-correlations and cross-correlation measured at different transmission of the QPC with those when D=1 and to fit with the expected values (fig 5.9). We find that $i_A = 126fA/\sqrt{Hz}$ and $i_B = 150fA/\sqrt{Hz}$.

5.4.2 DC shotnoise measurement

Figure (5.12) reports the shotnoise generated by a QPC at transmission of 0.3 versus the DC bias applied on the contacts. We choose a transmission below 0.5 to avoid the 0.7

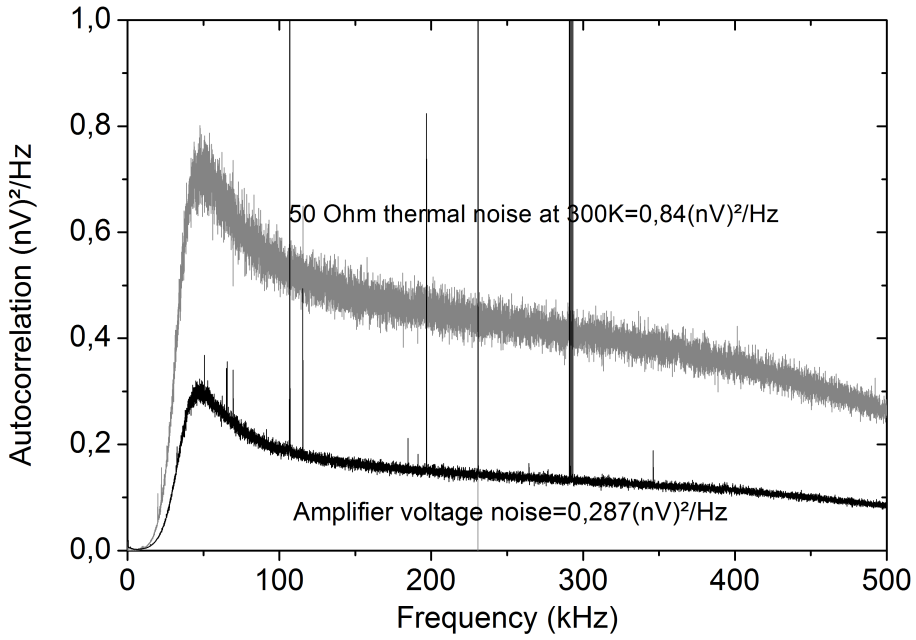

Figure 5.8: Voltage noise calibration

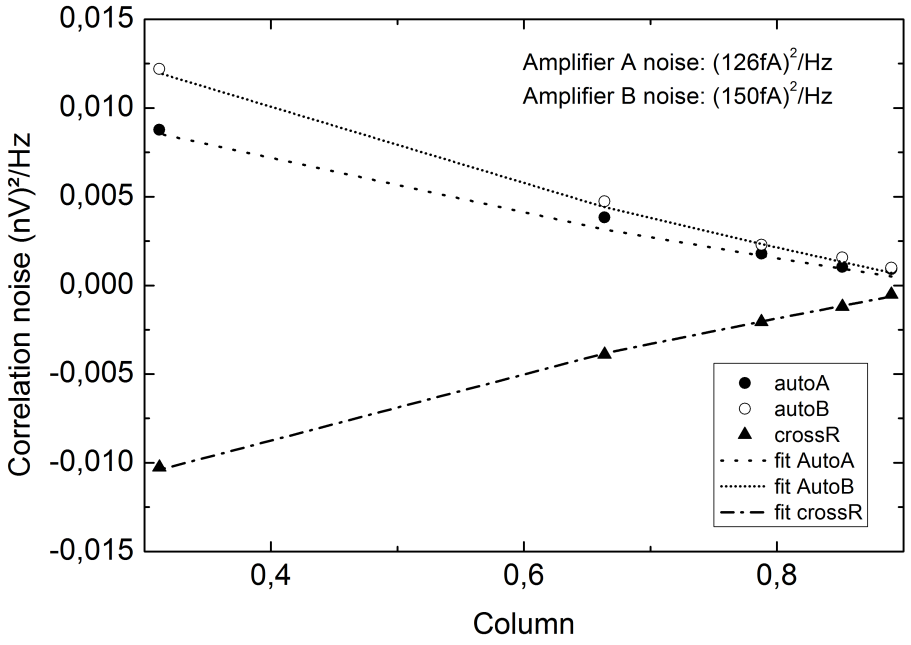

Figure 5.9: Calibration of current noise of the amplifiers

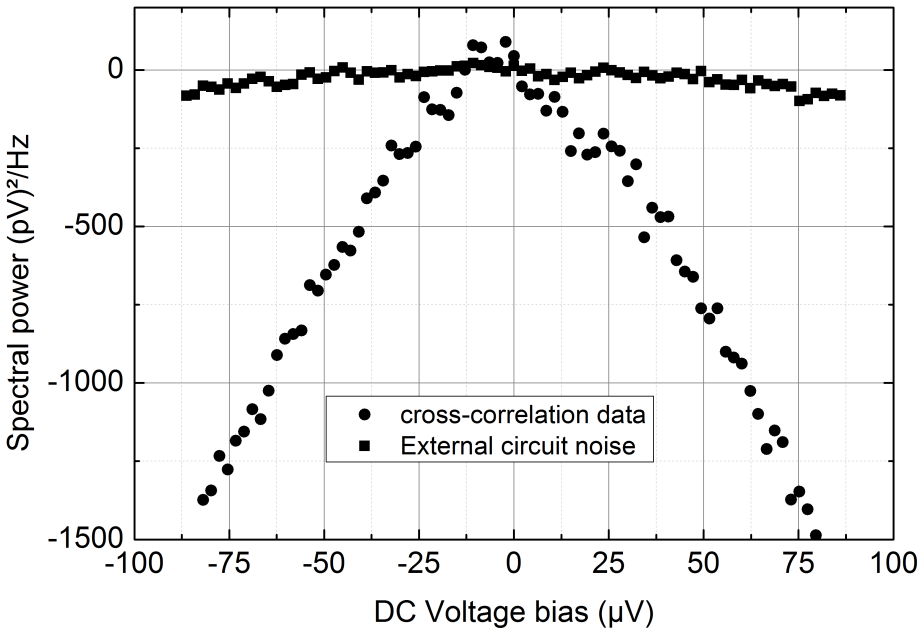

Figure 5.10: Differential crosscorrelation signal as a function of the DC voltage bias (full dots). Contribution of the amplifier current noise in the differential cross-correlation due to voltage dependent transmission of the QPC (full squares)

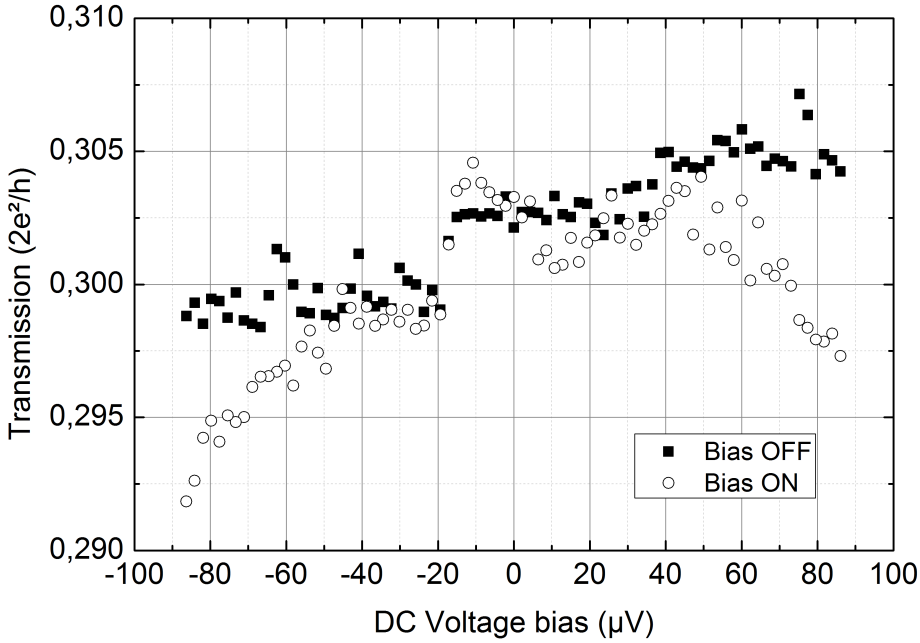

Figure 5.11: Transmission of the QPC associated to the differential crosscorrelation measurement, when the signal is ON (open dots), when the signal is OFF (full dots)

anomaly of the fano factor [35, 121]. The transmission value of the QPC has been recorded simulteanously during the ON-OFF measurement and is reported on figure (5.10). During the measure, the transmission drifted a little as shown by the transmission taken during OFF measurement (full black dot curve). The voltage-dependence of the transmission can be observed by comparing the transmission measured when DC bias is applied (ON curve in open dots) with the transmission of OFF measurement. Using the feedback technique, the variation of transmission is reduced to a few percents.

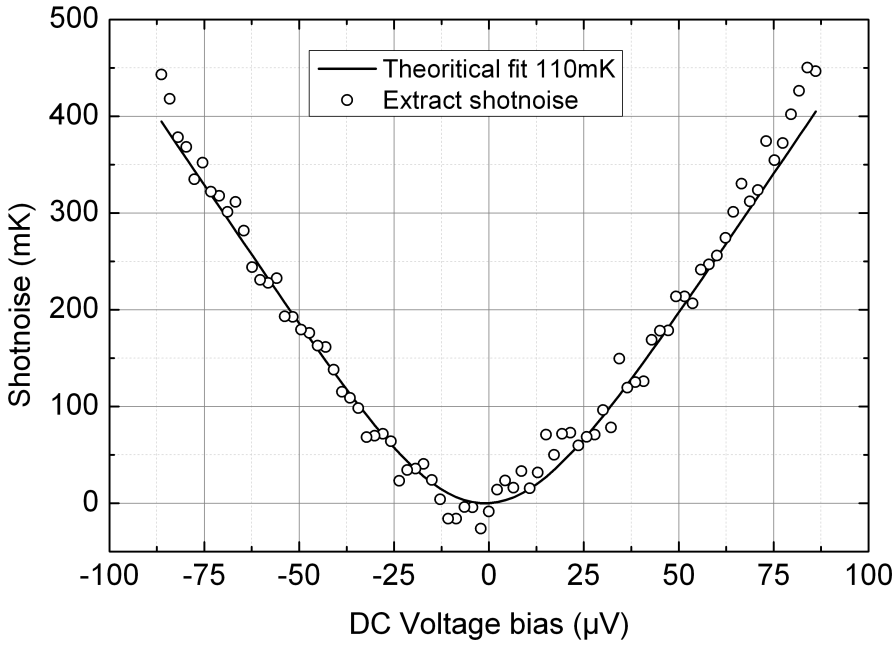

Figure 5.12: Shotnoise extracted from differential crosscorrelation data of figure 5.4.2 (open dots). Best theoretical fit with a electronic temperature of 110mK (black line)

Then the contribution of the current noises of the external circuit (i_A^2 and i_B^2) can be computed and substracted to the raw data (fig. (5.4.2)), as well as the coefficient of $\langle i_C^2 \rangle$ in equation (5.5). The data are in good agreement with the DC shotnoise (5.22) [77].

$$S_I = 2\frac{2e^2}{h}D(1-D)eV \coth \frac{eV}{2k_BT} \tag{5.22}$$

With equation (5.22), the electronic temperature of the sample can be evaluated to 110mK. The shotnoise data depart from the theoretical fit when the DC bias is above $60\mu V$, which we can attribute to Joule heating of the sample that increases the temperature and the thermal noise S_{th} when the bias is applied. We will study these heating effects in chapter 7.

5.4.3 The parasitic noise from the pulse-tube

A resistor thermometer RUO2 is placed near the sample and indicates a temperature of 22mK. However the sample electronic temperature is far larger, and cannot be explained by the temperature of the inner conductor, nor by photon radiation. The auto-correlation spectrum shows many peaks up to 100kHz (fig.(5.13)). The total voltage fluctuation they represent is estimated to be equivalent to 40mK. Yet the frequencies lower than 1kHz are cut-off by the amplifier passband, and the total noise may be larger. The peaks are due to the pulse tube operation: they completely disappear when we stop the pulse-tube. However the physical relation between the pulse-tube operation and those electronic peaks is not clear. For example, the peak magnitude increase with the cryostat temperature, which seems to indicate that there is more than just an electromagnetic perturbation of the pulse tube.

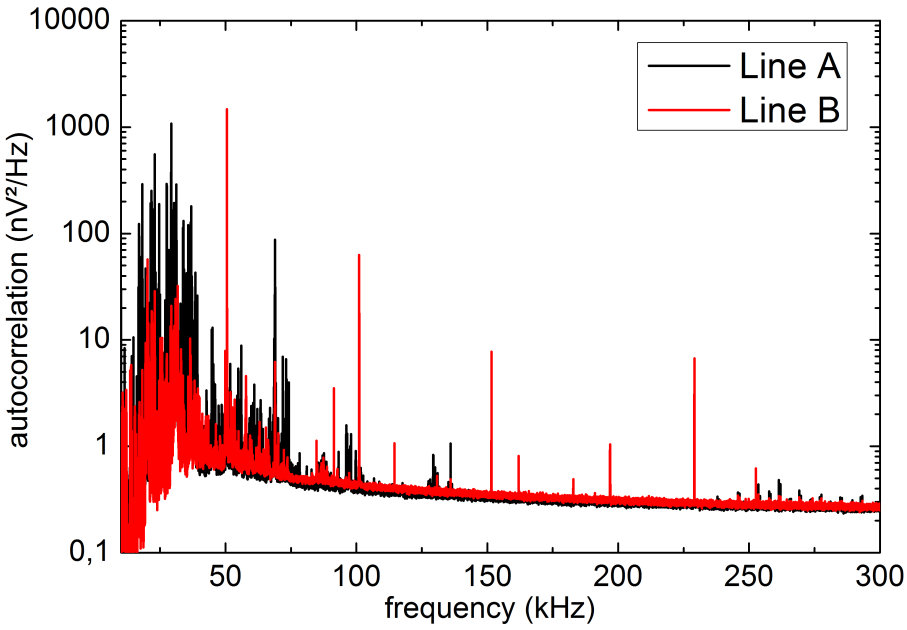

Figure 5.13: Autocorrelations spectrum

We have tried to investigate further the relation between those perturbating peaks, the pulse tube cycle and the electronic temperature. The Acquiris card was synchronized with the pulse-tube cycle by means of a microphone placed on the pulse-tube. Then S_I in the frequency reange of 1kHz-100kHz is recorded during a short time t=65ms compared to the cycle period (660ms). the acquisition is launched at different times of the cycle. Simulteanously, the acoustic noise of the pulse-tube was measured. The figure (5.14) reports S_I. Clearly, the perturbation magnitude follow the cycle. There is a delay that can be explained by the operating

cycle of the pulse tube. Then we have proceeded to a shotnoise measurement synchronised during the period of the cycle where S_I is the lowest. We find that the electronic temperature is reduced to 70mK. However only one sixth of the cycle can be used for measurement, so this technique is not experimentally worthy for long experiments.

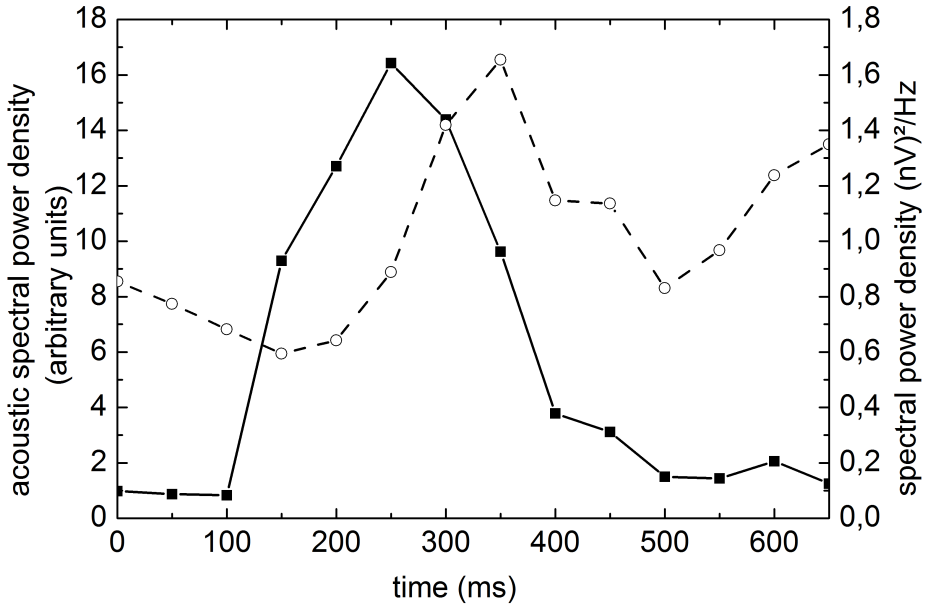

Figure 5.14: dash line: acoustic noise of the pulse tube during the operating cycle that last 600ms. solid line average spectral power on the range 1kHz-20kHz (region of the parasitic peaks) of the autocorrelation on line B during the operating cycle that last 600ms. The Acquiris card is synchronized with the operating cycle of the pulse-tube and acquire data during 65ms after a certain delay.

5.5 Conclusion

To our knowledge, we implement one of the first cross-correlation noise detection set-up in a Helium free cryostat. As shown by the numerical studies, the excess nosie N_+ to be detected for our studies is of the order of 0.1 to 0.5 quasi-particles per period and contributes to spectral power of the shot-noise by about $10^{-29}A^2/Hz$. DC shotnoise measurement confirms that the sensitivity of the set-up could reach this value in a few minutes. The electronic temperature extracted from the DC shotnoise is about 110mK, which is slightly above these of similar experimental set-up that use broad band RF coaxial lines in wet cryostats [7, 44, 94, 124]. The pulse tube technology of Helium Free cryostat adds some perturbation that heats up the

electronic temperature by at least 30 or 40mK. We are working on modification on the set-up and the cryostat to reduce these perturbations and improve the electronic temperature. First we would like to shift the frequency range of the detection towards 1Mhz with a resonant circuit that will suppress the current noise peaks due to the pulse tube in the 10kHz range. The use of cryogenic amplifiers will limit the capacitive shunt of the coaxial cables, enlarge the frequency range of detection and so reduce the time measurement. Second, we suspect vibrations to mediate the acoustic noise produced by the pulse tube and induce the electric perturbations in the circuit. So we are working closely with the cryogenic team on reducing the acoustic noise by modifying the pulse-tube helium injection in the cryostat.

Chapter 6

High-frequency implementation

In chapter 3, we discussed the necessity to use voltage pulse with frequency repetition at least in the gigahertz range in order to circumvent the characteristic thermal time $\hbar/k_BT$. Lorentzian pulses and other type of none monochromatic pulses have large spectrum. This requires to build a broad band RF circuit up to the highest frequency delivered by the Tektronix arbitrary wave generator (24Ghz). We may face a number of undesirable frequency-dependent attenuations or reflexions that can modify the shape of the pulses. The part more likely able to provide unwanted reflexion is the sample and the sample holder. In section (6.1) we explain how we designed our sample and sample holder by means of 3D electromagnetic transient solver CST environment. As the QPC resistance is far higher than the 50 Ohm impedance of RF circuits, the direct measure of frequencies transmission is not easily possible on the sample. So we develop an in-situ method to calibrate the transmission of RF frequency through photocurrent measurement, that we detail in section (6.2).

6.1 High-frequency design and simulation

6.1.1 Design of the sample

The sample design must ensure that the high-frequency pulses incoming on the QPC contacts or gates are free from deformation. However the mettalic conductor evaporated on the GaAs substrate is typically 100nm thick and induces too much too much attenuation at Ghz frequency [115]. In consequence, the coaxial lines need to be extend to the sample holder and the chip by coplanar waveguides (CPW). For the sample, the circuit design must fulfill the following specifications:

size reduction: The coplanar waveguides start at the level of the quantum point contact with dimensions starting from 50μm, and widening up to 0.5mm around the bonding pads, which is more compatible with the geometrical feature of standard coaxial lines. The widening

region is limited by th sample size, which is a square of 2.2mm.

reducing the cross-talk between CPW: At high frequencies, the high impedance of the sample (typically $R_0 = 12,9k\Omega$) may be shunted by the direct capacitance between the coplanar waveguides that arrive at the contacts. Similary a cross-talk between a contact line and a gate line may send an echo on the gate potential when a voltage is applied on the contact. Using grounded coplanar waveguides with thick groundplanes close to the device helps to confine the electromagnetic field in the waveguides and limit the cross-talk.

Figures (6.2) presents a optical photographies of the sample. The left and right (respectively top and bottom) coplanar waveguides bring voltage to the contacts pads (to the gates). The peculiar exponential size reduction of the CPW was inspired from previous works on coplanar waveguides size reduction [115]. The shape of the lines must keep the 50Ohm impedance constant and present smooth variations, otherwise reflection occur.

Furthermore there is another difficulty added by the small size of the sample. Indeed the approximation of infinite groundplanes is not valid and the geometries of the four coplanar guides are not independent from one another. However, there is a conformal mapping m that gives an equivalence between the electromagnetic field resolution in the case of the finite coplanar waveguide and the infinite coplanar waveguide (fig.(6.1)) [111, 115, 128]:

$$m: \quad z \to z\sqrt{\frac{c^2 - b^2}{c^2 - z^2}} \tag{6.1}$$

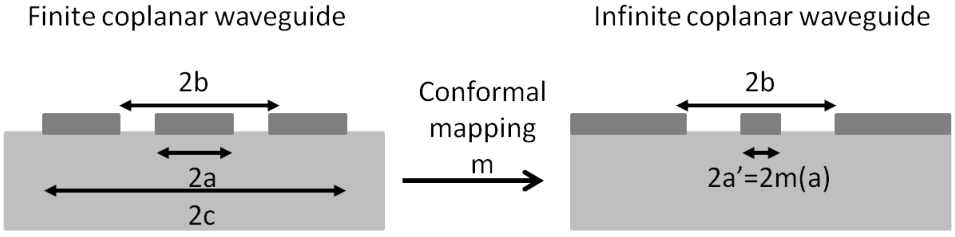

Figure 6.1: The conformal mapping between the coordinates of the finite groundplane CPW geometry and the infinite groundplane CPW. The inner board of the ground plane b is invariant, whereas the width of the inner conductor 2a is reduced to 2a'.

Computing the good ratio a'/b for an infinite ground coplanar waveguide of 50Ω impedance is given by several 2D solvers. The obtained values guide us to incrementaly build the four coplanar waveguides, then we validate the transmission of the four lines by 3D electromagnetic simulation with the transient solver of CST microwave studio software. All the dimensions are detailed in appendix (C)

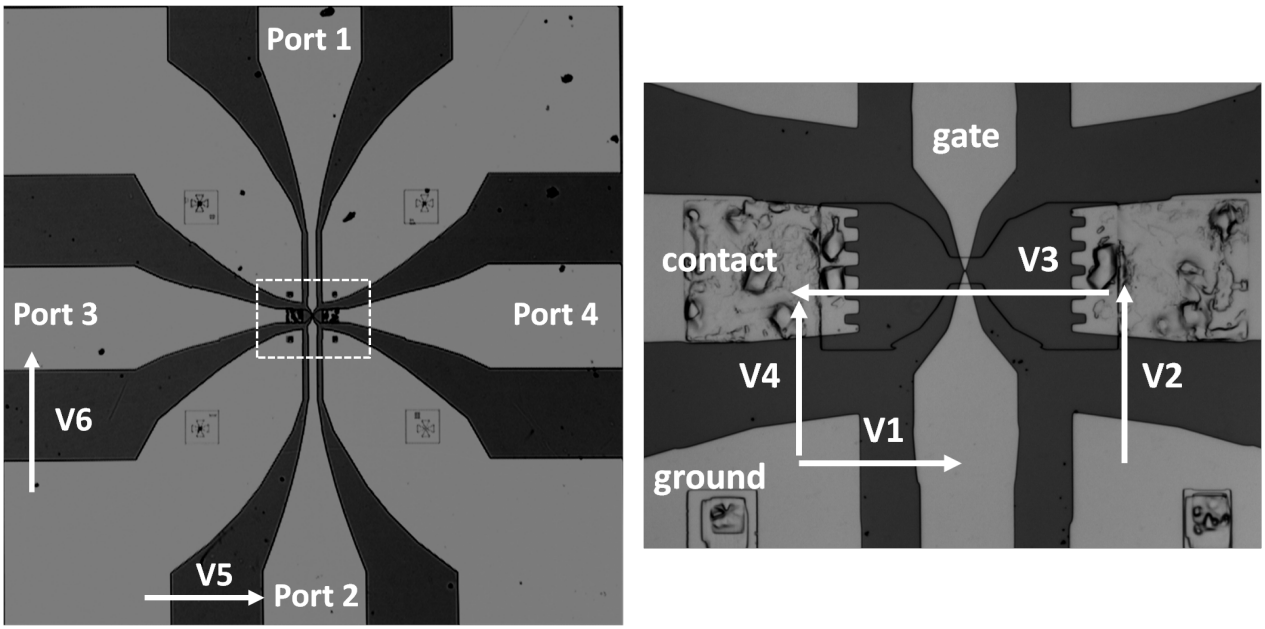

Figure 6.2: optical photography of a whole sample (left) and zoom on the quantum point contact region (right). The grey parts are the metallic conductors, whereas the dark areas are the Gallium Arsenide dielectric surface. Arrows represent the voltages computed by the CST simulation in figure (6.4)

Figures (6.3) show the simulation of the amplitude and argument of the scattering parameters between the four ports of the sample. Port 1 and 2 are the coplanar waveguides of the gates and ports 3 and 4 those of the contacts (see fig.(6.2)). These ports are placed at the boundaries of the sample, at the end of each coplanar wave guide. As the quantum point contact has high impedance compared to 50Ω, its conductance is simply set to 0 in the CST simulation.

In consequence, total reflection is expected for the contact ports 3 and 4, except when the capacitive coupling between the two CPW starts to shunt the QPC resistor at high frequencies. Indeed the reflection amplitude $|S(3,3)|$ is nearly one up to 12Ghz and starts to decreases slowly to 0.9 at 20GHz, while the transmission amplitude $|S(4,3)|$ (equal to $|S(3,4)|$) increases slowly from 0 to 0.05. We note moreover that there is a small leak towards the gates when we consider the transmission amplitude $|S(4,1)|$ (equal by symmetry to $|S(3,1)|$ and $|S(3,2)|$). It also corresponds to a capacitive shunt between these CPW. We can extract the value of the equivalent capacitor between the contacts from S(3,4) to the order of 3fF, which is in agreement with the rough geometric estimation. Attenuation in the coplanar lines can be estimated by computing $1 - |S(3,3)|^2 + 2\,|S(3,1)|^2 + |S(3,4)|^2$. At 20Ghz, nearly 0.9 of the input power is transmitted or reflected, which means that only 10% of the power is dissipated in the circuit.

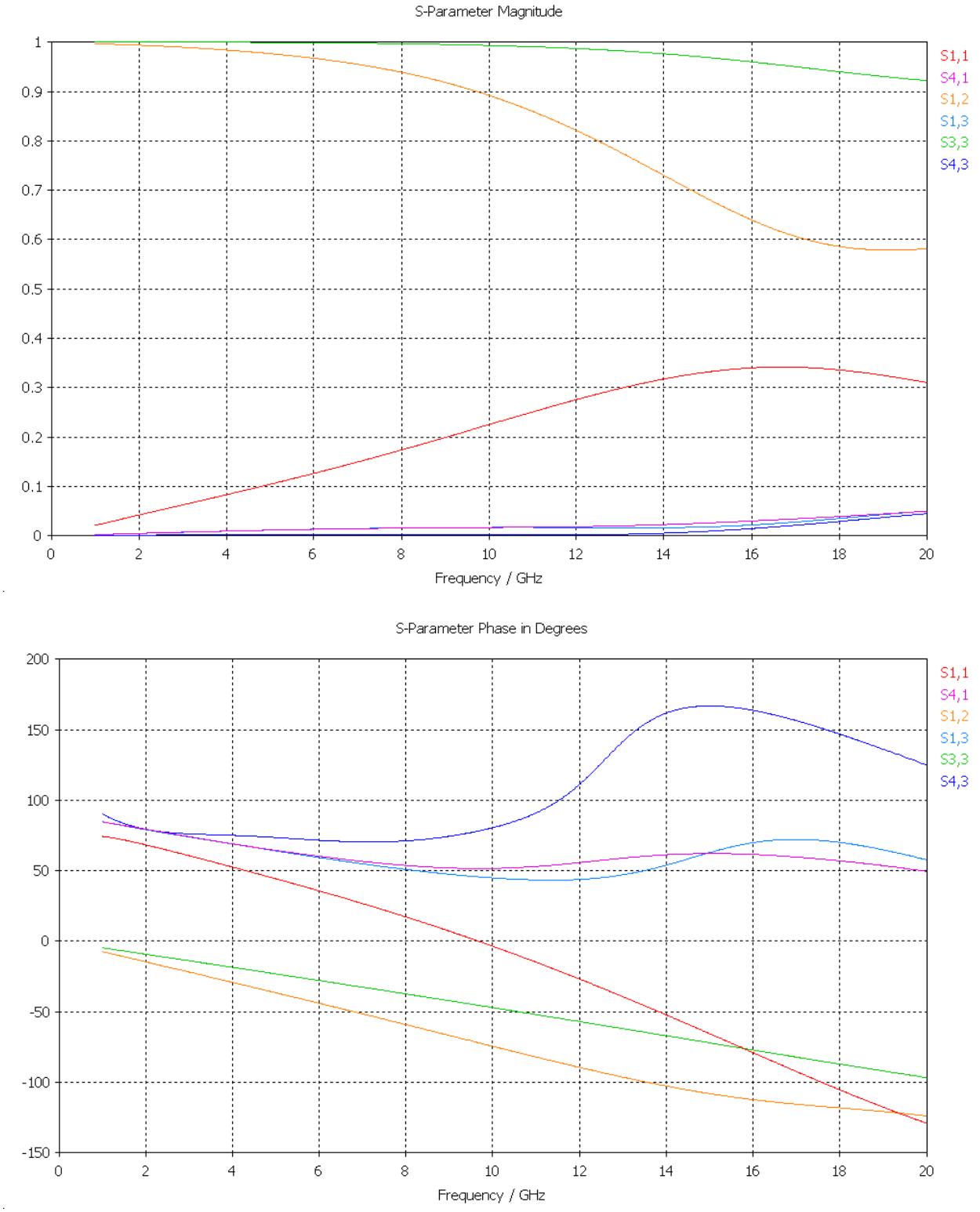

Figure 6.3: Amplitude (top figure) and phase (bottom figure) of the scattering parameters of the transmission mattrix between the four coplanar waveguides, computed by the CST simulation.

When we consider the gates ports 1 and 2, we see that the transmission amplitude $|S(1,2)|$ between them increases from zero to 0.35 around 16Ghz, which reflects the fact that the capacitor created by the tips is more important. Attenuation is also more important in the thin coplanar waveguides of the gates: $|S(1,1)|^2 + 2|S(3,1)|^2 + |S(1,2)|^2 \approx 0.5$, which means that nearly 50% of the power is dissipated in the circuit at 20Ghz .

This analysis can be confirmed in time domain by comparing the voltage responses on several interesting points of the device to the pulse used by CST for the transient solver (fig.(6.4)). The voltage input V6 is applied at the entry of the coplanar waveguide 3 (see fig.(6.2)). Then the effective voltage applied between the contacts of the sample V3 can be compared to the voltage V4 that arrives on the contact at the end of the coplanar waveguide: there is just small discranpancies between them and V6. The transmitted voltages to the other contact V2 after the QPC remains small, and so are the echos on the gates V1 and V5.

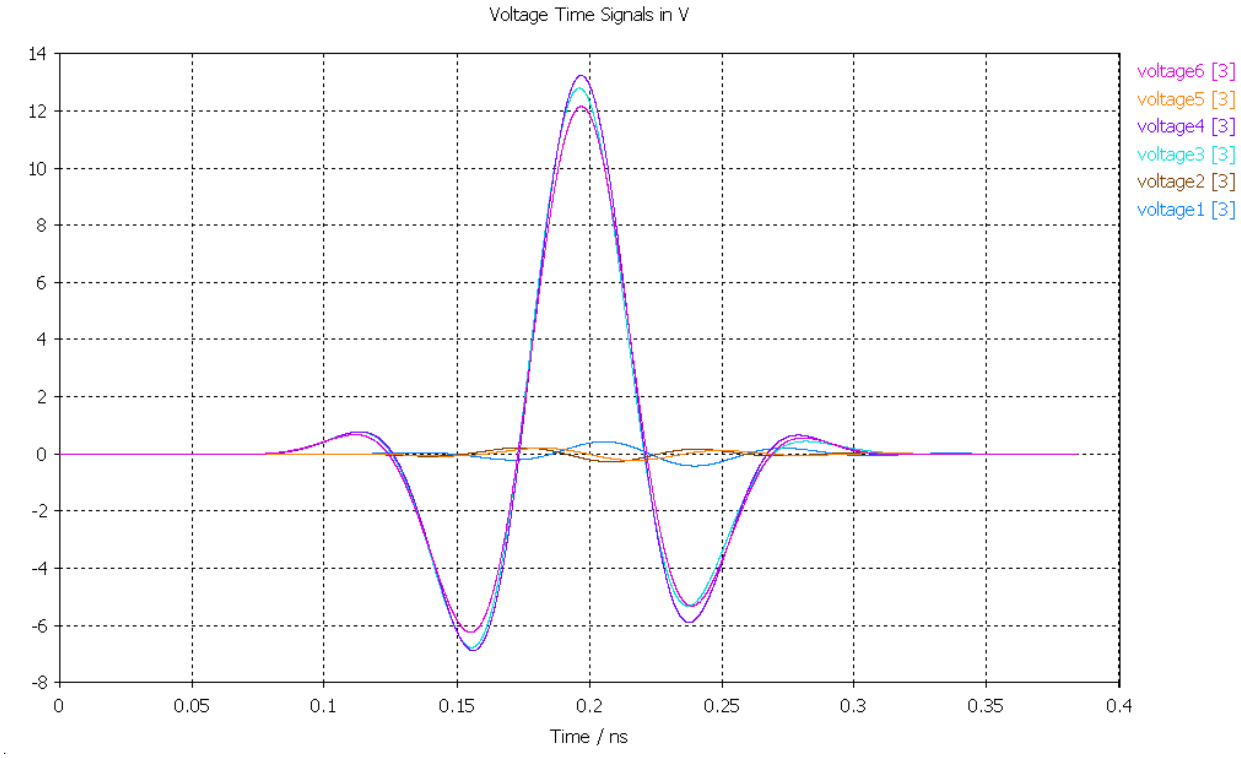

Figure 6.4: CST simulation of the time response of the device to a voltage pulse V6 applied on port 3, i.e. on the coplanar waveguide leading to the left contact of the sample. The voltage shape is the second derivative of a Gaussian, a typical shape adapted for time solver of 3D electromagnetic problem. The voltage responses V1 to V5 are taken on interesting point of the device, represented on figure (6.2).

6.1.2 Design of the chip carrier

The electromagnetic properties of CPW patterned on Gallium Arsenide substrate are pretty different from these of the SMA standard coaxial circuit. Consequently, the print card board (PCB) that holds the sample is designed to interface the coaxial circuit with the sample. The PCB adapts the dielectric constant discrepancy between GaAs and Teflon, and the coplanar wave-guide geometry on the sample to the coaxial wave-guide geometry.

the dielectric constant discrepancy: The dielectric constant GaAs (12.8 [85]) are much different. In a coaxial line or a CPW designed to be 50Ω, the dielectric constant impacts the ratio between the diameter (or width) of the core conductor and the distance between the two conductors. In consequence, the interface between two RF circuits with different dielectric constants can induce unwanted reflections. The goemetrical control of the interface between the GaAs sample and the chip-carrier is not easy to control. The sample is actually put in a little socket (2.2mm large) carved in the PCB and connected to CPW by micro-bonding. In order to limit electromagnetic mismatchs, the PCB subtrate must have a dielectric constant close to the GaAs dielectric constant. Consequently the PCB is carved on a Roger TMM10 substrate (9.2 at 10Ghz [1]), a commercial laminated substrate for PCB that shows good stability under temperature variation and good response to high frequencies.

the geometrical constraints: In future experiments, the sample holder will be inserted in the center of the high field magnet that will equip the cryostat. This reduces the sample holder size to a few centimeters, and prevents to use K connector to interfece the PCB with the coaxial cable. Small RF right angle pcb-coaxial adaptors are necessary: mini-SMP standard is available for frequencies up to 40Ghz even in the right-angle configuration. The mini-SMP dimensions are not far from the CPW dimension at the interface of the sample, so lines size reduction on the PCB present no difficulty.

The sample holder was also designed with the help of CST solver to check two critical features. First, the soldering pattern of the mini-SMP adaptor required a special design to transmit perfectly the high frequencies up to 30GHz (see Appendix C for the pattern details). Second, a regular and dense pattern of via-holes must be added in the ground planes of the CPW. Via-holes are drilled in the PCB and filled with metal in order to ensure a good continuity between the ground planes on both sides of the insulator and limit parasitic waveguide type modes.

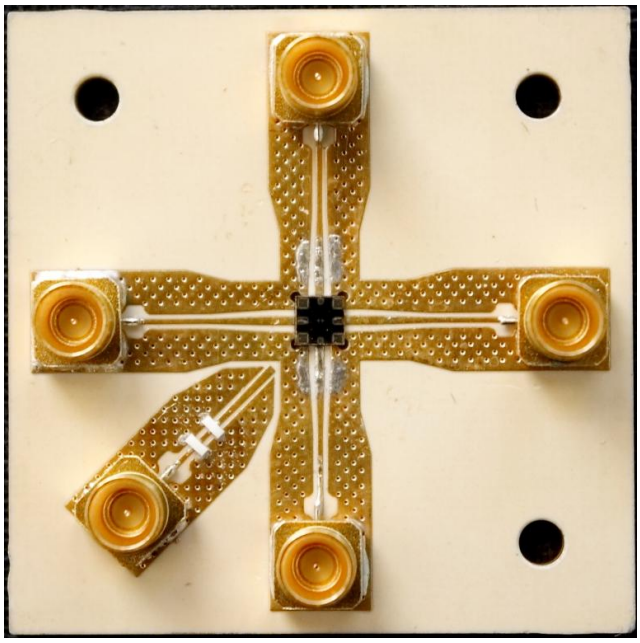

Figure 6.5: Photography of the RF chip-carrier with the sample inserted in its socket right in the center. The PCB is 4cm square, the sample 2.2mm large. The bonding pads of the sample can be seen in dark gold. They indicate the coplanar-waveguides ends on the sample, which dimensions match these of the CPW on the PCB. The electrical connection is done by alumium wire bonding between the sample and the pcb. Via-holes of 200μm diameter are regularly drilled in the groundplane to ensure the potential continuity with the back ground plane.

6.2 In-situ characterisation of the High frequency transmission using photocurrent

6.2.1 How is a photocurrent generate?

Considering the saddle shape potential formed at the QPC as a saddle potential point [20] allows to estimate the transmission dependence with energy. When a AC voltage is applied on a contact, electrons excited above the Fermi level and holes excited below the Fermi level do not see the same transmission and a residual DC current, called photocurrent, establishes through the QPC. Quantitatively the photocurrent can be derived from a Taylor development of $D(\varepsilon)$ in the average current (eq. (3.14)):

$$\begin{aligned}
\frac{1}{\mathcal{T}}\int_0^{\mathcal{T}} \langle I\rangle &= e\left(\langle N_h\rangle - \langle N_e\rangle\right) \\
&= e\int_{-\infty}^{\infty} d\varepsilon D(\varepsilon)\sum_{n\in\mathbb{Z}} |P_{AC}(n)|^2 \left(f(\varepsilon) - f(\varepsilon+(q+n)h\nu)\right) \\
&= e\int_{-\infty}^{\infty} \left(D(0) + \frac{\partial D}{\partial \varepsilon}\varepsilon\right)\sum_{n\in\mathbb{Z}} |P_{AC}(n)|^2 \left(f(\varepsilon) - f(\varepsilon+(q+n)h\nu)\right) \\
&= eqD - \frac{e\partial D}{2\partial\varepsilon}\sum_{n\in\mathbb{Z}} |P_{AC}(n)|^2 (q+n)^2\nu^2
\end{aligned} \tag{6.2}$$

At zero temperature, on can recognize the Fourier transform of

$$V(t)e^{i\varphi(t)} = \sum_{n\in\mathbb{Z}} (q+n)\nu P_{AC}^* e^{2i\pi\nu(n+q)}$$

and use the isometric property of the Fourier transformation:

$$\langle I\rangle = -\frac{e^2}{\hbar} e \frac{\partial D}{\partial\varepsilon}\frac{\langle V^2\rangle}{2} \tag{6.3}$$

Equation (6.3) tells that the photocurrent can be identified to a classical rectification. The effect is valid at all frequencies (in the range where the Taylor development remains valid, i.e. if $h\nu$ remains small compared to the characteristic energy of the saddle shape potential of the QPC). Note that there is no microscopic information contained about the granularity of the current. On the other side, it appears as a power measurement of the excitation applied between the contacts of the QPC, and can be use to analyze the response of the set-up to RF excitations. Indeed, the transmission of a high frequency signal to the contacts of the QPC may differ from the circuit theoretical specifications, due to undesirable resonances or reflections. The RF lines and components scattering parameters can be verified by means of a vector networks analyzer at room temperature. However such a measurement is difficult on a real sample because the QPC resistance is much more than 50Ω. Moreover, the components RF response may differ at low temperature from their value at 300K. The photocurrent is thus a very interesting tool to in-situ characterize the RF setup at low temperature.

6.2.2 Measurement of the photocurrent

To detect the photocurrent we use a chopping technique which consists in modulating the RF injection at a frequency of a few kHz and measuring the modulated response with a lock-

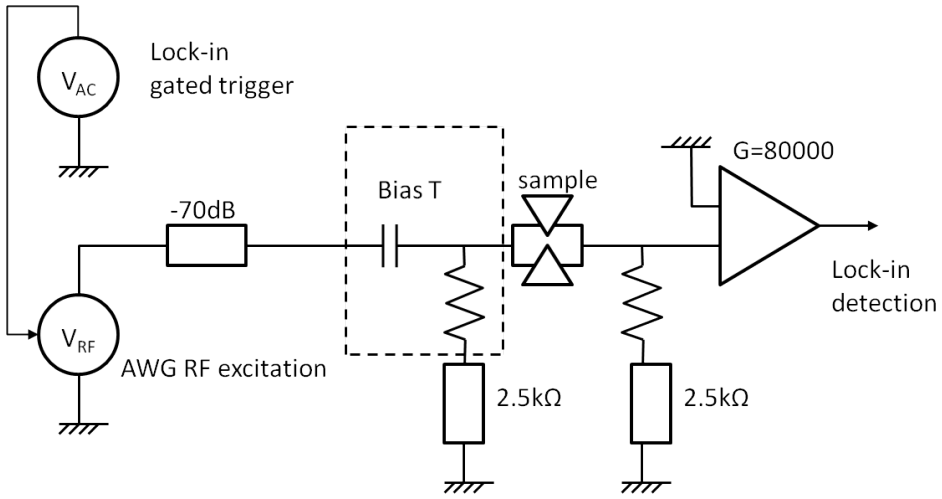

Figure 6.6: Schematics of the set-up for the photocurrent measurement. A lock-in output triggers the AWG generator that sends an RF signal only during half the period of the lock-in frequency.

in. We proposed two kinds of set-up performing this chopping photocurrent measurement, depending on the possibilities of the sources generators we used. The AWG possesses an external gated trigger capability, so the RF generation can be directly monitored by the output of the lock-in (Fig (6.6)).

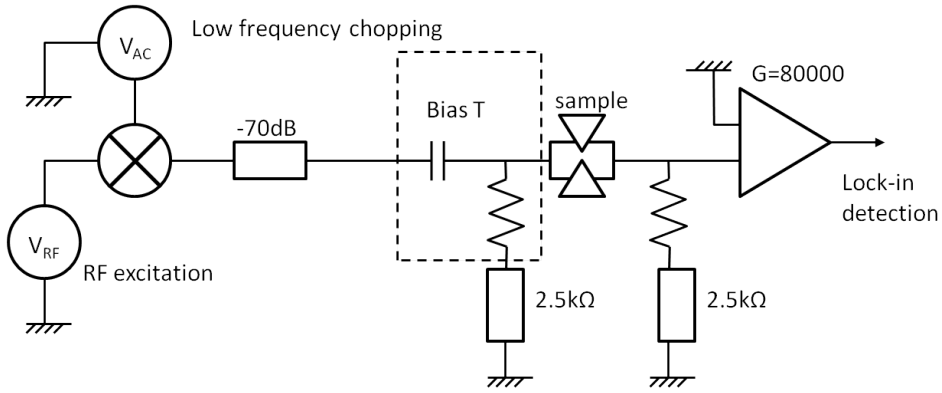

Figure 6.7: Schematic for the photocurrent measurement. A squarewave signal is sent on the DC output of a broad-band mixer, that chops the RF signal entering the RF input of the mixer. The chopped signal is injected through on one RF line of the set-up. The lock-in detection is done at the reference set by the squarewave generator.

However, the harmonic generator MXG Agilent PSG N5183A used for the RF line cali-

bration is not equipped with an external gated trigger, so we chopped the RF excitation by the means of a mixer (Fig (6.7)).

6.2.3 Experimental dependence of the photocurrent

As the photocurrent is proportional to the power of the excitation, it differs for waveforms of different shape having the same amplitude and the same mean value. Figures (6.8) reports photocurrent measurements for several useful waveforms with respect to their peak-to-peak voltage value in the top figure, and to their effective power in the bottom one. The photocurrent gives a clear signature of each waveform. For example, the response amplitude to a squarewave is twice this to a sinewave and thrice the one to a trianglewave, in agreement with the power hierarchie of the signals. When plotted with respect to the effective power of the excitations (figure (6.8) bottom), the photocurrent response of all waveforms aligns on the same curve. The power-dependence of the photocurrent is linear up to effective power of the order of 100pW. For higher power, the photocurrent is no more proportionnal to the power, because higher orders $\partial^n I/\partial\varepsilon^n$ are no more neglectable.

Measuring the photocurrent response gives an indication about the shape of the pulses $V(t)$ that effectively arrives on the QPC, but it is only the effective power of $V(t)$. As $V(t)$ can be decomposed into its harmonics, we can go further if we have the knowledge of the photocurrent response for each frequency. This gives the frequency spectrum response of the circuit coupling to the QPC. Small voltages should be used to keep the linear regime of the photocurrent with the power. Figure (6.9) shows the photocurrent response on the total frequency range of the set-up (2-24Ghz). To attest that the measure is performed in the linear regime at all frequency, the photocurrent is measured at different voltage power. The regular spacing between the curves prooves the linearity of the photocurrent with the power.

However, to be convince that the photocurrent frequency-dependence in figure (6.9) is only due to attenuation in the RF circuit, we need to investigate the consistency of the signal with different set of parameters. In particular, we have to verify that the QPC transmission is not sensitive to the applied frequency.

Figure (6.10) maps the photocurrent response to a sinewave of 500mV amplitude at the output of the generator, with respect to the gate voltage and the frequency of the excitation. The gate voltage is swept from pinch-off (-0,23V) to the first plateau (-0,19V). Figure (6.9) is avertical cut at Vg=-0.22V.
The pattern of the photocurrent response when the gate is swept is identical for all the frequencies. On the other axis, the dependence of the photocurrent with respect of the frequency is also proportional for any voltage gate. As predicted by Equation (6.3), the photocurrent appears indeed as a product of the transmission-dependent part and a power dependent part. There is no frequency dependance of the transmission in this frequency range.

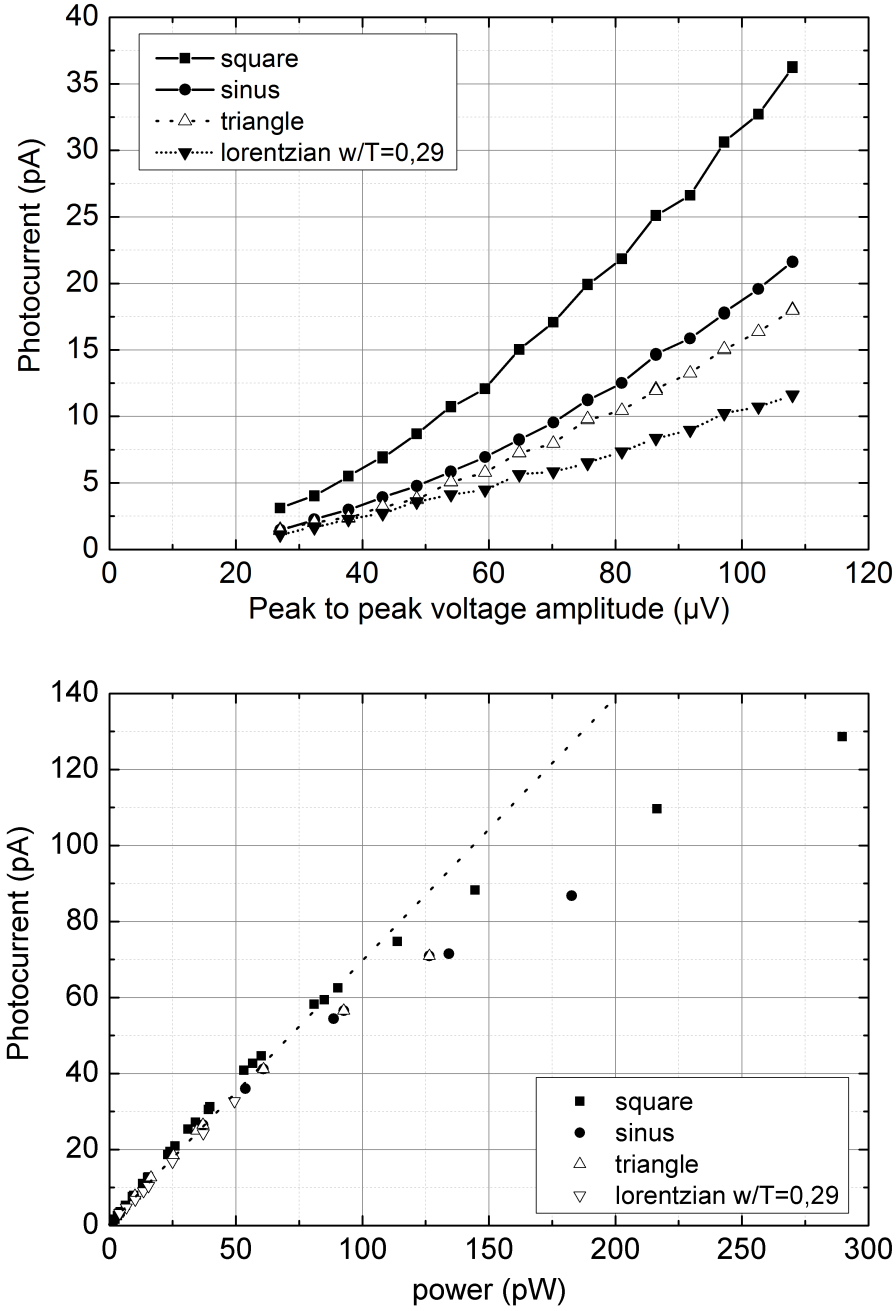

Figure 6.8: Photocurrent response for different waveforms of the same amplitude and frequency (2,5Ghz). Top figure: the response is plotted as function as the peak to peak voltage amplitude of the signals across the sample. Bottom figure: the same response is plotted with respect to the power of the waveform voltages. The dot line materialize the linear fit at low power.

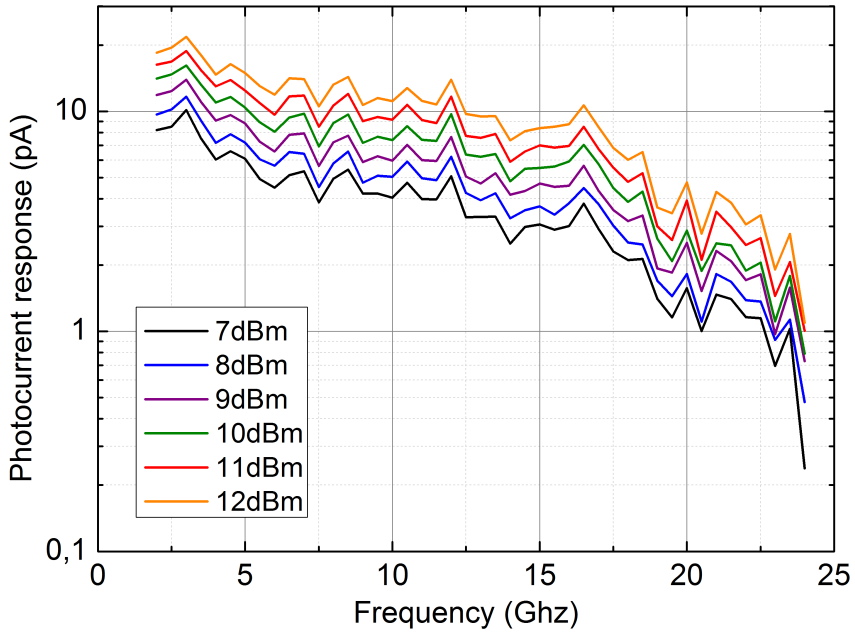

Figure 6.9: Frequency dependence of the photocurrent at Vg=-0.22V. The spectrum is measured for several power of the excitation, that varies from 7dB to 12dBm at the output of the generator.

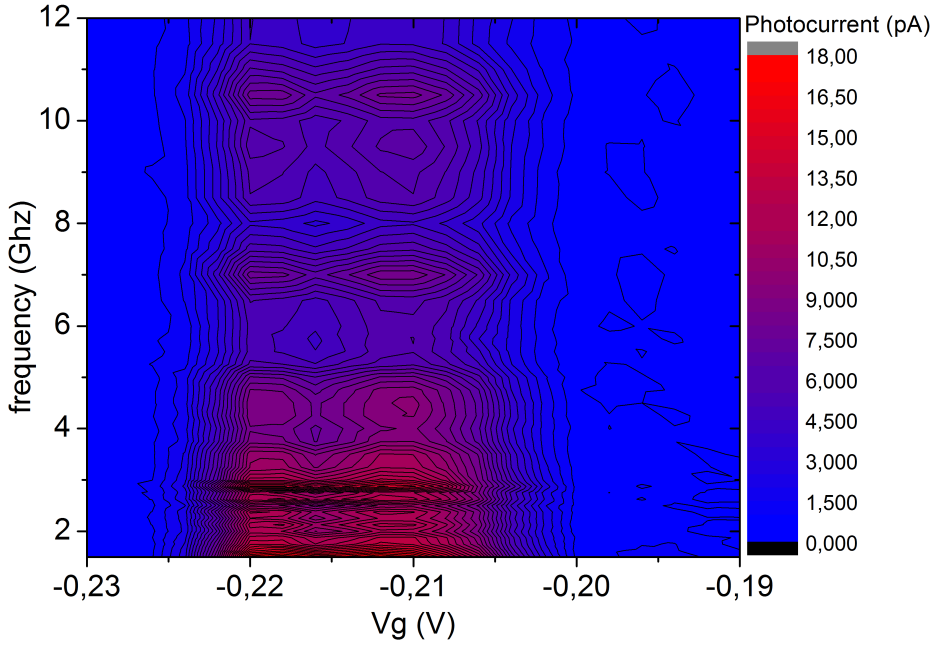

Figure 6.10: Photocurrent response to a sinewave output signal of $0{,}5V_{pp}$, with respect to the frequency of the signal (vertical axis) and the gate voltage (horizontal axis). The gate voltage sweep corresponds to the D=0 (-0.23V) to D=1 (-0.19V).

6.2.4 Comparison of the photocurrent to other derivative of conductance measurement

In figure(6.9), the photocurrent response gives access to the attenuation spectrum of the RF line A, but the values are only known in relative units. To give a correspondance between the photocurrent and the absolute power arrinving at on the QPC, $\frac{\partial D}{\partial \varepsilon}$ has to be measured by another method.

Second harmonic response at low frequency

The photocurrent, called rectification at low frequency, can be related to the second harmonic current response of a non-linear component to an AC voltage excitation $V(t) = V_0 \cos(\omega t)$:

$$I(t) = I\left(V_0 \cos(\omega t)\right) = GV_0 \cos(\omega t) + \frac{\partial G}{\partial V}\frac{V_0^2 \cos^2(\omega t)}{2} = GV_0 \cos(\omega t) + \frac{\partial G}{\partial V}\frac{V_0^2(1-\cos(2\omega t))}{4} \tag{6.4}$$

Both responses are proportional to the power of the signal and the derivative of the conductance (I2f) with respect to voltage. Contrary to RF signal transmission, a low frequency signal undergoes no attenuation or capacitive shunt, so the effective voltage applied across the sample is accurately known. Therefore we can compare the high-frequency photocurrent response to I2f at low frequency in order to give the absolute correspondance between the photocurrent response and the effective power of the RF signal applied on the sample. As lock-in amplifiers can perform second harmonic measurement, the experimental implementation is really straitforward (Fig 6.11).

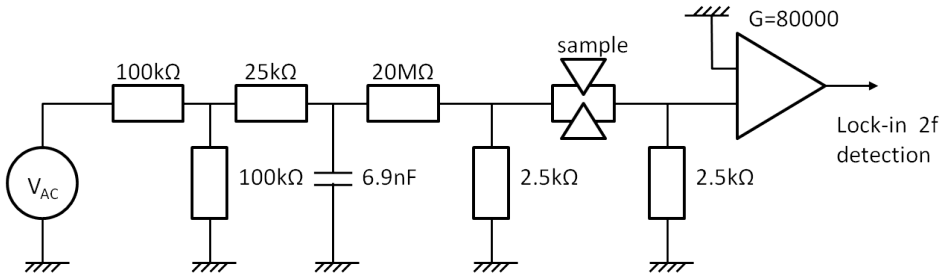

Figure 6.11: Schematics for the second harmonic measurement

When we sweep the voltage gate, the photocurrent response to a RF excitation is very similar with the second harmonic current response (I2f) to a low frequency signal (Fig. (6.12) and Fig. (6.13)). As the low frequency excitation is injected through the low frequency lines with 2.5kOhm load the voltage bias applied to the sample $V_{DS} = \frac{RZi_{pol}}{(R+2Z)}$ is transmission dependent whereas the RF lines are 50Ohm and the RF voltage bias does not change with the QPC resistance. So the signal I2f has been compensated in Fig. (6.12) and Fig. (6.13))

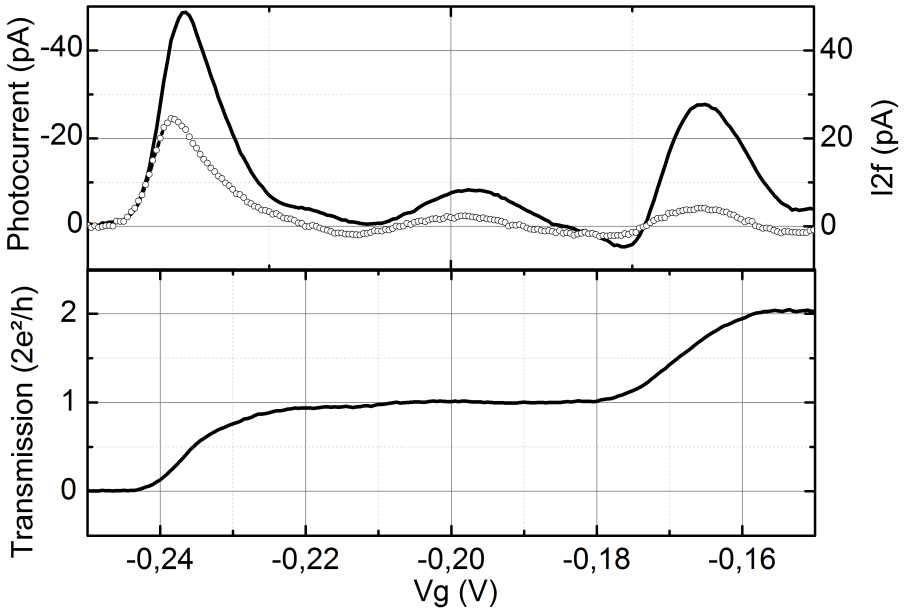

Figure 6.12: **top figure:** photocurrent response to a RF square signal at 2,5Ghz (black solid line) and second harmonic of the current I2f flowing across the sample when the alternative bias at 1kHz is applied (open-dot curve) with respect to the voltage gate. **bottom figure:** transmission of the QPC corresponding the photocurrent and I2f measurement, with respect to the voltage gate.

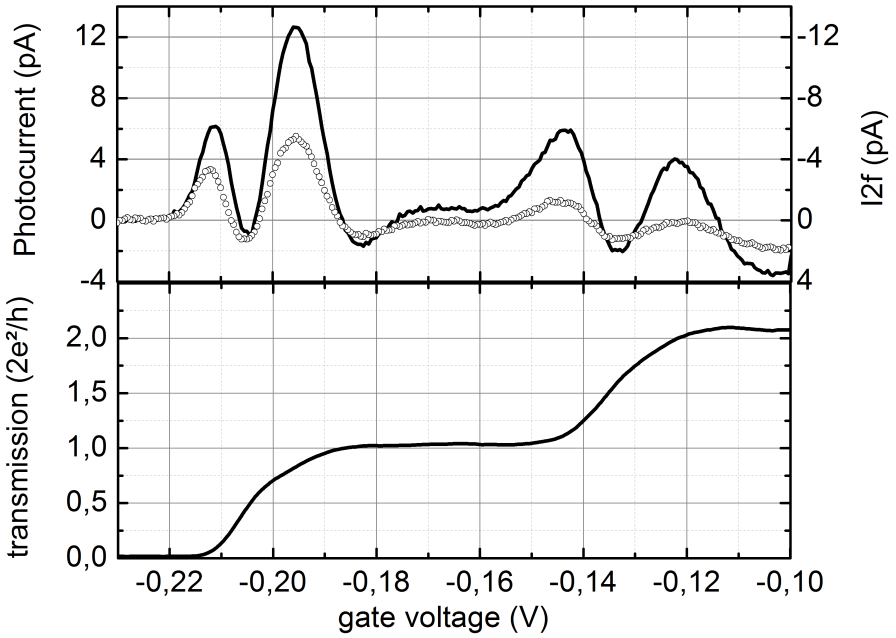

Figure 6.13: Same measures than above for the same sample after having warming up the cryostat. Contrary to the above picture, the 0.7 structure is visible on the conductance and corresponds to a suppression of the photocurrent and I2f.

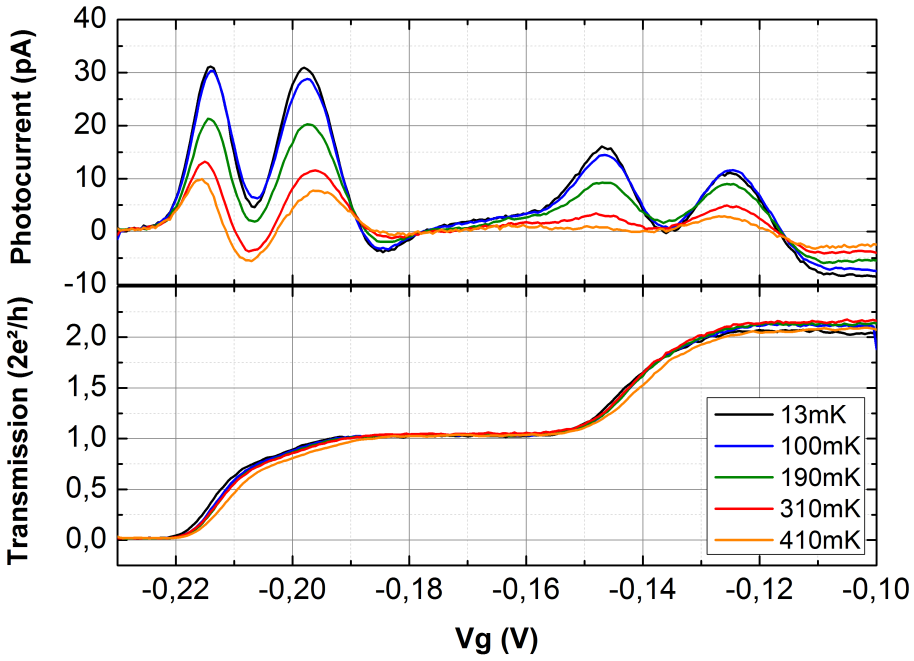

Figure 6.14: photocurrent response and QPC transmission at several temperature. The 0.7 structure stays visible as the temperature increases in constrast with a resonance on the second plateau

to take in account the variation of V_{DS}. Then the proportionnality between the two signals is striking.

During the run when the data of the first figure were collected, the QPC presented no strong 0.7 structure, and $\partial G/\partial V_{ds}$ has a single bell shape on the first plateau. The data reported on the second figure (6.13) have been obtained after subsequent warm up. The QPC configuration had changed and a 0.7 structure could be observed in the QPC transmission. Then a the double frequency response and the photocurrent show a double peaks feature. In fact the QPC configuration is not perfectly reproducible at each cooling down, even if the gate voltage is set at the same value during the cryostat cooling, and that the cooling from an helium free cryostat is automatic controlled. We are able to achieve reproducible features for the conductance (same pinch-off voltage, same number of plateaus), but the photocurrent feature with gate voltage are most often different from one run to another. Nevertheless, when a strong 0,7 structure is visible, such as in Fig (6.13) case, the photocurrent is suppressed around this transmission. This induces the double peaks feature of the photocurrent between the pinch-off and the first plateau. This signature of the 0.7 structure is studied in figure (6.14) at several temperatures. There is also another double peak feature between the first and the second plateaus. This second feature vanishes rapidely with temperature: this suggests that the feature could be due to a resonance of the QPC. On the contrary, the double-peak structure

is still visible at 410mK between the pinch-off and the second plateau. This is in agreement with previous works about the temperatures dependence of the 0.7 structure [31, 76], where the 0.7 structure is still visible at a few kelvins. This conforts the fact that the 0.7 structure has a high characteristic energy (a few hundreds of mK) compared to resonances [116].

Variation of the differential conductance

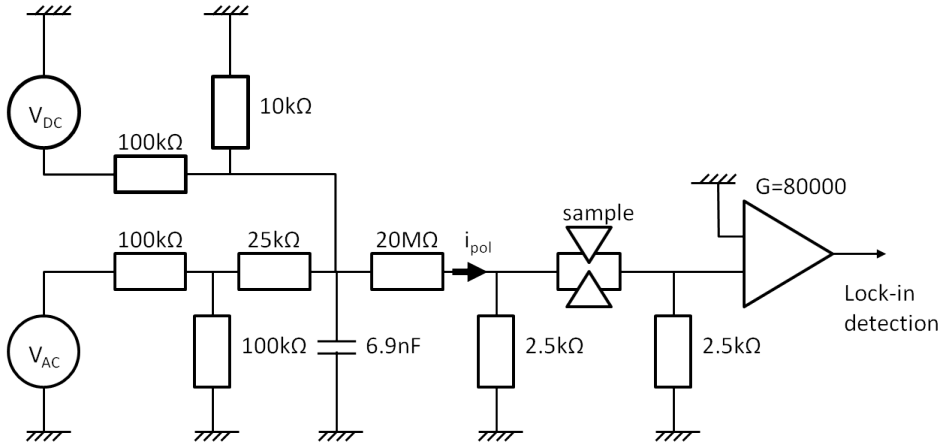

Figure 6.15: Scheme of the set-up for differential conductance measurement.

Considering again the potential saddle point model developped by Büttiker [19] and the equation (4.5), a simple way to reach $\frac{\partial D}{\partial \varepsilon}$ is to measure the variation of the QPC differential conductance when an additional DC bias is applied to a contact (Fig.(6.15)). The differential conductance measurement is performed by means of lock-in detection at 1kHz. AC voltage bias is chosen to be small (a few μV) compared to the typical range of DC bias (around 100μV).

Measurements are reported on figure (6.16) for different gate voltages. The transmission variation with V_{DC} is linear around 0. The dependence is suppressed when the transmission reaches a plateau. However for many transmission values, the variation is sublinear for V_{DC} above 50μV. This is in agreement with the sublinear variation of the photocurrent response to power in figure (6.8). Consequently to extract the first order of dependence of the conductance with respect to the DC bias voltage, we fit each curve by a four order polynomial and show the results on figure (6.17). From the derivative $\partial D/\partial V_{sample}$ we also derive two other derivatives: $\partial D/\partial V_{QPC}$ which is the derivative of the transmission with respect to the voltage bias applied on the QPC region (V_{sample} is the total voltage bias applied on the sample, i.e. on the QPC and the contacts), and $\partial G/\partial V_{sample}$, which is the derivative of the total conductance of the sample with respect to the voltage bias. The derivative takes the shape of a bell curve between plateaus, as expected from the model of Büttiker [19]. Here the measurements

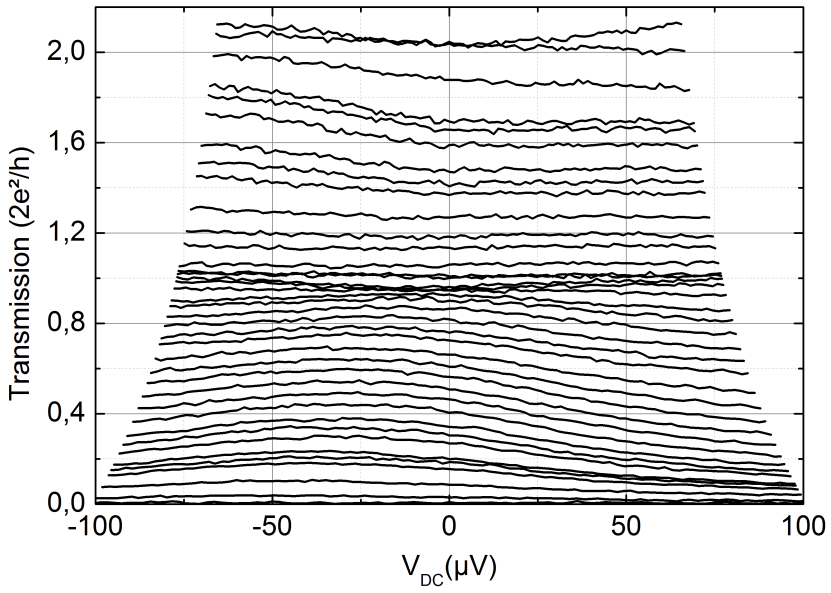

Figure 6.16: Variation of the QPC transmission with the DC voltage bias. Each solid line corresponds to a fixed gate voltage V_g when V_{DC} is swept.

correspond to those of figure (6.12), where no 0.7 structure was visible.

Figure (6.18) shows the conductance derivative $\partial G/\partial V_{sample}$ computed from the differential conductance dependence with the DC voltage bias and the I2f response of figure (6.12). $\partial G/\partial V_{sample}$ was extract from I2f response using equation (6.4) and taking in account the rectification of the voltage injection due to the QPC resistance variation. The photocurrent is plotted on a picoampere scale. It is almost proportionnal the other two measurements. Note that the photocurrent is in fact proportionnal to $\partial G/\partial V_{sample}$, and not $\partial D/\partial V_{QPC}$, as it would be expected from equation (6.3). It is also the same for the second harmonic measurement. This suggests that the contact resistance present also non-linearities that add to the QPC energy dependence resistance.

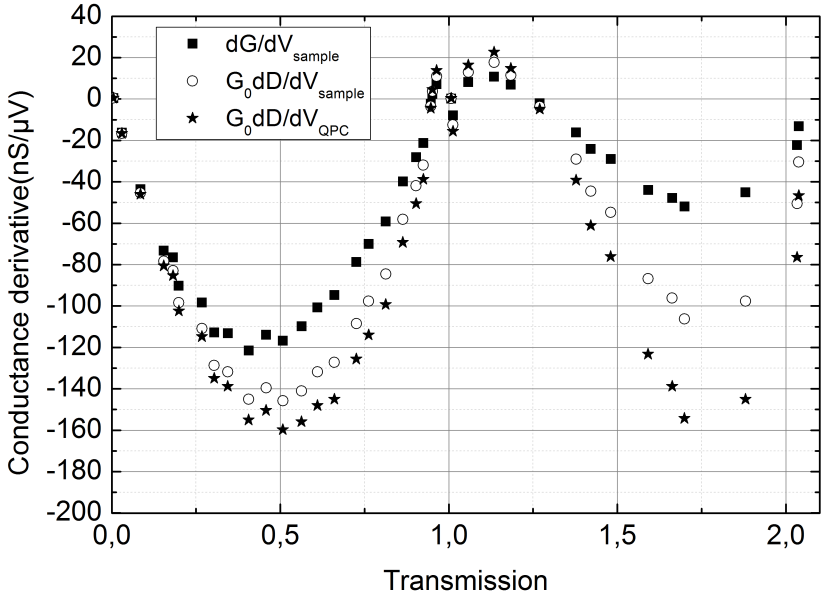

Figure 6.17: Several derivative extracted from the differential conductance measurement: (square) $\partial G/\partial V_{sample}$ (open dots) $\partial D/\partial V_{sample}$,(stars)$\partial D/\partial V_{QPC}$.

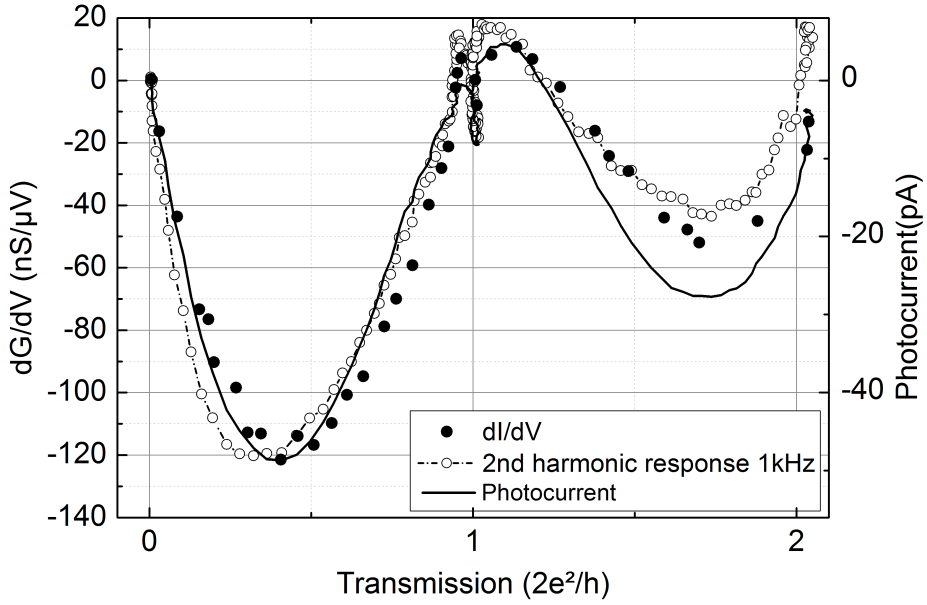

Figure 6.18: The derivative of the sample conductance with respect to the voltage bias for the QPC transmission between the pinch-off and the second plateau. The derivative is obtained by the two methods: polynomial extraction from the bias voltage dependence of the differential conductance dI/dV (black dots), second harmonic response at 1kHz (dash line and open dots). the photocurrent measurement (solid line) is proportionnal to this derivative.

6.2.5 Calibrating the RF power of the QPC using photocurrent

We divide the I2f response obtain in figure (6.13) by the effective drain-source voltage to obtain the $\frac{\partial G}{\partial V_{sample}}$ coefficient of Eq (6.4) and plot the photocurrent with respect to this value (Fig (6.19)). The proportionality is striking and the slope gives the effective RF power value. Thus the attenuation of the coaxial line A at 2.5Ghz is 71.8dB, which is comparable to the attenuator value of -70dB. The additionnal 2dB loss is compatible with the attenuation expected for the coaxial cables that are 2m long at 2.5Ghz. Combining this absolute value to the frequency dependence of the photocurrent (Figure (6.9)), we are able to compute the absolute attenuation of the two coaxial lines A and B (Fig (6.20)). Both lines show similar transmission up to 8Ghz. The transmission in the line A which is remarkably flat on the whole frequency range. Line B is more lossy above 8Ghz but is still acceptable. Note that above 18Ghz the measurement are less relevant because it the frequency exceeds the broad-band range of the mixer used for the calibration measurement.

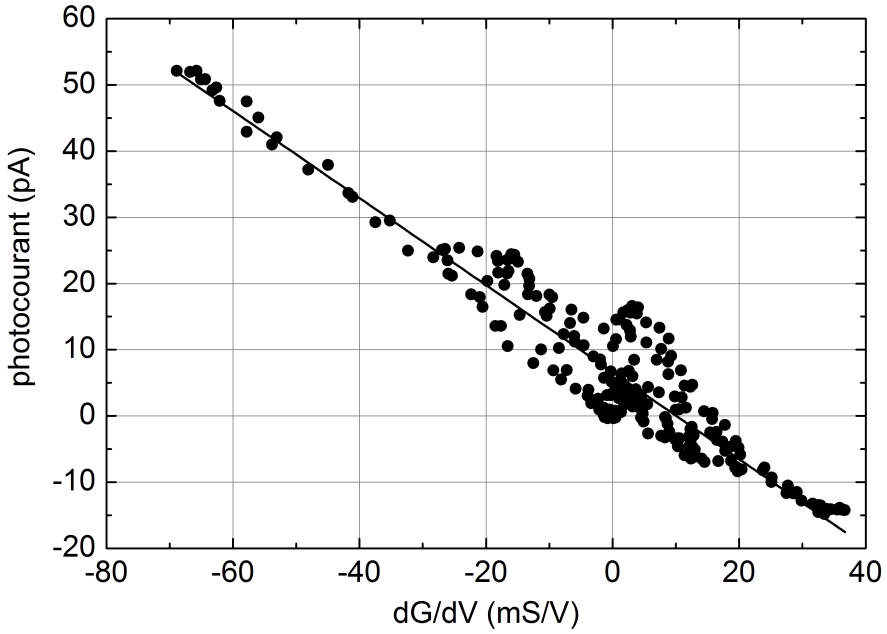

Figure 6.19: Proportionnal relation between the photocurrent and $\partial G/\partial V$ of figure(6.13). The data are plotted in black dots. The slope of the linear fit is equal to the power of the voltages applied on the sample at 2.5Ghz.

The photocurrent measurements give access to the power attenuation of the RF signal. Yet dephasing and multiple reflections may affect pulse signals. The attenuation profile of the two coaxial lines do not present strong resonances, so we can expect that the dephasing will not be a problem. However, if the phase of harmonic signal arriving on the sample could

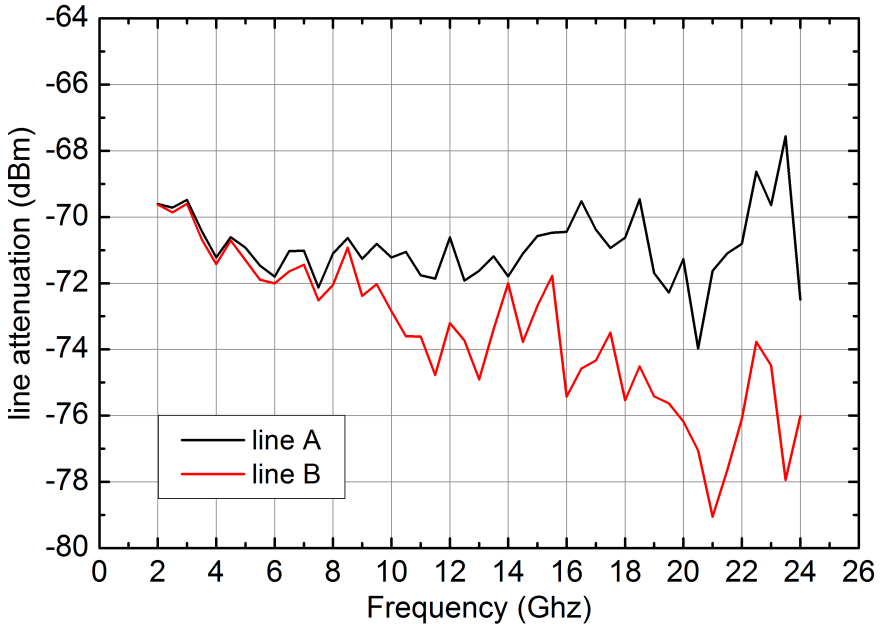

Figure 6.20: Absolute attenuation of the RF coaxial lines extracted from the photocurrent measurement

be measured, the characterization of the transmission lines would be complete. We are able to answer partially to this question by an interference photocurrent experiment, i.e. injecting two identical signals on the two coaxial lines with a variable dephasing. The output signal from the waveform generator is split by a broad band power divider. A broad band dephasor is inserted on one line in order to control the phase between both lines. Because the photocurrent is proportional to the square value of the voltage drain-source bias applied to the QPC, the response is a sinusoidal function of the phase ϕ between the voltages $V_1 = a\cos(2\pi ft + \phi)$ and $V_2 = b\cos(2\pi ft)$ that are effectively applied on each contact of the QPC:

$$\left\langle (V_1 - V_2)^2 \right\rangle = \frac{a^2 + b^2 - 2ab\cos\phi}{2} \tag{6.5}$$

Figure (6.21) show for the photocurrent response for some frequencies. The path delay δ added by the dephasor is expressed in degree per Ghz. As expected, the photocurrent shows a sinusoidal shape of the same frequency than the signal when we change the path by δ. We can analyse the frequency dependence of the phase acquired by the two signals and extract the parameters a, b and the dependence of ϕ with f. a and b frequency dependence confirm the transmission spectrum of each line A and B obtained by the direct measurement in figure (6.20). ϕ frequency dependence should be purely linear if there is no perturbation in the phase of the signal due to undesirable reflections. The results are reported in Fig (6.22). the phase

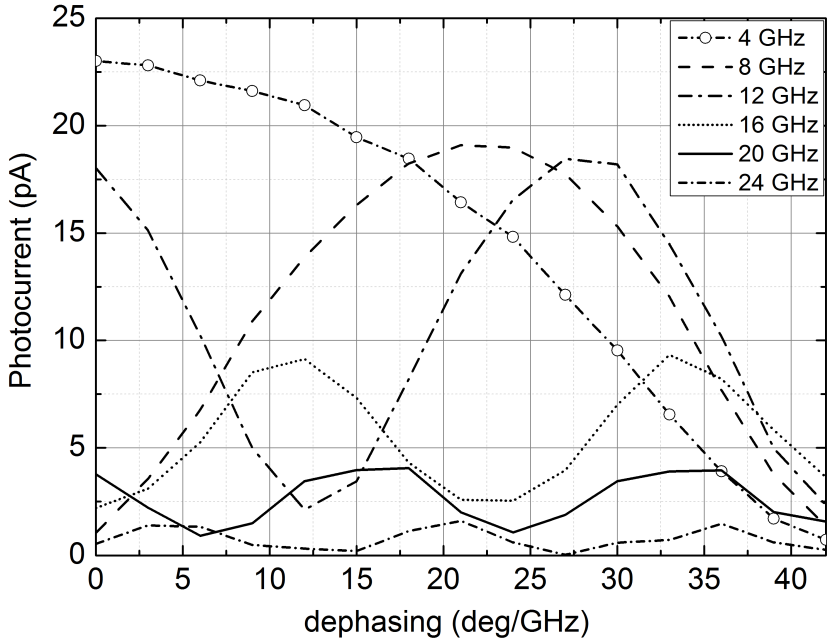

Figure 6.21: Photocurrent response to the dephasing between the harmonic signals injected in line A and B, for several sinewave frequencies. The photocurrent is a sine function of the dephasing, which frequency is proportionnal to the sine frequency. Maxima and minima of the photocurrent gives access to the attenuation of the coaxial lines.

is fairly linear, and $\phi = 2\pi 0.875 f$ when f is expressed in Ghz. The broad band dephasor introduces a nominal path of $\phi_0 = 2\pi 0.982 f$, which means that the path difference due to the set-up itself is about $0.1 c/ns = 3cm$.

6.3 Conclusion

Applying sub-nanosecond non-harmonic voltage pulses on the quantum point contact requires a specific coplanar waveguide design on the sample and the chip-carrier in order to have the best and flattest transmission of the RF lines on a large frequency broad-band (0-24Ghz). Simulations on 3D electromagnetic transient solver helps us to design the coplanar waveguides.

We have studied experimentally the photocurrent response to RF voltage pulses in the frequency range 2-24GHz. The photocurrent is due to the energy-dependent transmission of the QPC. It is proportionnal to the derivative of the transmission with respect to the energy and to the power of the applied voltage. The study of the photocurrent response to harmonic excitations gives access to the attenuation of the RF lines and indicates that there was no major resonance or reflection in the lines on the working frequency range.

As it is proportionnal to the power of the excitation, the photocurrent response differs for

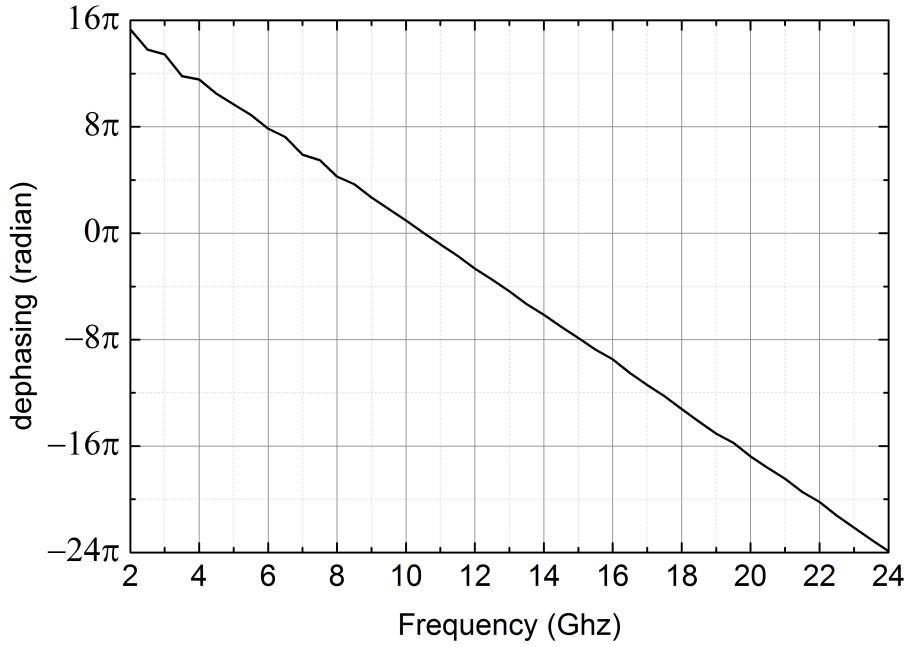

;

Figure 6.22: Phase delay between the sinewave sent on lines A and B with respect to the frequency, introduced by the path difference between the two lines.

different voltage pulses of the same amplitude. It gives additionnal information to the results of shotnoise produced by the voltage pulses that are described in the next chapter.

Chapter 7

Detection of Lorentzian pulses minimal excitations

According to the numerical study of chapter 3, the detection of the excess noise reveals the spurious quasi-particles produced by the RF pulses. This gives a proper signature of the waveform really applied on the QPC and information on the injection of charge through the quantum wire.

Prior to this study, it is necessary to characterize the exact electronic temperature in the QPC when voltage pulses are applied This enables to make quantitative comparison between experiments and theory. Indeed, dissipation increases the electronic temperature aboce the base electronic temperature (110mK) obtained by the DC shotnoise measurement. On the conductance plateaus only Johnson-Nyquist noise remains and this gives a quantitative estimation of the dissipation induced by RF pulses (section 7.1).

It is interesting to study a generalization of RF pulse injection by dissociating the DC part from the AC part of the voltage bias. This leads to a kind of spectroscopy of the excited states created by the AC pulses (section 7.2). Consequently we were able to characterize different voltages pulses applied on the QPC by this method 7.2.2, and compare the excited states induced by sinewaves, squarewaves and Lorentzian pulses. The data show excellent agreement with the theoretical values of S_I0 at finite temperature, which confirms the validity of Levitov and Lesovik theory [86] in a QPC.

Although the electronic temperature is too high to be able to detect the oscillation features of the excess noise N_+ with the transferred charge per pulse q, the data obtained on these three different waveforms confirm that N_+ is very small in the case of Lorentzian pulses, even for non-integer values, whereas N_+ increases logarithmically with q for squarewaves. The data obtained for a sinewave at 16GHz show the saturation of N_+ and are in excellent quantitative agreement with the theoretical values (section 7.3).

7.1 Estimation of the real electronic temperature due to the dissipation of the RF pulses

7.1.1 Quantitative characterization of the Joule heating due to RF pulses

At very low temperature, the electronic temperature can be dramatically increased by the Joule dissipation when a bias voltage of a few tens of microvolts is applied. This is enhanced by the fact that hot electron relaxation through electron-phonon scattering gets weaker as the temperature is reduced, so that only electron diffusion cooling occurs. There are several works having addressed electron cooling in 2DEGs. We refer to Mittal et al [100], who have studied heating effects for different 2DEG mobility. They showed experimentally that the electron-phonon cooling rate varies like T^5 at subKelvin temperature, as predicted by Price's theory [114]:

$$P_{e-ph} \approx 3.3 \times 10^6 n^{-0.5} A \left(T_e^5 - T_{ph}^5\right) \tag{7.1}$$

where n is the electron density of the 2DEG and A the surface of the device. They used in the above formula numerical factors that are specific for a single-subband AlGaAs/GaAs heterojunction. On the other hand, heat is also evacuated towards the leads by the conducting electron of the 2DEG (electron diffusion cooling). The heat flow P_{e-diff} carried by the electrons that diffuse in the lead is given by the Wiedemann-Franz formula [5], which relates the thermal conductivity to the electrical conductivity σ via the Wiedmann-Franz constant $\mathcal{L}$:

$$P_{e-diff} = -\sigma \mathcal{L} T \nabla T \tag{7.2}$$

$$\mathcal{L} = \frac{\pi^2 k_B^2}{3e^2} = 24.4 nW.\Omega.K^{-2}$$

When this flux is dominant compared to the electron-phonon cooling (eq. 7.1), the temperature mapping in the 2DEG can be estimated by the integration of the heat flux over the mesa. It leads to an analogous equation of the electronic resistance I(V), but for the heat flow $P_{e-diff}(T^2)$ and the square of temperature, where R is the total resistance of the mesa:

$$P_{e-diff} = \mathcal{L} \frac{T_{QPC}^2 - T_{contact}^2}{R} \tag{7.3}$$

For a sample of $n = 10^{11} cm^{-2}$, $\mu = 1.24 \times 10^5 cm^2/Vs$ and a number of square of 20, Mittal et al. determined that electron cooling through phonon emission dominates the Wiedemann-Franz heat flow through electron diffusion for temperatures typically above 100mK. For our sample, which has a higher mobility $\mu = 2 \times 10^6 cm^2/Vs$ and less squares (about five), the

total resistance of the 2D leads is about 150 Ohms (chapter 4). Then the Price equation (7.1) and the electron cooling flow estimation (7.3) indicate that the Wiedemann-Franz regime is valid for temperatures up to 300mK.

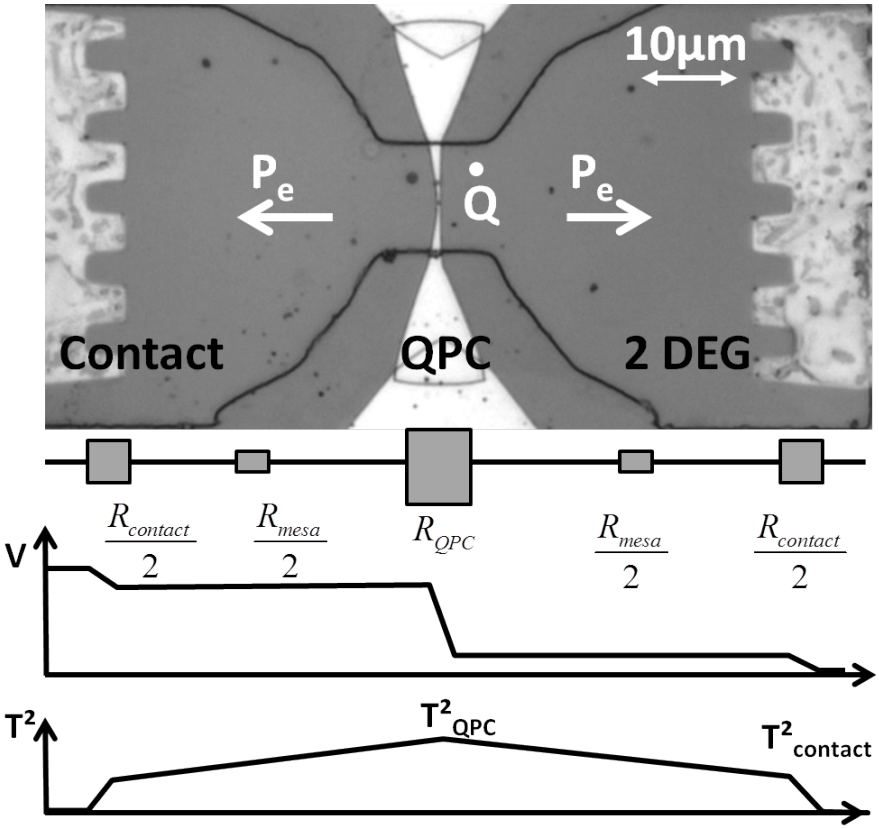

Figure 7.1: Temperature variation in the mesa due to the Joule dissipation at the QPC and in the contacts.

To quantify the increase of temperature with voltage amplitude we can compare the measured values with a theoretical estimation where the heat is only evacuated by hot electrons diffusion (Wiedmann-Franz law). As the sample temperature do not exceed 300mK, electron cooling by electron-phonon interaction (eq. 7.1) can be disregarded. In consequence, in the stationnary regime, the dissipation $\dot{Q} = DG_0 \langle V_{DS} \rangle^2$ is balanced by the heat flux that flows on both sides of the QPC, $2P_{e-diff}$. The voltage drops mainly on the QPC, which has a much higher resistance (typically 12900Ω at the first plateau and 6450Ω at the second plateau) than the mesa ($R \approx 150\Omega$). But electrons are ballistic in the QPC, so the power dissipation occurs in a region of the mesa where the excited quasi-particles loose their energy by inelastic scattering (figure (7.1)). In the 2DEG reservoirs, this region is about 10μm around the QPC. So we can assume that the power dissipation only occurs in this region close to the QPC.

In the contacts, the dissipation $\rho_c I^2$ occurs homogeneously, where ρ_c is the linear resistance of the contacts and I the current flowing through the sample. Then the heat flow follows the equation:

$$\frac{dP_{e-diff}}{dx} = \rho_c I^2 = -\frac{d^2(T^2)}{2dx^2}\frac{\mathcal{L}}{\rho_c} \tag{7.4}$$

Consequently the temperature rises in the contact from the base temperature of the leads that we consider to be equal to the base electronic temperature T_{leads} to the temperature of the contact $T_{contacts}$:

$$T^2_{contacts} - T^2_{leads} = \frac{R_{contacts}}{4\mathcal{L}}\left(\frac{R_{contacts}}{2}I^2 + DG_0\left\langle V^2_{DS}\right\rangle\right) \tag{7.5}$$

In equation, $R_{contacts}$ is the resistance of the contacts in series, D is the transmission of the sample, G_0 the quantum of conductance, $\langle V^2_{DS}\rangle$ the average of the square of the applied voltage i.e. the square of rms value. Then the electronic temperature in the region of the QPC establishes at the following value [77]:

$$T^2_e = T^2_{leads} + \frac{6e^2}{\pi^2 k_B^2}\frac{R_{Contacts}DG_0}{4}\left(1 + \frac{R_{Contacts}DG_0}{2}\right)\left\langle V^2_{DS}\right\rangle \tag{7.6}$$

To inject few electrons per period at frequencies above 5GHz, voltage pulses with amplitude up to 100μV are recquired. Consequently the electron heating due to Joule effect needs to be investigated.

Heating effect can be conveniently measured through the Johnson-Nyquist noise [62, 105] on plateaus of conductance, where the shotnoise contribution is suppressed [77]. Figure (7.2) shows the experimental increase of temperature in the sample due to Joule heating under DC voltage bias, a sinewave bias and lorentzian pulses bias. data are taken on the first plateau.

The power of the RF voltage pulses are experimentally measured at the output of the generator using a quadratic detector. The extracted rms value combined with the attenuation of the RF lines (see chapter 6) allows us to compute the rms amplitude arriving on the sample. Figure (7.2) shows that the temperature increase does not depend on the voltage shape, but only on the voltage power (which is expressed by the rms amplitude). Note that this support the naive idea that the sample can be considered as a pure resistive element even at Gigahertz operating frequencies. No capacitive shunt effect is noticable in that range, as expected from the electromagnetic simulations lead in section 6.1.

Figure (7.3) shows the increase of temperature as function of the DC bias when the QPC is set at the first and second plateau of conductance (dots), and the estimation computed with the above formula (7.6), when the base electronic temperature of the sample is set to 110mK, which is in ingreement with the temperature found by the DC shotnoise measurement.

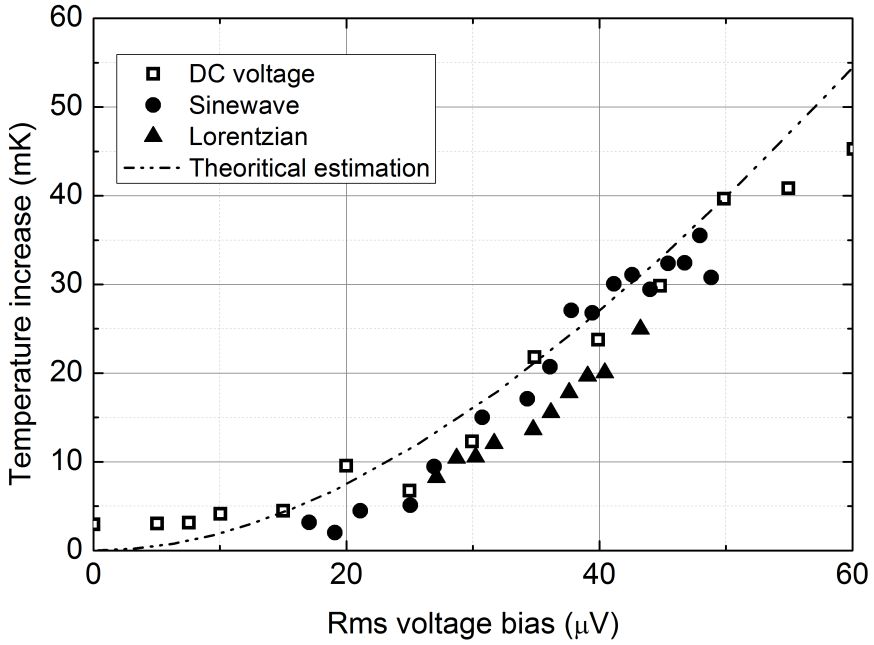

Figure 7.2: Variation of the sample temperature deduced from the Johnson-Nyquist noise as function of the amplitude of voltage bias for DC voltage (open squares), and as function of the rms amplitude of sinewave (dots) and Lorentzian periodic pulses (triangles).

7.1.2 Taking the heating effect into account in the theoretical estimation of the excess noise

From equation (7.6), the temperature variation can be estimated for any kind of RF pulses applied to the contacts and inserted in the theoretical estimation of the shotnoise. The rather low transmission used in theses experiments (D=0.35) limits the Joule effects to few dozen of mK even for a voltage of a hundred of microvolts.

The excess noise measurement implies to substract the noise measured when only the DC part of the voltage is applied to the sample (OFF measurement), to the noise detected when both DC and AC parts of the voltage are applied (ON measurement). The increase of temperature differs from ON and OFF situation. So the temperature is computed separatly for the ON and OFF measurement, then inserted in the noise formula (7.7) to obtain the theoretical noise when both DC and AC voltage are applied, or when only the DC part is applied. Finally the two values are substracted to obtain the theoretical estimation of the excess noise and compare it to the experimental data.

$$S_I(0) = 4\frac{e^2D^2}{h}k_BT_e + 2\frac{e^2}{h}D(1-D)\sum_{n\in\mathbb{Z}}|P_{AC}(n)|^2h(q+n)\nu\coth\left(\frac{h(q+n)\nu}{2k_BT_e}\right) \qquad (7.7)$$

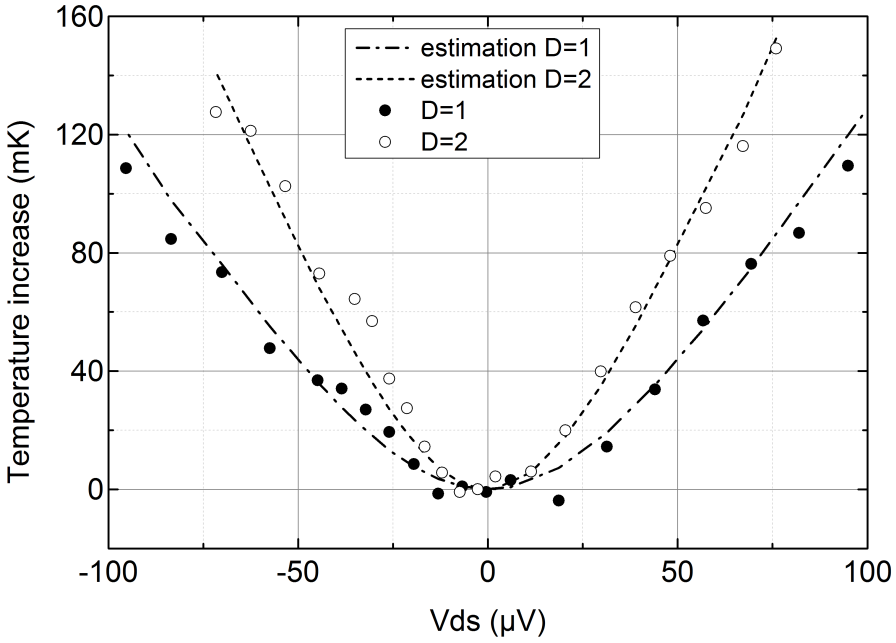

Figure 7.3: Variation of the QPC temperature deduced from the Johnson-Nyquist noise as function of the DC bias, at the first plateau (filled dots) and the second plateau (open dots). The theoretical estimation from equation (7.6) are plotted in dashed and dotted lines, assuming a base electronic temperature T=110mK, as the only adjustable parameter

7.2 Excess noise measurement as a signature of the pulse shape

7.2.1 The excess noise spectroscopy protocol

Periodic voltage can be decomposed in $V_{DC} + V_{AC}(t)$. The transferred charge per pulse $q = eV_{DC}/h\nu$ is set by the continuous part. The fourier transform P^* of $exp(i\varphi(t))$ is equal to the the fourier transform P^*_{AC} associated to the alternative part of the voltage, shifted by $eV_{DC}/\hbar$ (see section 3.2). Moreover $P(\varepsilon)$, $\varepsilon > 0$, (resp. $P(\varepsilon)$, $\varepsilon < 0$) is responsible for the excitation of electrons above the Fermi sea (resp. holes below the Fermi sea). Consequently the shift of the spectrum P_{AC} ensures that the average numbers of emitted electrons and holes satisfy $\langle N_e \rangle - \langle N_h \rangle = q$.

When V_{DC} changes, not only the difference between emitted electrons and holes change, but also the total number of emitted particles. The figure (7.4) (a and b) sketchs the relation between $\langle N_e + N_h \rangle$ and P. As the spectrum P is shifted to the positive part (resp. to the negative part) by the addition of a positive V_{DC} (resp. negative), more electrons and less holes are produced (resp. less electrons and more holes), respecting the charge balance. Then, due

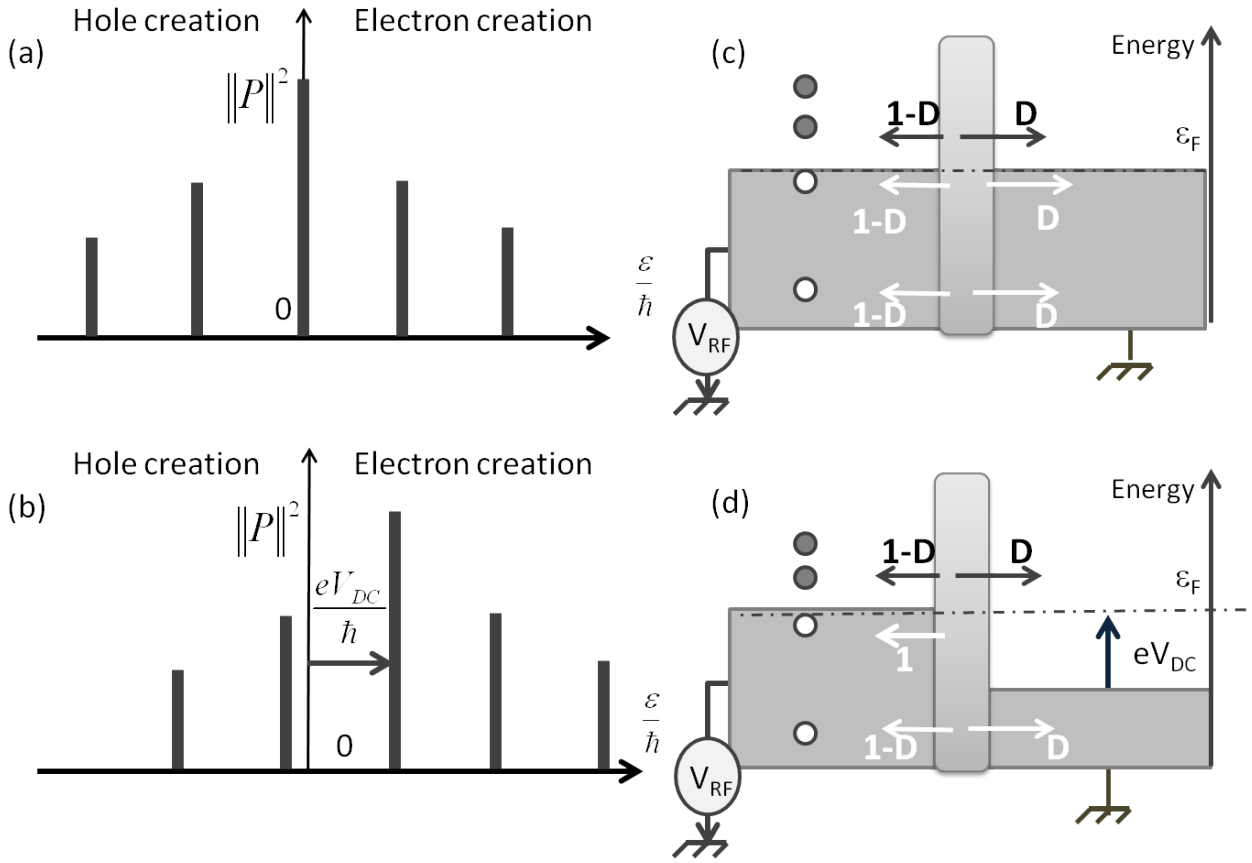

Figure 7.4: The electrons and holes creation is governed by the positive and negative distribution of the spectrum $|P|^2$, that is discrete in the case of a periodic voltage. (a) and (c): When $V_{DC} = 0$, $P = P_{AC}$, any excitation due to the alternative part of the voltage can be transferred through the barrier and N_+ is maximum. (b) and (d): When $V_{DC} \neq 0$, P is equal to P_{AC} translated by $eV_{DC}/\hbar$, N_+ is reduced, which can be physically interpretated by the fact that some excitations produced by the alternative part of the voltage antibunch at the barrier.

to the strong convergence of P at infinity, N_h (resp N_e) decrease to zero when V_{DC} gets to $\pm\infty$ while $\langle N_e + N_h \rangle / |q|$ tends to 1. This can be intuitively understood by the fact that the larger the DC part is compared to the AC part in V(t), the more V(t) looks like a continuous voltage and emits quasi-particles like a DC voltage. Because the spectrum P_{AC} is shifted in energy when q is modified, the excess number of excited particles $N_+ = \langle N_e \rangle + \langle N_h \rangle - |q|$ gives an indirect access to the magnitude of P_{AC}, and gives information on the spectroscopy of the photon-assisted excitations and measuring their population. Indeed the second derivative of $\langle N_h \rangle$ with respect to V_{DC}:

$$\frac{\partial^2 N_+}{\partial (eV_{DC})^2}(eV_{DC}) = 2 \sum_{n \in \mathbb{Z}} |P_{AC}(-n)|^2 \, \delta(eV_{DC} - nh\nu) - \delta(eV_{DC}) \tag{7.8}$$

A physical way to understand the evolution of N_+ with respect to V_{DC} is sketched in figure 7.4). When no $V_{DC} = 0$, all excitations contribute to shotnoise when $D < 1$ (figure (7.4) c). On the contrary, when the right reservoir is biased (figure d), the excitations that have energy between E_F and $E_F + eV_{DC}$ anti-bunch with the holes or electrons of the right reservoir (depending on the sign of V_{DC}) and their contribution to the shotnoise vanishes.

This noise spectroscopy method can be related to the theoretical proposals of Moskalets and Büttiker [103] and Grenier et al. [51] about the spectroscopy and tomography of the excited states produced by a mesoscopic capacitor source. Their protocols consist in a Hanbury Brown Twiss like experiment [56]: the electron flow coming from a mesoscopic capacitor source is sent on a QPC that acts like a beam splitter. A DC or AC voltage is applied on another arm of the beam splitter, and the induced excitations collide with the electron flow. Then the spectral power of the current noise gives access to information about the excited states.

We apply the above considerations to the case of periodic sine, square and lorentzian pulses. Contrary to the computation of section (3.7) and those of Vanevic et al. [142], where the amplitude of V_{AC} was scaled with q, here the V_{AC} stays fixed while V_{DC} is swept at arbitrary values. $\alpha = V_{AC}/V_{AC}^1$ expresses the amplitude of the alternative voltage compared to the reference shape associated to the transfer of 1 electron per pulse. For example:

- sinus:
$$V_{AC}(t) = \alpha \frac{h\nu}{e} \sin(2\pi\nu t)$$
- square:
$$V_{AC}(t) = \alpha \frac{h\nu}{e} \quad if \quad 0 < t < \mathcal{T}/2, \quad V(t) = -\alpha \frac{h\nu}{e} \quad if \quad \mathcal{T}/2 < t < \mathcal{T}$$
- lorentzian:
$$V_{AC}(t) = \frac{\alpha h\nu}{e} \frac{\cos(2\pi\nu t) - e^{-2\pi w\nu}}{\cosh(2\pi w\nu) - \cos(2\pi\nu t)}$$

The dependence of N_+ with respect to V_{DC} presents several interesting features that makes it completly relevant for the experimental investigation of charge injection. First, P_{AC} is discrete, so N_+ presents singularities at integer values of $\frac{eV_{DC}}{h\nu}$, i.e. when exactly an integer number of charge q is emitted. Second, the measure of N_+ through excess noise measurement gives a complementary signature of the shape of the voltage effectively applied on the QPC.

For sine (fig.7.5) and square waves (fig.7.6), N_+ is symmetric with q, because P_{AC} is even. P_{AC} is even for any V_{AC} that verifies the property: $\exists t_s$, $\forall t$, $V_{AC}(t) = -V_{AC}(t + t_s)$, which is the case for sinewave and squarewave. On the other side, assymetric voltage shapes like lorentzian pulses (fig. (7.7)) present strong assymetric P_{AC} spectrum and so assymetric N_+.

The spectrum for different α are reported on the figures (7.5), (7.6) and (7.7). The excess quasi-particles produced by squarewaves are more numerous and have higher energy than the one excited by sinewaves. This corresponds to the fact that P_{AC} is more extended in energy in the case of a squarewave than in the case of a sinewave. Even more striking, N_+ is zero when $q > \alpha$ for integer Lorentzian pulses of flux α. It gives a clear evidence that Lorentzian pulses achieve a transfer of quasi-particles with a minimal excitation.

The effect of finite temperature is shown on figure (7.8) for a sine wave, and on figure (7.9) for a lorentzian train of width $w = 0.1\mathcal{T}$. The amplitude parameter α is chosen to be 1 and 2. A finite temperature flattens the signal of N_+ and smoothes the singularities. Consequently the effective excess number of quasi-particle is no longer zero for the Lorentzian pulses at $q = 1$ and $q = 2$, and increases rapidely with temperature: when $kT = 0.3h\nu$, $N_+(1)$ is nearly half the maximum of N_+. Nevertheless, the suppression of noise at $q = \alpha$ is more robust to temperature for Lorentzian pulses that inject higher number of electron per cycle (figure 7.9). This can be understood by the fact that excitations of more electrons above the Fermi sea implies a higher distribution in energy, so that these excited electrons have less probability to be in the energy region affected by temperature $E_F + kT$.

For Lorentzian, the assymetry of N_+ is also attenuated by temperature, but in a less dramatic way. In fact, the relevant temperature associated with the asymmetry is given by the pulse width, which controls the exponential decay of the P_{AC} spectrum in equation (3.44), and so the long tail of N_+ at negative voltage. The smaller is the width, the higher is the average energy of excitations above the Fermi sea, and so the higher is the energy bias eV_{DC} to suppress their emission (figure (7.4)).

7.2.2 Results on experimental spectroscopy by excess noise

Figures (7.10),(7.12) and (7.14) display the experimental data of excess noise spectroscopy obtained for a sine wave, Lorentzian pulses and a square wave. Several amplitudes α of V_{AC} are tested. Photon-assisted shotnoise induced by sinewave was already studied by Schoelkopf and Reydellet [118, 125]. This is a a very good starting point to study other pulses. In figure (7.10), the measurements use a 16Ghz sinewave produced by a harmonic generator. This

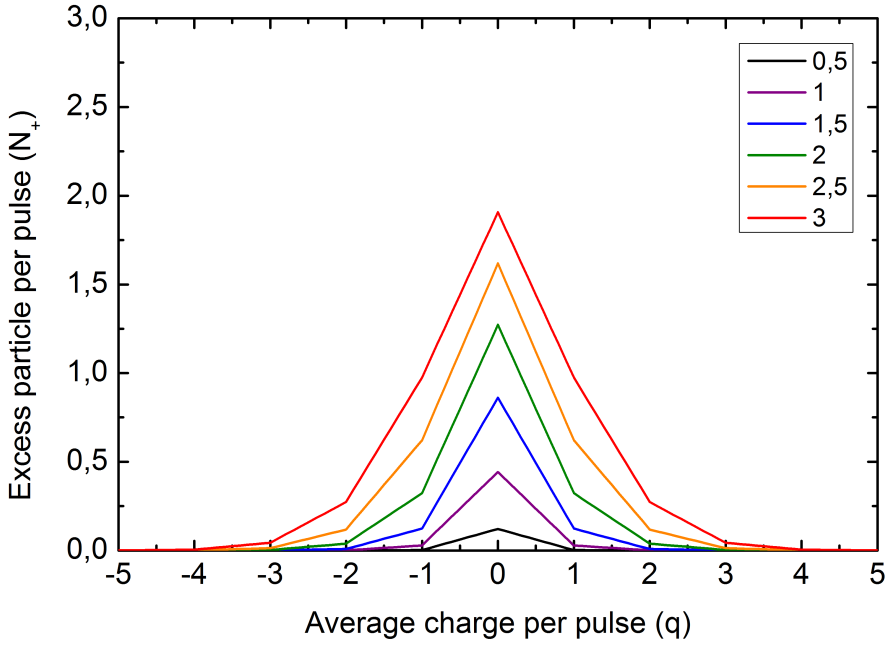

Figure 7.5: Average number of excess-particle N_+ as function of the transferred charge per pulses $q = eV_{DC}/h\nu$ for a voltage composed by a sinewave alternative part and a continuous part V_{DC}. The temperature is set zero. The different solid lines correspond to different amplitudes of the sinewave given by α.

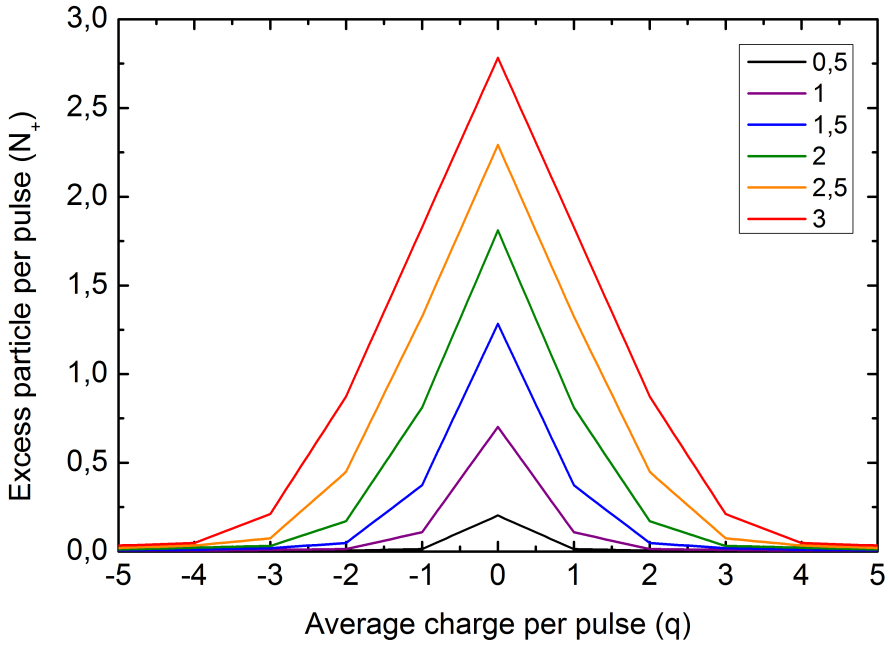

Figure 7.6: Average number of excess-particle N_+ as function of the transferred charge per pulses $q = eV_{DC}/h\nu$ for a voltage composed by a squarewave alternative part and a continuous part V_{DC}. The temperature is set to zero. The different solid lines correspond to different amplitudes of the squarewave given by α.

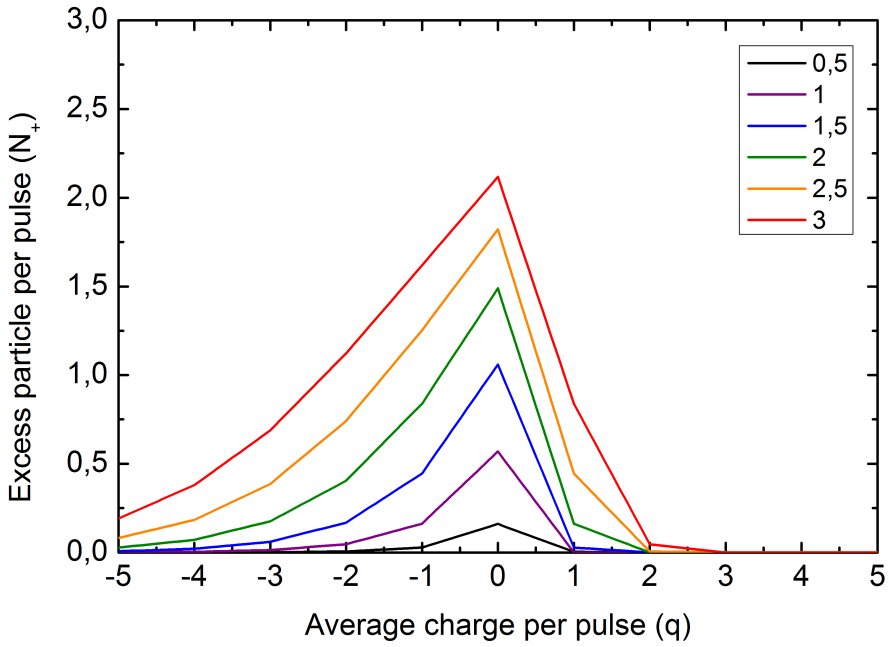

Figure 7.7: Average number of excess-particle N_+ as function of the transferred charge per pulses $q = eV_{DC}/h\nu$ for a voltage composed by the alternative part of periodic lorenztian pulses and a continuous part V_{DC}. $w/\mathcal{T} = 0.1$ The temperature is set zero. The different solid lines correspond to different amplitudes of the periodic lorenztian pulses given by α. Note that when α is an integer, the spectrum vanishes for $q > \alpha$. On the contrary, the spectrum is finite above α when α is non integer.

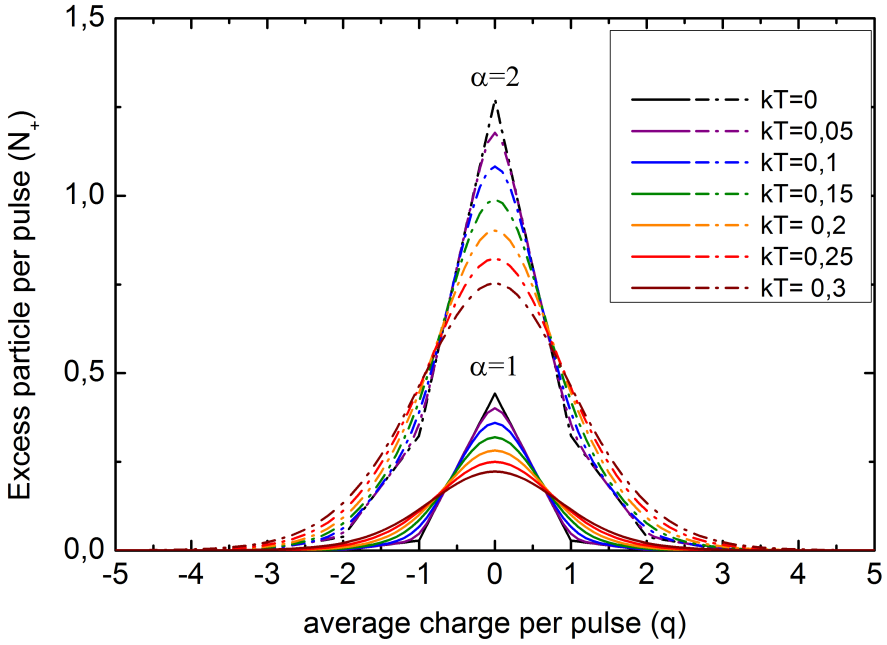

Figure 7.8: Variation of N_+ with the average transferred charge q for sinewave at finite temperature, kT is expressed in $h\nu$ units. The amplitude of the sinewave is $\alpha = 1$ (solid line), $\alpha = 2$ (dashed and dot line).

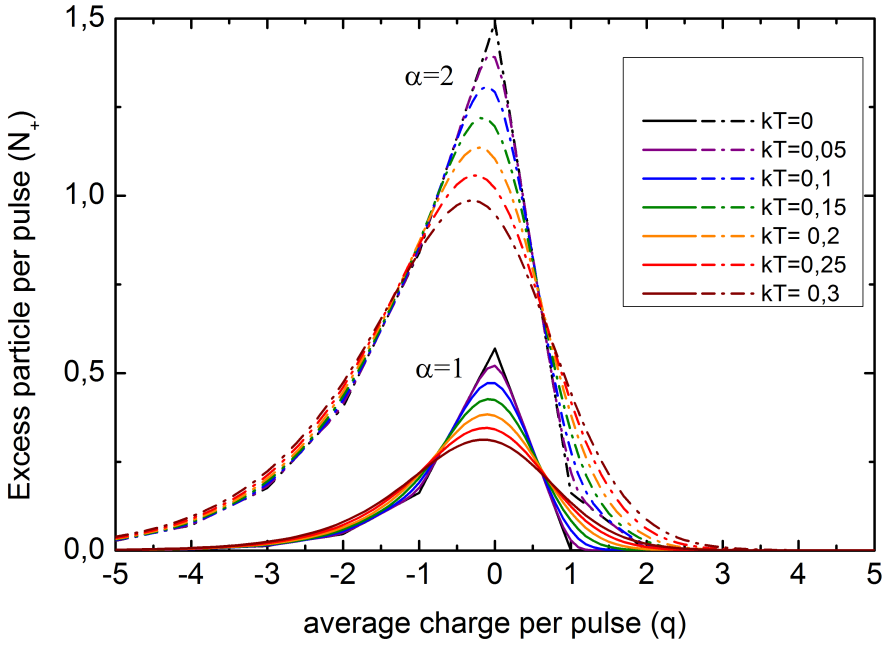

Figure 7.9: Variation of N_+ with the average transferred charge q for lorentzian pulses of width $w = 0.1\mathcal{T}$ at finite temperature, kT is expressed in $h\nu$ units. The amplitude of the alternative part of the lorentzian pulses is $\alpha = 1$ (solid line), $\alpha = 2$ (dashed and dot line).

high frequency was chosen in order to be far above the electronic temperature of 110mK ($h\nu/k_B \approx 800mK$). The symmetry of N_+ for the sinewave is clearly visible, and changes in slope can be distinguished at $q = \pm 1$.

The Lorentzian and the square waveforms are produced by the Textronik AWG 7122B. Lorentzian pulses repetition frequency is 4.8GHz and their width $w = 50ps$. This is the best parameters found including the generator frequency limitations to achieve the condition $h\nu > k_B T$ with the minimal number of points required by the generator to define a curve that looks like a Lorentzian. As expected, the curves are assymetric in the case of the Lorentzian shape. This assymetry can be observed by the difference $A(q) = N_+(-q) - N_+(q)$ on figure (7.13). Note that at T=0, the maximum of the assymetry parameter $|A(q)|$ would be at $q = \pm 1$. Here, the maximum of $|A(q)|$ is displaced towards $q = \pm 2$ because of the finite temperature, that smooths the excess noise spectrum.

The analysis is more complicated in the case of the square wave that should show a symmetric spectrum: we can distinguish a recurrent slight asymmetry in the three curves (figure (7.14)). This can be explained by the imperfection of the square signal that is effectively generated by the AWG 7122B. At frequencies above 6Ghz the AWG clearly generates a imperfect and assymetric square. That is why the frequency of the square is chosen lower (5Ghz). The signal purity is better at this frequency, although the symmetry imperfection is still noticeable in the excess noise spectrum assymetry, particularly when q is large, which corresponds to the high frequencies excitations.

7.2.3 Comparison of the theoretical value and the excess noise measurement

Theoretical fit showed on the noise figures (7.10),(7.12) and (7.14) take in account the heating effects and the estimation of the amplitude of the voltage bias from the RF calibration measurement of the attenuation of the RF lines.

For the theoretical fits of the data showed in figures (7.10), (7.12) and (7.14), we start from the electronic based temperature given by the DC shotnoise measurement $T \approx 110mK$, and the attenuation response of the set-up calibrated by the photocurrent. The RF pulses were sent through the RF line A, which has the flattest frequency response, so the pulses ware not much modified by the set-up. These parameters are known to a finite accuracy (say about 10%) and the parameters have been slightly adjusted to obtain the best fitting for the set of amplitude parameters fixed by the generator output.

For each data point, the effective temperature is computed for the ON and OFF measurements, and put in the computation of the resulting noise $S_I(ON) - S_I(OFF)$. For the three data set, the base temperature of 120mK gives the best fit, except the highest amplitude of

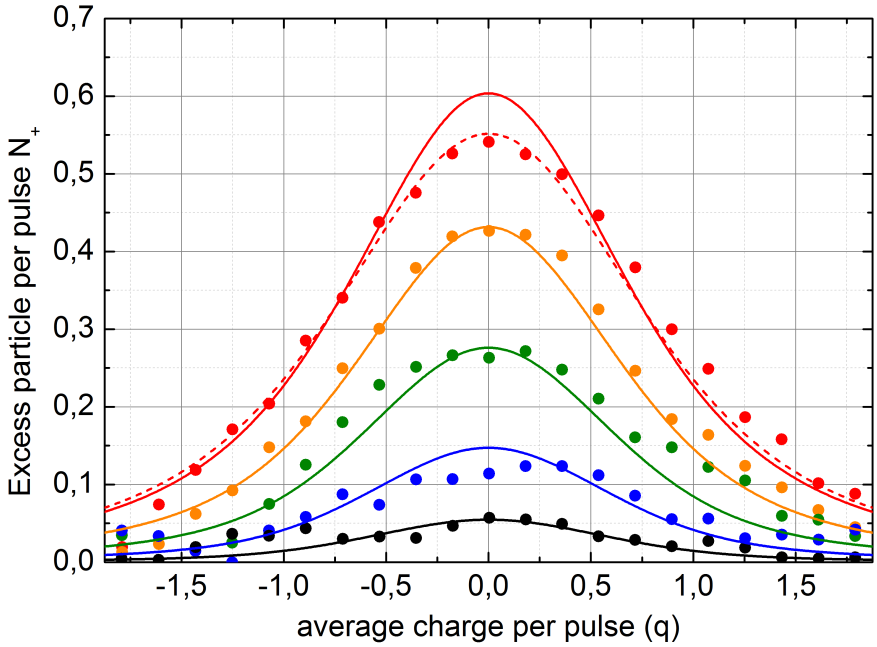

Figure 7.10: Excess noise spectroscopy for sinus pulses of $\nu = 16$GHz. Data (dots) for several voltage amplitude fitted (thick lines) by α=[0.38,0.63,0.88,1.13,1.38] at base temperature T=120mK. Thermal effects are computed through the Wiedemann-Franz law. dash-line: fit of the last curve with parameter α=1.38 and base temperature T=150mK, that is in better agreement with the fit at 120mK.

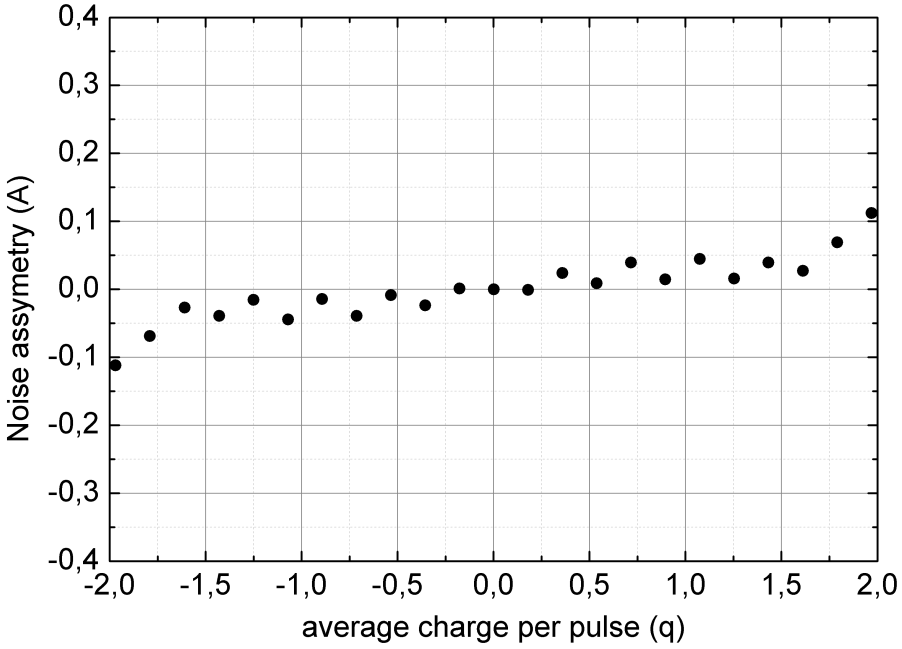

Figure 7.11: Assymetry of the excess noise $A(q) = N_+(-q) - N_+(q)$ in the spectroscopy measurement (7.10) for the alternative part of the sinepulses $\alpha = 1.38$

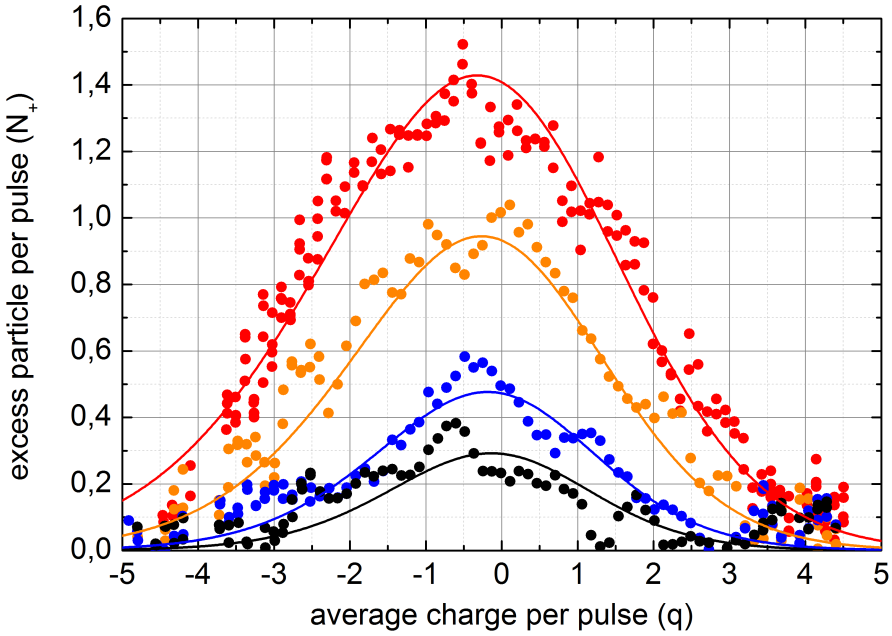

Figure 7.12: Excess noise spectroscopy for Lorentzian pulses of $\nu = 4.8$GHz and $w = 50$ps. Data (dots) for several α fitted (thick lines) by α=[2.4,3.2,4.8,6.4] and the base temperature T=120mK.

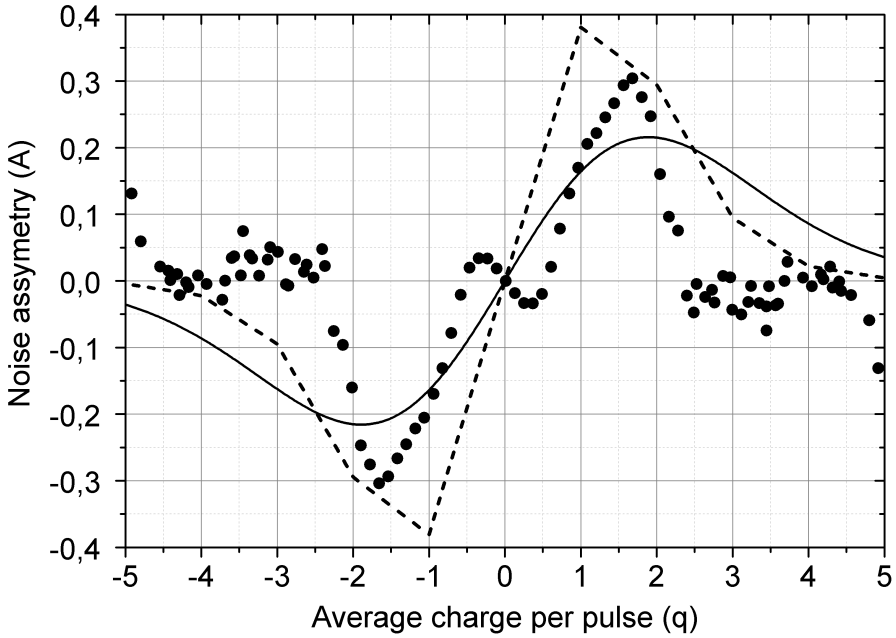

Figure 7.13: Dots: Assymetry of the excess noise $A(q) = N_+(-q) - N_+(q)$ in the spectroscopy measurement (7.12) for the alternative part of the Lorentzian pulse $\alpha = 4.8$. Solid line: Assymetry of the theoretical fit with finite temperature. Dashed line: Assymetry of the excess noise at T=0.

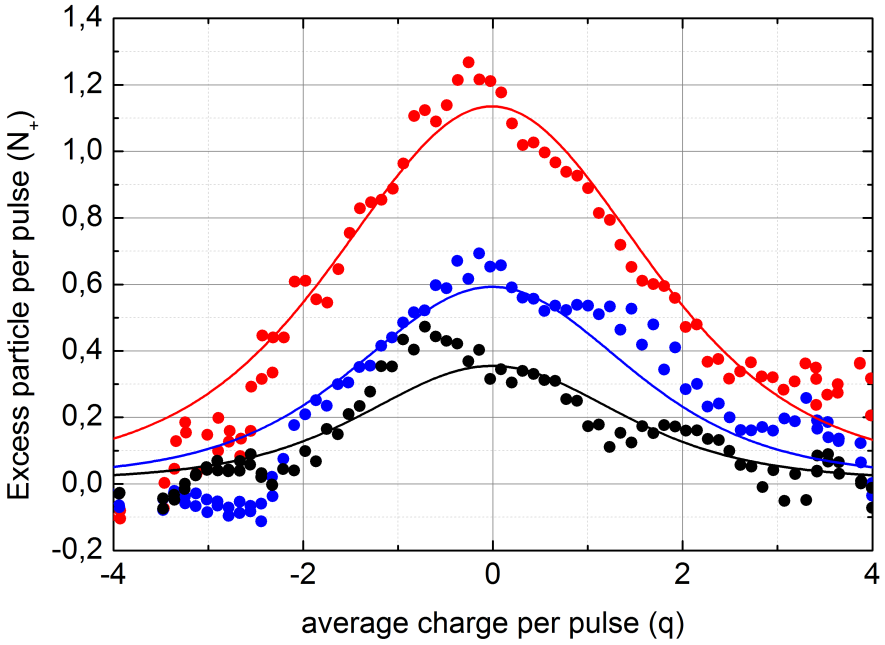

Figure 7.14: Excess noise spectroscopy for square pulses of $\nu = 5$GHz. Data (dots) for several voltage amplitude fitted (thick lines) by α=[1.3,1.8,2.62] at base temperature T=120mK.

sine pulse. For this curve, an effective base temperature of 150mK gives better fit, which indicates some extra heating in the circuit or some external voltage noise acting.

With a only a small adjustement on two parameters that have been estimated through independent measurement, the experimental results are in quantitative agreement with the theoretical estimations. This confirms the validity of Levitov and Lesovik's description of the quasiparticles emission processes in a ballistic quantum wire when arbitrary voltage pulses are applied.

7.3 First indication of the high purity of the Lorentzian voltage pulse source

Let's go back to the reliability question of a voltage pulse quasi-particle source. The quality of this source is given by the fluctuation of the number of quasi-particles injected per pulse, $N_e + N_h = |q| + N_+$. The smaller the average number of excess quasi-particles N_+ is, the better the voltage pulse injection approachs the minimal excitation case and so the smaller are the fluctuations of $N_e + N_h$. At finite temperature, the effective number of particle N_+ given by the excess noise replaces the proper notion of N_+ at T=0 and quantifies the extra

excitations injected in the circuit.

The sinewave used in all measurements has a frequency of 16GHz for the following reason. As predicted by the numerical computation in chapter 3, the oscillating variation of the excess excited quasi-particles N_+ with the transferred charge q is completely washed out when temperature excesses $0.2h\nu$. With a sample rate of up to 24 giga-samples per second, the arbitrary waveform generator from Tektronics can inject well defined periodic Lorentzian pulses with a maximum frequency rate of about 5Ghz.

As the effective electronic temperature of the sample found is 110mK, the oscillatory variation of N_+ with q is completly smoothed for accessible Lorentzian pulses. However, the RF synthetizer can inject sinewave of higher frequencies. This is why we have choosen to measure N_+ dependence with q using sine pulses $q\frac{h\nu}{e}(\sin(2\pi\nu t)+1)$ at 16Ghz. For this frequency, $kT/h\nu = 0.12$, and the local minima of N_+ should be visible. The measure is reported on figure (7.15). Unfortunately, oscillations are still not visible on this curve because of Joule effects that increase the electronic temperature. Yet, this temperature increase can be estimated for each voltage amplitude by the method described in the previous section: starting from the base electronic temperature of 120mK when the amplitude of the voltage pulses are close to zero, the effective temperature of the sample rises to about 200mK for $q = 2$ (fig. 7.15). These values are reported in the theoretical estimation of N_+ for each value of the transferred charge q (dash line): the theoretical fit is in good agreement for small values of q, but it tends to too high values when $q > 1.5$. On the other side, a theoretical estimation with a constant electronic temperature of 200mK matches better the data, especially their tendency to converge towards a value around 0.15. This means that there must be another heating effect in the circuit at high voltage amplitudes, as we have already mentioned for the excess noise spectroscopy using sinewave (figure (7.10)).

The excess noise produced by sine pulses, square pulses and Lorentzian pulses correspond to data in the excess spectroscopy measurements for which $\alpha = q$. Theses points are reported in figure (7.16), as well as the data for sinepulses of figure (7.15). Lorentzian and square pulses used for the measurement have close repetition frequencies and so close temperature ratio $k_BT/h\nu$. They give an interesting comparison. Even at finite temperature and non integer value of transferred charge, the Lorentzian voltage pulse source show a small excess number of particles (less than 0.05 particle per pulse). This gives **a voltage pulse source with a 98% purity**. In comparison N_+ increases clearly with q for a squarewave, and is already equal to 0.2 for $q \approx 1$ (20% of purity). The excess noise is still 10% compared to the DC shotnoise at $q = 3$, which show the slow convergence of the square pulses injection towards the classical limit ($N_+ \ll q$). Thus the squarewave is clearly not a suitable shape for voltage pulse source, contrary to Lorentzian pulses. As for the sinepulse, the excess noise increases for $q < 1$ and then stays roughly around a value of 0.15.

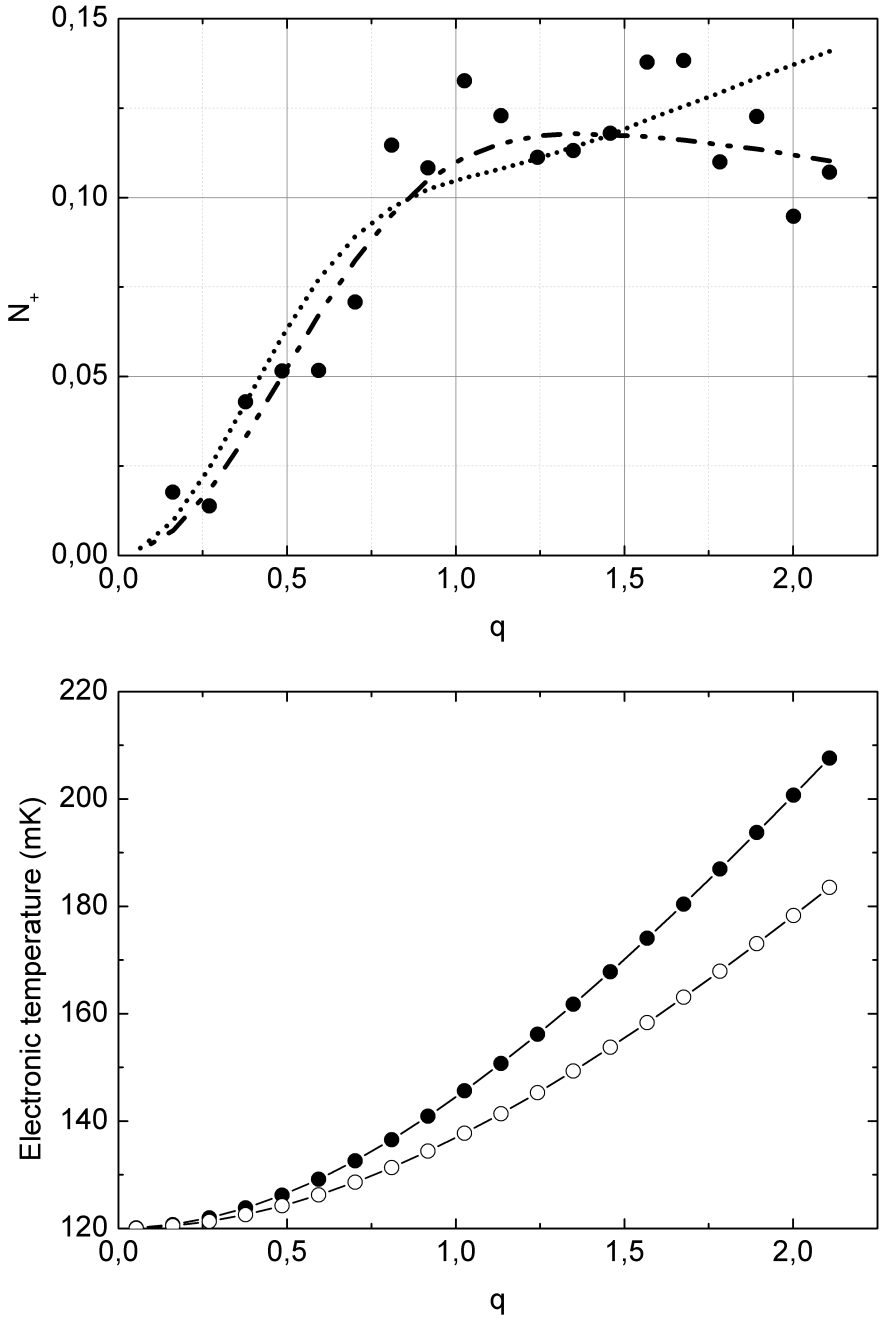

Figure 7.15: **Top:** Black dots: Measurement of excess noise N_+ for sine pulses: $q\frac{h\nu}{e}(\sin(2\pi\nu t)+1)$. Dash-dotted line: theoretical value of N_+ for an electronic temperature of 200mK. Dotted line: theoretical fit of N_+, taking in account the Joule heating, starting from a electronic temperature of 120mK when no voltage is applied. **Bottom:** Estimation of the electronic temperature due to Joule heating. filled dots: when the sinepulses are applied (ON measurement) open dots: when only the average value $V_{DC} = qh\nu/e$ is applied.

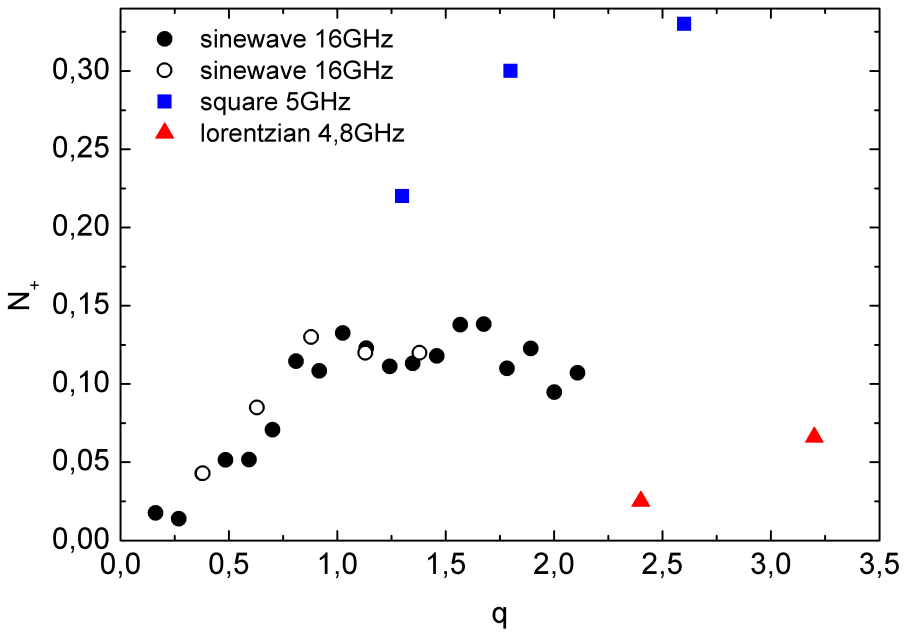

Figure 7.16: Excess number of particles from the excess noise spectroscopy data when $\alpha = q$. open dot: sinewave, blue squares: squarewave, red triangles: lorentzians. filled dots: excess noise measurement for a for sine pulses: $q\frac{h\nu}{e}(\sin(2\pi\nu t) + 1)$ at 16Ghz.

7.4 Conclusion

We investigate the excess particle number created for the injection of q charges with voltage pulses of different shape (sinewave, squarewave and Lorentzian). Excess noise spectroscopy gives us access to photon absorption and emission energy distribution for each pulses, and enlight the particularities of Lorentzian voltage pulses. Even at finite temperature and non integer value of transferred charge, the Lorentzian voltage pulse source show a small excess number of particles (less than 0.05 particle per pulse). In comparison, sinewave injects a surplus of 0.1 quasi-particles when $q > 1$, and the N_+ increases logarithmically with q for a squarewave.

Experimental results have been compared to theoretical estimations and are in quantitative agreement without adjustable parameters. This confirms the validity of Levitov and Lesovik's description of the quasiparticles emission processes in a ballistic quantum wire when arbitrary voltage pulses are applied.

Chapter 8

Additionnal discussion on the experimental results

In the previous chapter, excess noise measurements are found in quantitative agreement with the generalized photon-assited shotnoise theory of Levitov and Lesovik [86], and they have shown that a minimum of excitations is found for the Lorentzian voltage pulse electron source. Here we discuss further how the experimental results discard alternative interpretations and in which measure they are free or extra artefacts. First, the experimental results are compared to a possible false positive noise induced by the transmission energy-dependence of the QPC (section 8.1). Second, the generalized photon-assisted shotnoise theory is confronted to the quasi-static shotnoise regime approximation (section 8.2). The dynamic character of the quasi-particle emission is put into evidence by the experimental excess noise of the voltage pulse source.

The experimental data are also related to recent measurements on biharmonic pulses done by Gabelli and Reulet [44] in section 8.3.

Finally, a Hong-Ou-Mandel [58]like experiment is performed by applying identical pulses on both contacts with a controlled time delay. This enables to study the time extension of the quasi-particle packet produced by a voltage pulse (section 8.4).

8.1 Contributions due to transmission energy-dependence in the noise

The effect of the transmission energy-dependence on the DC shotnoise have been studied in several works [21, 38]. At the first order, $\partial D/\partial\varepsilon$ induces an assymetric term with respect to the DC bias. Small compared to the first term of DC shotnoise, it can nevertheless be of comparable to the excess noise N_+ when RF pulses are applied. Consequently the contribution of the photocurrent could be an experimental false positive. We need to estimate this contribution to check that our data actually correspond to N_+ and not to the contributions

due to the transmission nonlinearities.

Taking into account the energy dependence of the transmission in the current-current correlator $B(t,t',x)$ and developping to the first order of $\partial D/\partial\varepsilon$, the contribution due to transmission non-linearities δS_I to the noise can be recovered for any arbitrary periodic voltage $V(t)$ at T=0:

$$\delta S_I = 2e\frac{e^2}{h}(1-2D(E_F))\frac{\partial D}{\partial \varepsilon}\sum_{-\infty}^{\infty}|P_{AC}(n)|^2\frac{(q+n)^3(h\nu)^2}{2|q+n|} \tag{8.1}$$

Figure (8.1) shows the contribution δS_I in the excess noise spectroscopy measurement, for sinewave, squarewave and lorentzian pulses of $w = 0.1\mathcal{T}$. δS_I is the difference between δS_I when V(t) is applied on the QPC and δS_I when only V_{DC} is applied on the QPC. It is expressed in reduced units

$$\delta N_+ = \delta S_I/(2e\frac{e^2}{h}(1-2D(E_F))(h\nu)^2\frac{\partial D}{\partial \varepsilon}$$

δN_+ is uneven for sinewave and squarewave, whereas it is assymetric for Lorentzian pulses. It tends to a finite value $N_+(\infty)$ at high average number of charge per pulse, and $\lim_{q=-\infty}\delta N_+ = -\lim_{q=\infty}\delta N_+ = -\delta N_+(\infty)$. $\delta N_+(\infty)$ depends on the shape and amplitude of V_{AC} (fig. 8.2). It increases like the square of the amplitude of V_{AC}.

The contribution δS_I corresponds to the shotnoise of an equivalent number of particle N_{eq} per pulse:

$$N_{eq} = \frac{1-2D}{2(1-D)}(h\nu)\frac{\partial D}{\partial \varepsilon}\delta N_+$$

When no feedback is applied on the gate, the QPC conductance dependence can reach $100nS/\mu V$ in figure (6.17). The measurements have been done at a transmission D=0.3. Then in the excess noise spectroscopy measurements using Lorentzian and squarewave et 5Ghz, $N_{eq} < 0.04$, and in the measurements using a sinewave at 16GHz, $N_{eq} < 0.03$. Consequently, this contribution is much smaller than the excess noise N_+ produced by excess quasiparticles, and can be disregarded.

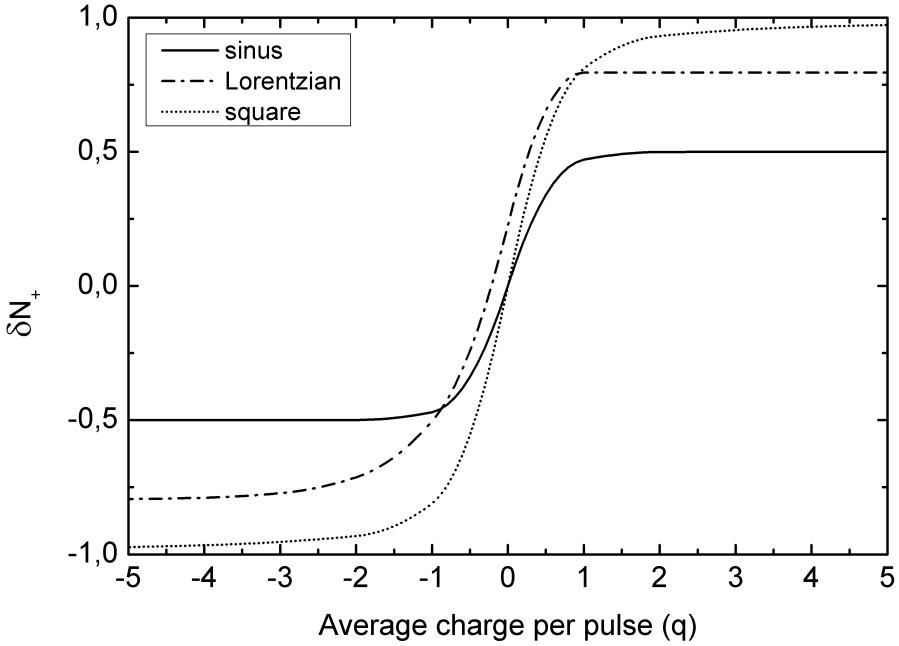

Figure 8.1: Added contribution δN_+ in the excess noise due to the energy-dependence of the transmission with respect of q, for different voltage pulses: sinewave (Solid line), Lorentzian pulses (dot-dashed line), and squarewave (dotted line). The amplitude of the alternative part $\alpha = 1$.

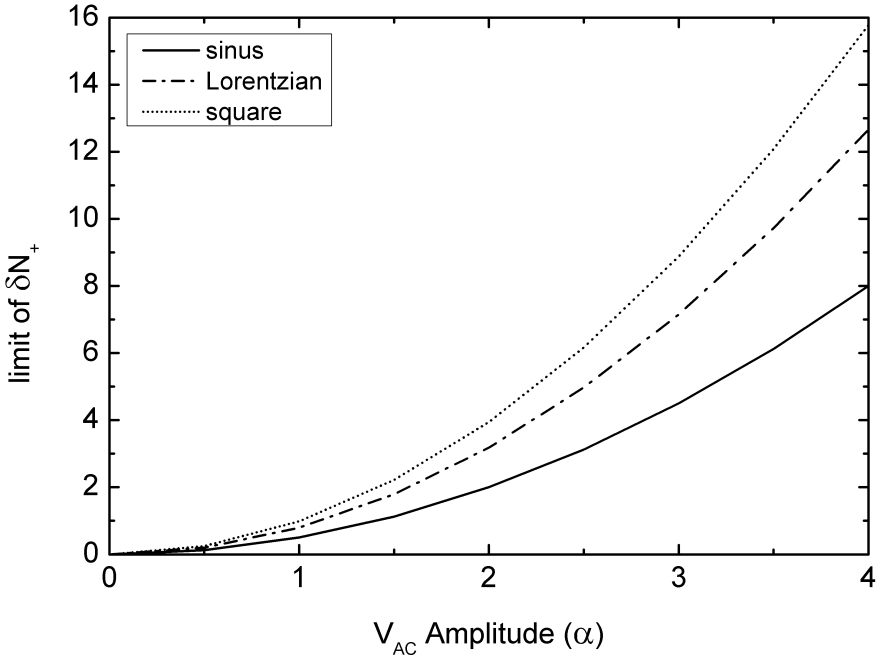

Figure 8.2: Maximum of δN_+ as function of the V_{AC} amplitude, for different voltage pulses: sinewave (Solid line), Lorentzian pulses (dot-dashed line), and squarewave (dotted line)

8.2 Are the excess noise data distinguishable from a time average of the DC shotnoise over the V(t)?

Following Reydellet et al. [118], it is necessary to discuss in which aspect the experimental measures of N_+ show new quantum features present in the photon-assisted shot noise which have no similar counterpart in the dc quantum shot noise. The photon-assisted shotnoise produced by V(t) can be compared with the effective DC shotnoise associated with a quasi-static averaging of V(t), i.e. $\langle |V| \rangle$ (quasi-static approximation of the shotnoise). We define M as this mean value expressed in unit of quasiparticles per pulse, and as $M_+ = M - q$, its difference with the average charge transferred per pulse.

$$M = \frac{1}{\mathcal{T}} \int_0^{\mathcal{T}} \frac{e|V(t)|}{h\nu} dt \tag{8.2}$$

At zero temperature, there are clear qualitative discrepancies between the expected M_+ and N_+. Figures (8.3) and (8.4) report M_+ and N_+ in a excess noise spectroscopy protocol. V(t) is composed of an arbitrary DC voltage $V_{DC} = qh\nu/e$ added to the AC part respectively of a sinewave and of Lorentzian pulses. The amplitude of the alternative part of the signal is set to $\alpha = 1$.

First, in the excess noise spectroscopy M_+ cannot present the quantum singularities at integer values of q. More importantly, M_+ is zero for any kind of voltage pulses that take only positive or negative values. In consequence, $M_+ = 0$ as soon as $V_{DC} < -max(V_{AC})$ or $V_{DC} > -min(V_{AC})$. *This is an essential difference between the photon-assisted description and the quasi-static approximation: in the quasi-static approximation, any voltage pulse source would be a perfect quasi-particle source!* Compared to the excess number of particle N_+ and its oscillating dependence of q (figure (3.4)), $M_+ = 0$ for sine, square and Lorentzian pulses, and any other kind of pulses V(t) that take only positive values.

N_+ and M_+ are quantitatively very close, especially when the amplitude of the alternative voltage α corresponds to more than one electron injected per pulse. They are even closer at finite temperature (fig. 8.5). First the singularities of N_+ are smoothed. Second M_+ is now also an effective number corresponding to the excess noise in the quasi-static approximation :

$$M_+ = \frac{1}{\mathcal{T}} \int_0^{\mathcal{T}} \frac{eV(t)}{h\nu} coth\left(\frac{eV(t)}{2k_BT}\right) dt - qcoth\left(\frac{qh\nu}{2k_BT}\right) \tag{8.3}$$

However, the values computed for M_+ can not explain the excess noise produced by the sinepulses in figure (7.15). Figure (8.6) compares the expected values of M_+ corresponding to sinepulses $q\frac{h\nu}{e}(\sin(2\pi\nu t) + 1)$ at 16Ghz, and the measurements. The heating effects have

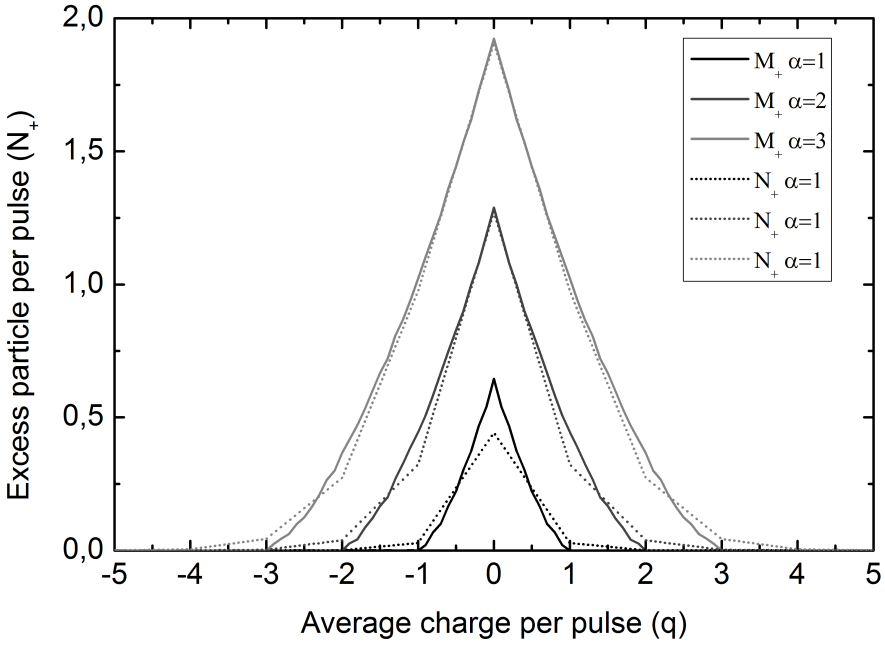

Figure 8.3: Numerical computation of the excess noise obtained in a adiabatic approximation M_+ and in the photon-assisted frame N_+, as function of the transferred charge per pulses $q = eV_{DC}/h\nu$ for a voltage composed by a sine wave alternative part and a continuous part V_{DC}. The temperature is set to zero.

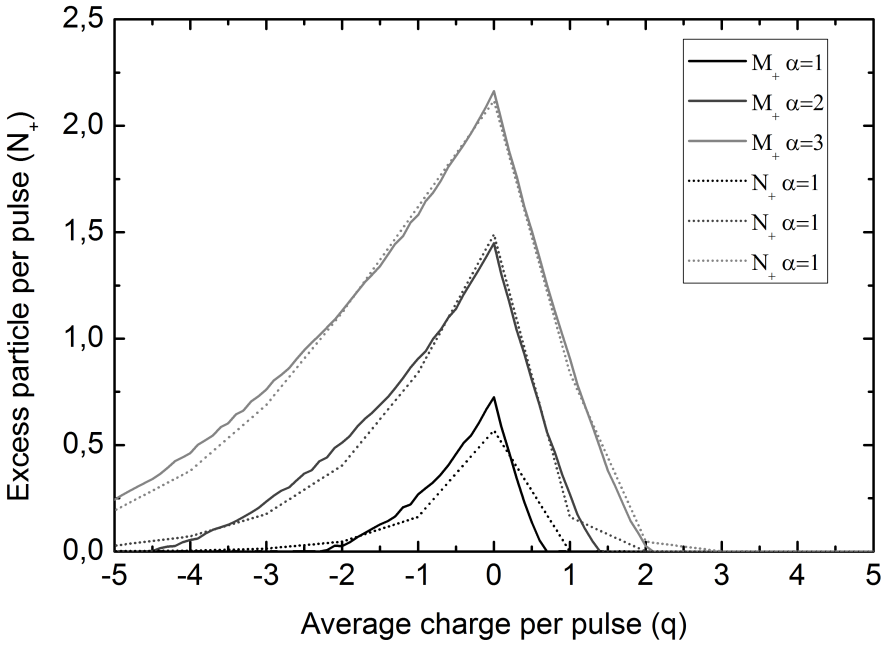

Figure 8.4: Numerical computation of the excess noise obtained in a adiabatic approximation M_+ and in the photon-assisted frame N_+, as function of the transferred charge per pulses $q = eV_{DC}/h\nu$ for a voltage composed by lorentzian alternative part of $w = 0.1\mathcal{T}$ and a continuous part V_{DC}. The temperature is set to zero.

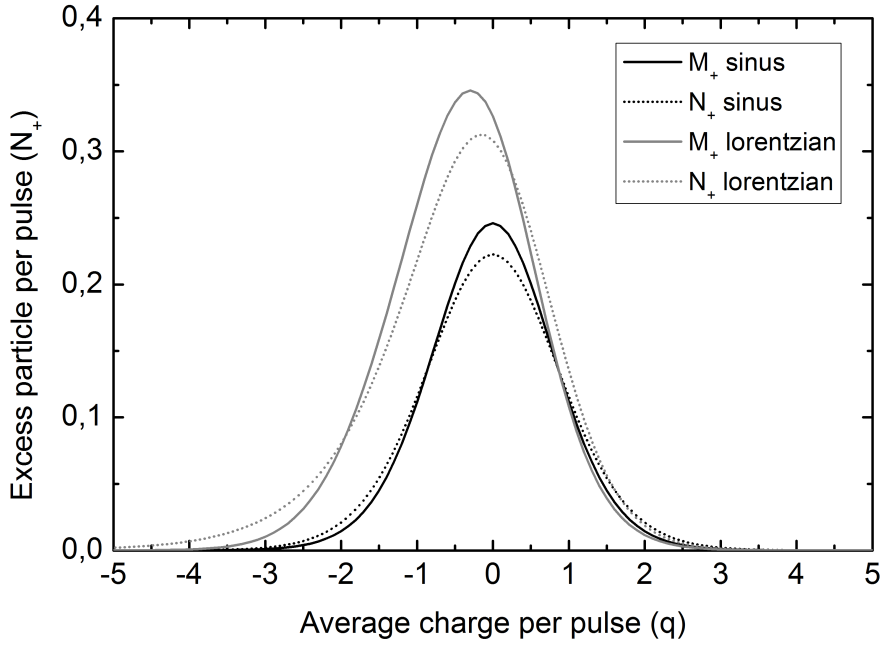

Figure 8.5: Numerical computation of the excess noise obtained in a adiabatic approximation M_+ and in the photon-assisted frame N_+, as function of the transferred charge per pulses $q = eV_{DC}/h\nu$ for a voltage composed by lorentzian alternative part of $w = 0.1\mathcal{T}$ and a continuous part V_{DC}. The temperature is set to $kT = 0.3h\nu$. $\alpha = 1$.

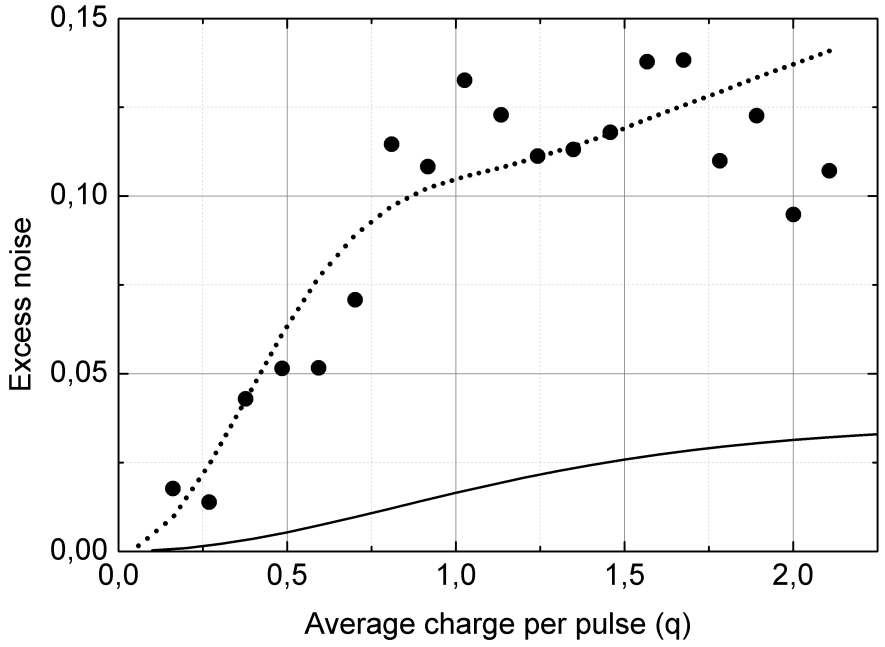

Figure 8.6: Filled dot: Excess noise measurement produced by sinepulses at 16GHZ with respect to the average charge per pulse q. Dotted line: Theoretical estimation of N_+ in the photon-assited description. Solid Line: Numerical computation of the excess noise M_+ in the quasi-static approximation

been taken in account in the same method than the computation of N_+ for theoretical fit, starting from a electronic temperature of 120mK. The amplitude of M_+ is much smaller than the excess noise.

So the excess quasiparticles produced by the sine pulses can not be explained by the effective DC shotnoise associated with the averaging over a quasi-static voltage $V(t)$. This enlights how the RF voltage pulse source physics can be only described in the frame of photon-assisted shotnoise, and underlines that the injection of quasi-particles by RF pulses is not trivial.

8.3 Comparison with a related experiment

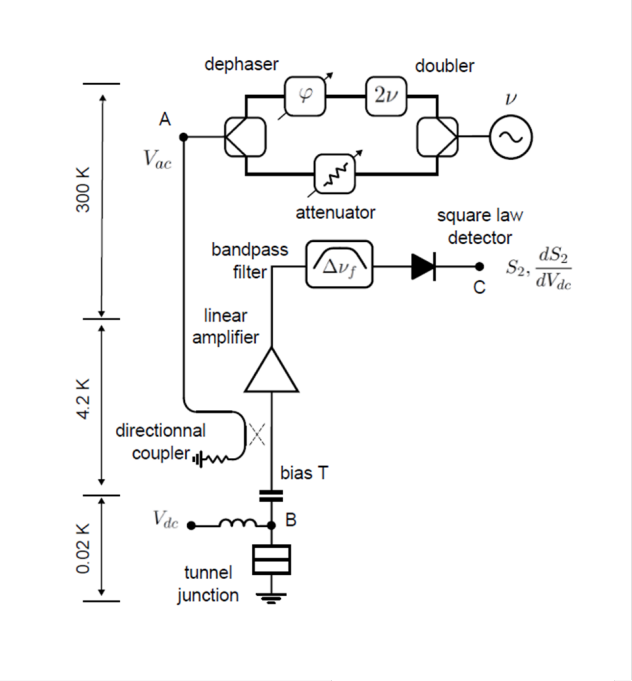

Figure 8.7: Experimental set-up in preprint [44]. To generate the bi-harmonic signal, the out-put of the sinewave generator is split into to arms. In the upper arm, a frequency doubler followed by a dephasor produce the second harmonic component. The second harmonic power is far smaller that the first harmonic input due to the frequency doubler response, so in the lower arm, the amplitude of the first harmonic is adjusted tuned by an attenuator. Both signals are recombined and sent on the sample through a directionnal coupler. The DC component is added by means of a bias T. Low frequency noise is measured on the range 0.5-1.8Ghz by low noise cryogenic amplifiers.

A very recent preprint [44] reports an attempt to compare the spectroscopy of the noise

produced by non-harmonic excitations to a sinewave. A tunnel junction is used instead of a quantum point contact. Contrary to a quantum point contact, numerous channels pass through the tunnel junction with a very small transmission, so that the overall impedance of the tunnel junction is far smaller than the QPC one (about 50Ω). As a consequence, the fano factor is fixed to one, contrary to the QPC fano factor $(1-D)$, but basically the photon-assited shot-noise physics are the same in both devices. This low impedance makes noise measurements easier in terms of sensitivity as the sample impedance matches the 50Ω detector impedance. However, the impossibility to set transmission to unity prevents the possibility to check the contributions of photon-assisted shotnoise and thermal excitation.

Their set-up is described in figure (8.7). They study the noise response to a biharmonic excitation $V(t) = V_{DC}+V_1\cos(2\pi\nu t)+V_2\cos(4\pi\nu t+\theta)$, where ν=10Ghz and $V_1 = 2V_2 = 5.4h\nu$, and θ can be tuned by a broad band dephasor from 0 to 2π. The periodic train of lorentzian pulses of width w and flux q can be decomposed in the following Fourier serie:

$$Lor(t) = \frac{qh\nu}{e}\frac{1-e^{-4\pi w\nu}}{1+e^{-4\pi w\nu}-2e^{-2\pi w\nu}\cos(2\pi\nu t)} = \sum_{n\in\mathbb{Z}^*} 2\cos(2\pi\nu nt)e^{-2\pi\nu nw}+1 \qquad (8.4)$$

So when $\theta = 0$ and $V_{DC} = V_1$ (resp. $\theta = \pi$ and $V_{DC} = -V_1$), the bi-harmonic waveform approaches the lorentzian periodic pulses $Lor(t)$ of width $w = \ln\left(\frac{V_1}{V_2}\right)\frac{\mathcal{T}}{2\pi} = 0.11\mathcal{T}$ and injecting charge per pulses $q = 5.4$.

Figure (8.8 b) present the current noise $S_{2,ac}$ response when the DC current is swept: by substracting the DC shotnoise curve (cross symbol) to the others curves, one obtains the excess noise spectroscopy. Theses measurements are performed at T=70mK, so $kT/h\nu = 0.14$. In the figure, blue and red curves correspond to the approaching lorentzian pulses of $q = \pm 5.4$. The assymetry in $S_{2,ac}$ for theses excitations, is clearly visible, and can be compared to the assymetry of the excess noise in our measurements (figure 7.12. O and π shifted curves mirror each other with regard to $V_{DC} = 0$, which confirms the flip of the spectrum P_{AC}. On the other side, the bi-harmonic with $\theta = \pi/2$ and the sinewave are symmetrical excitations and as expected, their noise spectrum $S_{2,ac}$ is symmetric with V_{DC}.

In the preprint data [44], $q = eV_{DC}/h\nu = \pm 5.4 = \alpha$ show the excess noise of the voltage-pulse quasi-particle source. The differences between the noise produced by the DC shotnoise, the approaching Lorentzian (i.e. the red curve at $q = -5.4$ and the blue curve at $q = 5.4$) and the sinewave are very small, yet the asymptotic behaviour towards the DC shotnoise of the curves suggest that the approching Lorentzian pulses produce less excess noise than the sinewave one. Note that the green signal($\theta = \pi/2$) and the other biharmonic signal (the red curve at $q = 5.4$ and the blue curve at $q = -5.4$), that completely differ from lorentzian pulses produce far more noise than the others.

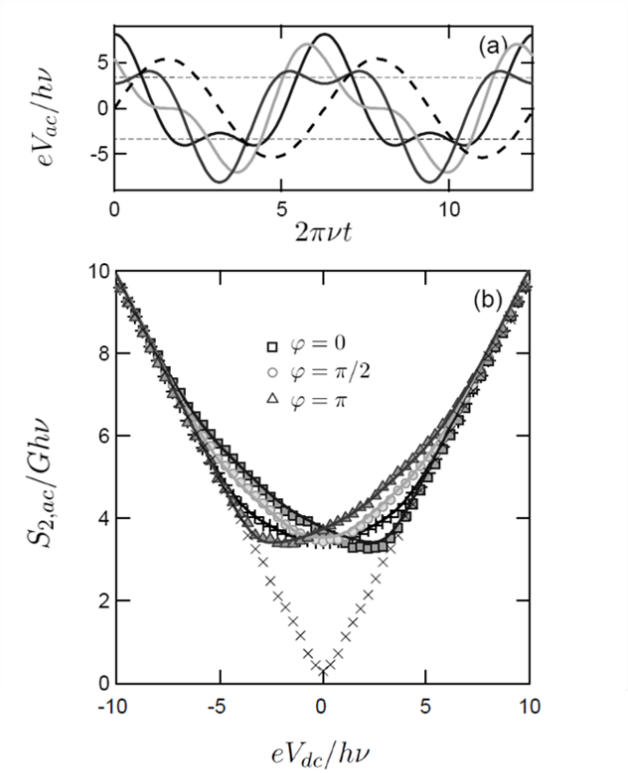

Figure 8.8: (a) Shape of the ac component of the excitation, depending on the phase shift: $\theta = 0$ (black solid line), $\theta = \pi/2$ (grey line), $\theta = \pi$ (dark grey line). Dashed line: excitation when $V_2 = 0$. (b)Normalized photon-assisted shotnoise $S_{2,ac}/Gh\nu$ as function of $eV_{DC}/h\nu$, for the different RF excitations: bi-harmonic signals with $V_1 = 2V_2 = 5.4h\nu$ and $\theta = 0$ (squares), $\theta = \pi/2$ (dots), $\theta = \pi$ (triangles); sinewave at 10Ghz $V_1 = 5.4h\nu$ (plus symbols); DC shotnoise (no RF excitations) (cross symbols). The solid lines plot the theoretical predictions.

8.4 Hong-Ou-Mandel like experiment to probe the electron wavepacket extension

An interesting question to address is the time extension of the excitations packet produced by a voltage pulse. Indeed, this time extension is of importance for future interference experiment with few electrons [55]. A way to address the question is to make excitations to collide on an electron beam-splitter, as proposed by many theoretical works [18, 47, 63, 106, 123]. This is the Fermionic analog of the Hong Ou Mandel experiment for photons [58]. Here two identical periodic voltage pulses $V_1(t)$ and $V_1(t + \theta)$ are injected on the two contacts of the QPC. A broad band phase-shifter is placed on one RF line to control the phase delay θ between the voltage pulses. Contrary to bosons that bunch when they arrive simultaneously on the beam splitter, the fermions antibunch and a suppression of the noise should be measured when the

voltage pulses are in phase (figure 8.9).

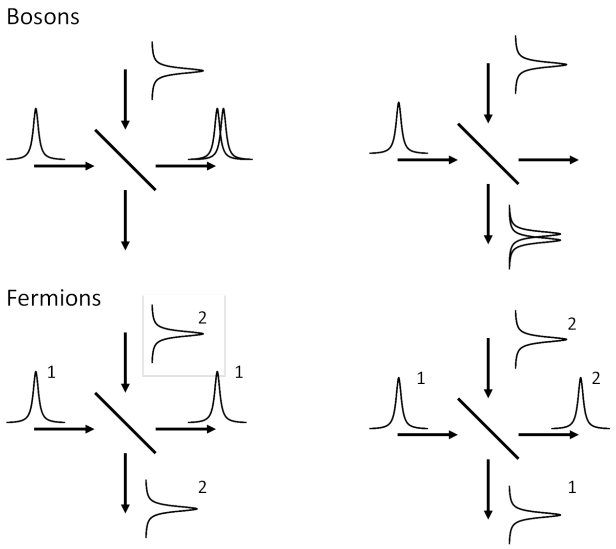

Figure 8.9: Hong-Ou-Mandel collider principle. Particles emitted from two sources are split on a beam-splitter. Bosons bunch with each other, whereas fermions antibunch.

In the case of a two terminal conductor, the HOM-like experiment can be equivalently mapped to a single emittor problem thanks to gauge transformation. Applying simultaneously the voltages $V_1(t)$ and $V_2(t)$ on respectively the left and the right contact of the quantum wire is rigourously equivalent to applying the difference $V_1(t) - V_2(t)$ on the left contact only. So the present collider experiment is equivalent to apply a variable voltage $V_1(t) - V_1(t + \theta)$, which is a superposition of a train of positive pulses and a train a negative pulses with a phase delay θ. In fact, the two quasi-particles emittors and the beam splitter are gathered on the QPC. Note that in quantum Hall Effect, the same equivalence holds even if the incoming and outgoing edge states are spatially separated.

In the collider point of vue, the delay θ modifies the overlap of the electronic wavefunction arriving from the left and the right contacts. For $\theta = 0$, there is a perfect overlap and the antibunching due to Fermi statistics gives a zero noise. In the gauge transformed description, $V_1(t) - V_1(t + \theta) = 0$ at $\theta = 0$, and no quasi-particle is emitted.

When $\theta \neq 0$, the noise gives information on the time overlap of V_1 and V_2. In the collider point of vue, the anti-bunching of the excitations decreases when $\theta \to \pi$, so the noise increases. In the single emitter point of vue, the time separation of positive and negative pulses leads to a partial emission of the quasi-particle wavepackets that would be produced by V_1 alone and V_2 alone.

Figure (8.10) show the excess noise measured in this HOM like experiment, for a sinewave and a lorentzian pulse train of width $w = 0.16\mathcal{T}$, as a function of the delay θ introduced by

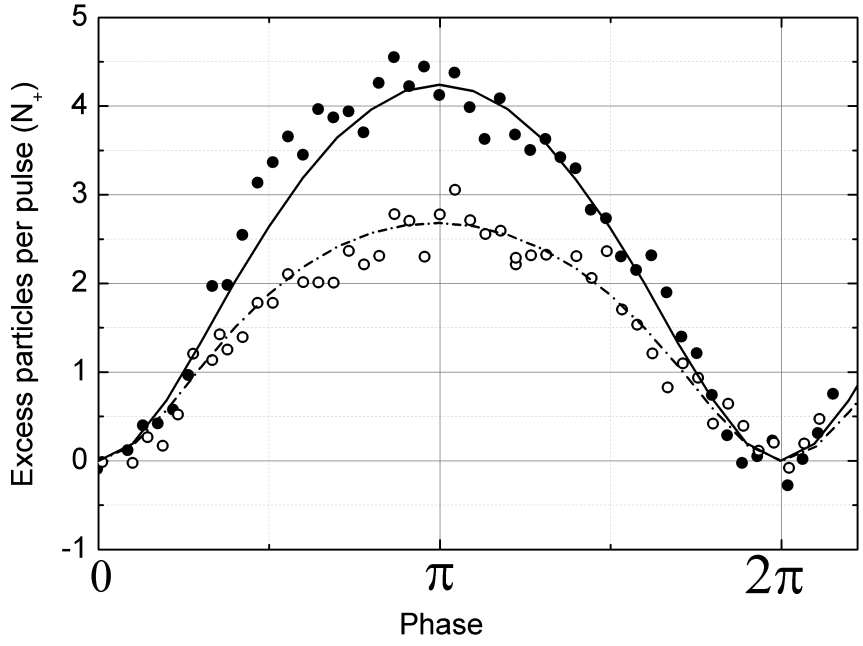

Figure 8.10: Excess noise measured as function of the phase θ between the arriving voltages $V_1(t)$ and $V_2(t)$ on contact 1 and 2 of the QPC. Filled dot: the voltage $V_1(t)$ and $V_2(t)$ are a sine wave of 2.6Ghz and $\alpha = 4.5$. Open dot $V_1(t)$ and $V_2(t)$ are a lorentzian pulse train of width $w = 0.16\mathcal{T}$ of frequency 2.6Ghz and $\alpha = 4.5$. the solid and dashed lines are the theoretical estimation of the excess noise for respectively the sine wave and the lorentzian pulses.

the phase-shifter. The repetition frequency is 2.6Ghz and the number of charge per pulse is set to $q = 4.5$. The data are in excellent agreement with theoretical fit computed with the same technique described in the previous section 7.1.

The two curves show how wavepackets interact with each other [63]. When the delay between opposite wavepackets is maximum ($\theta = \pi$), the excess noise is still reduced compared to the noise that would be produced if the wavepackets were scattered independently, i.e. to the sum of the noises that would produce $V_1(t)$ and $V_2(t)$ alone. At the estimated temperature of 130mK, this sum is equal to 9.6 particles per pulse for the Lorentzian pulses and 10 particles per pulses for the sinewave. The data show an excess noise of respectively 2.5 and 4.2 particles per pulses. In the HOM like point of vue, this means that more than half the quasi-particles are involved in antibunching processes. Equivalently in the one emitter transformation, these quasi-particles have not been emitted.

This indicates clearly that the wavepackets injected by the Lorentzian pulses have a larger extension than these emitted by the sinewave, even if the width of the Lorentzian pulses is relatively small: $w = 0.16\mathcal{T}$. For the same reason, the dip in the noise around $\theta = 0$ is more

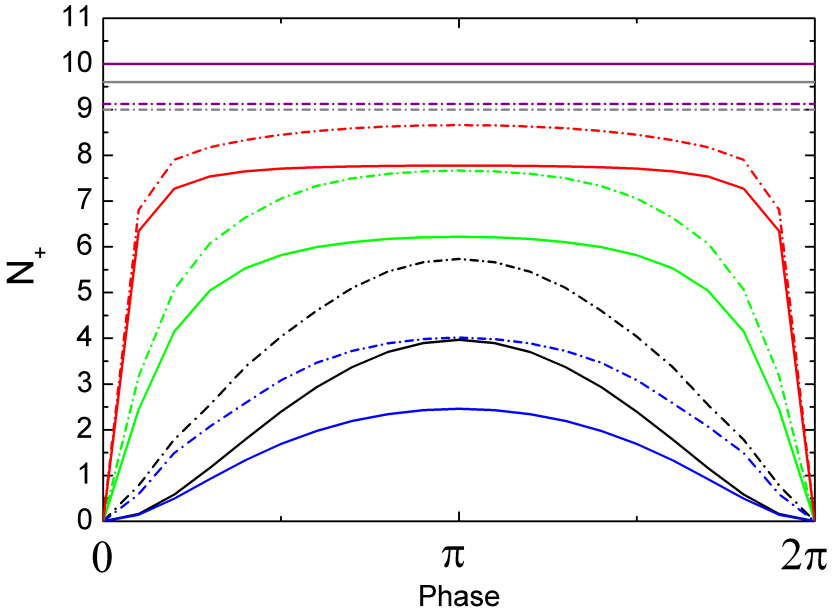

Figure 8.11: Excess number of particle N_+ at T=130mK (solid lines) and T=0 (dash-dotted lines) as function of the phase delay θ. The flux of the colliding pulses is set to q=4.5. Black lines: for sinepulses. Blue lines: lorentzian pulses of width $w = 0.16\mathcal{T}$. Green lines: lorentzian pulses of widths $w = 0.04\mathcal{T}$. Red lines: lorentzian pulses of widths $w = 0.01\mathcal{T}$. Theoretical limits of N_+ if the time delay between pulses was infinite are represented in solid line at T=130mK and dash-dotted lines at T=0mk, respectively in purple for sinewave and grey for lorentzian pulses.

extended for the Lorentzian pulses than for the sinewave.

This is in agreement with the numerical computation of N_+ produced for the HOM like experiment with Lorentzian pulses of different widths and a sinewave of $q = 4.5$ (Figure (8.11)). In figure (8.11), N_+ has been computed for T=130mK (solid line) and T=0 (dash-dotted line). The total noise that would be produced if the wavepackets scattered independently is also drawn.

Lets focus first on the values of N_+ at $\theta = \pi$. When $w/\mathcal{T}$ decreases, the colliding pulses are more and more separated and N_+ tends towards the sum of the number of quasi-particles produced by the two train of pulses. The ratio $w/\mathcal{T}$ is equal to 0.16, 0.04 and 0.01 respectively for the three lorentzian pulses, so N_+ tends slowly towards this limit. This is linked to the fact that Lorentzian pulses generate wavepackets with a Lorentzian time extension, so that when $w/\mathcal{T}$ increases, the overlapping between repeated pulses make V(t) to tend rapidely towards the DC limit.

The larger $w/\mathcal{T}$ is, the more sensitive is the noise to finite temperature. The dip around $\theta = 0$ is clearly enlarged for sinewave and Lorentzian pulses of $w/\mathcal{T} = 0.16$. Indeed, the thermal agitation suppresses the excess noise due to quasi-particles excited in the range $E_F \pm k_B T$. For these experimental waveforms, $k_B T/h\nu \approx 1$ and the contribution of most injected quasi-particles vanishes.

On the contrary, for sharper Lorentzian pulses, the width of the dip is less affected by the temperature. For small values of $w/\mathcal{T}$, it is equal to $4\pi w/\mathcal{T}$. This can be explained by the typical energy of the excitations h/w, which gets much larger than kT_B when the pulse width w decreases. Consequenlty the exicted quasi-particles contribution to the noise is not suppressed by the thermal agitation.

8.5 Conclusion

Excess noise measurements put in evidence the dynamic nature of quasi-particles injection by voltage pulses. This emission is complex and depend on the voltage pulses shape. The quasi-particle wavepacket extension can be investigated through a pulse collider experiment, than enlights the inuence of electron filled wavepacket antibunching.

Chapter 9

Conclusion and Prospects

9.1 Conclusion

Most of the available single-electron sources are essentially single-charge injectors. They control the transferred charge sometimes up to metrological standards [46, 71], but have not demonstrated yet the capability to control the kind of quasi-particles excitations they emit. The mesoscopic capacitor source [36,94] is the only single-quasiparticle source available today that emits a coherent electron followed by a hole and open the field to interference experiments with a single particle [15,51,55]. However, to investigate the Full counting statistics of a mesoscopic conductor and to extend coherence experiments to few particles, an n-electron source that could inject coherent wavepackets of an arbitrary and controlled number of indistinguishable electrons is required.

Levitov, Lesovik and collaborators have theoretically proposed a way to realize such an n-electron source, by applying Lorentzian voltage pulses on a ballistic quantum wire [59, 84]. When some voltage pulse of flux $q = e/h \int_{-\infty}^{\infty} V(t)dt$ is repeatedly applied on a perfectly transmitted single channel mode of a quantum wire, the device acts as a perfect current source that emits exactly q charges per period. However, it is not a reliable quasi-particle injector, for the charge q is generally accompagnied by a statistical number of quasi-particles N_+, the total charge of which is neutral. Remarkably, N_+ vanishes for Lorentzian pulses of integer flux, and this leads to a reliable n-electron source. When the channel is not perfectly transmitted, the shot-noise is proportionnal to the total number of excited quasi-particles per pulses [86]. Thus it enables to test the quality of the Lorentzian voltage pulsed source by measuring N_+. For any voltage pulse shape, N_+ presents interesting oscillations behaviour as a function of q, with local minima at integer number of q. These minima reach zero only for Lorentzian pulses.

Our numerical study at finite temperature show that this reduction of N_+ for integer

number of q requires to work at high repetition frequency ν so that with $k_BT \ll 0.2h\nu$. At dilution cryostat temperature (around 20mK) this implies to use frequency above 3Ghz. We have implemented this n-electron source by applying sub-nanosecond pulses on a quantum point contact (QPC) realized in a clean bidimensionnal electron gas of GaAs/AlGaAs heterostructure. The quantum point contact fulfills all the requirements of the Lesovik and Levitov theory, and can be use simultaneously as a source and a beam splitter to detect the quasi-particles. Moreover, the subnanosecond voltage pulses define quasi-particle wavepackets with an extension far below the phase coherence length in the 2DEG; so they ensure the coherence of this n-electron source that enables interference experiments.

To our knowledge, we have implemented one of the first cross-correlation noise detection set-up in a Helium free cryostat. As shown by the numerical studies, N_+ is of the order of 0.1 to 0.5 quasi-particles per period and contributes to the spectral power of the shot-noise by about $10^{-29}A^2/Hz$. DC shotnoise measurement confirms that the sensitivity of the set-up could reach this value in a few minutes. The electronic temperature extracted from the DC shotnoise is about 110mK, which is slightly above these of similar experimental set-up that use broad band RF coaxial lines in wet cryostats [7, 44, 94, 124]. We confirm that the pulse tube technology of Helium Free cryostat adds some perturbations that heat up the electronic temperature by at least 30 or 40mK. We are working on modification on the set-up and the cryostat to reduce these perturbations and improve the electronic temperature.

Applying sub-nanosecond non-harmonic voltage pulses on the quantum point contact requires a specific coplanar waveguide design on the sample and the chip-carrier in order to have the best and flattest transmission of the RF lines on a large frequency broad-band (0-24Ghz). Simulations on 3D electromagnetic transient solver has helped us to design the coplanar waveguides. The photocurrent detection has enabled to calibrate in-situ the attenuation of the RF lines. It has indicated that there is no major resonance or reflexion in the lines on the working frequency range.

We have investigated the excess particle number created for the injection of q charges with voltage pulses of different shape (sinewave, squarewave and Lorentzian). Excess noise spectroscopy gives access to photon absorption and emission energy distribution for each pulses, and enlight the particularities of Lorentzian voltage pulses. Even at finite temperature and non integer value of transferred charge, the Lorentzian voltage pulse source show a small excess number of particles (less than 0.05 particles per pulse). In comparison, sinewave injects a amount of 0.1 extra quasi-particles when $q > 1$, and the N_+ increases logarithmically with q for a squarewave. The excess noise due to RF voltage pulses is a signature of the photon-assisted shotnoise process, it can not be described by an averaging of the DC shotnoise over a quasi-static voltage V(t). Finally, through an Hong-Ou-Mandel like experiment, we have investigated the wavepacket extension produced by a lorentzian and a sine pulses.

Experimental results have been compared to theoretical estimations and are in quantitative agreement without adjustable parameters. This confirms the validity of Levitov and Lesovik's description of the quasiparticles emission processes in a ballistic quantum wire when arbitrary voltage pulses are applied.

9.2 Going further

The finite temperature is the main limitation of the voltage pulse source. The next improvements of the actual set-up is to reduce the ratio $k_BT/h\nu$. The first possibility is to work at higher frequencies. This implies the developpement of a dedicaced Lorentzian voltage source, for the fastest AWG are limited to 24Gs/s. Increasing the repetition frequency also implies the augmentation of the voltage pulses amplitude, and non-linearities of the QPC may then become a real problem.

The second possibility is to reduce the electronic temperature of the sample. Reducing k_BT and keeping the repetition frequency at a few Ghz also favours a longer phase coherence length, so a longer quasi-particle life time. Suppressing the perturbations coming from the pulse tube is one of the major challenge.

The Lorentzian voltage pulse source opens ways to quantum experiments with a controlled number of electrons. Many interesting theoretical proposals using the mesoscopic capacitor source [36,94] can be extended to the case of this n-electron source. Coupled to one or several Machs-Zehnder interferometers, this voltage source can give information of the wavepacket coherence of n undistinguishable electrons [33, 51, 55], or produce entangled states [123, 129]. Coupled to a single-charge detector, the Lorentzian voltage pulse source can lead to the Full Counting Statistic determination of a mesoscopic circuit.

Finally, we would like to open the discussion about the possibility to extend the beautiful properties of Lorentzian pulses. The essential property of the Lorentzian voltage pulses with integer flux lays in the spectrum P^* of $\exp(i\varphi(t))$ that induces only photon absorption or only photon emission. As the Fermi sea is infinitely deep, the collective displacement of the Fermi sea upwards or downwards on the energy scale excites only electrons or only holes. Can it be generalized to other systems than the ballistic quantum wire? We may think to interacting systems such as injection of fractional excitations in the quantum Hall regime.

Also, the linear dispersion of energy around the Fermi sea and the metallic property of the quantum wire seem not critical hypothesis in the Levitov and Lesovik theory. It would be very insteresting to look if the Lorentzian pulse property could be verified in a semi-conductor system with a small gap. This could actually lead to a quasi-particle source that would be less sensitive to finite temperature effects, because there would be less thermal excited electrons and holes in the reservoirs.

Appendix A

Current and noise formula in continuous Fourier formalism

Emitted charge, quasi-particle number and spectral power of noise are derived in chapter 3 for periodic voltage. The following section extend the formulas of chapter 3 for non-periodic voltage, using the formalism of continuous Fourier transform. This is especially the case for unique voltage pulse. Note that some of the quantities are not always available due to divergence [82].

A.1 Average current and transferred charge per pulse

From equation (3.13) the statistic average of the current operator can be derived:

$$\langle I(t,x)\rangle = \frac{eD}{h}\int_{-\infty}^{\infty}\int_{-\infty}^{\infty}\frac{d\eta d\eta'}{h^2}\int_{-\infty}^{\infty} P^*_{\eta\varepsilon}P_{\eta'\varepsilon}e^{i(\eta'-\eta)/\hbar t_+}f_L(\varepsilon) - e^{i(\eta'-\eta)/\hbar t_-}h^2\delta_{\eta'\varepsilon}\delta_{\eta\varepsilon}f_R(\varepsilon)d\varepsilon \quad \text{(A.1)}$$

We follow the same calculation path than in chapter 3, noting that

$$\int_{-\infty}^{\infty} P^*_{\eta\varepsilon}P_{\eta'\varepsilon}\frac{d\varepsilon}{h^2} = \int_{-\infty}^{\infty}\frac{dt}{h}e^{-i\varphi(t)+i\varphi(t)+i(\eta'-\eta)/\hbar t} = \delta_{\eta'\eta} \quad \text{(A.2)}$$

to recover the time-dependent Landauer relation when the two reservoirs are at the same temperature:

$$\begin{aligned}\langle I(t,x)\rangle &= \frac{eD}{h}\int_{-\infty}^{\infty}\int_{-\infty}^{\infty}\frac{d\kappa d\kappa'}{h^2}\int_{-\infty}^{\infty}\left(P_\kappa^* P_{\kappa'} e^{i(\kappa-\kappa')/\hbar t_+} - e^{i(\kappa-\kappa')/\hbar t_-} h^2\delta_\kappa\delta_{\kappa'}\right)(f(\varepsilon)-f(\varepsilon-\kappa))\,d\varepsilon \\ &= \frac{eD}{h}\int_{-\infty}^{\infty}\int_{-\infty}^{\infty}\frac{d\kappa d\kappa'}{h^2}\left(P_\kappa^* P_{\kappa'} e^{i(\kappa-\kappa')/\hbar t_+} - e^{i(\kappa-\kappa')/\hbar t_-} h^2\delta_\kappa\delta_{\kappa'}\right)\kappa \\ &= \frac{e^2D}{h}V(t-x/v_F) \qquad (A.3)\end{aligned}$$

In consequence, for a single pulse $V(t)$ of total flux $q=\phi(\infty)/(2\pi)$, the total transferred charge is equal to

$$\langle Q\rangle = \int_{-\infty}^{\infty} dt\frac{e^2D}{h}\langle I(t,x)\rangle = \frac{e^2D}{h}\int_{-\infty}^{\infty}V(t)dt = eqD \qquad (A.4)$$

A.2 Current-current correlators

the thermal fluctuation of the reservoirs

As explained in chapter 3, $L_{Th}(t,t',x)$ and $R_{Th}(t,t',x)$ are due to the exchange between particles of the same reservoir. Consequently they are invariant by gauge transformation and do not depend on the voltage shape. It is straitforward for the right reservoir term $R_{Th}(t,t',x)$. For $L_{Th}(t,t',x)$, this can be recovered by introducing the definition the Fourier transform P^* in the expression (A.5):

$$e^{i\varphi(t)} = \int_{-\infty}^{\infty}\frac{d\varepsilon}{h}P^*(\frac{\varepsilon}{\hbar})e^{-i\varepsilon t/\hbar}$$

$$L_{Th}(t,t',x) = \frac{e^2D^2}{h^6}\int_{-\infty}^{\infty}dpdqdrds\int_{-\infty}^{\infty}d\varepsilon d\varepsilon' f_L(\varepsilon)(1-f_L(\varepsilon'))P^*_{p\varepsilon}P_{q\varepsilon'}P^*_{r\varepsilon'}P_{s\varepsilon}e^{i/\hbar\left((q-p)t_+ +(s-r)t'_+\right)} \qquad (A.5)$$

Then

$$L_{Th}(t,t',x) = R_{Th}(t,t',x) = \frac{e^2D^2}{h^2}\int_{-\infty}^{\infty}d\varepsilon d\varepsilon' f_L(\varepsilon)(1-f_L(\varepsilon'))e^{i/\hbar(\varepsilon-\varepsilon')(t_+-t'_+)} \qquad (A.6)$$

the partition noise

$B_{ex}(t,t',x)$ in the current-current correlator exchange term counts the exchange between particles of different reservoir. It leads to the shotnoise when the transmission D is below 1.

$$B_{ex}(t,t') = \frac{e^2}{h^5} D(1-D) \int_{-\infty}^{\infty} dpdq \int_{-\infty}^{\infty} d\varepsilon d\varepsilon^{'} P^{*}_{p\varepsilon} P_{q\varepsilon}$$
$$\Big(f_R(\varepsilon')(1-f_L(\varepsilon)) e^{i/\hbar((q-p)t_+ + (p-\varepsilon')(t'_+ - t_+))} + f_L(\varepsilon)(1-f_R(\varepsilon')) e^{i/\hbar((q-p)t'_+ + (p-\varepsilon')(t_+ - t'_+))} \Big) \quad \text{(A.7)}$$

A.3 Charge fluctuations

When $B_{ex}(t+\tau,t)$ can be integrated over t and Fourier transformed to obtain the spectral power of the partition noise, then $S_{part}(\omega)$ is equal to:

$$S_{part}(\omega) = 2\frac{e^2}{h} D(1-D) \int_{-\infty}^{\infty} \frac{d\varepsilon d\varepsilon^{'}}{h^2} \left| P_{\varepsilon\varepsilon'} \right|^2 \left(f(\varepsilon)(1-f(\varepsilon'+\omega\hbar)) + f(\varepsilon'-\omega\hbar)(1-f(\varepsilon)) \right) \quad \text{(A.8)}$$

Note that in the case of a unique voltage pulse of flux q, $S_{part}(0)$ exists only if q is an integer value [82]. In this case, it is possible to introduce the average number $\langle N_e \rangle$ and $\langle N_h \rangle$

$$\langle N_e \rangle = \int |P_{\varepsilon\varepsilon'}|^2 f_L(\varepsilon)(1-f_R(\varepsilon')) \frac{d\varepsilon d\varepsilon^{'}}{h^2} \quad \text{(A.9)}$$

$$\langle N_h \rangle = \int |P_{\varepsilon'\varepsilon}|^2 f_R(\varepsilon')(1-f_L(\varepsilon)) \frac{d\varepsilon d\varepsilon^{'}}{h^2} \quad \text{(A.10)}$$

When both reservoirs are at zero temperature, these equations simplify into:

$$\langle N_e \rangle = \int_{0}^{\infty} \eta |P(\frac{\eta}{\hbar})|^2 \frac{d\eta}{h^2} \quad \text{(A.11)}$$

$$\langle N_h \rangle = -\int_{-\infty}^{0} \eta |P(\frac{\eta}{\hbar})|^2 \frac{d\eta}{h^2} \quad \text{(A.12)}$$

Then, identifying the terms in $S_{part}(0)$, one recovers that the partition noise is equal to the fluctuations due to the independent scattering of excited electrons and holes produced by the voltage pulse:

$$S_{part}(0) = 2\frac{e^2}{h} D\,(1-D)\,(\langle N_e\rangle + \langle N_h\rangle) \tag{A.13}$$

At finite temperature the total spectral power of the noise is equal to:

$$S_I(0) = 4k_BT\frac{e^2D^2}{h} + 2\frac{e^2}{h} D\,(1-D) \int_{-\infty}^{\infty} \eta coth(\frac{\eta}{2k_BT})|P(\frac{\eta}{\hbar})|^2 \frac{d\eta}{h^2} \tag{A.14}$$

Appendix B

Sample fabrication details

B.1 Chips preparation

Before proceeding to the lithography steps, the GaAs sample are cleaved from the main wafer by means of a diamond scriber, following the crystallographic axis. They are first cleaned in a Chlorhydric acid bath (HCl 3% in concentration, during 15s) and rinsed in dionized water, to remove any oxidation particles. Then they are cleaned into an acetone with ultrasound to remove dust and organic material, then rinsed in isopropanol to remove the acetone trace and finally dried under nitrogen flow.

B.2 Mask deposition

The sample surface must be absolutely free from dust or organic trace before depositing the photo-resist. First they have to be dried using a hotplate at 170C during 2mn in order to remove any kind of solvent. Then the photoresist is deposit by spin-coating. We choose to make our samples entirely by electronic beam lithography because we wanted flexibility on our design and only few number of similar samples was needed.

We chose to deposit a monolayer of PMMA A8 by spin-coating at 10s at 1500 tr/mn then 6000 tr/mn. The average thickness of the monolayer is about $1\mu m$.It is then baked during 2mn at 170C. The use of this monolayer allows a resolution of a dozen of nanometers under E-beam lithography, which is usefull for defining the tips of the gates. Furthermore it can be easily removed in a hot acetone bath after 15 mn.

After baking, the sample is exposed under e-beam lithography, with a typical dose of $250\mu C/cm^2$, except for the smallest details like the tips for which a special calibration is necessary (see below). Then the pattern is developped in a bath of pure MIBK during 40s, and the developpement is stopped by dropping the sample in an isopropanol bath. PMMA is a positive resist, which means that the insolated region will be removed by the MIBK, whereas the other regions of the layer will remain on the sample. After rinsing with isopropanol the

PMMA mask is ready to be used to other process steps. After the patterning process (metal deposition, etching etc...) the photo resist marsk is lifted off in hot acetone during 15mn and then rinsed in isopropanol and dried to another photoresist spin-coating.

Note: sample must not be too small, otherwise the layer of resist will not be extended properly by spin-coating and its width will not be uniform. It is typically better to use piece of GaAs that are at least 2mm large.

B.3 Alignement cross deposition

Before the device itself, it is convenient to pattern crosses that will give a precise mark for the alignement lithography step. Having different marks for the far field and the near field of the MEB is essential to make a good alignement without burning the center region of the sample (where the QPC will be). It is convenient to evaporate a layer of 5nm of titanium and 120nm of Gold to obtain crosses that will have a good contrast with AsGa under the e-beam microscope.

B.4 Mesa etching

Mask is developed in negative, so that only the region where the 2DEG mesa should remain is protected by resin. The other exposed region is attacked in a Pirana solution bath, that contains sulfuric acid, hydrogen peroxide and water (proportion: H_2SO_4:0.5 ml, H_20_2: 4ml, H_2O: 50ml). The surface is etched by oxydo-reduction, the depth can be controlled by a profilometer. The typical etch rate is about 6nm/s. Typically a dwell time of 45s in the Pirana solution leads to an etching of 300nm. Then we rinse again the sample in water, remove the photo-resist in aceton and rinse it with isopropanol before going to the next step of lithography.

Note: Generally mesa etching induces damages on metal patterns that have already been deposited on the surface, because it etches the semi-conductor under the metal. It is better to protect the alignement crosses with resin before the etching.

B.5 Contact deposition

To contact the 2DEG that is typically burried 100nm below the surface of the semi-conducting heterostructure, one has to transform the Schottky barrier formed at the metal-semiconductor interface into a low resistive ohmic contact. According to Schottky-Mott theory in order to obtain ohmic contact to n-type semiconductor the work function of metal should be smaller than that of the semiconductor. But it has been found experimentally that the energy barrier

betwwen the metal and the gas was essentially controlled by the acceptor-like surface states of the n-type GaAs metal interface. However, the Schottky barrier can be lowered in this case by the diffusion of the metal into semiconductor that creates a sufficient doping of the interface. The metallic alloy AuGeNi is commonly used to form contact for GaAs. The eutectic AuGe melts at 353°C and some substitutions in the semiconductor crystal takes place: Gold atom replaces Arsenium, Germanium replaces Gallium [16, 52]. Adding a layer of nickel between GaAs and AuGe improves the metal wetting. It also reduces the diffusion for Ge and As out of the contact. First a phase of NiAs is generated, that transforms into Ni_2GeAs in the following [17]. This phase is supposed to control the contact resistance by the production of donnors and to prevent an excessive diffusion of As and Ga. However there is an optimum of concentration (about 25% [50]) of Nickel in the alloy because it is also an acceptor and diffuses rapidly. Because of the tread-off between the formation of donnors and acceptors, the annealing process plays a crucial role in contact formation and should be operate around 465°C [52].

Just before proceeding to the deposition, the sample is cleaned in diluted Chlorhydric acid bath (HCl 3% during 20s). An eutectic alloy of Au-Ge-Ni of weight composition 84% Gold, 12 % Germanium 12 and 4% Nickel, was used for the deposition in a Joule evaporator. We wait a pression of the order of $10^{-6} mbar$ before deposition and then evaporate the total amount of alloy contained in the crucible (a layer of about 170nm of alloys is deposited on the chip). Then the PMMA is removed in an hot aceton bath and the sample is rinsed with isopropanol.

The annealing is performed under hydrogen and nitrogen controlled atmosphere near the fusion temperature of the eutectic alloy. The steps are the following:

1. we wait 1mn by blowing nitrogen gaz (150L/H)in the chamber to decrease the concentration of oxygen.

2. we blow dihydrogen (80L/H) and nitrogen in the chamber to get a reductive atmosphere during 3mn.

3. we heat the sample by steps, making a ramp of 30s to 230C, waiting 30s at this temperature, then going up to 475C in 30s.

4. We stay at the annealing temperature of 475C during 2mn, then we down to 230C in 30s, stay at this temperature during 30s and stop heating. We wait 3min before stopping the gaz flow of dihydrogen and nitrogen.

We do this cycle twice, and then wait until the oven temperature is below 50C to open the oven. Contacting the 2DEG was not always sucessfull and remains one of the key point to improve. The lower contact resistance we achieved is about a 2.4kOhm at low temperature, which is not so good when we compare with the best values obtained on the similar 2DEG.

Note: The alloy AuGeNi can also be used to make good bonding pads for the sample, because it better resist to the ultrasonic bonding compare to the thin Ti-Au metal that is used to make the RF lines.

B.6 Gates depositions

The last step of the process is to pattern the gates and the coaxial lines. The split gate requires a precision of a few hundred of nanometers. For this level of detail the process parameters are critical, because a small deviation in the exposure or the developpement time induces visible changes on the tips shape. Lift-off of small photoresist region can also failed if the sample has been under or over exposed. For example electronic photography of tips obtained for different exposure dose are reproduced on figure. Under a dose of $250\mu C/cm^2$, small residu of PMMA are not lift-off: the resist has been under exposed. The tips are to close from each other and even touch over a dose of $380\mu C/cm^2$ (figure B.1). In consequence a typical dose of $290\mu C/cm^2$ corresponding to a developpement time in MIBK of 40s was chosen. A regular check with dose tests is necessary to adjust the dose parameter to the natural evolution of the MEB lamp. After developpement a layer of 5nm of titanium and 120nm of Gold is deposited by electron-beam evaporator.

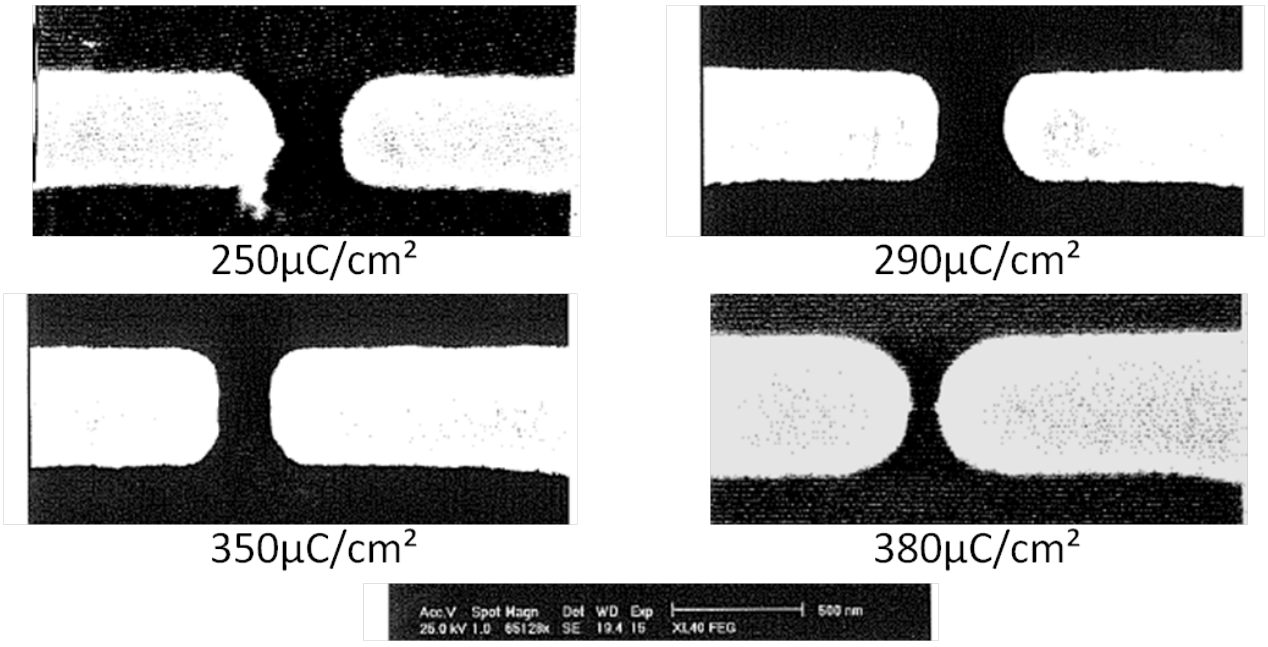

Figure B.1: split gates shape as function of the exposure time. Resist was developped in MIBK during 40s.

Appendix C

Sample and pcb details

C.1 Sample high frequency design

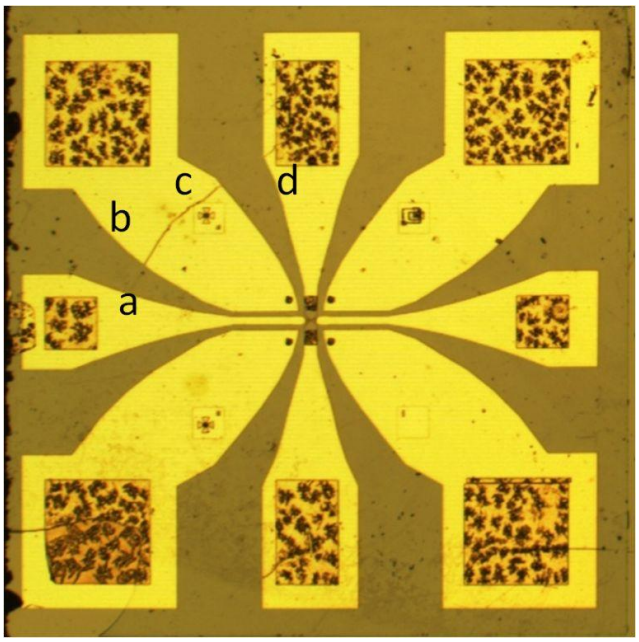

Figure C.1: optical photography of the sample.

The interesting dimensions of lines a, b, c, d which define the coaxial waveguide are reported on figure (C.1). The following table gives the exact coordinates of these polygonal lines. The reference of the axis is taken at the center of the sample.

gate CPW central conductor a		gate CPW ground plane b	
x	y	x	y
-1100	183	-1100	510
-910	183	-910	510
-810	145	-800	367
-700	107	-700	268
-600	77	-600	189
-500	51	-500	130
-400	30	-481	119
-300	15	-400	71
-70	15	-300	35.5
-52.5	17	-47.5	35.5
contact CPW central conductor d		contact CPW ground plane c	
x	y	x	y
183	1100	-510	1100
183	630	-510	630
136	530	-367	550
104	430	-309	479
80	330	-268	430
50.6	230	-189	330
25.2	130	-121	230
		-70	130
		-60	96
23.1	70	-52	70

Table C.1: dimension of the coplanar waveguides of the sample. lengths are given in μm

C.2 Chip-carrier High frequency design

The chip-carrier substrate is a $381\mu m$ thick Rogers TMM10 laminate, with a $17{,}5\mu m$ thick copper base. The $2\mu m$ gold layer has been plated on the copper to prevent oxydation. A thick copper plate of 1mm is bound to the circuit background using silver loaded conductive adhesive to make the center socket where is placed the sample (fig. (C.2)).

Via-holes with a diameter of $300\mu m$ are regularly drilled in the laminate, they are plated with copper and gold to ensure conductivity. The center socket is a 2.2mm square, with $300\mu m$ clearance holes at the corners.

Rosenberger 18s101-40ml5 right-angle mini-SMP connectors are placed on each soldering footprint detailed in fig. (C.3).

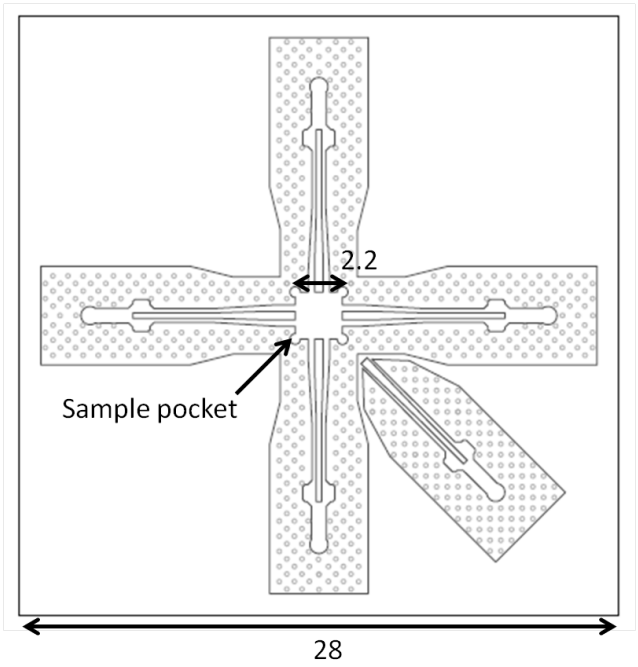

Figure C.2: sample holder scheme. lengths are given in mm

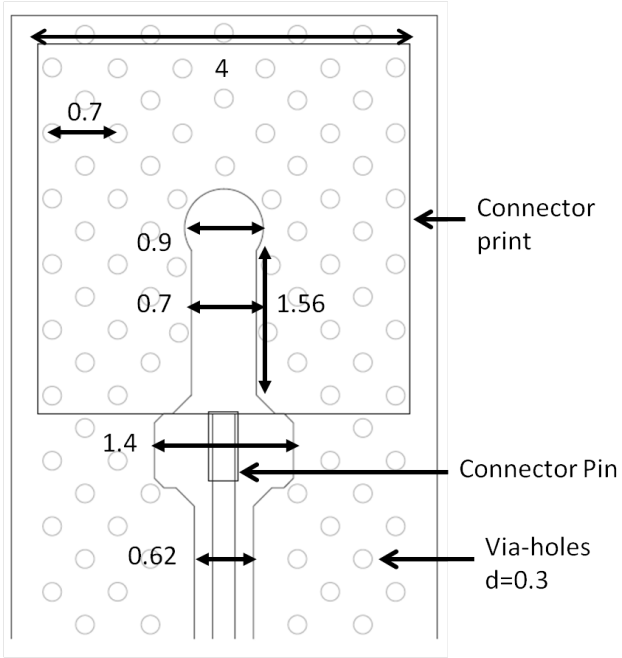

Figure C.3: zoom on the soldering footprint of the mini-SMP connectors. lengths are given in mm

Appendix D

Measurement set-up: experimental details

D.1 Parasitic Noises from electronics

Lock-in amplifier has to be entirely disconnected from the ground of the cryostat, for it is quite a noisy instrument. The AC signal of the generator pass through an isolation amplifier Burr-Brown ISO122. This device digitalized the signal with a ripple frequency of 500kHz and transferred the signal from the input circuit to the output circuit through a diode. In this process, the signal from DC to 100kHz is transferred, but the grounds are separated. The conductance measurement is done on differential mode.

The Yokogawa DC voltage generator output is disconnected from the ground of the instrument. Both AC and DC voltage pass through a pi-filter murata of 7nF before entering the polarisation resistor and the cryostat (D.1).

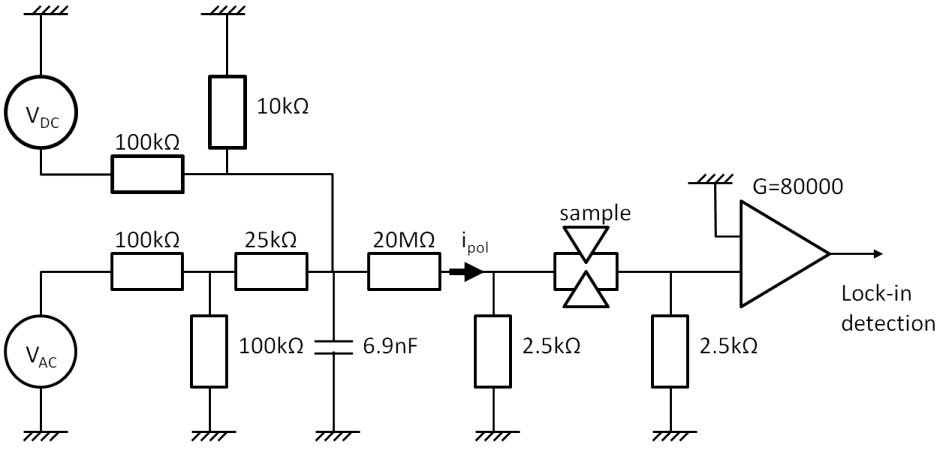

Figure D.1: Low frequency injection

The gate is controlled by batteries. A serie of RC filter ($660k\Omega$ and 330pF) and a murata pi-filter are added on the line to protect the sample gates from any voltage peaks and to filter the line.

On the measurement lines, amplifiers are put on separated batteries, their alimentation are filtered with RC capacitors, because of regulators that used kHz frequency. An isolation transformator is inserted before the butterworth filters in order to disconnect the ground of the cryostat from the computer.

D.2 Physical specifications of the coaxial cables

coaxial type	KMCO TCR219CG
center conductor diameter (mm)	0.51
center conductor material	Silver plated Phosphor Bronze
center resistivity at 300K (Ω/m)	0.13
center thermal conductivity at 1K mW/(cm.K)	0.5×10^{-2}
dielectric width external diameter (mm)	1.61
dielectric material	Porous PTFE
shield diameter (mm)	2.19
shield material	Stainless steel
shield resistivity at 300K (Ω/m)	0.072
shield thermal conductivity at 1K mW/(cm.K)	2.6×10^{-2}
nominal capacitance(pF/m)	100
characteristic impedance (Ω)	50
coaxial type	YOTEM Cu-Ni
center conductor diameter (mm)	0.51
center conductor material	Cu-Ni
center resistivity at 300K (Ω/m)	1.7
center thermal conductivity at 1K mW/(cm.K)	0.125×10^{-2}
dielectric width external diameter (mm)	1.61
dielectric material	PTFE
shield diameter (mm)	2.19
shield material	Cu-Ni
shield resistivity at 300K (Ω/m)	0.2
shield thermal conductivity at 1K mW/(cm.K)	1.04×10^{-2}
nominal capacitance(pF/m)	100
characteristic impedance (Ω)	50

Table D.1: Technical specifications for RF coaxial cable

coaxial type	Lakeshore SS
center conductor diameter (mm)	0.2
center conductor material	304 Stainless steel
center resistivity at 300K (Ω/m)	23.6
center thermal conductivity at 1K mW/(cm.K)	0.06×10^{-2}
dielectric width external diameter (mm)	0.4
dielectric material	Teflon
shield diameter (mm)	0.711
shield material	304 braided stainless
shield resistivity at 300K (Ω/m)	3.61
shield thermal conductivity at 1K mW/(cm.K)	0.4×10^{-2}
nominal capacitance(pF/m)	173.9
characteristic impedance (Ω)	40
coaxial type	Homemade cable
center conductor diameter (mm)	0.071
center conductor material	ISAOhm
center resistivity at 300K (Ω/m)	333
center thermal conductivity at 1K mW/(cm.K)	10^{-5}
dielectric width external diameter (mm)	0.8
dielectric material	none
shield diameter (mm)	1.2
shield material	Cr-Ni
shield resistivity at 300K (Ω/m)	10
shield thermal conductivity at 1K mW/(cm.K)	0.04×10^{-2}
nominal capacitance(pF/m)	100
characteristic impedance (Ω)	50

Table D.2: Technical specifications for low frequency coaxial cable

Material	$\kappa\,(mW/(cm.K))$
Steel	$1.5T$
Cupro-nickel	$0.6T$
Manganin	$0.94T^{1.2}$
Copper	$600 - 10^4 T$
Teflon	$30 \times 10^{-3} T^2$
Nickel-Chrome (Inconel)	$0.05T^{1.5}$
Phosphor Bronze	$2.7T^{1.16}$

Table D.3: Thermal conductivity at low temperature for typical material [2,68,110,140]. The temperature reference is 1K

Bibliography

[1] http://www.rogerscorp.com/documents/728/acm/TMM-Thermoset-laminate-data-sheet-TMM3-TMM4-TMM6-TMM10-TMM10i.aspx.

[2] 1ere ecole d'automne Aussois, editor. *Detection de rayonnements a tres basse temperatures*, 1991.

[3] Mathias Albert, Christian Flindt, and Markus Büttiker. Accuracy of the quantum capacitor as a single-electron source. *Physical Review B*, 82(4), July 2010.

[4] P. W. Anderson. Infrared Catastrophe in Fermi Gases with Local Scattering Potentials. *Physical Review Letters*, 18(24):1049–1051, June 1967.

[5] N. W. Ashcroft and N. D. Mermin. *Solid State Physics*. Saunders, 1976.

[6] G. Aĭzin, Godfrey Gumbs, and M. Pepper. Screening of the surface-acoustic-wave potential by a metal gate and the quantization of the acoustoelectric current in a narrow channel. *Physical Review B*, 58(16):10589–10596, October 1998.

[7] E. Zakka Bajjani, J. Ségala, F. Portier, P. Roche, D. C. Glattli, A. Cavanna, and Y. Jin. Experimental Test of the High-Frequency Quantum Shot Noise Theory in a Quantum Point Contact. *Physical Review Letters*, 99(23):236803+, December 2007.

[8] C. Barnes, J. Shilton, and A. Robinson. Quantum computation using electrons trapped by surface acoustic waves. *Physical Review B*, 62(12):8410–8419, September 2000.

[9] F. Battista and P. Samuelsson. Proposal for nonlocal electron-hole turnstile in the quantum Hall regime. *Physical Review B*, 83(12), March 2011.

[10] K. F. Berggren, T. J. Thornton, D. J. Newson, and M. Pepper. Magnetic Depopulation of 1D Subbands in a Narrow 2D Electron Gas in a GaAs:AlGaAs Heterojunction. *Physical Review Letters*, 57:1769–1772, October 1986.

[11] H. Birk, M. J. M. de Jong, and C. Schönenberger. Shot-Noise Suppression in the Single-Electron Tunneling Regime. *Physical Review Letters*, 75:1610–1613, August 1995.

[12] Ya Blanter and M. Büttiker. Shot noise in mesoscopic conductors. *Physics Reports*, 336(1-2):1–166, September 2000.

[13] M. D. Blumenthal, B. Kaestner, L. Li, S. Giblin, T. J. B. M. Janssen, M. Pepper, D. Anderson, G. Jones, and D. A. Ritchie. Gigahertz quantized charge pumping. *Nature Physics*, 3(5):343–347, April 2007.

[14] Marc Bockrath, David H. Cobden, Paul L. McEuen, Nasreen G. Chopra, A. Zettl, Andreas Thess, and R. E. Smalley. Single-Electron Transport in Ropes of Carbon Nanotubes. *Science*, 275(5308):1922–1925, March 1997.

[15] E. Bocquillon, F. D. Parmentier, C. Grenier, J. M. Berroir, P. Degiovanni, D. C. Glattli, B. Plaçais, A. Cavanna, Y. Jin, and G. Fève. Electron quantum optics : partitioning electrons one by one. February 2012.

[16] Norman Braslau. Ohmic contacts to GaAs. *Thin Solid Films*, 104(3-4):391–397, June 1983.

[17] R. A. Bruce and G. R. Piercy. An improved AuGeNi ohmic contact to n-type GaAs. *Solid-State Electronics*, 30(7):729–737, July 1987.

[18] Guido Burkard and Daniel Loss. Lower Bound for Electron Spin Entanglement from Beam Splitter Current Correlations. *Physical Review Letters*, 91:087903+, August 2003.

[19] M. Büttiker. Quantized transmission of a saddle-point constriction. *Physical Review B*, 41:7906–7909, April 1990.

[20] M. Büttiker. Scattering theory of thermal and excess noise in open conductors. *Physical Review Letters*, 65(23):2901–2904, December 1990.

[21] M. Büttiker. Role of scattering amplitudes in frequency-dependent current fluctuations in small conductors. *Physical Review B*, 45:3807–3810, February 1992.

[22] M. Büttiker. Scattering theory of current and intensity noise correlations in conductors and wave guides. *Physical Review B*, 46(19):12485–12507, November 1992.

[23] M. Büttiker, Y. Imry, R. Landauer, and S. Pinhas. Generalized many-channel conductance formula with application to small rings. *Physical Review B*, 31(10):6207–6215, May 1985.

[24] A. V. Chaplik. . *Zh. Eksp. Teor. Fiz. 60, 1845 [Sov. Phys. JETP 33, 997]*, 1971.

[25] Jean C. Charlier, Xavier Blase, and Stephan Roche. Electronic and transport properties of nanotubes. *Reviews of Modern Physics*, 79(2):677–732, May 2007.

[26] J. Cunningham, V. I. Talyanskii, J. M. Shilton, M. Pepper, A. Kristensen, and P. E. Lindelof. High-frequency single-electron transport and the quantized acoustoelectric effect. *Physica B: Condensed Matter*, 280(1-4):493–494, May 2000.

[27] J. Cunningham, V. I. Talyanskii, J. M. Shilton, M. Pepper, A. Kristensen, and P. E. Lindelof. Single-electron acoustic charge transport on shallow-etched channels in a perpendicular magnetic field. *Physical Review B*, 62:1564–1567, July 2000.

[28] J. Cunningham, V. I. Talyanskii, J. M. Shilton, M. Pepper, M. Y. Simmons, and D. A. Ritchie. Single-electron acoustic charge transport by two counterpropagating surface acoustic wave beams. *Physical Review B*, 60:4850–4855, August 1999.

[29] W. C. Daywitt. Exact principal mode field for a lossy coaxial line. *IEEE Transactions on Microwave Theory and Techniques*, 39(8):1313–1322, August 1991.

[30] M. D. M. De Jong and C. W. J. Beenakker. *Shot Noise in mesoscopic systems*. Kluwer Academic publishers, 1997.

[31] R. de Picciotto, L. N. Pfeiffer, K. W. Baldwin, and K. W. West. Temperature-dependent 0.7 structure in the conductance of cleaved-edge-overgrowth one-dimensional wires. *Physical Review B*, 72:033319+, July 2005.

[32] C. C. Dean and M. Pepper. The transition from two- to one-dimensional electronic transport in narrow silicon accumulation layers. *Journal of Physics C: Solid State Physics*, 15(36):L1287+, December 1982.

[33] P. Degiovanni, Ch, and G. Fève. Decoherence and relaxation of single-electron excitations in quantum Hall edge channels. *Physical Review B*, 80(24):241307+, December 2009.

[34] Michel H. Devoret, Daniel Esteve, and Cristian Urbina. Single-electron transfer in metallic nanostructures. *Nature*, 360(6404):547–553, December 1992.

[35] L. DiCarlo, Y. Zhang, D. T. McClure, D. J. Reilly, C. M. Marcus, L. N. Pfeiffer, and K. W. West. Shot-Noise Signatures of 0.7 Structure and Spin in a Quantum Point Contact. *Physical Review Letters*, 97:036810+, July 2006.

[36] G. Feve, A. Mahe, J. M. Berroir, T. Kontos, B. Placais, D. C. Glattli, A. Cavanna, B. Etienne, and Y. Jin. An On-Demand Coherent Single-Electron Source. *Science*, 316(5828):1169–1172, May 2007.

[37] Karsten Flensberg, Qian Niu, and Michael Pustilnik. Nonadiabaticity and single-electron transport driven by surface acoustic waves. *Physical Review B*, 60(24):R16291–R16294, December 1999.

[38] Heidi Forster and Markus Buttiker. Fluctuation relations without micro-reversibility for two-terminal conductors, July 2009.

[39] Akira Fujiwara, Katsuhiko Nishiguchi, and Yukinori Ono. Nanoampere charge pump by single-electron ratchet using silicon nanowire metal-oxide-semiconductor field-effect transistor. *Applied Physics Letters*, 92(4):042102+, 2008.

[40] T. A. Fulton and G. J. Dolan. Observation of single-electron charging effects in small tunnel junctions. *Physical Review Letters*, 59(1):109–112, July 1987.

[41] Stephen D. Gaalema, Richard J. Schwartz, and Robert L. Gunshor. Acoustic surface wave interaction charge-coupled device. *Applied Physics Letters*, 29(2):82–83, 1976.

[42] J. Gabelli, G. Feve, J. M. Berroir, B. Placais, A. Cavanna, B. Etienne, Y. Jin, and D. C. Glattli. Violation of Kirchhoff's Laws for a Coherent RC Circuit. *Science*, 313(5786):499–502, July 2006.

[43] J. Gabelli and B. Reulet. Dynamics of Quantum Noise in a Tunnel Junction under ac Excitation. *Physical Review Letters*, 100(2):026601+, January 2008.

[44] Julien Gabelli and Bertrand Reulet. Shaping a time-dependent excitation to control the electron distribution function: noise minimization in a tunnel junction. May 2012.

[45] L. J. Geerligs, V. F. Anderegg, P. A. M. Holweg, J. E. Mooij, H. Pothier, D. Esteve, C. Urbina, and M. H. Devoret. Frequency-locked turnstile device for single electrons. *Physical Review Letters*, 64(22):2691–2694, May 1990.

[46] S. P. Giblin, M. Kataoka, J. D. Fletcher, P. See, T. J. B. M. Janssen, J. P. Griffiths, G. A. C. Jones, I. Farrer, and D. A. Ritchie. Single electron pumps: towards a quantum representation of the ampere. March 2012.

[47] Vittorio Giovannetti, Diego Frustaglia, Fabio Taddei, and Rosario Fazio. Electronic Hong-Ou-Mandel interferometer for multimode entanglement detection. *Physical Review B*, 74:115315+, September 2006.

[48] Gabriele F. Giuliani and John J. Quinn. Lifetime of a quasiparticle in a two-dimensional electron gas. *Physical Review B*, 26:4421–4428, October 1982.

[49] D. C. Glattli, P. Jacques, A. Kumar, P. Pari, and L. Saminadayar. A noise detection scheme with 10 mK noise temperature resolution for semiconductor single electron tunneling devices. *Journal of Applied Physics*, 81(11):7350–7356, 1997.

[50] Oktay Göktaş, Jochen Weber, Jürgen Weis, and Klaus von Klitzing. Alloyed ohmic contacts to two-dimensional electron system in AlGaAs/GaAs heterostructures down to submicron length scale. *Physica E: Low-dimensional Systems and Nanostructures*, 40(5):1579–1581, March 2008.

[51] C. Grenier, R. Hervé, E. Bocquillon, F. D. Parmentier, B. Plaçais, J. M. Berroir, G. Fève, and P. Degiovanni. Single-electron quantum tomography in quantum Hall edge channels. *New Journal of Physics*, 13(9):093007+, September 2011.

[52] R. P. Gupta and W. S. Khokle. Gallium-vacancy-dependent diffusion model of ohmic contacts to GaAs. *Solid-State Electronics*, 28(8):823–830, August 1985.

[53] S. Gustavsson, R. Leturcq, T. Ihn, K. Ensslin, M. Reinwald, and W. Wegscheider. Measurements of higher-order noise correlations in a quantum dot with a finite bandwidth detector. *Physical Review B*, 75:075314+, February 2007.

[54] S. Gustavsson, R. Leturcq, B. Simovič, R. Schleser, T. Ihn, P. Studerus, K. Ensslin, D. C. Driscoll, and A. C. Gossard. Counting Statistics of Single Electron Transport in a Quantum Dot. *Physical Review Letters*, 96:076605+, February 2006.

[55] Géraldine Haack, Michael Moskalets, Janine Splettstoesser, and Markus Büttiker. Coherence of single-electron sources from Mach-Zehnder interferometry. *Physical Review B*, 84:081303+, August 2011.

[56] R. Hanbury Brown and R. Q. Twiss. A test of a new type of stellar interferometer on Sirius. *Nature*, 178:1046–1048, November 1956.

[57] Sylvain Hermelin, Shintaro Takada, Michihisa Yamamoto, Seigo Tarucha, Andreas D. Wieck, Laurent Saminadayar, Christopher Bäuerle, and Tristan Meunier. Electrons surfing on a sound wave as a platform for quantum optics with flying electrons. *Nature*, 477(7365):435–438, September 2011.

[58] C. K. Hong, Z. Y. Ou, and L. Mandel. Measurement of subpicosecond time intervals between two photons by interference. *Physical Review Letters*, 59(18):2044–2046, November 1987.

[59] D. A. Ivanov, H. W. Lee, and L. S. Levitov. Coherent states of alternating current. *Physical Review Letters B*, 56:6839–6850, 1997.

[60] T. J. B. M. Janssen and A. Hartland. Accuracy of quantized single-electron current in a one-dimensional channel. *Physica B: Condensed Matter*, 284-288:1790–1791, July 2000.

[61] Yang Ji, Yunchul Chung, D. Sprinzak, M. Heiblum, D. Mahalu, and Hadas Shtrikman. An electronic MachZehnder interferometer. *Nature*, 422(6930):415–418, March 2003.

[62] J. B. Johnson. Thermal Agitation of Electricity in Conductors. *Physical Review Online Archive (Prola)*, 32(1):97–109, July 1928.

[63] T. Jonckheere, J. Rech, C. Wahl, and T. Martin. Electron and hole Hong-Ou-Mandel interferometry, April 2012.

[64] T. Jonckheere, T. Stoll, J. Rech, and T. Martin. Real-time simulation of finite-frequency noise from a single-electron emitter. *Physical Review B*, 85:045321+, January 2012.

[65] P. Karbownik, A. Baranska, A. Szerling, W. Macherzynski, E. Papis, K. Kosiel, M. Bugajski, M. Tlaczala, and R. Rafa Jakiela. Low resistance ohmic contacts to n-GaAs for application in GaAs/AlGaAs quantum cascade lasers. *Optica Applicata*, 39:655+, 2009.

[66] M. Kataoka, M. R. Astley, A. L. Thorn, D. K. L. Oi, C. H. W. Barnes, C. J. B. Ford, D. Anderson, G. A. C. Jones, I. Farrer, D. A. Ritchie, and M. Pepper. Coherent Time Evolution of a Single-Electron Wave Function. *Physical Review Letters*, 102:156801+, April 2009.

[67] M. Kataoka, J. D. Fletcher, P. See, S. P. Giblin, T. J. B. M. Janssen, J. P. Griffiths, G. A. C. Jones, I. Farrer, and D. A. Ritchie. Tunable Nonadiabatic Excitation in a Single-Electron Quantum Dot. *Physical Review Letters*, 106:126801+, March 2011.

[68] Kaye and Laby. *Tables of Physical & Chemical Constants*. http://www.kayelaby.npl.co.uk/, 16 edition, 1995.

[69] J. Keeling, I. Klich, and L. S. Levitov. Minimal Excitation States of Electrons in One-Dimensional Wires. *Physical Review Letters*, 97(11):116403+, September 2006.

[70] J. Keeling, A. V. Shytov, and L. S. Levitov. Coherent Particle Transfer in an On-Demand Single-Electron Source. *Physical Review Letters*, 101(19):196404+, November 2008.

[71] Mark W. Keller, John M. Martinis, Neil M. Zimmerman, and Andrew H. Steinbach. Accuracy of electron counting using a 7-junction electron pump. *Applied Physics Letters*, 69(12):1804–1806, 1996.

[72] Israel Klich and Leonid Levitov. Quantum Noise as an Entanglement Meter. *Physical Review Letters*, 102(10):100502+, 2009.

[73] L. P. Kouwenhoven, S. Jauhar, J. Orenstein, P. L. McEuen, Y. Nagamune, J. Motohisa, and H. Sakaki. Observation of Photon-Assisted Tunneling through a Quantum Dot. *Physical Review Letters*, 73:3443–3446, December 1994.

[74] L. P. Kouwenhoven, A. T. Johnson, N. C. van der Vaart, C. J. P. M. Harmans, and C. T. Foxon. Quantized current in a quantum-dot turnstile using oscillating tunnel barriers. *Physical Review Letters*, 67(12):1626–1629, September 1991.

[75] J. M. Krans, Van, J. M. Ruitenbeek, V. Fisun, V., I. Yanson, K., De, and L. J. Jongh. The signature of conductance quantization in metallic point contacts. *Nature*, 375(6534):767–769, June 1995.

[76] A. Kristensen, H. Bruus, A. E. Hansen, J. B. Jensen, P. E. Lindelof, C. J. Marckmann, J. Nygaard, C. B. Sørensen, F. Beuscher, A. Forchel, and M. Michel. Bias and temperature dependence of the 0.7 conductance anomaly in quantum point contacts. *Physical Review B*, 62:10950–10957, October 2000.

[77] A. Kumar, L. Saminadayar, D. C. Glattli, Y. Jin, and B. Etienne. Experimental Test of the Quantum Shot Noise Reduction Theory. *Physical Review Letters*, 76(15):2778–2781, April 1996.

[78] L. D. Landau. Oscillations in a Fermi-liquid. *Sov. Phys. JETP*, 5:101+, 1957.

[79] L. D. Landau. Theory of Fermi-liquids. *Sov. Phys. JETP*, 3:920+, 1957.

[80] L. D. Landau and E. M. Lifshitz. *Quantum Mechanics*, volume 3. Pergamon Press, 1958.

[81] R. Landauer. Spatial Variation of Currents and Fields Due to Localized Scatterers in Metallic Conduction. *IBM Journal of Research and Development*, 1(3):223–231, July 1957.

[82] Hyunwoo Lee and L. S. Levitov. Estimate of Minimal Noise in a Quantum Conductor. July 1995.

[83] G. B. Lesovik. Effect of random voltage on equilibrium current fluctuations in a quantum conductor. *JETP Letters*, 60:815+, December 1994.

[84] G. B. Lesovik and L. S. Levitov. Noise in an ac biased junction: Nonstationary Aharonov-Bohm effect. *Physical Review Letters*, 72:538–541, January 1994.

[85] M. Levinshtein, S. Rumyantsev, and M. Shur, editors. *Hanbooks series on semiconductors parameters, Ternary and Quaternary III-V compounds*, volume 2. World Scientific Publishing and Co, 1998.

[86] L. S. Levitov and G. B. Lesovik. Charge distribution in quantum shot noise. *JETP letters*, 58:225–230, August 1993.

[87] Yuan P. Li, D. C. Tsui, J. J. Heremans, J. A. Simmons, and G. W. Weimann. Low-frequency noise in transport through quantum point contacts. *Applied Physics Letters*, 57(8):774–776, 1990.

[88] Y. X. Liang, Q. Dong, M. C. Cheng, U. Gennser, A. Cavanna, and Y. Jin. Insight into low frequency noise induced by gate leakage current in AlGaAs/GaAs high electron mobility transistors at 4.2 K. *Applied Physics Letters*, 99(11):113505+, 2011.

[89] F. Liefrink, J. I. Dijkhuis, M. J. M. de Jong, L. W. Molenkamp, and H. van Houten. Experimental study of reduced shot noise in a diffusive mesoscopic conductor. *Physical Review B*, 49:14066–14069, May 1994.

[90] F. Liefrink, J. I. Dijkhuis, and H. van Houten. Low-frequency noise in quantum point contacts. *Semiconductor Science and Technology*, 9(12):2178+.

[91] R. C. Liu, B. Odom, Y. Yamamoto, and S. Tarucha. Quantum interference in electron collision. *Nature*, 391(6664):263–265, January 1998.

[92] R. C. Liu, Y. Yamamoto, and S. Tarucha. Signs of quantum statistical effects in electron collision. *Physica B: Condensed Matter*, 249-251:152–156, June 1998.

[93] S. V. Lotkhov, S. A. Bogoslovsky, A. B. Zorin, and J. Niemeyer. Operation of a three-junction single-electron pump with on-chip resistors. *Applied Physics Letters*, 78(7):946–948, 2001.

[94] A. Mahé, F. Parmentier, E. Bocquillon, J. M. Berroir, D. Glattli, T. Kontos, B. Plaçais, G. Fève, A. Cavanna, and Y. Jin. Current correlations of an on-demand single-electron emitter. *Physical Review B*, 82(20), November 2010.

[95] A. Mahé, F. Parmentier, G. Fève, J. M. Berroir, T. Kontos, A. Cavanna, B. Etienne, Y. Jin, D. Glattli, and B. Plaçais. Subnanosecond Single Electron Source in the Time-Domain. *Journal of Low Temperature Physics*, 153(5):339–349, December 2008.

[96] P. Maksym. Quantized electron transport through a time-dependent potential barrier. *Physical Review B*, 61(7):4727–4730, February 2000.

[97] Th Martin and R. Landauer. Wave-packet approach to noise in multichannel mesoscopic systems. *Physical Review B*, 45(4):1742–1755, January 1992.

[98] John M. Martinis, M. Nahum, and Hans D. Jensen. Metrological accuracy of the electron pump. *Physical Review Letters*, 72(6):904–907, February 1994.

[99] R. P. G. McNeil, M. Kataoka, C. J. B. Ford, C. H. W. Barnes, D. Anderson, G. A. C. Jones, I. Farrer, and D. A. Ritchie. On-demand single-electron transfer between distant quantum dots. *Nature*, 477(7365):439–442, September 2011.

[100] A. Mittal, R. G. Wheeler, M. W. Keller, D. E. Prober, and R. N. Sacks. Electron-phonon scattering rates in GaAs/AlGaAs 2DEG samples below 0.5 K. *Surface Science*, 361-362:537–541, July 1996.

[101] M. Moskalets and M. Büttiker. Floquet scattering theory of quantum pumps. *Physical Review B*, 66(20):205320+, November 2002.

[102] M. Moskalets, P. Samuelsson, and M. Büttiker. Quantized Dynamics of a Coherent Capacitor. *Physical Review Letters*, 100(8):086601+, February 2008.

[103] Michael Moskalets and Markus Büttiker. Spectroscopy of electron flows with single- and two-particle emitters. *Physical Review B*, 83:035316+, January 2011.

[104] Simon E. Nigg, Rosa López, and Markus Büttiker. Mesoscopic Charge Relaxation. *Physical Review Letters*, 97(20):206804+, November 2006.

[105] H. Nyquist. Thermal Agitation of Electric Charge in Conductors. *Physical Review Online Archive (Prola)*, 32(1):110–113, July 1928.

[106] S. Ol'khovskaya, J. Splettstoesser, M. Moskalets, and M. Büttiker. Shot Noise of a Mesoscopic Two-Particle Collider. *Physical Review Letters*, 101(16):166802+, October 2008.

[107] Jukka P. Pekola, Juha J. Vartiainen, Mikko Möttönen, Olli-Pentti Saira, Matthias Meschke, and Dmitri V. Averin. Hybrid single-electron transistor as a source of quantized electric current. *Nature Physics*, 4(2):120–124, February 2008.

[108] Loren Pfeiffer, K. W. West, H. L. Stormer, and K. W. Baldwin. Electron mobilities exceeding 10[sup 7] cm[sup 2]/V s in modulation-doped GaAs. *Applied Physics Letters*, 55(18):1888–1890, 1989.

[109] M. Pioro-Ladrière, John Davies, A. Long, A. Sachrajda, Louis Gaudreau, P. Zawadzki, J. Lapointe, J. Gupta, Z. Wasilewski, and S. Studenikin. Origin of switching noise in GaAsAlxGa1xAs lateral gated devices. *Physical Review B*, 72(11), September 2005.

[110] Franck Pobell. *Matter and Methods at low temperatures, 2nd Edition.* Springer, 1996 edition.

[111] G. E. Ponchak, E. M. Tentzeris, and L. P. B. Katehi. Characterization of finite ground coplanar waveguide with narrow ground planes. *Int. J. Microcircuits and Elect. Pack.*, 20:167–173, 1997.

[112] H. Pothier, P. Lafarge, C. Urbina, D. Esteve, and M. H. Devoret. Single-Electron Pump Based on Charging Effects. *EPL (Europhysics Letters)*, 17(3):249+, January 1992.

[113] A. Prêtre, H. Thomas, and M. Büttiker. Dynamic admittance of mesoscopic conductors: Discrete-potential model. *Physical Review B*, 54(11):8130–8143, September 1996.

[114] Peter J. Price. Hot electrons in a GaAs heterolayer at low temperature. *Journal of Applied Physics*, 53(10):6863–6866, 1982.

[115] Simon Ramo, John R. Whinnery, and Theodore Van Duzer. *Fields and waves in communication electronics, 3rd Edition.* John Wiley and sons, 1994.

[116] D. J. Reilly. Phenomenological model for the 0.7 conductance feature in quantum wires. *Physical Review B*, 72(3):033309+, July 2005.

[117] B. Reulet, J. Senzier, and D. E. Prober. Environmental Effects in the Third Moment of Voltage Fluctuations in a Tunnel Junction. *Physical Review Letters*, 91(19):196601+, November 2003.

[118] L. H. Reydellet, P. Roche, D. C. Glattli, B. Etienne, and Y. Jin. Quantum Partition Noise of Photon-Created Electron-Hole Pairs. *Physical Review Letters*, 90(17):176803+, April 2003.

[119] M. Reznikov, M. Heiblum, Hadas Shtrikman, and D. Mahalu. Temporal Correlation of Electrons: Suppression of Shot Noise in a Ballistic Quantum Point Contact. *Physical Review Letters*, 75:3340–3343, October 1995.

[120] A. Robinson and C. Barnes. Classical dynamics of electrons in quantized-acoustoelectric-current devices. *Physical Review B*, 63(16), April 2001.

[121] P. Roche, J. Ségala, D. C. Glattli, J. T. Nicholls, M. Pepper, A. C. Graham, K. J. Thomas, M. Y. Simmons, and D. A. Ritchie. Fano Factor Reduction on the 0.7 Conductance Structure of a Ballistic One-Dimensional Wire. *Physical Review Letters*, 93:116602+, September 2004.

[122] Valentin S. Rychkov, Mikhail L. Polianski, and Markus Büttiker. Photon-assisted electron-hole shot noise in multiterminal conductors. *Physical Review B*, 72(15):155326+, October 2005.

[123] P. Samuelsson, E. V. Sukhorukov, and M. Büttiker. Two-particle aharonov-bohm effect and entanglement in the electronic hanbury brown˘twiss setup. *Physical Review Letters*, 92(2):026805+, January 2004.

[124] R. J. Schoelkopf, P. J. Burke, A. A. Kozhevnikov, D. E. Prober, and M. J. Rooks. Frequency Dependence of Shot Noise in a Diffusive Mesoscopic Conductor. *Physical Review Letters*, 78(17):3370–3373, April 1997.

[125] R. J. Schoelkopf, A. A. Kozhevnikov, D. E. Prober, and M. J. Rooks. Observation of "Photon-Assisted" Shot Noise in a Phase-Coherent Conductor. *Physical Review Letters*, 80:2437–2440, March 1998.

[126] Yu Sharvin. on the possible method for studying fermi surfaces. *Zh. Eksp. Teor. Fiz.*, 48:984+, 1965.

[127] J. M. Shilton, V. I. Talyanskii, M. Pepper, D. A. Ritchie, J. E. F. Frost, C. J. B. Ford, C. G. Smith, and G. A. C. Jones. High-frequency single-electron transport in a quasi-one-dimensional GaAs channel induced by surface acoustic waves. *Journal of Physics: Condensed Matter*, 8(38):L531+, September 1996.

[128] Rainee N. Simons. *Coplanar waveguide circuits, components ans systems*. John Wiley and sons, 2001.

[129] Janine Splettstoesser, Michael Moskalets, and Markus Büttiker. Two-Particle Nonlocal Aharonov-Bohm Effect from Two Single-Particle Emitters. *Physical Review Letters*, 103(7):076804+, August 2009.

[130] Janine Splettstoesser, Sveta Ol'khovskaya, Michael Moskalets, and Markus Büttiker. Electron counting with a two-particle emitter. *Physical Review B*, 78(20):205110+, November 2008.

[131] H. L. Störmer. Electron mobilities in modulation-doped GaAs-(AlGa)As heterostructures. *Surface Science*, 132(1-3):519–526, September 1983.

[132] H. L. Störmer, R. Dingle, A. C. Gossard, W. Wiegmann, and M. D. Sturge. Twodimensional electron gas at differentially doped GaAsAlxGa1xAs heterojunction interface. *Journal of Vacuum Science and Technology*, 16:1517–1519, September 1979.

[133] Horst L. Stormer. The fractionnal quantum hall effect. December 1998.

[134] M. Switkes, C. M. Marcus, K. Campman, and A. C. Gossard. An Adiabatic Quantum Electron Pump. *Science*, 283(5409):1905–1908, March 1999.

[135] V. I. Talyanskii, J. M. Shilton, M. Pepper, C. G. Smith, C. J. B. Ford, E. H. Linfield, D. A. Ritchie, and G. A. C. Jones. Single-electron transport in a one-dimensional channel by high-frequency surface acoustic waves. *Physical Review B*, 56:15180–15184, December 1997.

[136] Sander J. Tans, Michel H. Devoret, Hongjie Dai, Andreas Thess, Richard E. Smalley, L. J. Geerligs, and Cees Dekker. Individual single-wall carbon nanotubes as quantum wires. *Nature*, 386(6624):474–477, April 1997.

[137] K. J. Thomas, J. T. Nicholls, N. J. Appleyard, M. Y. Simmons, M. Pepper, D. R. Mace, W. R. Tribe, and D. A. Ritchie. Interaction effects in a one-dimensional constriction. *Physical Review B*, 58:4846–4852, August 1998.

[138] K. J. Thomas, J. T. Nicholls, M. Y. Simmons, M. Pepper, D. R. Mace, and D. A. Ritchie. Possible Spin Polarization in a One-Dimensional Electron Gas. *Physical Review Letters*, 77(1):135–138, July 1996.

[139] T. J. Thornton, M. Pepper, H. Ahmed, D. Andrews, and G. J. Davies. One-Dimensional Conduction in the 2D Electron Gas of a GaAs-AlGaAs Heterojunction. *Physical Review Letters*, 56:1198–1201, March 1986.

[140] Tuttle. Thermal and electrical conductivitymeasurements of cda 510 phosphor bronze.

[141] B. J. van Wees, H. van Houten, C. W. J. Beenakker, J. G. Williamson, L. P. Kouwenhoven, D. van der Marel, and C. T. Foxon. Quantized conductance of point contacts in a two-dimensional electron gas. *Physical Review Letters*, 60(9):848–850, February 1988.

[142] Mihajlo Vanević, Yuli V. Nazarov, and Wolfgang Belzig. Elementary Events of Electron Transfer in a Voltage-Driven Quantum Point Contact. *Physical Review Letters*, 99(7):076601+, August 2007.

[143] S. Washburn, R. J. Haug, K. Y. Lee, and J. M. Hong. Noise from backscattered electrons in the integer and fractional quantized Hall effects. *Physical Review B*, 44:3875–3879, August 1991.

[144] D. A. Wharam, T. J. Thornton, R. Newbury, M. Pepper, H. Ahmed, J. E. F. Frost, D. G. Hasko, D. C. Peacock, D. A. Ritchie, and G. A. C. Jones. One-dimensional transport and the quantisation of the ballistic resistance. *Journal of Physics C: Solid State Physics*, 21(8):L209+, March 1988.

[145] A. Yacoby, U. Sivan, C. P. Umbach, and J. M. Hong. Interference and dephasing by electron-electron interaction on length scales shorter than the elastic mean free path. *Physical Review Letters*, 66:1938–1941, April 1991.

[146] Yu, G. Gershon, D. Shovkun, Levitov, and M. Reznikov. Measurement of Counting Statistics of Electron Transport in a Tunnel Junction. *Physical Review Letters*, 95(17):176601+, October 2005.

[147] H. Z. Zheng, H. P. Wei, D. C. Tsui, and G. Weimann. Gate-controlled transport in narrow gaas/algaas heterostructures. *Physical Review B*, 34:5635–5638, October 1986.